Direct Grid Connection and Low Voltage Ride-Through for a Slip Synchronous-Permanent Magnet Wind Turbine Generator

by

Ulwin Hoffmann

Thesis presented in partial fulfilment of the requirements for the degree of Master of Science in Engineering at Stellenbosch University

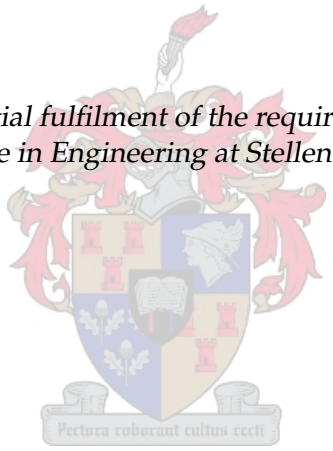

Supervisor: Prof. Maarten Jan Kamper

Department of Electrical & Electronic Engineering,
University of Stellenbosch,
Private Bag X1, 7602 Matieland, South Africa.

March 2012

DECLARATION

By submitting this thesis electronically, I declare that the entirety of the work contained therein is my own, original work, that I am the sole author thereof (save to the extent explicitly otherwise stated), that reproduction and publication thereof by Stellenbosch University will not infringe any third party rights and that I have not previously in its entirety or in part submitted it for obtaining any qualification.

Date: March 2012 .....

ABSTRACT

Direct Grid Connection and Low Voltage Ride-Through for a Slip Synchronous-Permanent Magnet Wind Turbine Generator

U. Hoffmann

Department of Electrical & Electronic Engineering,
University of Stellenbosch,
Private Bag X1, 7602 Matieland, South Africa.

Thesis: MScEng (Elec)

March 2012

The slip synchronous-permanent magnet generator (SS-PMG) is a direct-driven, direct-to-grid generator for wind turbine applications. This investigation focuses on achieving automated grid connection and low voltage ride-through for a small-scale SS-PMG. To reduce cost and complexity, components such as blade pitch controllers and frequency converters are avoided. Instead, electromagnetic braking is employed to control turbine speed prior to grid synchronisation and compensation resistances are used to facilitate grid fault ride-through.

The conditions under which the SS-PMG can be successfully synchronised with the grid are determined, indicating a need for speed control. An evaluation of electromagnetic braking strategies reveals that satisfactory speed control performance can be achieved when employing back-to-back thyristors to switch in the braking load. Simulations show that controlled synchronisation can be executed successfully under turbulent wind conditions. All controllable parameters are held within safe limits, but the SS-PMG terminal voltage drop is higher than desired.

Compensation is developed to allow the SS-PMG to ride through the voltage dip profile specified by the Irish distribution code. It is found that a combination of series and shunt resistances is necessary to shield the SS-PMG from the voltage dip, while balancing active power transfer. The flexibility offered by thyristor switching of the shunt braking load is instrumental in coping with turbulent wind conditions and unbalanced dips. The South African voltage dip profile is also managed with conditional success.

Following on from the theoretical design, the grid connection controller is implemented for practical testing purposes. Protection functions are developed to ensure safe operation under various contingencies. Before testing, problems with the operation of the thyristors are overcome.

Practical testing shows that grid synchronisation can be undertaken safely by obeying the theoretically determined conditions. The speed control mechanism is also shown to achieve acceptable dynamic performance. Finally, the SS-PMG is incorporated into a functioning wind turbine system and automated grid connection is demonstrated under turbulent wind conditions.

Future investigations may be focused on optimal control strategies, alternative solid-state switching schemes, and reactive power control. Low voltage ride-through should also be optimised for the South African dip profile and validated experimentally.

UITTREKSEL

Direkte Netwerkkoppeling en Lae Spanning Deurry van 'n Glip-Sinchroon Permanente Magneet Windturbine Generator

("Direct Grid Connection and Low Voltage Ride-Through for a Slip Synchronous-Permanent Magnet Wind Turbine Generator")

U. Hoffmann

Departement Elektries & Elektroniese Ingenieurswese,
Universiteit van Stellenbosch,
Privaatsak X1, 7602 Matieland, Suid Afrika.

Tesis: MScIng (Elek)

Maart 2012

Die glip-sinchroon permanente magneet generator (GS-PMG) is 'n direkte dryf, direkte netwerkgekoppelde generator vir windturbine toepassings. Hierdie ondersoek fokus op die bereiking van 'n ge-outomatiseerde netwerkkoppeling en lae spanning deurry vir 'n kleinskaalse GS-PMG. Om kostes en kompleksiteit te verminder, word komponente soos lemsteekbeheerders en frekwensie-omsetters vermy. In plaas daarvan word elektromagnetiese remwerking gebruik om die turbine spoed, voorgaande net-werksinchronisasie, te beheer, en word kompensasieweerstande gebruik om netwerkfoutdeurry te handhaaf.

Die omstandighede waaronder die GS-PMG suksesvol met die netwerk gesinchroniseer kan word, is vasgestel en dit het die behoefte aan spoedbeheer uitgewys. 'n Evaluering van elektromagnetiese remstrategië wys uit dat 'n bevredigende spoedbeheervermoë verkry kan word as anti-parallelle tiristors gebruik word om die remlas te skakel. Simulasies wys dat beheerde netwerksinchronisasie suksesvol uitgevoer kan word, selfs onder turbulente windtoestande. Alle beheerbare parameters is binne veilige perke gehou, maar die GS-PMG se klemspanningsval is gevind as hoë as verwag.

Kompensasie is ontwikkel om die GS-PMG toe te laat om deur die spanningsvalprofiel, soos gespesifieer deur die Ierse distribusiekode, te ry. Dit is gevind dat 'n kombinasie van serie- en parallelle weerstande nodig is om die GS-PMG teen die spanningsval te beskerm, terwyl aktiewe drywingsoordrag gebalanseer word. Die buigbaarheid wat verkry word met die tiristorskakeling van die parallele weerstand is noodsaaklik in die hanteering van turbulente windtoestande en ongebalanseerde spanningsvalle. Die Suid-Afrikaanse spanningsvalprofiel is ook met voorwaardelike sukses hanteer.

In opvolg van die teoretiese ontwerp is die netwerkkoppelingsbeheerder vir praktiese toetsdoeleindes in werking gestel. Beskermingsfunksies is ontwikkel om veilige werking onder verskeie gebeurlikhede te verseker. Die probleme met die werking van die tiristors is oorkom voor die aanvang van die toetse.

Die praktiese toetse bewys dat netwerksinchronisasie veilig gedoen kan word deur die teoretiese bepaalde voorwaardes te volg. Dit is ook getoon dat met die spoedbeheermeganisme aanvaarbare dinamiese gedrag verkry kan word. Ten laaste is die GS-PMG in 'n werkende windturbinestelsel geïnkorporeer en outomatiese netwerkkoppeling is onder turbulente windtoestande gedemonstreer.

Toekomstige ondersoeke kan toegespits word op optimale beheerstrategië, alternatiewe vaste toestand skakelingskemas en reaktiewe drywingsbeheer. Lae spanning deurry moet nog vir die Suid-Afrikaanse spanningsprofiel ge-optimeer en eksperimenteel bevestig word.

ACKNOWLEDGEMENTS

I am overwhelmingly grateful to God for His grace and provision in my life.

I also owe a great debt of gratitude to my fellow students and the technical staff in the EMLab and Electrical Engineering Workshop, who contributed ideas, practical assistance and positive morale. Especially to Ivan Hobbs, Johannes Potgieter, David Groenewald, Petro Petzer, Andre Swart, Murray Jumat, Fred Fourie, Will Esterhuyse, Herman du Preez, and Abri Stegmann.

Prof. Maarten Kamper contributed conceptually and materially to this work, making it possible in the first place. I am deeply appreciative of this and of his supervision throughout the project.

Finally, I am thankful to my family and friends, who have offered unfailing support.

Figure 1: A successful day at the office.

DEDICATIONS

To my family members, who have supported me from the very beginning of my studies.

LIST OF PUBLICATIONS

Conference Proceedings

1. U. Hoffmann and M.J. Kamper, "Low Voltage Ride-Through Compensation for a Slip-Permanent Magnet Wind Turbine Generator," *20th Southern African Universities Power Engineering Conference (SAUPEC)*, Cape Town, South Africa, July 2011, pp. 191 – 196.

2. U. Hoffmann, P. Bouwer, and M.J. Kamper, "Direct Grid Connection of a Slip-Permanent Magnet Wind Turbine Generator," *3rd IEEE Energy Conversion Congress and Exposition (ECCE)*, Phoenix, Arizona, September 2011, pp. 2373 – 2380.

CONTENTS

LIST OF FIGURES

LIST OF TABLES

NOMENCLATURE

Abbreviations

Abbreviation	Description
ADC	Analogue to Digital Converter
AOA	Angle of Attack
BEM	Blade Element Momentum
BR	(Shunt) Braking Resistor
CSG	Conventional Synchronous Generator
DC	Direct Current
DFIG	Doubly-Fed Induction Generator
DG	Distributed Generation
WRSG	Wound Rotor Synchronous Generator
EG	Embedded Generation
EKF	Extended Kalman Filter
EMF	Electromotive Force
FAC	Firing Angle Controller
FACTS	Flexible Alternating Current Transmission System
FRT	Fault Ride-Through
GB	Gearbox
GCC	Grid Connection Controller
HV	High Voltage
IDE	Integrated Development Environment
IG	Induction Generator
IGBT	Insulated-Gate Bipolar Transistor
IM	Induction Motor
IPP	Independent Power Producer
ISR	Interrupt Service Routine
LV	Low Voltage
LVRT	Low Voltage Ride-Through
MCU	Micro-Controller Unit
MPPT	Maximum Power Point Tracking
MV	Medium Voltage
NERSA	National Energy Regulator of South Africa
O&M	Operations and Maintenance
PAC	Phase Angle Control
PCC	Point of Common Coupling

Abbreviation	Description
PGC	Point of Generator Connection
PI	Proportional-Integral
PV	Photovoltaic
PLL	Phase-Locked Loop
PMG	Permanent Magnet Generator
PMIG	Permanent Magnet Induction Generator
PM-LVRT	Power Mapping Low Voltage Ride-Through
PMSG	Permanent Magnet Synchronous Generator
RMS	Root Mean Squared
ROCOF	Rate of Change of Frequency
SCIG	Squirrel Cage Induction Generator
SFR	Synchronous Frequency Range
SG	Synchronous Generator
SKO	Simplified Kalman Observer
SMD	Spring-Mass-Damper
SMO	Sliding Mode Observer
SPI	Serial Peripheral Interface
SR	Series (Compensation) Resistor
SSC	Solid-State Converter
SS-PMG	Slip Synchronous-Permanent Magnet Generator
STATCOM	Static Synchronous Compensator
SVC	Static VAR Compensator
THD	Total Harmonic Distortion
VSI	Voltage Source Inverter
VSD	Variable Speed Drive
WECS	Wind Energy Conversion System(s)
WTG	Wind Turbine Generator
WRIG	Wound Rotor Induction Generator

Symbols

Parameter	Description	Unit
A_t	swept area of wind turbine rotor	[m^2]
B_m	PM-rotor viscous friction coefficient	[Nm/rad^{-1}]
B_{m0}	PM-rotor turbine static friction constant	[Nm]
B_r	slip-rotor viscous friction coefficient	[Nm/rad^{-1}]
B_{r0}	slip-rotor static friction constant	[Nm]
C_{br}	braking torque boosting capacitance	[F]

Parameter	Description	Unit
C_c	compensating capacitance	[F]
C_{cs}	shunt compensating capacitance	[F]
c_p	coefficient of performance	[#]
D_t	wind turbine rotor diameter	[m]
$\mathbf{E_{gen}}$	Induced SS-PMG EMF phasor	[V]
E_{grid}	network source RMS phase voltage	[V]
e	voltage error signal	[V]
e_f	time-dependent faulted grid voltage	[V]
e_α	instantaneous induced α voltage component	[V]
e_β	instantaneous induced β voltage component	[V]
f_{err}	instantaneous electrical frequency error	[Hz]
f_{gen}	instantaneous electrical frequency of generator	[Hz]
f_{grid}	instantaneous electrical frequency of grid	[Hz]
f_R	rated electrical frequency	[Hz]
f_s	ADC sampling frequency	[Hz]
H_l	linear thyristor load command	[#]
H_{th}	direct thyristor load command	[#]
h_t	wind turbine hub height	[m]
$\mathbf{I_{gen}}$	SS-PMG current phasor	[A]
I_R	rated line current	[A]
I_{rms}	Average RMS current for sample period	[A]
i	sampling index	[#]
i_a	instantaneous phase-A current	[A]
i_b	instantaneous phase-B current	[A]
i_c	instantaneous phase-C current	[A]
i_{dr}	instantaneous d-axis slip-rotor current	[A]
i_{ds}	instantaneous d-axis stator current	[A]
$\bar{i}_{gen}$	SS-PMG terminal current space vector	[A]
i_{qr}	instantaneous q-axis slip-rotor current	[A]
i_{qs}	instantaneous q-axis stator current	[A]
i_α	instantaneous α current component	[A]
i_β	instantaneous β current component	[A]
J_m	PM-rotor turbine rotational inertia	[kg·m^2]
J_t	wind turbine rotational inertia	[kg·m^2]
J_{tr}	wind turbine and slip-rotor rotational inertia	[kg·m^2]
J_r	slip-rotor rotational inertia	[kg·m^2]
K_F	shaping filter gain	[#]
K_i	integral gain for PI speed controller	[#]

Parameter	Description	Unit
K_p	proportional gain for PI speed controller	[#]
$K_{\phi i}$	integral gain for PI phase angle controller	[#]
$K_{\phi p}$	proportional gain for PI phase angle controller	[#]
k	sample number	[#]
k_σ	terrain roughness proportionality constant	[#]
L	wind turbulence length	[m]
L_{ds}	stator d-axis inductance	[H]
L_{dr}	slip-rotor d-axis inductance	[H]
L_{qs}	stator q-axis inductance	[H]
L_{qr}	slip-rotor q-axis inductance	[H]
L_s	stator inductance	[H]
M_p	speed overshoot	[%]
m_1	first Nichita constant	[#]
m_2	second Nichita constant	[#]
N	sample window size	[#]
N_p	number of generator poles	[#]
N_{zc}	number of zero-crossings	[#]
P_{gen}	real power output of SS-PMG	[W]
P_t	wind turbine power output	[W]
R_B	thyristor bulk resistance	[Ω]
R_{br}	braking resistance	[Ω]
R_{dx}	equivalent resistance of distribution transformer	[p.u.]
R_{grid}	equivalent resistance of electrical network	[Ω]
R_R	thyristor reverse resistance	[Ω]
R_r	slip-rotor resistance	[Ω]
R_s	stator resistance	[Ω]
R_{sr}	series compensation resistance	[Ω]
R_t	radius of wind turbine rotor	[m]
R_{ux}	equivalent resistance of unit transformer	[p.u.]
R_x	equivalent resistance of grid-tie transformers	[Ω]
S_R	rated apparent power	[VA]
T_m	Net PM-rotor torque	[Nm]
T_n	Net shaft torque	[Nm]
T_p	Net slip-rotor torque	[Nm]
T_R	rated input torque	[Nm]
T_r	electromagnetic counter torque developed by slip-rotor	[Nm]
T_s	electromagnetic counter torque developed by stator	[Nm]
T_t	torque developed by wind turbine	[Nm]

Parameter	Description	Unit
t	simulation time	[s]
t_c	contactor actuation delay	[s]
t_F	shaping filter time constant	[s]
t_{int}	zero-crossing measurement time interval	[s]
t_p	peak time	[s]
t_r	rise time	[s]
t_{rem}	removal delay time	[s]
t_S	wind speed sampling time interval	[s]
t_s	2% settling time	[s]
V_F	thyristor forward voltage	[V]
V_{gen}	SS-PMG RMS terminal voltage	[V]
$\mathbf{V_{gen}}$	SS-PMG terminal voltage phasor	[V]
V_{grid}	PGC RMS terminal voltage	[V]
$\mathbf{V_{grid}}$	PGC terminal voltage phasor	[V]
V_R	effective (RMS) voltage applied to resistive load	[V]
V_{RMS}	generic RMS voltage	[V]
V_{win}	sampling window voltage	[V]
v_{ds}	instantaneous d-axis stator voltage	[V]
$\overline{v}_{gen}$	SS-PMG terminal voltage space vector	[V]
$\overline{v}_{grid}$	grid (PGC) voltage space vector	[V]
v_{gen}	instantaneous SS-PMG terminal voltage	[V]
v_{grid}	instantaneous PGC terminal voltage	[V]
v_i	instantaneous voltage sample	[V]
v_{qs}	instantaneous q-axis stator voltage	[V]
v_α	instantaneous α-axis voltage	[V]
$\overline{v}_{\alpha\beta}$	generic $\alpha\beta$ voltage space vector	[V]
v_β	instantaneous β-axis voltage	[V]
U_w	mean wind speed	[m/s]
u_w	instantaneous effective wind speed	[m/s]
V_min	minimum grid voltage threshold	[V]
V_res	restored grid voltage level	[V]
v_a	instantaneous phase-A voltage	[V]
v_b	instantaneous phase-B voltage	[V]
v_c	instantaneous phase-C voltage	[V]
v_d	instantaneous direct voltage	[V]
v_q	instantaneous quadrature voltage	[V]
v_R	rated line voltage	[V]
X_{dx}	equivalent reactance of distribution transformer	[p.u.]

Parameter	Description	Unit
X_{grid}	equivalent reactance of electrical network	[Ω]
X_{ux}	equivalent reactance of unit transformer	[p.u.]
X_x	equivalent reactance of grid-tie transformers	[Ω]
α	thyristor firing delay angle	[elec. $^\circ$]
γ	spatial filter decay factor	[#]
Δf	frequency difference	[Hz]
Δf_t	frequency difference threshold	[Hz]
$\Delta\phi$	voltage phase angle difference	[elec. $^\circ$]
$\Delta\phi_t$	voltage phase angle difference threshold	[elec. $^\circ$]
Δv	voltage magnitude difference	[V]
Δv_t	voltage magnitude difference threshold	[V]
θ	generator rotor angle (relative to grid)	[elec. $^\circ$]
θ_{est}	estimated generator rotor angle	[elec. $^\circ$]
λ_{mr}	PM-flux linkage on slip-rotor side	[Wb·t]
λ_{ms}	PM-flux linkage on stator side	[Wb·t]
μ	spatial filter constant	[#]
ρ	air density	kg·m^{-3}
σ	standard deviation	[#]
σ_u	turbulent intensity standard deviation	[#]
$\phi_{\alpha\beta}$	angle of generic $\alpha\beta$ voltage space vector	[elec. $^\circ$]
ϕ_{gen}	angle of SS-PMG terminal voltage space vector	[elec. $^\circ$]
ϕ_{grid}	angle of grid voltage space vector	[elec. $^\circ$]
ω_m	mechanical rotational velocity of the PM-rotor	[mech. rad/s]
ω_{me}	electrical rotational velocity of the PM-rotor	[elec. rad/s]
ω_{est}	estimated electrical rotational velocity	[elec. rad/s]
ω_R	rated rotational speed	[mech. rad/s]
ω_{sl}	rotational slip velocity	[mech. rad/s]
ω_{sle}	electrical rotational slip velocity	[elec. rad/s]
ω_t	rotational velocity of the wind turbine rotor	[mech. rad/s]

Definition of Terms

There are a number of ambiguous terms used to refer to different components and systems in the field of wind energy conversion. The following definitions attempt to establish a consistent reference scheme for use in this document.

- WECS: the complete mechanical-electrical system that comprises wind turbine, generator, mechanical drive train, as well as the control system and grid interface components, if present. This term can be singular or plural, depending on the context.

- WTG: an electrical generator, specifically designed for use in a WECS. Certain subcategories are relevant to the discussions which follow:
  - IG: typically, a squirrel-cage induction generator but can also refer to wound-rotor machines, where the rotor is not connected to a converter.
  - DFIG: a wound-rotor induction generator whose rotor is fed by a frequency converter.
  - WRSG: a wound rotor synchronous generator with controllable excitation and, typically, a large number of salient poles.
  - PMSG: a synchronous generator, where the rotor develops flux through the use of permanent magnets. Pole count is usually medium to high.
  - SS-PMG: a hybrid machine with both synchronous and slip characteristics, discussed in detail in Chapters 1 and 3.
  - SG: any type of synchronous generator, including WRSG, PMSG, and SS-PMG.
- Multibrid: a WECS with a multi-pole permanent magnet WTG that makes use of a one- or two-stage gearbox and a full-scale frequency converter. Intended to achieve optimal power-price ratio for MW-class systems.
- Topology: in the context of a WECS, this term refers to the nature and configuration of components that comprise the system. The type of turbine, mechanical transmission, generator, and grid connection mechanism (e.g. frequency converter) and how these components are arranged constitutes the topology of the WECS.
- FRT: the action of remaining connected to the electrical network during faults, in order to avoid a significant loss of WTG power production immediately after the fault [2]. A specific example of this is LVRT, which refers to situations where a voltage dip occurs on the electrical network.
- Power Control Capability: being able to provide grid support. In other words, to assist in maintaining the stability of the grid in terms of frequency and voltage.
- DG: generation capacity which is connected to the distribution network, close to network loads. DG also typically makes use of non-conventional energy sources [7]. This is in contrast to conventional generating capacity, which feeds into the transmission network and is not necessarily close to the loads it supplies.
- CSG: a blanket term for the types of synchronous generator used in conventional steam, gas, hydro and nuclear power plants. This includes large salient-pole machines (for hydro) and more compact, high speed machines for other plants. The capability to control both prime mover and excitation is assumed in this case.

CHAPTER 1

INTRODUCTION

This work focuses on the direct grid connection and low voltage ride-through of a slip synchronous-permanent magnet generator (SS-PMG) for wind turbine applications. To give context to the sections which follow, the role of wind energy in a global and a South African context is discussed. This is followed by a comparison of the SS-PMG with contemporary grid-connected wind turbine generator topologies. The chapter concludes with the problem statement and objectives for this work.

1.1 A Global Perspective on Wind Energy

Contemporary society is energy intensive. This is especially true of developed nations, but is becoming ever more applicable to developing nations in Asia, Africa and South America as well. One of the most efficient and convenient means to distribute and use energy is in the form of electricity. This implies that contemporary society is highly dependent upon electricity: a sufficient, reliable, and sustainable supply of electrical energy is essential for social development and stability.

For the last century, fossil fuels have constituted the most important primary energy source for the generation of electricity. There are, however, clear indications that total reliance on fossil fuels does not lead to a sufficient, reliable and sustainable supply of electrical energy. South Africa itself provided a dramatic illustration of this in recent times [8], although policy issues may also have been to blame in that case.

There is growing awareness that society's energy supply mix should be diversified to reduce reliance upon fossil fuels, particularly coal and oil. This transition is intended to improve security of supply, reduce harmful emissions, and can even be expected to limit costs as fossil fuel supplies dwindle over the next centuries. Alternative sources of energy span a wide spectrum from nuclear, geothermal, and large-scale hydro to emerging renewable technologies: small-scale hydro, wind, solar, tidal, and wave energy, to name but a few.

Wind power has emerged as a leading renewable energy technology over the last half-century. According to [1], wind accounted for 63,5 % of global renewable energy generation capacity in 2010 (excluding large-scale hydro power). Fig. 1.1 shows global installed wind power capacity over the last 15 years: today, wind power has a large installed base and has experienced an average annual growth rate of 27 % between 2005 and 2010.

Wind power is substantially cheaper than solar technologies on large scales, but prices of smaller systems are still restrictive. Without government incentives electricity from onshore utility-scale wind farms costs approximately 0,07 USD/kWh, whereas small-scale wind power systems deliver energy at an average of 0,20 USD/kWh [1]. Cost is thus a limiting factor for smaller users.

Compared to other alternative technologies, wind power is an attractive investment from an environmental perspective: according to [9], wind offers the lowest lifetime CO_2 emissions of all the new

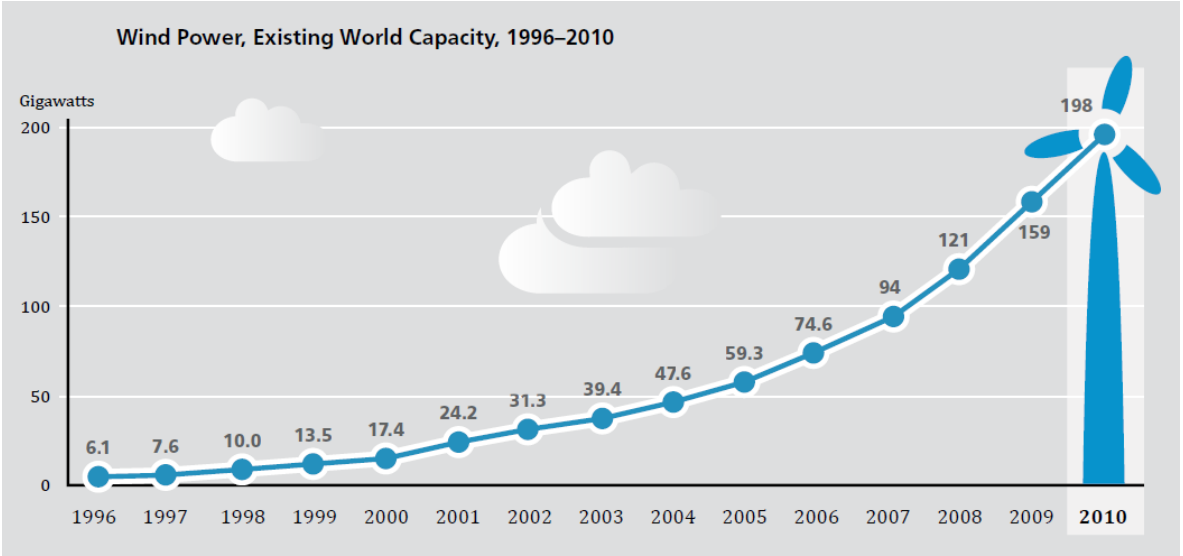

Figure 1.1: Global installed wind power capacity from 1996 to 2010. From: [1]

renewable technologies and is only bettered by large-scale hydro and nuclear. Energy payback time of wind power is the second shortest, after hydro, and is 3,16 times faster than nuclear.

Looking forward, a number of important global trends have emerged in the wind power sector [1]. Firstly, there has been a gradual uptake in offshore wind farm projects, even though onshore projects are still the most popular. Secondly, the average size of wind turbines in both onshore and offshore wind farms continues to increase. Additionally, gearbox-less designs are gaining market share, most likely as a result of better reliability.

On the other hand, small-scale grid-connected wind energy conversion systems are becoming increasingly popular. This correlates with broader geographic dispersal of wind power and more community ownership of projects. Interestingly, growth in wind power in 2010 was the greatest in the developing world. This was mostly due to massive expansion in China, but it does indicate that wind power is an important technology for developing nations.

From a control perspective, grid-connected WECS are increasingly being expected to perform similar functions to conventional power plants [2]. In other words, WECS should be able to provide frequency and voltage support to the electrical grid. Fault ride-through and power control capabilities are becoming important metrics in gauging the performance of new designs. This is to ensure stability of the electrical network when high concentrations of wind power are present.

Reflecting on the above trends, it is clear that wind power is already playing a role in the diversification of society's energy supply. Indeed, wind will continue to be an important renewable energy resource for the future. Growth is being experienced in both the large-scale and the small-scale wind power markets but technical requirements are becoming ever more onerous.

1.2 Wind Energy in South Africa

1.2.1 Large-Scale Prospects

South Africa appears to be on the cusp of substantial renewable energy development. The Integrated Resource Plan for Electricity 2010 – 2030 [10] makes provision for 17,8 GW of new grid-connected renewable energy-based generation. This equates to 42 % of planned new generation capacity, outside of that already under construction. Wind is expected to make the first and, ultimately, the most substantial contribution towards the renewable total, although the final breakdown is flexible.

In the first round of request for proposals (RFPs), wind power has been allocated 1850 MW of the total 3750 MW renewable capacity that is scheduled to come on line by 2016 [11]. The bulk of the wind power added to the grid is anticipated to be in the form of utility-scale wind farms, making use of MW-class turbines. Although localisation is considered in the application process, it is likely that most of the turbine and generator components will be purchased from foreign suppliers.

1.2.2 Small-Scale Prospects

Even though much attention is being focused on large-scale wind power projects in South Africa, global trends indicate that there is much to gain from developing the small-scale (sub 100 kW) market as well. This is especially true in the face of rapidly rising electricity costs [12].

It is noted by [13] that renewable energy is ideal for rural upliftment (electrification) in terms of cost, capacity and speed of deployment. It can also require relatively little O&M effort [14]. On the other hand, the most critical barriers to the adoption of renewable energy by developing nations appear to be cost [14] and awareness [15]. The best application for small-scale WECS will also vary, depending on local conditions and needs.

While large-scale WECS are used almost exclusively to supply energy to the national grid, smaller units can serve a variety of functions, for example:

- Powering a remote water pump through an 'electrical shaft'. This system replaces the conventional mechanical pumping system used on many farms for irrigation purposes with an electric pump powered by a WECS. The distance between pump and turbine can be substantial, allowing optimal siting of both components and the variability of the wind is not of concern, as long as a certain average amount of water can be pumped daily.

- Stand-alone operation. In such an application the WECS (possibly in combination with solar panels or a diesel generator) provides for all the electrical energy requirements of users in a remote location, where connection to the national grid would be too expensive. Such a system typically involves the use of storage batteries to level out the difference between instantaneous supply and demand. These systems are expensive on a per-kWh basis (3 to 7 times more than a utility scale wind farm [1]), but still undercut the cost of installing long transmission lines to reach the national grid.

- Grid-connected operation. In this case, the WECS is used to feed electrical energy into the national grid, either to reduce the owner's net energy consumption or purely to earn income through an IPP agreement. Compared to the stand-alone option, this approach has the advantage of using the grid as the energy storage medium: if the WECS is delivering more power than the user needs, this excess is absorbed by the grid and effectively offsets later use of grid-supplied energy when insufficient wind energy is available. As a result, this option may be undertaken with a lower capital investment and thus quicker pay-back period. However, this assumes that the user already has a sufficiently rated grid connection. The integration of the WECS with the grid must also be facilitated, but the state intends to ease this process by providing simplified tender documentation for projects of less than 5 MW [16].

1.2.3 Conclusion

The above discussions point towards a growing need for both large and small-scale WECS development in South Africa. Local manufacturers are already in operation [17; 18; 19] but, given the need for job creation and industrialisation, it would be logical to expand South African design and manufacturing capabilities in the wind energy sector.

In order to succeed, South African products will need to be cost-competitive and geared towards local applications. Affordability is a key issue: WECS are still prohibitively expensive for small investors, such as farmers or rural communities.

Both initial investment and lifetime costs need to be addressed. In this regard, grid-connected WECS are more appealing because they can be expected to offer better return on investment than stand-alone systems [14]. Operations and maintenance costs can be reduced by ensuring that technology is robust and that it can be serviced using local skills and equipment.

1.3 WECS Topologies

In this section we review the most popular WECS topologies for grid-connected applications, after which we introduce and compare the SS-PMG.

1.3.1 Type 1: Danish Concept IG

The so-called Danish Concept was developed in the 1950s [4] and was the first grid-tied topology to gain significant commercial success. It has been in wide use since the 1970s. In this design, represented by Fig. 1.2(a), a squirrel-cage IG is connected directly to the grid and is driven by a fixed speed wind turbine through a multi-stage gearbox. Stall-controlled turbines were originally used but, in later years, pitch control became popular.

A typical grid connection procedure for the IG is as follows [20; 21]: firstly, the wind is relied upon to accelerate the turbine-generator from rest (pitch control may be used to limit turbine torque at this stage). Once the generator is near synchronous speed, a soft-starter is employed to connect gradually to the grid. After grid connection is achieved and the soft-starter is bypassed with a contactor, one or more

shunt capacitor banks are connected to compensate for the steady-state reactive power requirements of the IG. Although smoother than a 'hard switch-on', this grid connection method still results in high transient currents and can negatively affect grid voltage stability.

Despite its long history and robust design, the Danish Concept is losing ground in terms of new installations [2]. Fig. 1.3 shows that newer designs are taking an ever larger share of the market. This is especially true for MW-class WECS and is a result of ever-increasing performance requirements from network operators and regulators.

Danish Concept WECS are inefficient at low wind speeds [22] and are incapable of MPPT. In addition, the SCIG does not provide sufficient grid voltage and frequency support during faults [23]. It also requires compensation to provide for its post-fault reactive power requirements [24; 25]. Finally, this type of WECS can become unstable on weak grids during turbulent wind conditions [26].

1.3.2 Type 2: DFIG

This topology is based around a DFIG driven by a variable speed wind turbine through a multi-stage gearbox. The stator of the DFIG is connected directly to the grid, while the wound rotor is connected through a partial-scale frequency converter, as shown in Fig. 1.2(b). DFIGs are typically more expensive and less robust than SCIGs [22] but have achieved a dominant market share in less than two decades of commercial operation (Fig. 1.3).

The primary appeal of the DFIG is better energy capture and reasonable economy. Because the DFIG is connected to a variable speed turbine, MPPT can be used to extract more energy from low

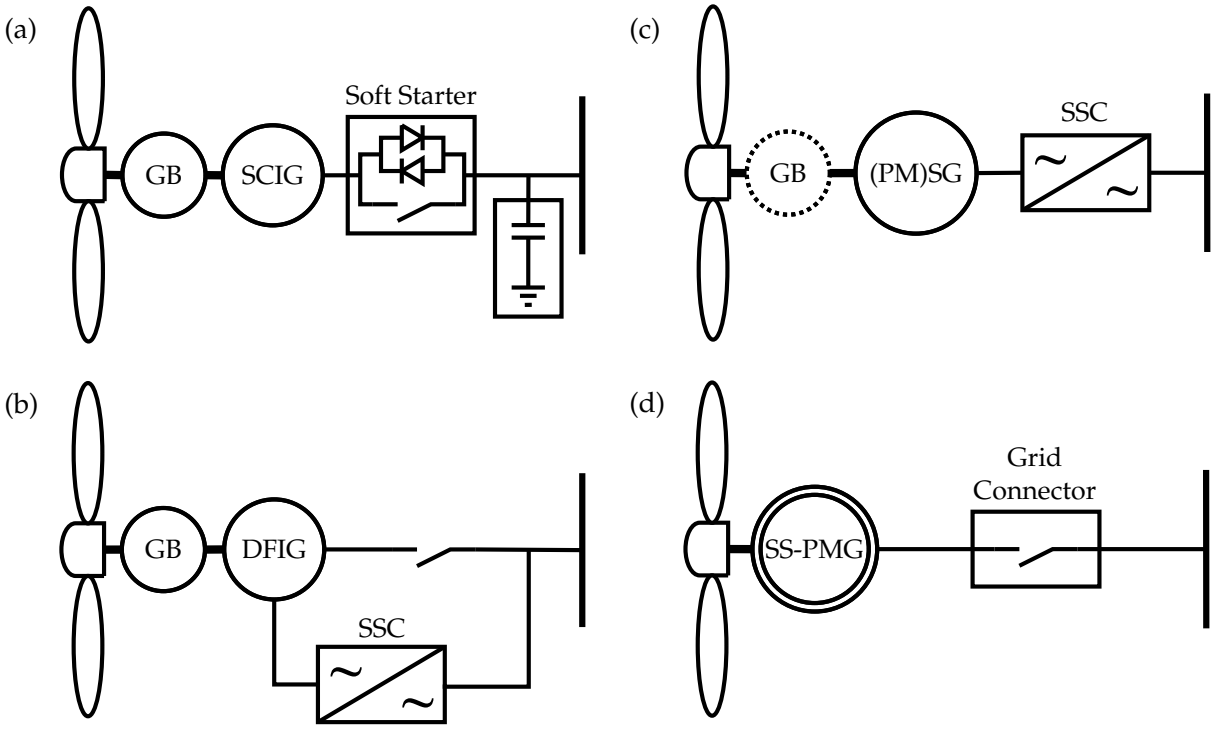

Figure 1.2: Single line diagrams of WECS topologies: (a) Danish Concept IG, (b) DFIG, (c) Full-Scale Converter Fed WTG, and (d) SS-PMG. The gearbox is optional in (c).

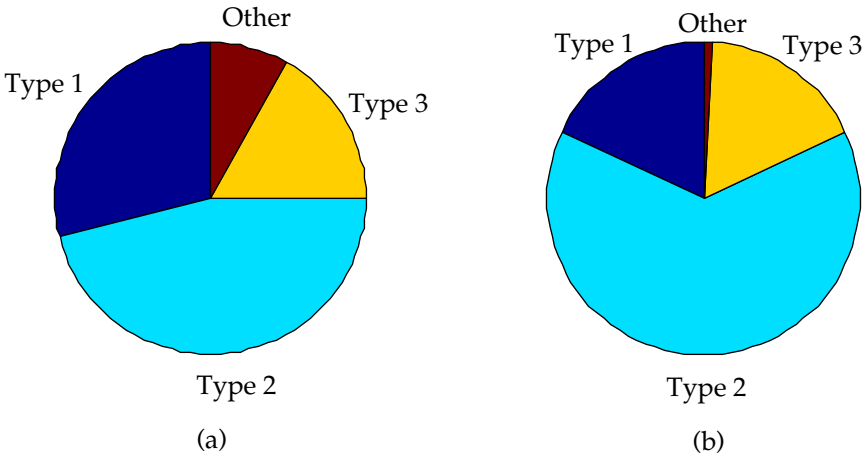

Figure 1.3: (a) Cumulative global market share of different WECS topologies in 2005 and (b) share of newly installed capacity in 2005 [2].

winds, while reducing mechanical stress and noise. Additionally, the DFIG can feed energy into the grid through its rotor, as well as its stator (energy flows are a function of wind conditions). There are, however, efficiency losses in both the converter and, especially, the gearbox [27].

Although the wound-rotor construction of the DFIG (with slip-rings) adds to cost and maintenance, the system requires a frequency converter with a kVA rating of only 25 % to 30 %. Other components—such as the turbine, gearbox, and nacelle—are very similar to those used in the Danish Concept. Upgrading to the DFIG concept was thus a natural step for many manufacturers.

Connecting a DFIG to the electrical grid entails meeting the same basic conditions as for CSGs [28; 21]. The stator voltages, frequency and phase angle must agree with the respective quantities on the grid. In this case, the wind is again relied upon to accelerate the turbine-generator from rest but synchronisation can occur as soon as cut-in rotational speed has been exceeded. Firstly, the converter itself synchronises with the grid and charges its DC bus. Once the converter is fully operational, it can bring the stator voltage magnitude, frequency, and phase angle into agreement with the grid by setting the rotor currents. The stator can then be connected smoothly to the grid by closing a contactor and active power transfer can commence.

The fault ride-through and grid support characteristics of a DFIG can be superior to that of an IG, but these aspects are a strong function of the control strategies employed in the converter. For example, the DFIG does not inherently contribute to network inertia in the way an IG or WRSG does. Extra control intervention is thus required to ensure that the DFIG provides useful inertial response for the network during faults [29]. In many cases, the converter is blocked during a fault and the rotor is switched on to a resistive load (crowbar) [30]. In such cases, the DFIG behaves like a normal IG during the fault.

1.3.3 Type 3: Converter-Fed WTG

This category includes any generator type that is connected to the grid through a full-scale frequency converter. Popular generator choices include WRSGs, PMSGs, and IGs. A variable speed wind turbine is used in all cases but the presence of a gearbox is optional, as shown in Fig. 1.2(c).

The use of a full-scale converter has many potential outcomes, but the universal advantage is improved controllability [2]. The type of converter can also vary, but the most promising options are the back-to-back VSI, the matrix converter, and the multi-level converter [22]. The converter is generally responsible for helping to achieve MPPT, while providing controllable active and reactive power exchange with the grid. In this way, the WECS can better emulate a traditional power plant.

If a high pole-count generator is used then a gearbox can be avoided, which achieves higher efficiency, lower acoustic noise, less maintenance, and (potentially) higher reliability [31; 3]. Gearboxes have a poor reliability track record in many areas [32], which explains why full-scale converter designs are gaining popularity in offshore applications, where replacement costs are prohibitive. Another approach is to use a medium pole-count generator with a low-ratio gearbox, a concept termed 'multibrid' [27].

Since the generator is never directly connected to the grid, it is only necessary for the grid side of the converter to synchronise itself with the electrical network. As such, synchronisation is smooth and can occur as soon the generator has exceeded cut-in rotational speed (or even beforehand).

With the correct control algorithms, full-scale converter WECS can meet fault ride-through and grid support requirements, including frequency support [33]. Performance in this regard is far superior to type 1 systems [2] but transferring all power through a converter does result in an efficiency penalty. Comprehensive protection must also be employed to protect the power electronics, which are particularly sensitive to over-currents.

A full-scale converter-fed PMSG is proving a popular choice for small-scale, grid-connected WECS [34]. The multi-pole PMSG avoids the need for electrical excitation or a gearbox, thus achieving a simple and efficient layout [27]. The cost of permanent magnet material and power electronics can, however, be prohibitive.

1.3.4 SS-PMG

The SS-PMG is a hybrid WTG design, which brings together beneficial aspects of both IGs and PMSGs [35; 36]. The proposed SS-PMG WECS employs neither a gearbox nor a frequency converter, as can be seen in Fig. 1.2(d). Instead, the SS-PMG is driven directly by a fixed speed wind turbine. Grid connection is also direct, through a grid connection controller, with no power electronics in use during normal operation.

1.3.4.1 Operating Principle

Direct grid connection of a conventional PMSG is regarded as problematic [22; 37; 38]. This is due to the very lightly damped relationship between power and generator torque angle, which can easily lead to instability. CSGs actually exhibit similar behaviour and generally have damper windings to counteract the problem.

Because damper windings are difficult to install in high pole-count generators, other solutions have been proposed for direct grid-connected (PM)SGs. These include the use of an external mechanical damper [3]; a hydrodynamic gearbox with adjustable vanes [39]; and a star-point frequency converter

with a 20 % rating [40]. In contrast, the SS-PMG concept integrates the damping action, along with other beneficial characteristics, into the generator itself.

The SS-PMG is a two-stage generator, consisting essentially of two back-to-back PMSGs. A conceptual layout of a radial-flux SS-PMG is shown in Fig. 1.4. The turbine and slip-rotor are mechanically bonded and rotate in unison. In practice, the turbine blades are mounted directly on to the backplate of the slip-rotor. The PM-rotor is able to rotate freely, without any mechanical connection to the other components. The grid-connected stator is stationary and bonded firmly to the nacelle.

The slip-rotor can be implemented as a short-circuited wound rotor or as a cage rotor. Together with the corresponding half of the PM-rotor, it constitutes a short-circuited PMSG, which develops substantial torque as soon as there is relative motion between the two rotors.

The second half of the PM-rotor couples with the stator to form a grid-connected PMSG. This side of the machine is driven indirectly by the torque from the wind turbine, which is transmitted through the first slip-rotor stage. The advantage of this connection is that it introduces damping and allows for some rotational speed difference between the turbine and the PM-rotor.

Fig. 1.5(a) shows a spring-mass-damper analogy for the electromagnetic connection between the rotor and stator of a conventional PMSG when its stator is connected directly to the grid. The turbine and PM-rotor constitute one mass, while the grid-connected stator forms another. There is virtually no damping in the connection between the two masses, which means that any disturbance introduced on the grid or turbine side will result in sustained oscillations between the rotor and stator.

In comparison, the SMD analogy for a grid-connected SS-PMG is shown in Fig. 1.5(b). In this case, there are effectively three masses: the turbine and slip-rotor; the PM-rotor; and the grid-connected stator. Although the connection between the PM-rotor and the stator is still very lightly damped, it is possible to avoid oscillations in this connection by making it substantially stiffer than the connection between the slip-rotor and the PM-rotor.

If the slip-rotor to PM-rotor connection is less stiff, then any disturbances will cause an oscillation

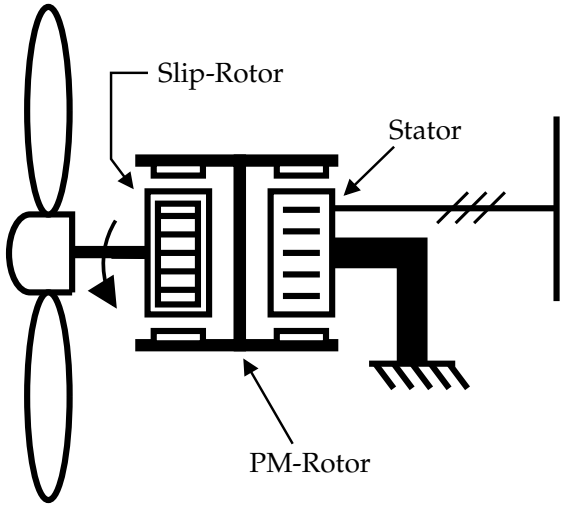

Figure 1.4: Cross-section of a conceptual SS-PMG layout.

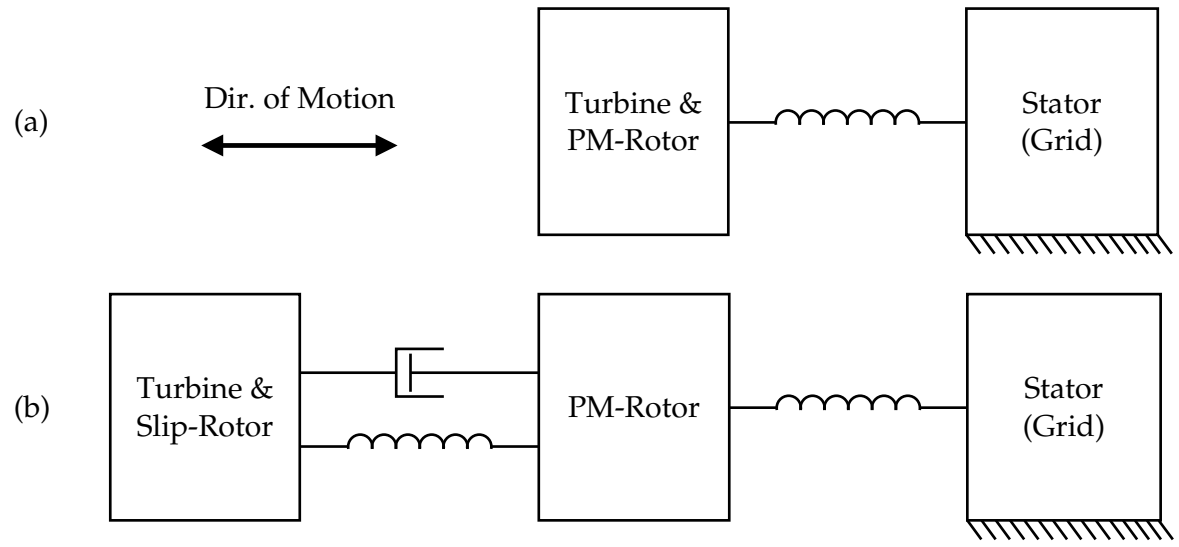

Figure 1.5: Spring-Mass-Damper analogy of (a) Conventional PMSG and (b) SS-PMG. Original concept from [3].

to develop between these two masses (in this case the PM-rotor and stator effectively form a single mass). Any such oscillations will quickly be attenuated because the slip-rotor to PM-rotor connection is sufficiently damped. As a result, the SS-PMG will be able to remain connected to the grid in a stable manner, despite torque disturbances from wind gusts and tower shadow effects [41].

An additional advantage of the SS-PMG design is that the turbine speed can vary (approximately $\pm 5\,\%$) even while the PM-rotor speed is effectively fixed at synchronous speed. This means that the energy present in a wind gust can be captured as an increase in the rotational kinetic energy of the turbine and slip-rotor. This energy can then be delivered in a more gradual manner to the grid, without imposing harsh mechanical loads on the turbine or injecting a current spike on to the network. Like the torque filtering described above, this behaviour is inherent to the SS-PMG and requires no control intervention to take place.

The characteristics of the SS-PMG discussed thus far show strong resemblance to those of a grid-connected IG. However, the SS-PMG is, in fact, superior to an IG in terms of its grid support capabilities. Since it is a direct-to-grid synchronous generator, the SS-PMG contributes positively towards network inertia and provides natural grid voltage support by supplying reactive power whenever the network voltage drops.

In [42] a permanent magnet induction generator, a relative of the SS-PMG, is connected to the grid in two ways. In the first case, the PMIG is switched on to the grid from standstill, which results in high rotor and stator currents. Synchronism is achieved, but with a settling time of more than 40 s. In the second case, the PMIG is brought to synchronous speed then connected to the grid with no attempt to match phase angles. This reduces transient currents, especially in the rotor, and achieves a much faster settling time.

The PMIG can be treated more like an IG than an SG in terms of grid connection. This corresponds with the objective of its design and is possible because the PM-induced flux linking its stator is relatively

weak. In comparison, the SS-PMG has significantly stronger PM-induced flux linkages and is designed to exhibit SG-like behaviour on its grid side. As a result, the grid connection techniques applied in [42] are not appropriate for the SS-PMG.

To synchronise the SS-PMG with the grid, the same conditions applied to CSGs and DFIGs need to be met: the generator voltage, frequency, and phase angle must all agree (to a certain extent) with the respective grid quantities. As in the DFIG case, the wind can be used to accelerate the turbine-generator from rest. Since synchronisation cannot take place as quickly as with the DFIG, a speed controller is required to limit acceleration and bring the SS-PMG to synchronous speed in a controlled manner. At the same time, the synchronisation conditions need to be monitored continuously so that the SS-PMG can be connected to the grid as soon as all conditions are met.

1.3.4.2 Small-Scale Grid-Connected WECS

Although the SS-PMG may well find application in large-scale WECS, its first phase of development is for small-scale grid-connected systems. As mentioned previously, the converter-fed PMSG is a popular candidate for this role so the SS-PMG must compare favourably with it for further investigation to be worthwhile.

The first complete SS-PMG-based WECS is still under development so system specifications are still provisional, however, certain basic assumptions can be made: on the scale under consideration (less than 50 kW) turbine blade pitch control is not employed due to cost restrictions. Passive yaw control, making use of a tail vane, is also preferred over more complex active systems. With this in mind, the SS-PMG and converter-fed PMSG concepts can be compared qualitatively at this point.

The converter-fed option allows for variable speed turbine operation and thus MPPT, which enables better energy capture under marginal wind conditions. The converter-fed WECS will thus typically capture 8 % to 15 % more energy per annum at sub-optimal wind sites [43]—if system availability is the same. Electronics were found to be the leading cause of failures in WECS after gearboxes, hydraulics, and pitch control actuators [44]. Since the other components are omitted in both designs, it is reasonable to assume that the presense of more electronics in the converter-fed WECS could lead to lower availability. This would narrow the difference in energy capture over the lifetime of the systems.

In terms of initial investment, the SS-PMG may undercut a converter-fed design of the same rating but this is highly dependent on permanent magnet prices, which are currently volatile. It can, however, be assumed that the O&M costs of the SS-PMG will be lower—since these costs can amount to between 65 % and 90 % of the initial investment [45], savings in this regard could be significant.

Looking at grid support and fault ride-through, converter-fed WTGs are known to perform well if the correct control algorithms are employed. The SS-PMG cannot offer the same level of controllability, but its inherent grid support characteristics are promising nonetheless. Avoiding in-line power electronics also makes the SS-PMG more resilient towards extreme or sustained grid faults.

On the whole, the SS-PMG and converter-fed PMSG appear closely matched for small-scale grid-connected applications. A more conclusive, quantitative comparison will become possible once a complete SS-PMG WECS has been developed. Operational experience with similarly rated systems would

be especially helpful. This, in itself, is motivation to continue with the development of a grid connection system for the SS-PMG.

1.4 Project Scope

1.4.1 Problem Statement

Wind power is an important and growing sector with continuous technological development. While large-scale WECS manufacturing is already a major worldwide industry, smaller WECS are becoming ever more commonplace. There is scope for both small and large WECS to be manufactured and sold in South Africa.

Small-scale wind power can support rural upliftment in a number of ways, such as electrifying remote settlements and offsetting grid energy use. Grid-connected systems provide the best return on investment because energy storage mechanisms are not required and preferential rates can be earned for energy supplied to the grid.

The full-scale converter-fed PMSG is the preferred option for small-scale grid-connected WECS. It avoids the use of a gearbox or pitch control to reduce cost and complexity. It is also efficient at low winds because no external excitation is required. However, the full-scale converter does incur cost, efficiency, and reliability penalties.

The SS-PMG is a hybrid generator design that can be connected directly to the grid without any form of frequency converter. Like the converter-fed PMSG, it does not require a gearbox and can be employed with a fixed-pitch turbine and passive yaw control for small-scale applications. It is expected to offer better reliability and lower lifetime costs when compared to the converter-fed PMSG.

To test the true merit of the SS-PMG, a mechanism must be developed to synchronise it to the electrical network, fulfilling the role of the grid connector in Fig. 1.2(d). Low voltage ride-through and other protection functions should also be implemented. This would allow for laboratory and field testing of an SS-PMG WECS. Such testing would, in turn, provide important performance data to evaluate the feasibility of this new topology.

1.4.2 Aim

The aim of this work is to design and implement a grid connection controller (GCC) that performs the functions described in the problem statement: synchronisation, LVRT, and protection of the SS-PMG for wind turbine applications. The controller should operate successfully under turbulent wind conditions.

The GCC should not add unreasonably to the cost or complexity of the WECS. It should be designed with simplicity and robustness in mind. Off-the-shelf components, which are affordable and freely available, should be used wherever possible so that servicing and repairs can be conducted easily by local operators.

1.4.3 Objectives

In order to develop a GCC that facilitates reliable grid connection of the SS-PMG, it is necessary to:

- Determine under what conditions the SS-PMG can be synchronised safely with the grid.
- Design a synchronisation mechanism, incorporating SS-PMG speed control, that can consistently satisfy these conditions.
- Design a compensator that ensures the SS-PMG can remain connected to the grid through voltage dips.
- Realise the GCC using affordable hardware so that practical investigations can be undertaken.
- Implement the control and additional compensation functions using a micro-controller.
- Test the performance of the GCC in the laboratory and as part of an operational WECS.

1.4.4 Contributions

This investigation contributes knowledge to the following areas relating to wind turbine applications:

- Requirements for, and feasibility of, connecting the SS-PMG directly to the grid.
- To what extent LVRT requirements for the SS-PMG can be met without reactive power compensation.
- Real-world performance of a small-scale WECS employing a direct-to-grid SS-PMG.

1.4.5 Constraints

- The MCU available for the GCC is a Texas Instruments F28027 which operates at 60 MHz. The ADC sampling rate is set at 1 kHz.
- Direct wind speed measurements (for example, through the use of an anemometer) are not available to the MCU.

1.5 Summary

In this chapter, an overview of wind power in both a global and a South African context has been presented. This points towards the relevance of small-scale and grid-connected wind power systems. Following this was a description of the most successful grid-connected WECS topologies, after which the SS-PMG was introduced and compared to the converter-fed PMSG topology for small-scale applications. The chapter concludes with a motivation for the work undertaken, as well as a statement of the aim and objectives of the work. The remainder of this document is arranged as follows:

- In Chapter 2 speed control and grid compensation techniques documented in literature are investigated. From this investigation appropriate techniques are selected for application in the GCC.
- Chapter 3 presents the modelling methods used for various parts of the SS-PMG WECS. Of particular importance here is the modelling of the SS-PMG itself and also of the turbulent wind.
- The synchronisation tolerance limits and speed controller are developed in Chapter 4, after which simulations are used to refine the control and verify the complete synchronisation operation under turbulent wind conditions.
- Chapter 5 begins with an investigation into standardised grid faults published by network operators, followed by a description of the LVRT compensators that are evaluated for the SS-PMG.

Simulation studies are then used to test and refine the compensation strategies until a final system is developed.

- The hardware realisation and programming of the GCC are presented in Chapter 6, including a discussion of implementation issues that were encountered.
- Chapter 7 documents the practical investigations in the laboratory and in the field that serve to verify the GCC design and implementation.
- Finally, conclusions and recommendations are presented in Chapter 8.

CHAPTER 2

CONTROL AND COMPENSATION METHODS

This chapter presents the proposed speed control and grid fault compensation mechanisms for the GCC, including techniques to measure SS-PMG and grid conditions. In each case the chosen approach is explained in the context of the system requirements and available alternatives. Priorities in the selection process are effectiveness, robustness, simplicity, and affordability.

2.1 Time-Varying Parameter Measurement

For the purposes of synchronisation and LVRT, the GCC must have access to information regarding the state of the SS-PMG and grid. Such information includes voltage magnitude and phase angle; frequency; and current magnitude and phase angle. Voltage and frequency information is required for the grid, as well as for the SS-PMG.

Minimising the number of sensors employed in the GCC is an important step in achieving robustness, simplicity and affordability. As a result, the GCC is only equipped with voltage and current sensors, as indicated in Fig. 2.1.

For the purposes of speed control and synchronisation, the frequency of the SS-PMG must be sampled rapidly and accurately. Voltage magnitude and phase angle for both SS-PMG and grid are also required. For LVRT, changes in grid voltage magnitude must be detected quickly—individual phases should thus be evaluated separately for unbalanced faults.

2.1.1 Voltage Magnitude, Phase Angle, and Frequency

To avoid the need for a mechanical sensor, the rotational frequency of the SS-PMG is to be determined along with voltage magnitude and phase angle by analysing the instantaneous 3-phase voltage signals. In selecting a measurement method, the possibility of noise and harmonics must be taken into account.

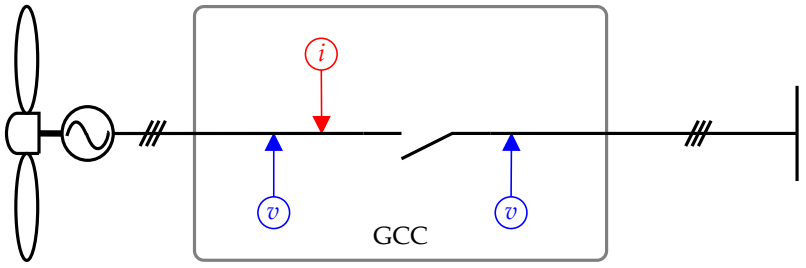

Figure 2.1: Single line outline of the GCC indicating sensor positioning. Instantaneous voltage sampling points are indicated by blue arrows and instantaneous current sampling points are indicated by red arrows.

2.1.1.1 Zero-Crossing Detection Methods

The detection of zero-crossings on one or multiple phases can be used as a means to determine frequency, as illustrated in Fig. 2.2. Two basic algorithms can be employed: counting zero-crossings that occur per unit of time, or counting the units of time required to achieve a certain number of zero-crossings. Both allow calculation of frequency through the basic formula given by Eqn (2.1). The former gives better linearity while the latter achieves finer resolution.

$$f = \frac{N_{zc} - 1}{2t_{int}} \tag{2.1}$$

The advantages of this approach are its simplicity and machine independence. However, it performs poorly when the signal is contaminated by harmonics or dips [46]. A trade-off must also be made between resolution and speed: sampling more zero-crossings or sampling over a longer period increases resolution but decreases update speed. This trade-off is results in unacceptable performance, even with clean balanced signals. Also, this approach only measures frequency, so additional analysis must be employed to determine voltage magnitude and rotor angle.

2.1.1.2 Space Vector Calculations

For a balanced system, the 3-phase natural voltages can be transformed into the stationary $\alpha\beta$ reference frame through the use of the Clarke transformation, given by Eqn (2.2).

$$\begin{bmatrix} v_\alpha \\ v_\beta \end{bmatrix} = \frac{2}{3} \begin{bmatrix} 1 & -0.5 & -0.5 \\ 0 & \frac{\sqrt{3}}{2} & -\frac{\sqrt{3}}{2} \end{bmatrix} \begin{bmatrix} v_a \\ v_b \\ v_c \end{bmatrix} \tag{2.2}$$

In this reference frame, v_α and v_β constitute orthogonal components of a rotating space vector $\overline{v}_{\alpha\beta}$, as shown in Fig. 2.3. Eqn (2.3) expresses how the peak voltage magnitude can be determined from the vector magnitude, while the phase angle can be calculated by Eqn (2.4). Finally, the rotational velocity can be determined by Eqn (2.5), which can be converted to frequency by Eqn (2.6).

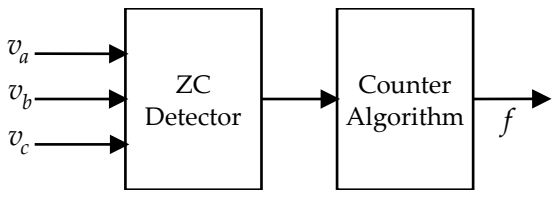

Figure 2.2: Block diagram for frequency measurement based on zero-crossing detection.

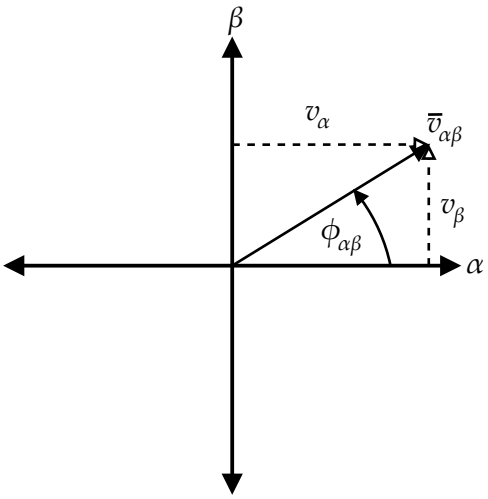

Figure 2.3: Rotating space vector composed of orthogonal $\alpha\beta$ components.

$$v_{\alpha\beta} = \sqrt{{v_\alpha}^2 + {v_\beta}^2} = \left\|\overline{v}_{\alpha\beta}\right\| \tag{2.3}$$

$$\phi_{\alpha\beta} = \arctan\frac{v_\beta}{v_\alpha} = \angle\overline{v}_{\alpha\beta} \tag{2.4}$$

$$\omega_{\alpha\beta} = \frac{\mathrm{d}\phi_{\alpha\beta}}{\mathrm{d}t} \tag{2.5}$$

$$f_{\alpha\beta} = \frac{\omega_{\alpha\beta}}{2\pi} \tag{2.6}$$

These calculations are computationally efficient and can be updated with every sample cycle of the controller. However, they are not accurate in the presence of harmonics or unbalanced faults. A variety of filters may be applied to the transformed quantities to improve the robustness of this approach to harmonics. Fig. 2.4 illustrates the generic algorithm that may be applied for determining phase angle, as proposed in [5; 38].

A simple low-pass filter approach is evaluated and rejected by [38] due to the estimator's sensitivity to amplitude and frequency disturbances. A resonant filter method is shown in [5] to achieve sufficient rejection of harmonics and performs well enough with minor notches as well. However, it is only suited to a system with a fixed fundamental frequency.

2.1.1.3 *DQ* Filtering

Eqn (2.7) expresses how the Park transformation can be used to convert stationary 3-phase *abc* components into synchronous *dq* components when a balanced system is assumed. Transformations between

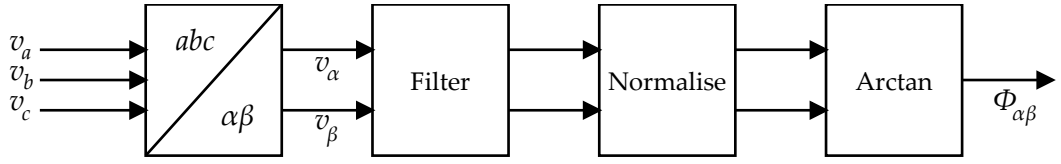

Figure 2.4: Generic block diagram for the calculation of phase angle using filtered $\alpha\beta$ quantities.

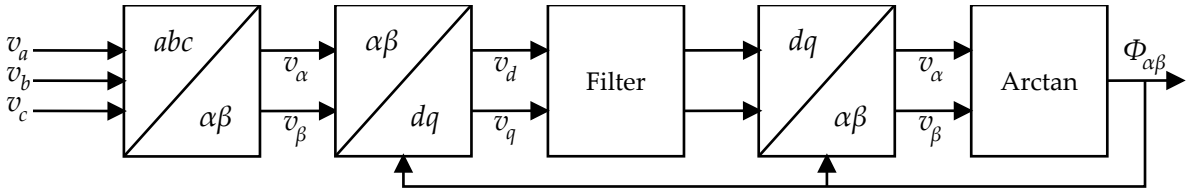

Figure 2.5: Generic block diagram for the calculation of phase angle using filtered intermediate dq quantities.

the $\alpha\beta$ and dq reference frames are also possible.

$$\begin{bmatrix} v_d \\ v_q \end{bmatrix} = \frac{2}{3} \begin{bmatrix} \cos\theta & \cos(\theta - \frac{2\pi}{3}) & \cos(\theta + \frac{2\pi}{3}) \\ \sin\theta & \sin(\theta - \frac{2\pi}{3}) & \sin(\theta + \frac{2\pi}{3}) \end{bmatrix} \begin{bmatrix} v_a \\ v_b \\ v_c \end{bmatrix} \tag{2.7}$$

It is proposed by [5] to use the dq reference frame as an intermediate step in the measurement process originally shown in Fig. 2.4. This extra step is useful because the dq components are effectively DC quantities so more filtering techniques can be applied. The new process for estimating the phase angle is illustrated in Fig. 2.5.

Using the dq transformation implies an extra computational burden and the delay signal cancellation filtering method applied by [5] is not practical since it is vulnerable to frequency variations. Other filters may, however, be investigated.

2.1.1.4 Space Vector Filtering

Space vector filtering, making use of the process shown in Fig. 2.6, has been proposed by [38] for grid voltage synchronisation. The algorithm is very similar to those studied in Section 2.1.1.2, but makes the assumption of constant frequency. The frequency variation encountered on the SS-PMG terminals before synchronisation makes this approach unsuitable for generator measurements.

2.1.1.5 Simplified Kalman Observer

The simplified Kalman observer (SKO) proposed in [47] can be used to estimate the rotor angle and rotational speed of a PMSG with a much lower computational burden than that of an extended Kalman filter (EKF). The estimator uses a constant gain matrix which is pre-computed and is not a function of the machine parameters. The real-time estimation process, as presented in [48], is represented in Fig. 2.7.

When compared to the PLL and sliding mode observer, the SKO emerges as the most promising estimator due to its accuracy, computational efficiency (compared to the EKF) and insensitivity to machine

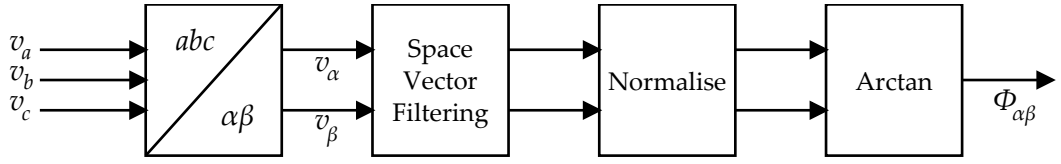

Figure 2.6: Block diagram for the calculation of phase angle using space vector filtered $\alpha\beta$ quantities.

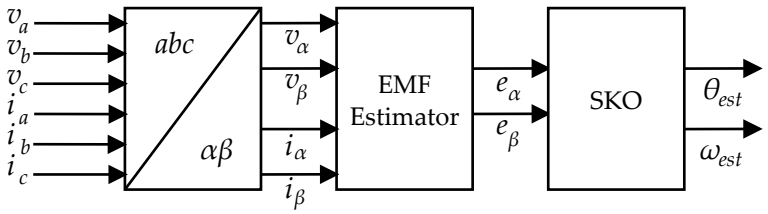

Figure 2.7: Block diagram of the SKO-based speed and position estimator.

parameter variations [48]. The SKO also does away with the need for low-pass filtering and associated delays. It should be noted that the SKO requires a sliding mode observer (SMO) to provide the estimated EMF input. Unlike the SKO, the SMO must be developed using the machine parameters [48].

2.1.1.6 Phase-Locked Loop

The phase-locked loop is a well established tool to estimate phase angle and frequency. As a result, many potential implementations of the PLL exist. A relatively simple option is the three-phase PLL or DQ-PLL, shown in Fig. 2.8, which is noted by [46] to be the de facto estimator used in frequency converters. The full *dq* transformation is required as part of the estimation process and additional steps may be necessary to cope sufficiently with unbalanced conditions [46; 49]. On the other hand, rejection of all disturbances up to and including unbalanced voltage dips is found to be acceptable in [5].

The DQ-PLL has a longer settling time than the the SKO and requires tuning of its parameters for effective operation. In the process of tuning, a trade-off between fast tracking and good filtering must be made [49]. Consequently, the DQ-PLL has relatively slow dynamics [5]. A variation on the DQ-PLL is the flux PLL described in [48], which uses an estimate of 3-phase generator flux as input. This method is not advantageous as it still requires careful tuning and involves more real-time computational steps.

Two other PLL approaches are introduced by [49]: the enhanced PLL and quadrature PLL. Both of these promise better handling of unbalanced 3-phase signals but the actual performance gains experienced may not be justified when weighed against the substantially higher computational burdens involved in their implementations. Each version requires four PLL circuits and only frequency is estimated.

Adaptive PLL, as introduced in [5] works independently on each phase and delivers frequency,

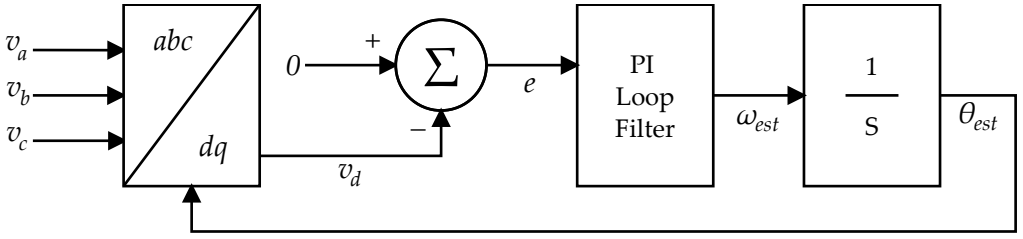

Figure 2.8: Block diagram of the basic DQ-PLL speed and position estimator. The loop aims to minimise v_d, thereby tracking the actual value of θ. The loop filter must be tuned to achieve an acceptable trade-off between speed and disturbance rejection.

amplitude and phase angle information. Its drawback is complexity and higher computational load than for the DQ-PLL.

2.1.1.7 Conclusion

After evaluating the methods described above, the filtered space vector calculations of Section 2.1.1.2 were chosen to be most appropriate for this system:

- The chosen method provides all the necessary parameters for both the grid and generator.
- Simulations and practical tests show that acceptable performance can be achieved with digital low-pass filtering applied to the transformed variables (this is illustrated in later chapters).
- Even with low-pass filtering, the computational burden is relatively light, especially since no redundant calculations need to be performed.
- The methods are stable and are not dependant upon machine parameters.
- The relatively low sampling frequency of 1 kHz and limited processing power of the MCU makes the more sophisticated estimation techniques unappealing.
- An additional algorithm may still be applied to provide fast and reliable detection of unbalanced grid voltage dips.

2.1.2 Grid Voltage Dip Detection

It is desirable to detect grid voltage dips within a quarter cycle, even with harmonics and imbalances present on the measured signals. A wide variety of techniques may be evaluated [50]:

- Space vector pulse width modulation.
- Fast Fourier transform.
- *dq* theory.
- Symmetrical components method.
- Peaks detection.
- Numerical matrix method.
- Wavelet transform.
- The Kalman filter.
- Sliding window digital RMS.

The *dq* theory method is appealing for 3-phase systems, but requires a trade-off between reliability and speed, as well as failing to cope with imbalanced faults and harmonics.

The Kalman filter has a settling time and only selected cases have been investigated in literature. Performance also varies depending on the starting angle of the fault. Sliding window digital RMS requires at least a half-cycle window but is reliable in the presence of harmonics. Detection can be made faster by including top and bottom RMS thresholds which, when exceeded, trigger detection. This method also shows some dependence on angle of initiation and severity of sag/swell. Detection times are generally below 7 ms.

A hybrid between the Kalman filter and digital RMS is proposed by [50]. This achieves faster and more consistent detection times, but is computationally intensive. For the purposes of this study, the

space vector analysis described previously is sufficient to detect balanced faults, but an RMS evaluation may be incorporated to detect unbalanced faults more reliably.

The recursive digital RMS calculation proposed by [50] is more efficient than the conventional sliding window form. The RMS voltage can be calculated with Eqn (2.8) and Eqn (2.9), using a sample window equivalent to one or more half-cycles.

$$V_{win}\left[N\right] = \sum_{i=1}^{N} {v_i}^2 \tag{2.8}$$

$$V_{RMS}\left[k\right] = \sqrt{\frac{V_{win}\left[k-1\right] - v^2\left[k-N\right] + v^2\left[k\right]}{N}} \tag{2.9}$$

V_{win} is the window voltage and N is the number of samples constituting an RMS sample window. v_i is the instantaneous voltage sample at index i. k is the sample number in the range $k = 1,2,3,4...$ This method applies to a single phase, so it must be implemented simultaneously for each phase. This extra computational burden may be justified if the improved grid voltage dip detection results in better compensator performance.

2.2 Generator Speed Control

2.2.1 Existing Techniques

Attaining synchronous speed reliably is an essential part of synchronising the SS-PMG, so a speed control mechanism must be selected and developed. Some WECS make use of pitch control to regulate turbine torque in order to control speed or minimise acceleration before grid connection [3; 20; 21]. This approach (or indeed any other aerodynamic control mechanism) is not possible for the small-scale SS-PMG because the turbine employed makes use of fixed pitch blades.

Mechanical (disc or drum) brakes often provide emergency braking capabilities on large-scale WECS. A similar brake could be employed to regulate speed, however, implementing such a mechanism would result in an unreasonable increase in the cost and complexity of a small-scale WECS. In addition, the brake would need to be oversized (in comparison with emergency-only applications) to accommodate sustained use.

A more feasible option for small-scale WECS is electromagnetic braking, where counter-torque produced by the generator itself is used to brake the turbine. All WECS make use of this effect during normal operation: the generator counter-torque balances turbine torque so that a steady speed is maintained. In that case, the load on to which the generator is coupled is typically the grid (or a battery bank in stand-alone systems). If the load is a resistor bank then the captured energy is wasted but braking is possible even prior to synchronisation.

Advantages of electromagnetic braking over aerodynamic controls include lower cost, less components requiring maintenance and, consequently, improved reliability [51]. Using an electrical braking resistor is fast, does not require external power (which makes it more reliable) and is thus well suited to wind turbines [52].

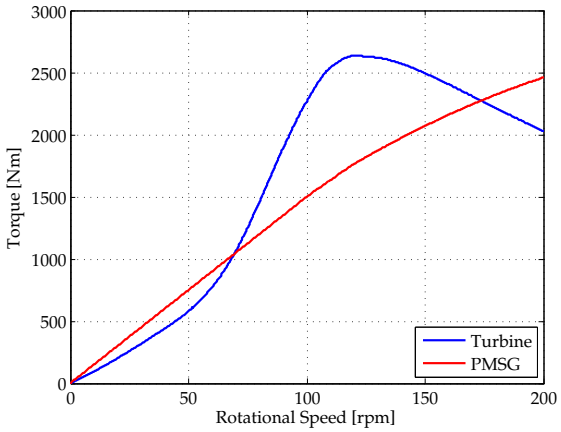

Figure 2.9: Typical relationship between turbine torque at a fixed wind speed and PMSG torque with a fixed resistive load as a function of rotational speed.

A disadvantage of electromagnetic braking is that the torque curves of PMSGs and wind turbines match very poorly, as illustrated in Fig. 2.9 for a generic case. On a resistive load, PMSG torque is roughly a linear function of rotational speed, whereas turbine torque at a constant wind speed is a highly non-linear function of rotational speed—especially with stall effects present.

One means to balance the torque curves is to vary the resistive load discretely by switching in different resistances [53]. In addition, a capacitance may be connected in shunt with the resistive load to counteract the effect of the stator inductance, thus increasing the available torque [54]. A drawback of discretely changing the resistive load is that it requires a trade-off to be made between control accuracy (more resistance stages) and cost (fewer resistance stages).

2.2.2 Proposed Speed Controller

To investigate the dynamic speed control potential of electromagnetic braking for the SS-PMG, the resistive braking system shown in Fig. 2.10 is proposed. The basic layout involves a single three-phase resistive load, which is switched by either a contactor or a back-to-back thyristor pack (triac). If the discrete (contactor-based) approach is employed then further resistive loads and contactors may be added in parallel with the first set to vary the braking torque that can be developed at any given rotational speed.

As an alternative to discrete braking, the thyristor pack can be implemented to achieve variable braking torque with a single resistive load. In this case, the effective voltage imposed on the load can be varied with the firing angle of the thyristors. In this way, the SS-PMG counter-torque can be continuously varied to respond to changing conditions without the need for multiple resistances.

The advantages of both approaches include an absence of moving parts; availability of off-the-shelf components; flexible siting of the controller (at the base of the turbine tower or in a control room, etc.); and no changes to existing turbine-generator hardware or nacelle mass. A capacitor bank can also be added in shunt with the resistances if extra torque is required. The discrete and variable braking strategies are developed and compared in Chapter 4.

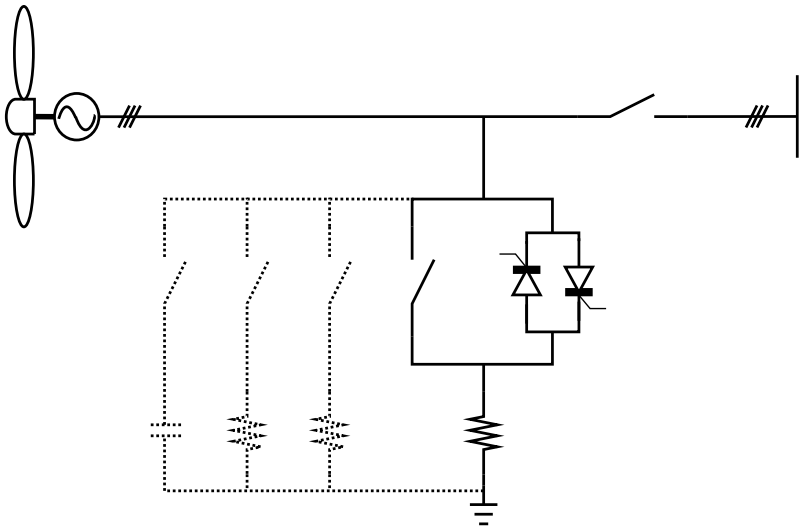

Figure 2.10: Line diagram of the proposed SS-PMG speed controller, showing optional extra resistor stages and a compensation capacitor

2.3 Grid Fault Compensation

After controlled synchronisation, the second aim of this investigation is to develop an LVRT compensator for the SS-PMG. Low voltage ride-through for an SG is defined as remaining in synchronism during and after a major grid voltage dip [39], which is to say that pole slipping should be avoided throughout the fault and recovery period. In other words, the generator rotor angle should remain safely below 180 ° at all times.

In addition to maintaining rotor angle stability, it is desirable to limit the maximum current transients that occur during faults. This is especially important for the protection of PM generators, which could experience demagnetisation if stator currents become excessive. Limiting currents is also necessary to ensure that protection circuitry does not trip as a result of instantaneous or thermal overload.

2.3.1 Existing Compensation Techniques for IGs

As discussed in Section 1.3, DFIG and full scale converter-fed WECS can generally achieve LVRT by the application of appropriate control algorithms in their converters. Dumping loads and pitch control may also be employed to manage excess active power during the fault [55; 30]. In contrast, Danish Concept IGs are directly connected to the grid, so must rely upon external intervention to manage LVRT. Since the SS-PMG is also connected directly to the grid, it may benefit from the same compensation techniques employed for IGs. The effectiveness of such techniques must, however, be investigated thoroughly since SGs display less damped response to grid faults than IGs do.

2.3.1.1 Turbine Pitch Control

Pitch control can play an important part in the LVRT protection of SCIGs since the tendency of such machines is to accelerate during terminal voltage dips [56]. However, the response of the pitch controller can be unacceptably slow [57; 55] and reliance on pitch control alone may place unreasonably high loads

on the mechanical system during power restoration [58]. Compared to pitch control (Fig. 2.11), active stall control achieves results with smaller angular changes, so can operate more quickly. However, neither form of control can be applied to the fixed pitch turbine employed in the SS-PMG WECS.

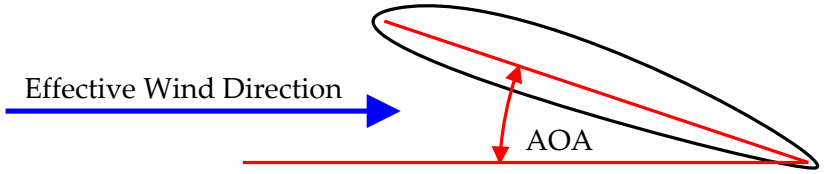

Figure 2.11: The angle of attack (AOA) of an aerofoil is the angle between its chord and the effective direction of the oncoming wind stream [4]. Both pitch control and active stall control twist the blade to change the AOA and limit turbine torque. Pitch control functions by reducing the AOA and, as a result, the induced lift. On the other hand, active stall control increases the AOA to induce stall.

2.3.1.2 Static VAR Compensator

The static VAR compensator (SVC), depicted in Fig. 2.12, is an element of flexible AC transmission systems which functions as a controllable VAR source or sink, depending on dynamic network requirements. The SVC can also assist in maintaining the transient stability of wind farms using Danish Concept IGs [59; 60; 61]. The SVC is particularly appropriate for IGs because it can maintain voltage stability by providing for the reactive power requirements of the generators during a grid fault.

The SVC cannot, however, manage the real power imbalance that takes place between a WTG and the grid during a fault. In addition, the cost and complexity of the components required would not be justified for a single WECS and the use of thyristors on the network would introduce harmonics.

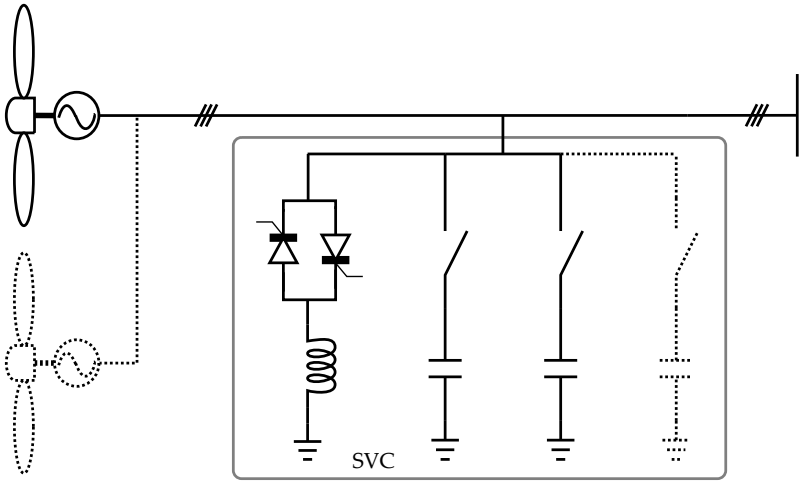

Figure 2.12: Line diagram of a basic SVC serving multiple IG WECS. Transformers typically found between the IGs, the SVC, and the grid are not shown.

2.3.1.3 STATCOM

A static synchronous compensator (STATCOM) is based on a voltage source inverter and is similar to the converters used in DFIG and full scale converter-fed topologies. The main difference is that WECS converters typically make use of back-to-back arrangements, with two inverters linked by a DC bus, whereas a STATCOM consists of a single inverter coupled to a DC bus. Fig. 2.13 shows that the STATCOM, like the SVC, is shunt-connected. IGBTs often serve as the semiconductor switches in these inverters.

STATCOMs are often used to improve power factor and voltage stability at network nodes [62]. Because of the switching devices employed, it can react faster than an SVC [54] and can vary its response continuously. A STATCOM has been shown to be more effective at stabilising IGs during grid faults than an SVC [61; 63]. Its drop-off in VAR response capability is proportional to voltage, not voltage squared (as with an SVC), so reduction in capabilities with voltage is less dramatic.

STATCOMs can also be used on a continuous basis to improve voltage quality at a node where wind power interfaces with the grid. Battery storage may be incorporated into the DC bus to allow for active power regulation as well [64]. The major disadvantage of using a STATCOM for LVRT is cost [58]. In the context of small-scale WECS, it would be more economical to employ a conventional PMSG with a full scale converter than an SS-PMG with a STATCOM.

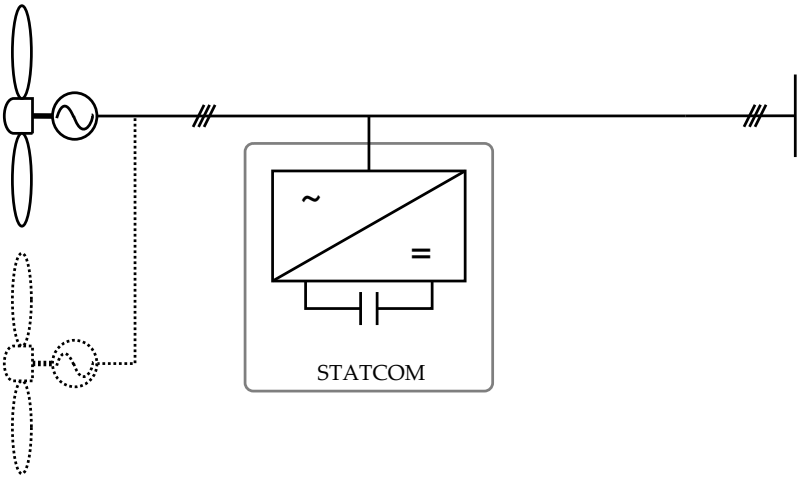

Figure 2.13: Line diagram of a STATCOM serving multiple IG WECS. Transformers typically found between the IGs, STATCOM, and the grid are not shown.

2.3.1.4 Shunt Braking Resistor

A shunt-connected braking resistor (BR) is defined by [65] as: "a fast load injection to absorb excess transient energy of an area which arises due to severe system disturbances." It is an established tool for stabilising conventional SGs after network faults [66; 32] and has also been proposed as a useful LVRT compensation mechanism for IG WTGs. In this case, the BR may be switched by either an electromech-

anical contactor or thyristors, as illustrated in Fig. 2.14. Thyristors have the advantage of faster response time (although there is still a half-cycle delay on any given phase) and lower maintenance requirements.

In [67] it is concluded that the BR is a cheap, simple and effective means to support IG stability during voltage dips. The damped nature of the IG's response makes slower electromechanical contactors acceptable. The BR is engaged at a terminal voltage threshold of 0,85 p.u. A BR is used in combination with reactive power compensation in [68] to achieve successful LVRT for IG WTGs—once again, terminal voltage is the watched quantity. In this case, contactor delay is taken as 20 ms.

From Fig. 2.14 it is clear that a BR LVRT compensator requires the same hardware as the proposed speed controller of Section 2.2.2. The BR compensator can thus be employed without affecting the cost or complexity of the SS-PMG WECS. However, it is unlikely to provide sufficient compensation for the SS-PMG on its own. The BR can only serve to absorb excess active power but cannot shield the generator from the voltage dip or control the flow of reactive power. Some further control intervention id necessary to protect the SS-PMG against significant over-current during faults.

2.3.1.5 Series Compensation Resistor

A series compensation resistor (SR), as shown in Fig. 2.15, can be inserted between a WTG and the grid to act as a buffer against voltage dips. The SR increases the effective line impedance between the generator and a fault, reducing transient currents while still absorbing active power. If the SR is designed correctly, the voltage drop across the resistance will ensure that the generator terminal voltage does not change significantly during a grid fault.

The SR is shown to be a cost-effective means of imparting stability to IGs through the course of successfully cleared grid faults [57]. Performance is on par with more expensive options, such as STATCOM, even during uncleared faults. However, the SR cannot control reactive power flow, so is incapable of power factor correction. The SR is nonetheless appealing due to very simple control, robustness and

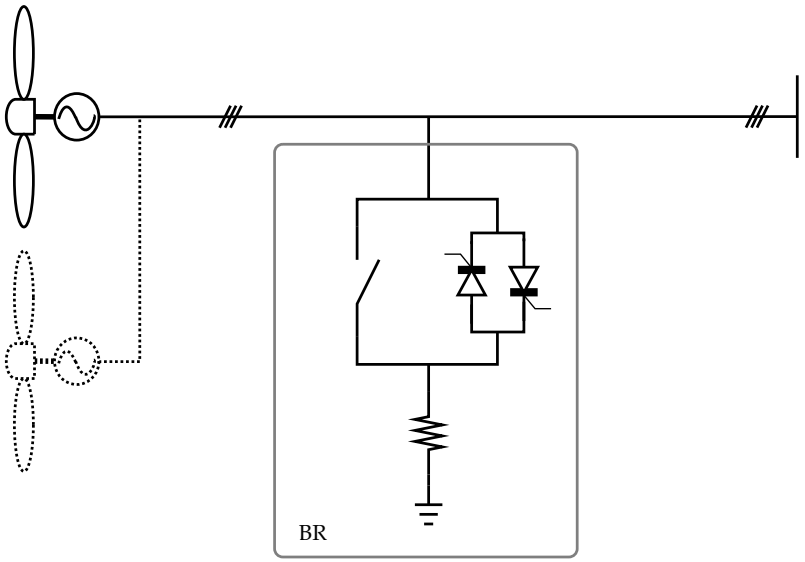

Figure 2.14: Line diagram of a BR compensator serving multiple IG WECS. Switching can be achieved by either a contactor or a back-to-back thyristor pack (triac).

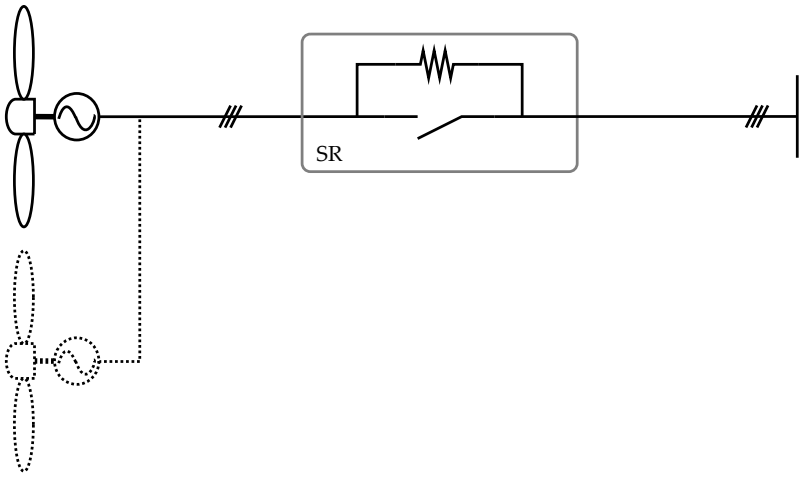

Figure 2.15: Line diagram of a SR compensator serving multiple IG WECS.

low cost (as well as easy retrofitting to existing WTGs).

According to [58], the SR approach is more effective than a BR in typical fault scenarios because its effect is depended upon current level, not voltage level. In that study, the SR is found to be effective for IG LVRT despite a 40 ms insertion delay and is typically switched in for less than 1 s. It is found that an SR with a 0,1 p.u. power rating performs better than a reactive power compensator with a 0,3 p.u. rating. Once again, the major advantage of the SR over SSC-based techniques is found to be cost.

The SR could be switched by thyristors, but both studies found contactor switching to be sufficient for IG WTGs. This approach then offers simple, robust and affordable ride-through compensation for IGs. PMSGs, on the other hand, exhibit a less damped response to faults than IGs, so the suitability of the SR for the SS-PMG is not guaranteed, although it is clearly worthy of investigation.

2.3.2 Proposed LVRT Compensator

The foregoing discussion suggests that the most viable, affordable, and robust LVRT compensator for the SS-PMG would be a combination of the BR and SR mechanisms. The BR component is already present as the speed control subsystem proposed earlier. The addition of an SR would improve the compensation potential dramatically without adding unreasonably to the complexity or cost of the system. The combined system, which constitutes the complete GCC, is illustrated in Fig. 2.16.

The proposed GCC is not equipped with any form of reactive power control so cannot undertake power factor correction, for example. Nonetheless, literature suggests that it will be capable of compensating for grid voltage dips with the objective of maintaining rotor angle stability and limiting transient current to an acceptable level.

2.4 Summary

In this chapter various techniques for measurement, speed control and grid fault compensation have been investigated. In each case, the most appropriate methods have been selected on the grounds of

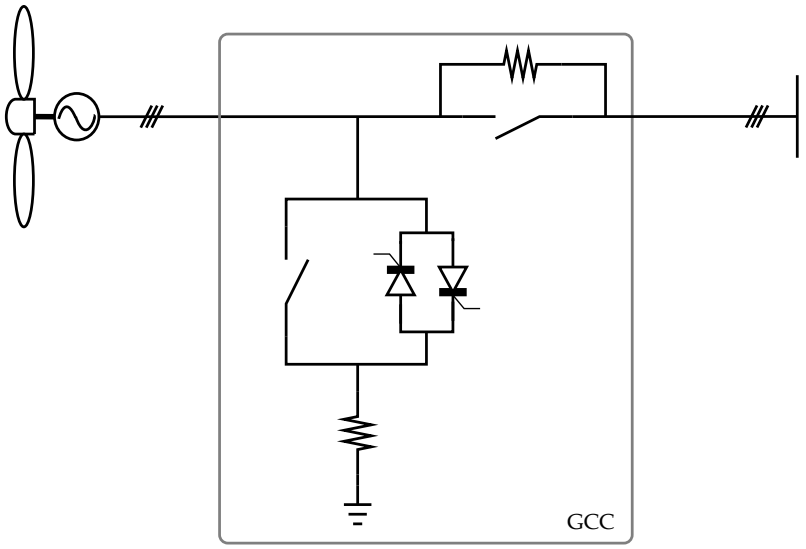

Figure 2.16: Line diagram of the GCC for the SS-PMG, showing the proposed BR and SR compensators for LVRT.

effectiveness, robustness, simplicity, and affordability. These components and techniques have been combined to constitute the proposed GCC for the SS-PMG. It is now necessary to develop and evaluate control strategies for synchronisation and LVRT, after which the system will be implemented in hardware for practical testing. In the next chapter, this process begins with the modelling of the complete WECS.

CHAPTER 3

MODELLING

This chapter explains the modelling techniques used for the various elements that constitute the wind turbine system, including: turbine, turbulent wind, SS-PMG, and electrical network. Experimental results are also shown to verify the validity of the chosen modelling approaches.

3.1 Turbine

The wind turbine used in this investigation is a three-blade up-wind horizontal axis design from *Aero Energy*, based in Potchefstroom, South Africa. The turbine has a diameter of 7,2 m and is designed for fixed pitch operation.

3.1.1 Power and Torque Curves

The turbine power and torque curves as a function of wind speed are shown in Fig. 3.1. The rated wind speed for the turbine is 11 m/s and the manufacturer does not provide performance data for wind speeds above this. As a result, turbine torque at higher wind speeds is extrapolated from the existing data.

The power curves of the turbine in Fig. 3.1(b) show relatively flat plateaus at higher rotational speeds. This makes the turbine suitable for fixed speed operation, although some advantage can be gained by employing variable speed and MPPT. The chosen fixed operating point for the SS-PMG when synchronised with the grid is 150 rpm [36].

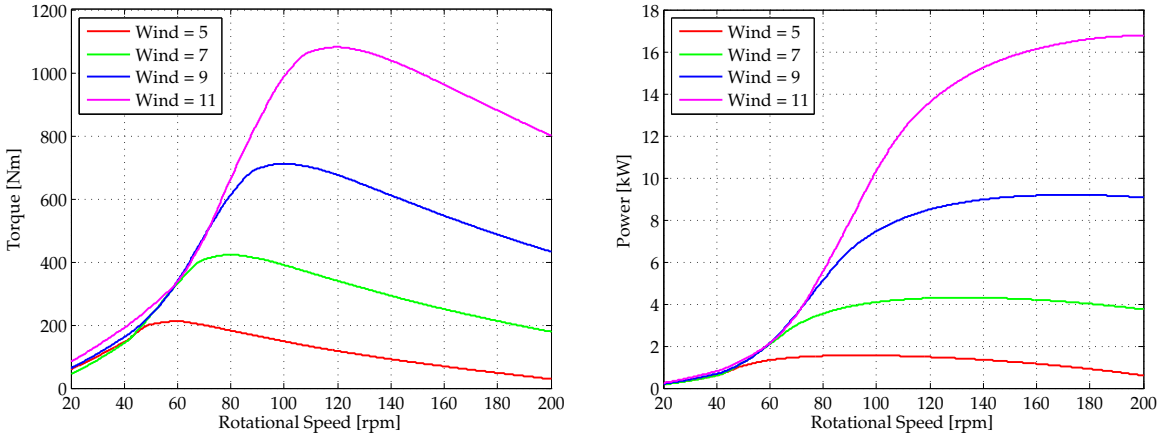

(a) Wind turbine torque as a function of rotational speed

(b) Wind turbine power as a function of rotational speed

Figure 3.1: Wind turbine curves as a function of rotational speed at different wind speeds.

3.1.2 Yaw Control

The yaw of a turbine refers to the angle between the incoming wind vector and the rotational axis of the turbine. To produce maximum torque and capture energy effectively, the turbine should always be aligned with the wind (the yaw angle should be zero), so some form of yaw control is necessary to ensure optimal performance of any WECS. Larger scale turbines typically have a yaw drive, which automatically directs the turbine into the wind based on directional information received from a nearby wind vane. The yaw drive can also steer the turbine out of the wind during gale force conditions.

The small-scale SS-PMG WECS is equipped with a simpler, more affordable yaw controller, shown in Fig. 3.2. A tail vane is responsible for steering the turbine into the wind. To protect the turbine during excessively strong winds, the turbine is offset from the yaw axis: in strong winds, the thrust produced by the wind flowing against the blades will generate a sufficient moment arm about the yaw axis to turn the turbine out of the wind. The tail vane is mounted on a spring-tensioned pivot, which allows the tail to fold inwards during strong winds to assist in this process.

The SS-PMG yaw controller cannot achieve perfect tracking, but responds quickly to changes in wind direction because of the relatively low system inertia about the yaw axis. To simplify modelling and simulations, it is assumed that the yaw angle is zero at all times. This is conservative, since some yaw error will exist in reality and this will reduce turbine torque for a given wind speed.

3.1.3 Dynamics

The turbine converts wind energy into rotational mechanical energy using lift effects. To faithfully model this aerodynamic process, the blade element momentum method or Navier-Stokes equations should be used [4; 69]. However, employing one of these methods in dynamic simulations has problematic implications [70]: detailed information is required about the turbine geometry and about the

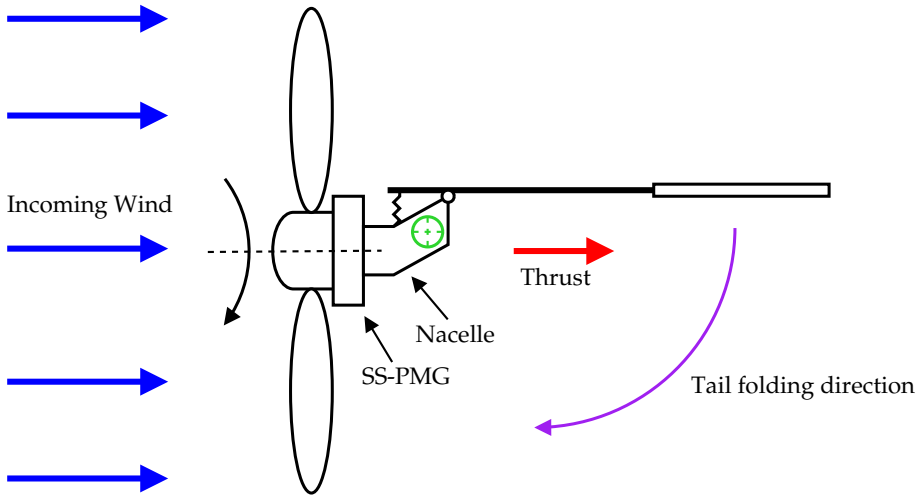

Figure 3.2: Simplified top-down representation of the SS-PMG WECS with the mechanical yaw controller. The thrust force vector produced by the action of the wind on the turbine is shown in red. The rotational centre-point of the nacelle (yaw axis) is shown in green.

incoming wind field (as opposed to a single wind speed vector). Since the required data are not readily available, these sophisticated methods are not practical to implement in this study.

In literature concerning grid interaction, the most commonly employed method for wind-to-turbine power conversion makes use of quasi-static equations [55; 71; 72; 27]. The algebraic relationship between wind speed, turbine speed and turbine power output is given by Eqn (3.1). For a fixed pitch turbine, the coefficient of power c_p is a sole function of the tip speed ratio λ, which is expressed in Eqn (3.2).

$$P_t = \frac{1}{2}\rho A_t c_p(\lambda) u_w^3 \tag{3.1}$$

$$\lambda = \frac{R_t \omega_t}{u_w} \tag{3.2}$$

The basic quasi-static method does not take rotational sampling, wind shear, or tower shadow into account, but these effects may be ignored for small-scale WECS, according to [73]. This simplification is further supported by evidence in [41] that the SS-PMG filters out the tower shadow effect, which is the most significant of the three factors [74]. Yaw error is also ignored, as explained previously. An important effect to consider, however, is disc averaging (the averaging effect of wind being sampled across the entire rotor area). Disc averaging is factored in to the wind-turbine interaction model described in Section 3.2.

To employ the basic quasi-static method, a $c_p(\lambda)$ curve is required for the turbine. This is effectively a dimensionless aggregation of the turbine power curves shown in Fig. 3.1(b). It was, however, found to be more accurate and computationally efficient to calculate turbine power output in Ansoft *Simplorer* through the use of a lookup table. As illustrated in Fig. 3.3, wind speed and turbine rotational speed serve as inputs to the table. An interpolated value of turbine power is then output for further calculations.

The rotational inertia and friction effects of the turbine are integrated into the mechanical system model of the SS-PMG which is described in Section 3.3.1. In addition, the influence of blade flexibility is ignored because the blades of small-scale WECS are not long enough to experience substantial deformations and induce oscillations, according to [75].

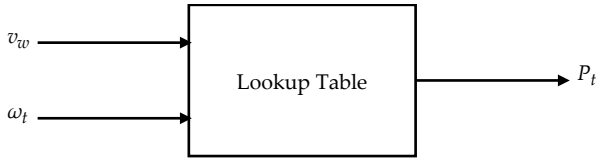

Figure 3.3: Lookup table method employed in simulations to determine turbine power output as a function of rotational speed and wind speed.

3.2 Wind

The wind conditions experienced by a turbine are a function of macro- and micro-geography, which includes climate, weather, and terrain effects. The hub height of the turbine is another important factor

in determining the nature of the wind conditions experienced. Variations in wind conditions occur on different time scale: seconds, minutes, hours, days, and months. The Van der Hoven model serves to model longer term variations, while the Von Karman model is better suited to model short term variations [73]. Both can be modified by setting parameters in order to take local conditions into account.

The focus of this study is not on energy yield over months or years, but rather on dynamic control of the WECS during short term events, such as synchronisation or a grid fault. As such, it is necessary to model only short term wind speed variations, on the order of seconds or a few minutes. For this purpose, it is sufficient to make use of the Von Karman model exclusively. The parameters for the model chosen should cause it to reflect typical conditions likely to be encountered by an SS-PMG WECS in South Africa.

A turbulent wind signal generator based on the development in [6] is shown in Fig. 3.4. This model produces two turbulent wind signals. The first is the turbulent wind as it would be sampled at a point source (by an anemometer, for example) and the second signal is the effective turbulent wind as experienced by the turbine once disc averaging is taken into account. Full details of the model and parameters chosen are given in Appendix B.

Examples of the output generated by the turbulent wind model in *Matlab-Simulink* are shown in Fig. 3.5. In each case, a different seed value was used and the mean wind speed was also varied between the two cases. The effect of the disc averaging is apparent and it is the averaged signal that is applied to the lookup table in Fig. 3.3 to determine the turbine torque output.

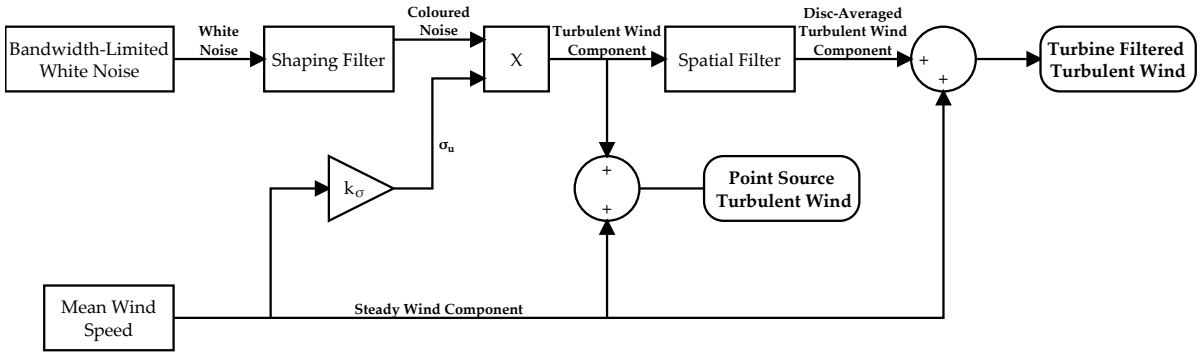

Figure 3.4: Block diagram of the turbulent wind signal generator. In addition to the point-source turbulent speed signal, a turbine disc-averaged signal is also output.

3.3 Slip Synchronous-Permanent Magnet Generator

The SS-PMG is described conceptually in Section 1.3.4. Here, the modelling of the SS-PMG is discussed in detail in the context of the complete WECS, as introduced in [41]. A comparison of steady-state performance predictions and measurements serves to verify the modelling methodology and parameter values.

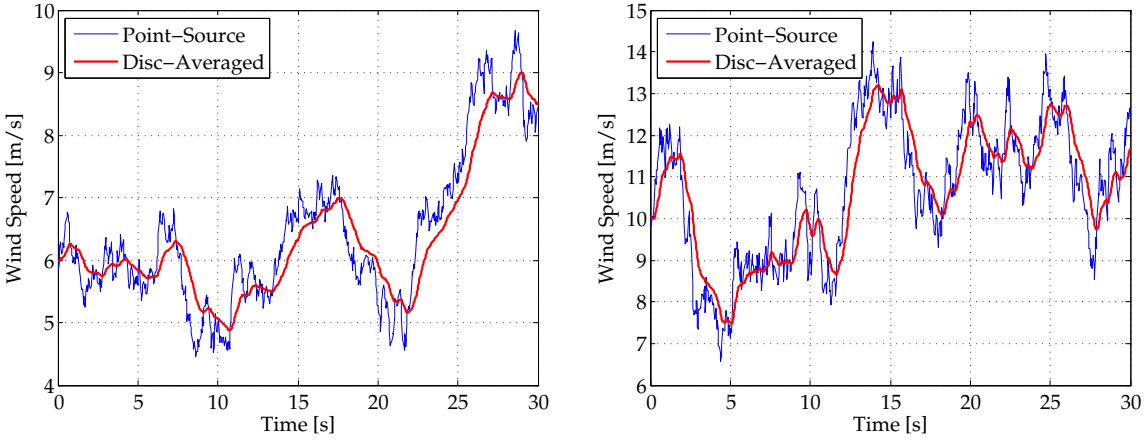

(a) Turbulent wind with a base speed of 6 m/s

(b) Turbulent wind with a base speed of 10 m/s

Figure 3.5: Examples of simulated turbulent wind time series.

3.3.1 System Modelling

A conceptualised cross-section of the SS-PMG is shown in Fig. 3.6(a). The first stage of the SS-PMG, composed of the slip-rotor and one side of the PM-rotor, is referred to as the 'slip-side'. The second stage, consisting of the stator and the other half of the PM-rotor, is labelled the 'sync-side' because it operates at synchronous speed when connected to the grid. The slip-side typically rotates at a fractionally higher speed than the sync-side and can undergo speed variations, depending on loading.

An exploded view of the SS-PMG is given in Fig. 3.6(b). The directions of rotation for the respective segments are indicated in blue, while the torque transmitted between the segments is shown in red. Power is transferred from the turbine to the grid in a two-stage process, as described qualitatively in Section 1.3.4.1. This process is now described mathematically for the purposes of numerical simulation.

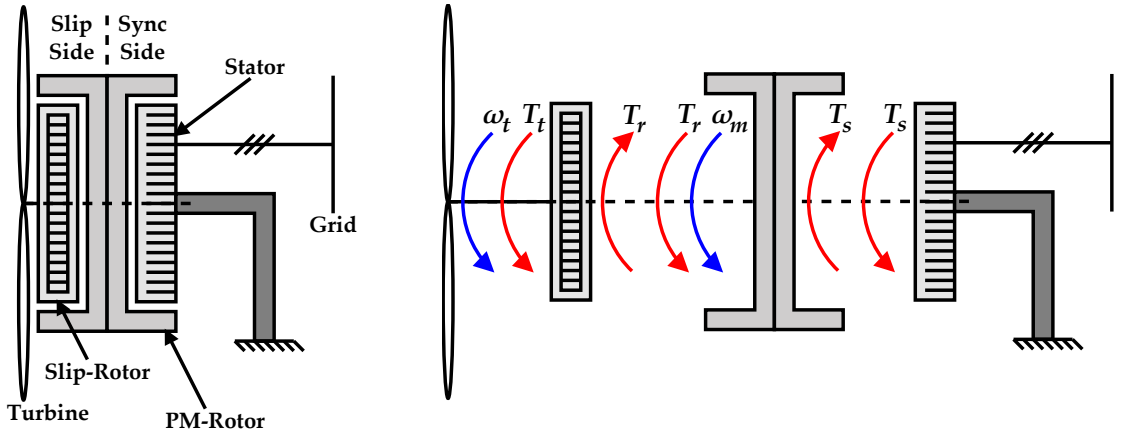

(a) Overview of the grid-connected SS-PMG, indicating major components

(b) Exploded view of the SS-PMG, indicating rotational directions in blue and torque transmission in red

Figure 3.6: Simplified cross-sectional views of the SS-PMG.

3.3.1.1 Electrical System

The electrical model of the SS-PMG is based on the Park model [76], which is formulated in the rotor-synchronous *dq* reference frame and is widely used for PMSG modelling [48; 71; 72]. Since both sides of the SS-PMG are, in fact, magnetically independent PMSGs, adapting the model is straightforward and the equivalent circuits for the slip-rotor and stator are almost identical. The fundamental difference, shown in Fig. 3.7, is that the slip-rotor is short-circuited, whereas the stator is not.

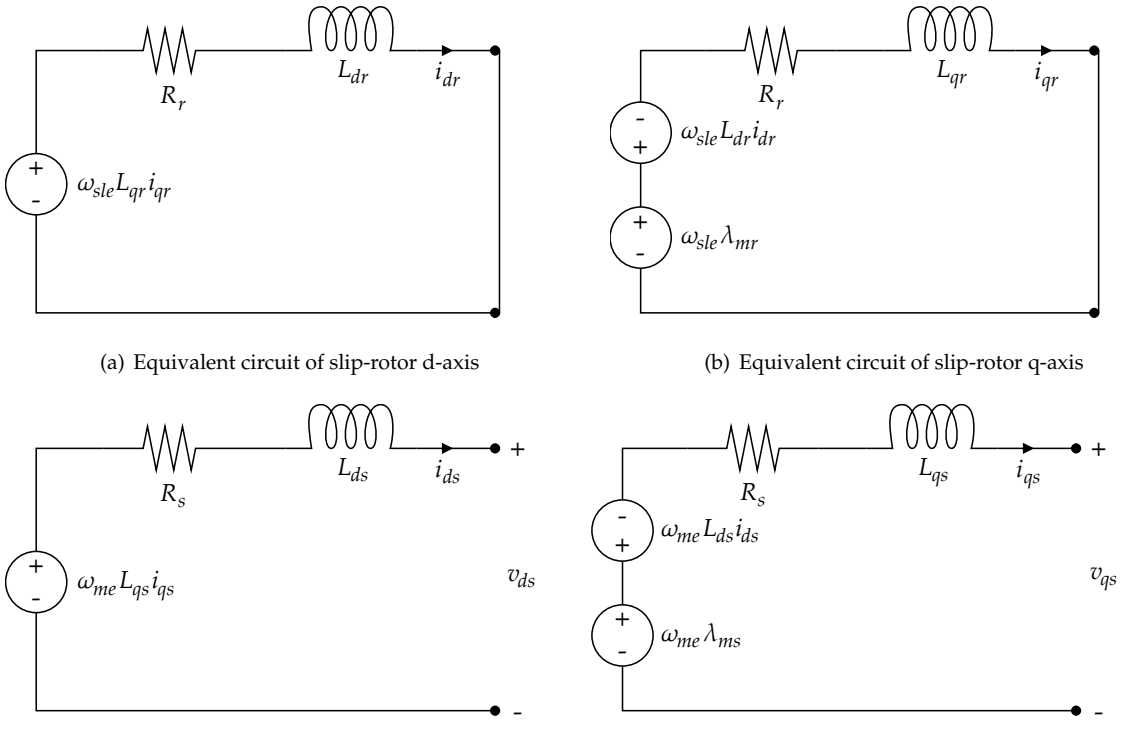

(a) Equivalent circuit of slip-rotor d-axis

(b) Equivalent circuit of slip-rotor q-axis

(c) Equivalent circuit of stator d-axis

(d) Equivalent circuit of stator q-axis

Figure 3.7: Equivalent *dq* electrical circuits for the SS-PMG slip-rotor and stator.

Analysis of the circuits in Fig. 3.7 leads to the development of the following differential equations to describe the electrical dynamics of the slip-rotor and stator:

$$0 = -i_{dr} R_r - L_{dr} \frac{\mathrm{d}i_{dr}}{\mathrm{d}t} + \omega_{sle} L_{qr} i_{qr} \tag{3.3}$$

$$0 = -i_{qr} R_r - L_{qr} \frac{\mathrm{d}i_{qr}}{\mathrm{d}t} - \omega_{sle} L_{dr} i_{dr} + \omega_{sle} \lambda_{mr} \tag{3.4}$$

$$v_{ds} = -i_{ds} R_s - l_{ds} \frac{\mathrm{d}i_{ds}}{\mathrm{d}t} + \omega_{me} L_{qs} i_{qs} \tag{3.5}$$

$$v_{qs} = -i_{qs} R_s - L_{qs} \frac{\mathrm{d}i_{qs}}{\mathrm{d}t} - \omega_{me} L_{ds} i_{ds} + \omega_{me} \lambda_{ms} \tag{3.6}$$

where

$$\omega_{me} = \frac{N_p}{2} \omega_m \tag{3.7}$$

$$\omega_{sle} = \frac{N_p}{2} (\omega_t - \omega_m) \tag{3.8}$$

The electromagnetic counter-torque developed by the slip-rotor and the stator is governed by Eqn (3.9) and Eqn (3.10), respectively:

$$T_r = \frac{3}{4}N_p[(L_{qr} - L_{dr})i_{dr}i_{qr} + \lambda_{mr}i_{qr}] \tag{3.9}$$

$$T_s = \frac{3}{4}N_p[(L_{qs} - L_{ds})i_{ds}i_{qs} + \lambda_{ms}i_{qs}] \tag{3.10}$$

The model presented here assumes constant dq inductances and PM-flux linkages [41]. Although this implies some loss of accuracy, it is a common assumption in literature and serves to simplify the numerical simulations while retaining the important dynamic characteristics of the SS-PMG. The values used are those calculated for operation at rated conditions, which is appropriate since most simulations focus on SS-PMG operation at or near synchronous speed and under load. A complete listing of parameter values is given in Appendix A.

3.3.1.2 Mechanical System

The mechanical system of the SS-PMG WECS is depicted conceptually in Fig. 3.8. The dynamics of this system are represented by Eqn (3.11) and Eqn (3.12). The B-terms incorporate all no-load rotational losses, as determined by laboratory measurements.

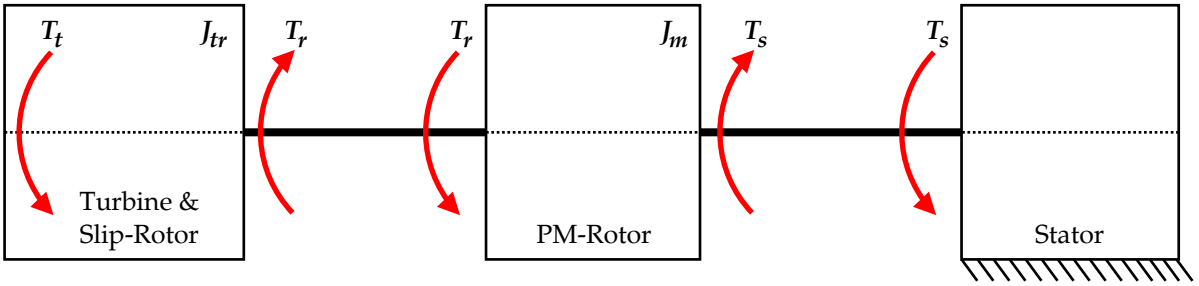

Figure 3.8: Block diagram of the torque-inertia interactions that take place in the mechanical aspect of the SS-PMG WECS.

$$T_t - T_r = T_p = J_{tr}\frac{d\omega_t}{dt} + B_r\omega_t + B_{r0} \tag{3.11}$$

$$T_r - T_s = T_m = J_m\frac{d\omega_m}{dt} + B_m\omega_m + B_{m0} \tag{3.12}$$

As indicated in Fig. 3.8, the turbine and slip-rotor are treated as a single component in the mechanical domain, with an inertia defined by Eqn (3.13). This is possible because the mechanical connection between the turbine and slip-rotor is sufficiently stiff compared to the electromagnetic coupling between the slip-rotor and PM-rotor.

$$J_{tr} = J_t + J_r \tag{3.13}$$

The complete electro-mechanical model of the SS-PMG is implemented in Ansoft *Simplorer* as a *VHDL-AMS* component block. This allows for a mixed modelling approach, where the electrical aspect of the SS-PMG is described in the *dq* reference frame while the controller components and electrical network are represented by conventional three-phase elements.

3.3.2 Experimental Verification: Steady-State Performance

A *Simplorer* model of the wind, turbine, and SS-PMG connected to a dumping load is shown in Fig. 3.9. To verify the accuracy of the SS-PMG model and the correctness of the chosen parameter values, two sets of steady-state measurements are compared to simulation results. The experimental results were obtained using the test setup described in Section 7.1.1.

Firstly, the no-load voltage and torque of the SS-PMG between zero and rated frequency can be compared. This is illustrated in Fig. 3.10, which shows that good agreement is achieved between measurement and simulation throughout the frequency range.

Secondly, the on-load performance of the SS-PMG is compared over the same frequency range. A three-phase resistive load of 6,1 Ω per phase was connected to the generator terminals, as depicted in Fig. 3.9. A comparison of the measured and simulated terminal voltage, phase current, and input (turbine) torque is illustrated in Fig. 3.11. Once again, good agreement is achieved over the whole frequency range, especially in terms of current and torque.

The results above show that the model and parameters chosen to represent the SS-PMG in simulation are sufficiently accurate in terms of steady-state predictions. It is now possible to incorporate an electrical network model and investigate the on-grid behaviour of the SS-PMG.

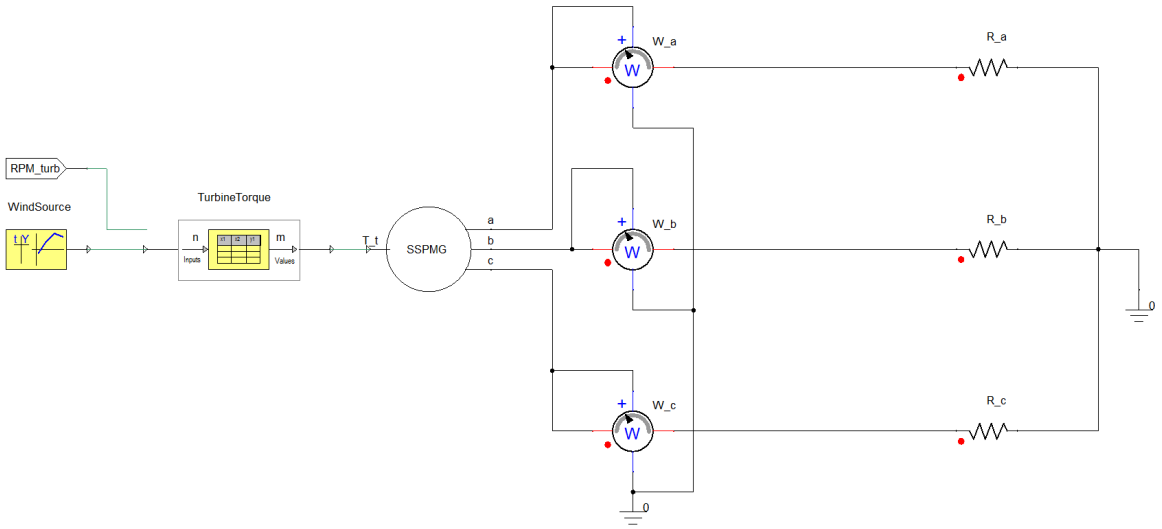

Figure 3.9: An Ansoft *Simplorer* model showing the wind speed input, turbine torque lookup table, and SS-PMG block connected to a three-phase resistive load. Wattmeters are used to measure voltage, current, and power.

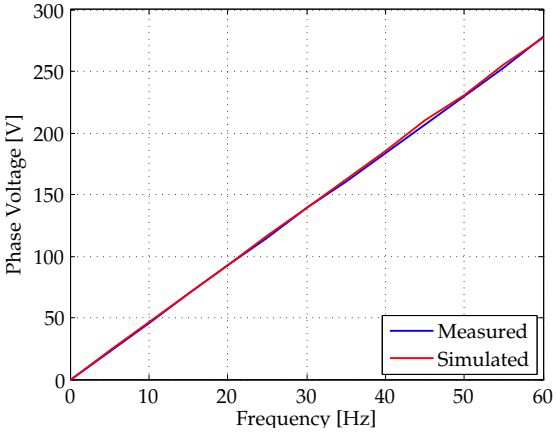

(a) SS-PMG no-load terminal voltage as a function of frequency

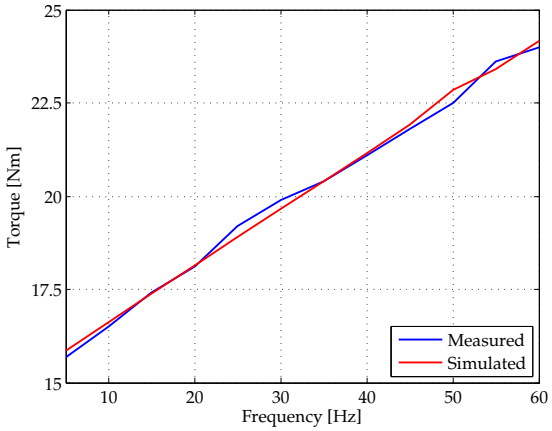

(b) SS-PMG no-load input torque (rotational losses) as a function of frequency

Figure 3.10: Comparison of simulated and measured data for no-load conditions.

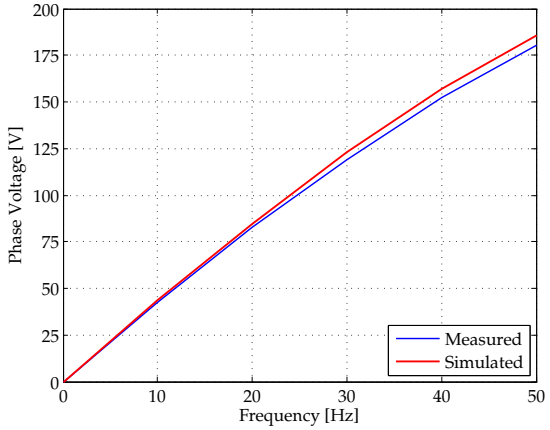

(a) SS-PMG on-load terminal voltage as a function of frequency

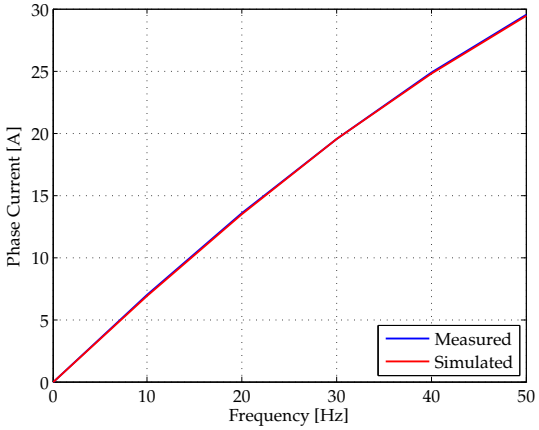

(b) SS-PMG on-load phase current as a function of frequency

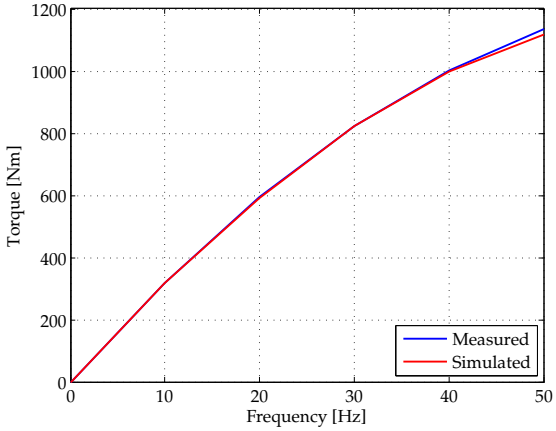

(c) SS-PMG on-load input torque as a function of frequency

Figure 3.11: Comparison of simulated and measured data for a 6,1 Ω resistive load case.

3.4 Grid-Connected Operation

Two specific SS-PMG-grid scenarios are covered within this study. The first is the synchronisation of the SS-PMG to a stable electrical network. The second is the interaction of the SS-PMG with a faulted network. Appropriate grid models for both cases are presented here, after which the measured and simulated responses of the SS-PMG to a short circuit fault are compared to verify the modelling approach used.

3.4.1 Equivalent Circuit Models for the Grid

The grid models employed need to provide realistic yet generalised response, while not imposing an unreasonable computational burden on simulations. Equivalent circuit models for the grid, based on an in-line impedance and source, are popular in literature [57; 58; 61] and meet the stated requirements.

3.4.1.1 Stable Grid

The equivalent circuit grid model used for synchronisation studies is shown in Fig. 3.12. An aggregated impedance value of 0,02 + j0,2 p.u. was derived from literature. However, it was elected to employ the more resistive case proposed by [77] where $R_{grid} = 0{,}15\,\Omega$ and $X_{grid} = 0{,}15\,\Omega$. These values result in a model that is more representative of rural distribution networks where the SS-PMG is likely to be installed.

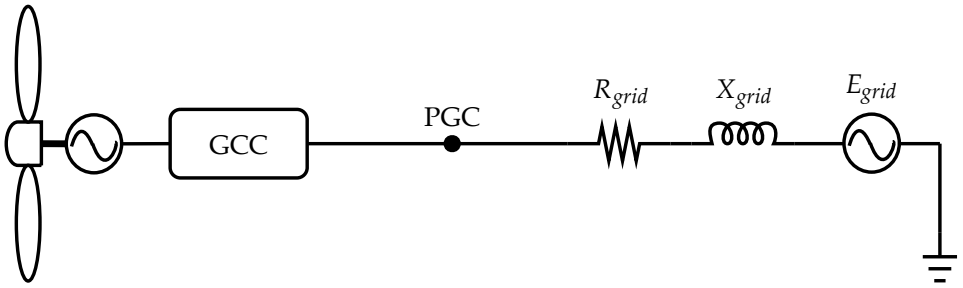

Figure 3.12: Per-phase line diagram showing the equivalent circuit representation of a stable grid for SS-PMG synchronisation simulations.

3.4.1.2 Faulted Grid

According to the grid code requirements discussed in Section 5.1, the WECS must be exposed to specified fault conditions at the PCC, which is typically at a medium voltage level or a high voltage level. As a result, one or more step-up transformers are located in series between the WTG and the fault. This is reflected in the equivalent circuit model chosen to represent the electrical network during the specified faults. The model is shown in Fig. 3.13.

The fault condition takes place at the PCC and is imposed by the time-dependent voltage source e_f, which follows a predefined voltage dip profile. The SS-PMG is connected to the grid at the PGC through the GCC. Between the fault and the PGC are two step-up transformers, which are represented by the

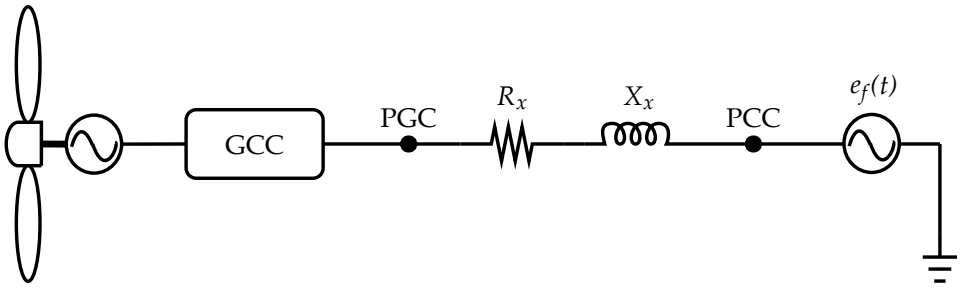

Figure 3.13: Per-phase line diagram representing the WECS and electrical network during a fault at the PCC. The time-dependent voltage source e_f imposes a pre-programmed voltage dip profile.

lumped in-line impedances shown. For the 25 kVA unit transformer (400 V to 10 kV) $R_{ux} = 0{,}02$ p.u. and $X_{ux} = 0{,}04$ p.u. on the transformer base. In the case of the 1000 kVA distribution transformer (10 kV to 110 kV) $R_{dx} = 0{,}01$ p.u. and $X_{dx} = 0{,}06$ p.u. on its base. The lumped values used in simulation are $R_x = 0{,}129\,\Omega$ and $X_x = 0{,}26\,\Omega$.

3.4.2 Experimental Verification: Dynamic Performance

To validate the accuracy of the *Simplorer* SS-PMG -grid model, as shown in Fig. 3.14, a short circuit test was performed at the PGC in the laboratory and simulation. In both cases, the following steps were followed:

1. Synchronise the SS-PMG with the grid.
2. Set the turbine torque to 500 Nm.
3. Open the grid contactor at $t = 0$ ms.
4. Close the short-circuit contactor at $t = 10$ ms.
5. Open the short-circuit contactor at $t = 190$ ms.
6. Close the grid contactor at $t = 200$ ms.

The effect of this test is to expose the loaded generator to a short circuit fault that is cleared after 180 ms. To avoid short-circuiting the grid in practice, the contactor between the SS-PMG and grid is opened before the short circuit is applied to the generator terminals. A delay is employed between operating the two contactors in order to avoid arcing. Although the full effect of a grid short circuit is not achieved, it is still possible from this test to evaluate the dynamic response of the SS-PMG itself to a short circuit and the interaction of the SS-PMG and grid at reconnection.

The simulated and measured voltage waveforms for this test are shown in Fig. 3.15(a) and Fig. 3.15(b), respectively. The two cases agree in terms of the magnitude of the voltage dip and the transient duration. *Simplorer* exhibits a tendency to predict excessive voltage spikes for the first simulation step after hard-switching loads with contactors, which is why the simulated case depicts significantly higher voltage spikes than the measured case. Judging by the number of voltage cycles during the fault, it would appear that the frequency of the SS-PMG in the measured case is double that of the simulated case. Examination of the current waveforms shows this to be false: it appears that the voltage probe used in the experiment is unable to resolve such small-scale signals correctly.

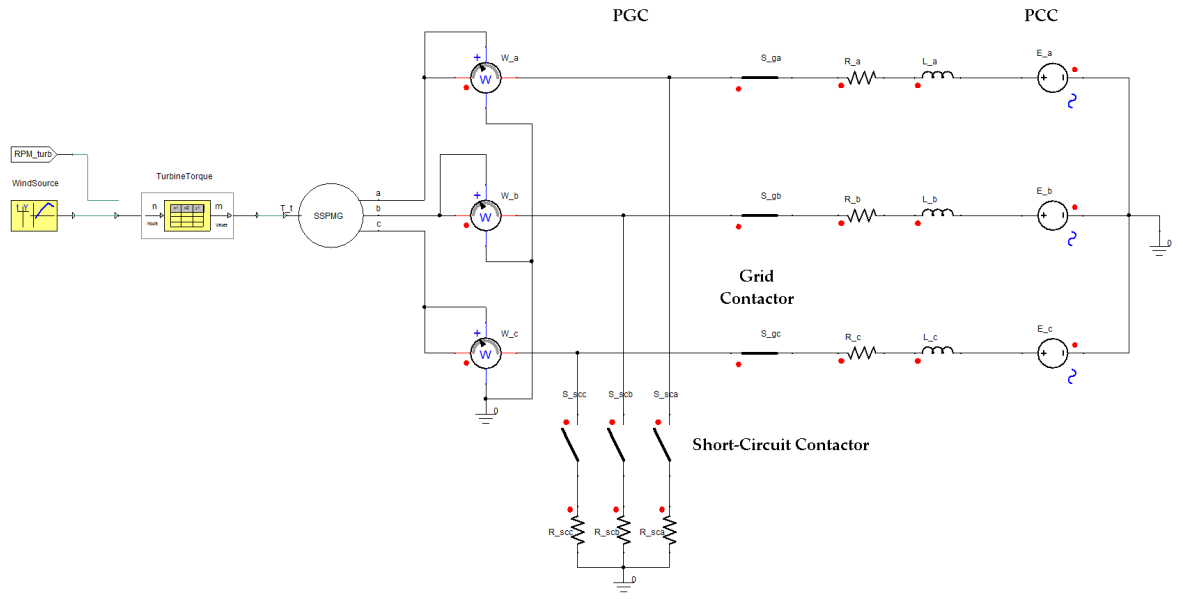

Figure 3.14: An Ansoft *Simplorer* model of the SS-PMG connected to the equivalent circuit for the grid with facility to generate a three-phase fault at the PGC.

The SS-PMG transient current is depicted for the simulated case in Fig. 3.15(c) and for the measured case in Fig. 3.15(d). The two cases show excellent agreement in terms of the initial current spike; the average current value during the fault; the decay of the DC-offset; and the number of cycles before reconnection. The measured case does show stronger post-fault current oscillations than the simulated case, although both are stable. This has been attributed to unstable interactions in the test bench drive-train.

Considering the simplicity of the SS-PMG model, the simulations have been shown to achieve reasonable agreement with practical measurements. Particularly, the key characteristics of the SS-PMG are depicted correctly. The *Simplorer* model presented here can thus be deemed appropriate the purposes of initial control design.

3.5 Controller Components

As far as possible, the components of the GCC are implemented in the WECS model in a manner that reflects their actual operational characteristics:

- Voltage and current measurements on the SS-PMG terminals, as well as grid voltage measurements, are made at a sampling rate of 1 kHz.
- The MCU is represented in simulations by *Simplorer* Equation Blocks which process instructions sequentially, as in the actual C-Code implementation.
- Contactors are represented by perfect switches with a 20 ms actuation delay. This is conservative since the measured delay for the contactors in the actual system is approximately 16 ms.
- Thyristors are represented by a *Simplorer* modelling block which employs an equivalent line model and parameter values, shown in Appendix A, from the manufacturer's data sheet.

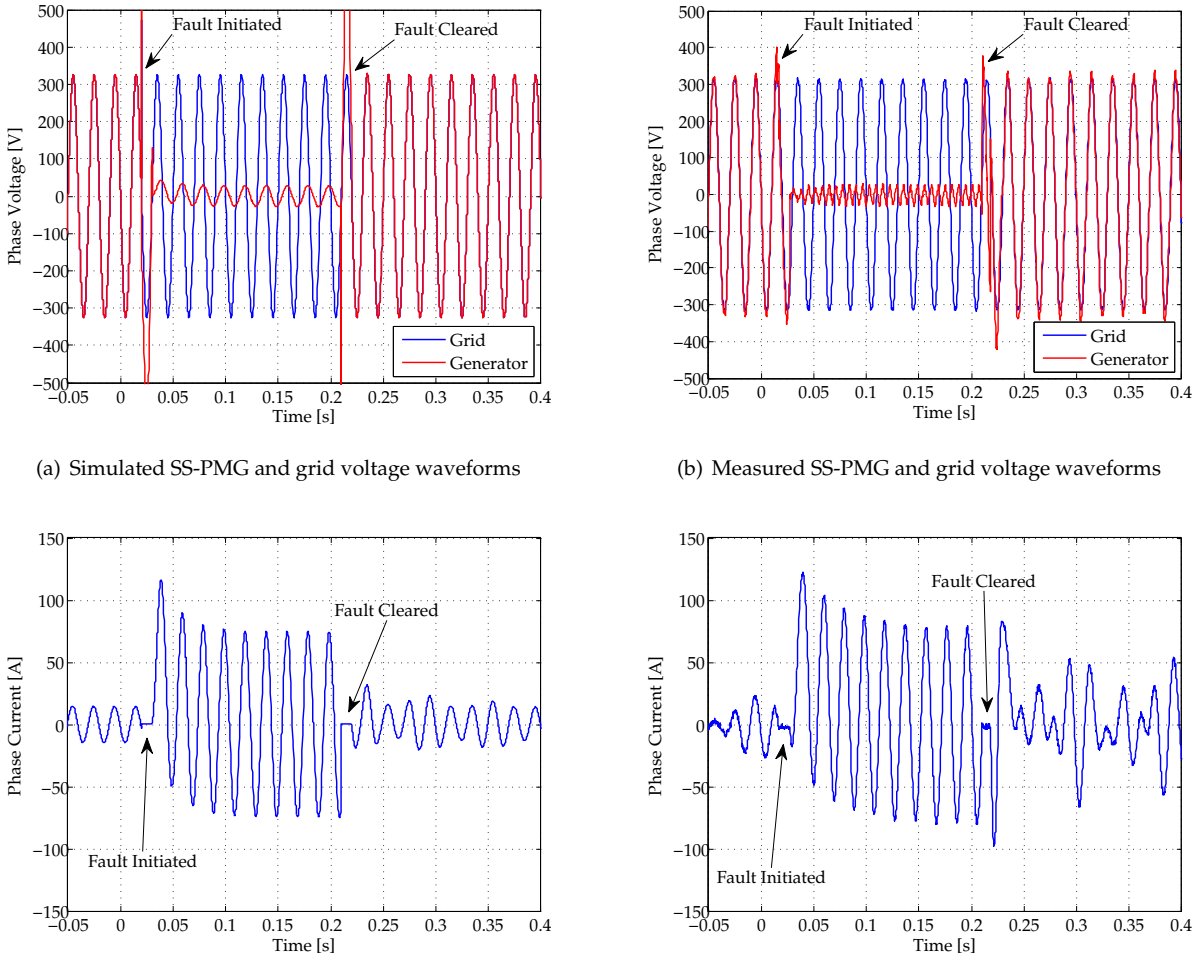

(a) Simulated SS-PMG and grid voltage waveforms

(b) Measured SS-PMG and grid voltage waveforms

(c) Simulated SS-PMG current waveform

(d) Measured SS-PMG current waveform

Figure 3.15: Comparison of simulated and measured data for a successfully cleared fault on the SS-PMG terminals while connected to the grid.

3.6 Summary

In this chapter, the modelling approaches used for various components of the SS-PMG WECS have been presented. This includes the turbine, wind, generator, grid, and controller. Results of simulations have also been compared with measured results from experiments to verify the accuracy of the chosen techniques. The tools discussed here are employed throughout the following two chapters to design and evaluate the GCC.

CHAPTER 4

GRID CONNECTION

In this chapter we investigate the conditions that allow for successful synchronisation of the SS-PMG to the electrical network. Once these requirements are in place, different speed control approaches, based on electromagnetic braking, are investigated and developed, as appropriate. Finally, the speed control and synchronisation functions are combined and tested in simulations.

4.1 Synchronisation Conditions

In this section, the conditions that must be satisfied to synchronise the SS-PMG successfully are investigated and threshold values for these conditions are determined. A synchronisation control strategy is then introduced.

4.1.1 Condition Evaluation

The requirements to achieve smooth synchronisation of the SS-PMG have already been discussed briefly in Chapter 1. These conditions can now be described quantitatively by comparing the grid and SS-PMG space vectors shown in Fig. 4.1, which are obtained through the transformations introduced in Section 2.1.1.2.

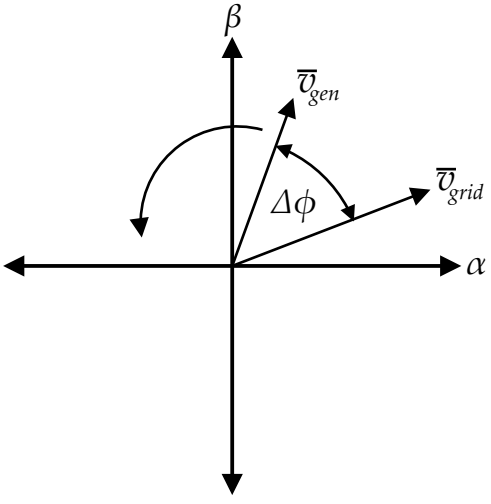

Figure 4.1: Rotating $\alpha\beta$ space vectors representing three-phase grid and SS-PMG voltage waveforms.

Firstly, the difference between grid and SS-PMG frequency Δf must be below the acceptable threshold value Δf_t:

$$\Delta f = \frac{1}{2\pi}\left(\frac{\mathrm{d}\phi_{grid}}{\mathrm{d}t} - \frac{\mathrm{d}\phi_{gen}}{\mathrm{d}t}\right) \tag{4.1}$$

$$|\Delta f| \leq \Delta f_t \tag{4.2}$$

Secondly, the RMS phase voltage magnitude difference ΔV must be less than the magnitude threshold ΔV_t. For a balanced three-phase system with sinusoidal waveforms:

$$\Delta V = \frac{v_{grid} - v_{gen}}{\sqrt{2}} \tag{4.3}$$

$$|\Delta V| \leq \Delta V_t \tag{4.4}$$

Finally, the voltage phase angle difference $\Delta\phi$ must be within the threshold $\Delta\phi_t$:

$$\Delta\phi = \phi_{grid} - \phi_{gen} \tag{4.5}$$

$$|\Delta\phi| \leq \Delta\phi_t \tag{4.6}$$

In addition to these requirements, turbine torque T_t and acceleration $\dot{\omega}_t$ should be minimised to reduce synchronisation transients. Since turbine torque cannot be controlled directly in this case, the net shaft torque $(T_t - T_s)$ should be as near to zero to possible to restrict $\dot{\omega}_t$.

4.1.2 Threshold Values from Literature

4.1.2.1 Previous Investigations

Tolerance bands for Δf and $\Delta\phi$ are developed in [3] for a direct-to-grid PMSG with a stator-mounted damping system. The assumption of zero net shaft torque is generally made and successful synchronisation is defined as occurring when pole-slipping is avoided. In the final design, synchronisation is possible at virtually any phase angle difference, as long as the speed difference is small enough. A typical synchronisation case involves $\Delta f = 2{,}5\,\mathrm{Hz}$, $\Delta\phi = 40\,^\circ$, and $\dot{\omega}_{me} = 22\,\mathrm{rad/s}$.

In [78] the tolerance margins chosen when synchronising an alternator to an SG-based WECS are $\Delta f_t = 0{,}25\,\mathrm{Hz}$ and $\Delta\phi_t = 10\,^\circ$. An unspecified degree of voltage magnitude agreement must also be achieved.

The low shaft stiffness of early SG WECS (for example, the US MOD-x designs) allows for relatively wide synchronisation tolerance bands, according to [79]. An Δf_t value of 'several percent' and $\Delta\phi_t$ of up to $70\,^\circ$ are deemed appropriate.

In these previous investigations, tolerance limits for synchronisation were chosen according to the effect of these limits on generator torque angle and other parameters. These effects are specific to both the generator design and the grid conditions encountered, however, network operators also impose universal synchronisation tolerance limits which must be adhered to.

4.1.2.2 Grid Code Requirements for Synchronisation

The voltage requirements for synchronising embedded generation to the Eskom distribution network are stated by [80] and are shown in Table 4.1. These requirements are derived directly from [81]. It is

also stated that the RMS voltage fluctuation at the PGC should not exceed 1 % if synchronisation is to take place regularly.

Table 4.1: Parameter limits for synchronisation with the Eskom distribution network.

Embedded Generator Rating [kVA]	Maximum Frequency Difference [Hz]	Maximum Voltage Difference [%]	Maximum Phase Angle Difference [°]
$0 \leq S < 500$	0,3	10	20
$500 \leq S < 1500$	0,2	5	15
$1500 \leq S$	0,1	3	10

4.1.3 SS-PMG Synchronisation Thresholds

The maximum allowable threshold values for synchronising the SS-PMG with the grid are given by Table 4.1 as $\Delta f_t = 0{,}3\,\text{Hz}$, $\Delta V_t = 10\,\%$, and $\Delta\phi_t = 20\,°$. However, observance of these limits does not necessarily imply that pole-slipping and over-current will be avoided for the SS-PMG under all operational wind conditions. This can only be confirmed by further investigations.

The requirements chosen to define safe synchronisation are as follows:

1. Rotor angle: $\theta < 120\,°$.
2. Instantaneous phase current: $i_{gen} < 2\,\text{p.u.}$

The rotor angle deviation limit is set to correspond to the threshold used by many utilities, in order to ensure an acceptable stability margin [82; 83]. The instantaneous current limit is set to reduce the possibility of voltage flicker. These requirements apply during and after synchronisation with wind speeds up to the operational maximum of $u_w = 12\,\text{m/s}$. Neither requirement may be violated, even when all synchronisation conditions are simultaneously at their respective threshold values.

4.1.3.1 Frequency Difference

The effect of varying Δf at synchronisation while $\Delta\phi = 0\,°$ is illustrated in Fig. 4.2. Two scenarios are evaluated: synchronisation under the lowest operational wind speed and under the highest operational wind speed. In the former case, turbine torque and acceleration are almost negligible, so only the effects of positive frequency differences ($\Delta f > 0\,\text{Hz}$) need to be evaluated. This is in contrast with the latter scenario, where turbine torque is significant and asymmetrical results are obtained.

When $\Delta f > 0\,\text{Hz}$ the turbine torque at high wind speeds is beneficial since it works to increase rotor speed and reduce the frequency difference, resulting in lower transients than in the low wind speed case. On the other hand, when $\Delta f < 0\,\text{Hz}$ the turbine torque must be overcome in order to reduce rotor speed. As a result, more severe transients are experienced when $\Delta f < 0\,\text{Hz}$ at high wind speeds.

Although transients increase steeply with Δf at low wind speeds, Fig. 4.2(a) shows that the specified current limit of 2 p.u. is not exceeded even when $\Delta f = 4\,\text{Hz}$. Similarly, the SS-PMG remains stable with maximum rotor angle never exceeding 60 ° for the range investigated (Fig. 4.2(b)). From a practical

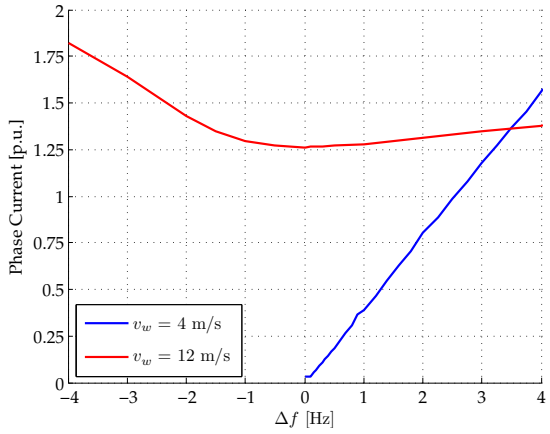

(a) Maximum phase current (across all phases) during synchronisation as a function of frequency difference

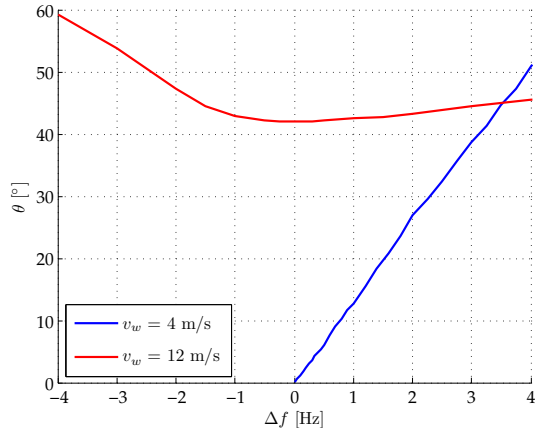

(b) Maximum rotor angle during synchronisation as a function of frequency difference

Figure 4.2: Maximum synchronisation transients for the SS-PMG as a function of frequency difference. Wind speeds are steady and phase angle difference is held at zero.

point of view, the frequency limit of $\Delta f_t = 0{,}3\,\text{Hz}$ appears overly restrictive. For example, allowing $\Delta f_t = 1{,}0\,\text{Hz}$ results in less than 0,5 p.u. maximum current when no other influences are present.

4.1.3.2 Phase Angle Difference

The effect of $\Delta\phi$ on synchronisation transients is illustrated in Fig. 4.3 for the same two wind scenarios discussed in the previous section. In Fig. 4.3(a) the low wind case shows a linear increase in maximum current with $\Delta\phi$, although the high wind case only adopts a similar linear curve at large phase angle differences. At smaller values of $\Delta\phi$, the effect of the turbine torque-related transients is dominant and $\Delta\phi$ has relatively little influence on peak current.

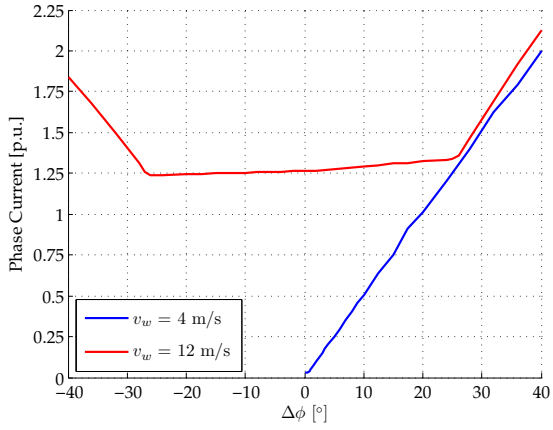

(a) Maximum phase current (across all phases) during synchronisation as a function of phase angle difference

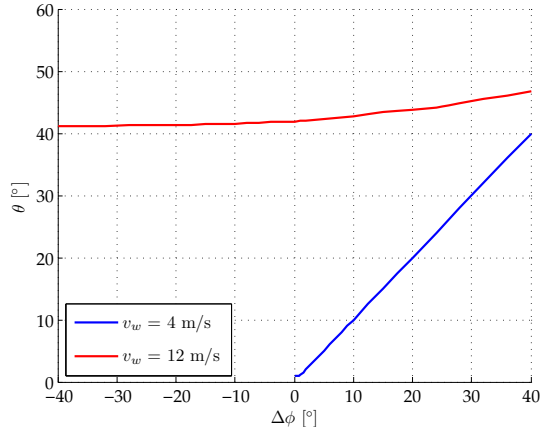

(b) Maximum rotor angle during synchronisation as a function of phase angle difference

Figure 4.3: Maximum synchronisation transients for the SS-PMG as a function of phase angle difference. Wind speeds are steady and frequency difference is held at zero.

The maximum rotor angle during synchronisation, illustrated in Fig. 4.3(b), shows similar trends to those observed with maximum current. However, the difference in real power between the low and high wind cases leads to a significant offset in the latter case. Compared to this offset, the increase in maximum rotor angle with $\Delta\phi$ is less significant than the increase in current.

From the results shown above, the required limit of $\Delta\phi_t = 20\,^\circ$ appears too large: even under low wind conditions this leads to a maximum synchronisation current of approximately 1 p.u. If the limit is reduced to $\Delta\phi_t = 10\,^\circ$ then the maximum current can be reduced to 0,5 p.u. at low wind. When combined with other factors, the maximum current limit of 2 p.u. should thus be achievable across the operational wind speed range.

4.1.3.3 RMS Voltage Difference

The final parameter to examine is voltage difference ΔV. The open terminal voltage of the SS-PMG is purely a function of frequency and cannot be modified externally since PM excitation is not dynamically controllable. Under no-load conditions the voltage difference limit $\Delta V_t = 10\,\%$ implies $\Delta V \leq 23{,}1\,\text{V}$. This limit will be adhered to as long as $\Delta f \leq 5\,\text{Hz}$. Loading the SS-PMG prior to synchronisation will cause a reduction in terminal voltage, which will, in turn, require a lower frequency difference threshold for synchronisation.

4.1.3.4 Combined Thresholds

The thresholds required by [80] are $\Delta f_t = 0{,}3\,\text{Hz}$ and $\Delta\phi_t = 20\,^\circ$. This set of limits, referred to as set A, is generic and applies to any SG. By examining the effects of Δf and $\Delta\phi$ individually, an alternative pair of threshold values for the SS-PMG, set B, can be proposed: $\Delta f_t = 1{,}0\,\text{Hz}$ and $\Delta\phi_t = 10\,^\circ$. The results of applying these two sets of threshold values across the operational wind speed range are shown in Fig. 4.4.

For the sake of brevity, only the worst case scenarios are shown in the figures. At synchronisation, both Δf and $\Delta\phi$ are held at their respective threshold values simultaneously. In each case, a negative frequency difference and a positive phase angle difference are employed because these have been shown have the largest effect on current and phase angle. Wind speed is steady, not turbulent.

Fig. 4.4(a) illustrates that set B allows for significantly lower current spikes during low winds, whereas both approaches achieve similar results under high winds. Applying set A leads to relatively large current maxima, even at low winds, because the SS-PMG is sensitive to phase angle misalignment at synchronisation.

The instantaneous load on the network caused during synchronisation with set A leads to a more severe drop in the phase voltage at the PGC than when using set B. This is illustrated in Fig. 4.5, which shows traces of the grid and SS-PMG voltage waveforms at synchronisation with a steady wind speed of 4 m/s. Fig. 4.5(a) illustrates that set A results in a 1,54 % phase voltage drop for the half-cycle after synchronisation. In Fig. 4.5(b) the drop caused with set B is 0,59 %.

The difference in PGC voltage drop between set A and set B is a significant consideration: the network voltage dip caused by synchronisation should be less than 1 % for synchronisation occuring at less

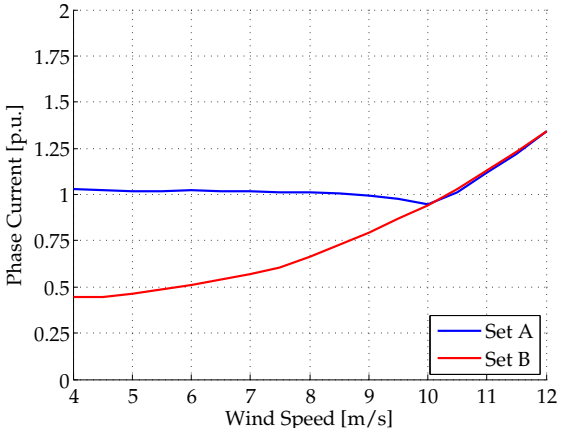

(a) Maximum phase current during synchronisation as a function of wind speed

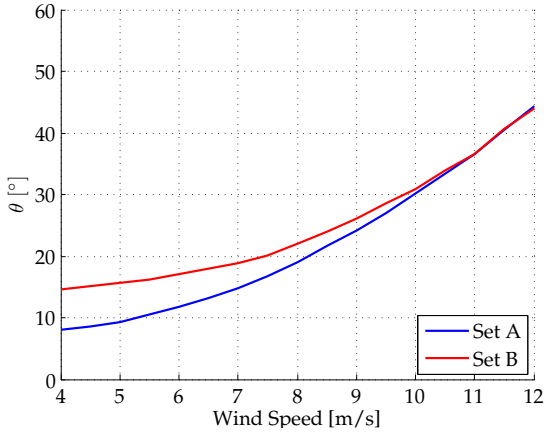

(b) Maximum rotor angle during synchronisation as a function of wind speed

Figure 4.4: Maximum synchronisation transients for the SS-PMG as a function of steady wind speed. Two different sets of threshold values are used: Set A with $\Delta f_t = -0{,}3\,\text{Hz}$ and $\Delta\phi_t = 20\,°$ and Set B with $\Delta f_t = -1{,}0\,\text{Hz}$ and $\Delta\phi_t = 10\,°$.

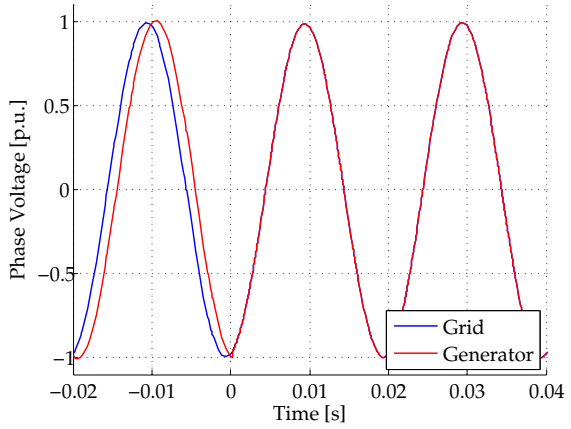

(a) Instantaneous grid and SS-PMG phase voltages during synchronisation with set A threshold values at low wind

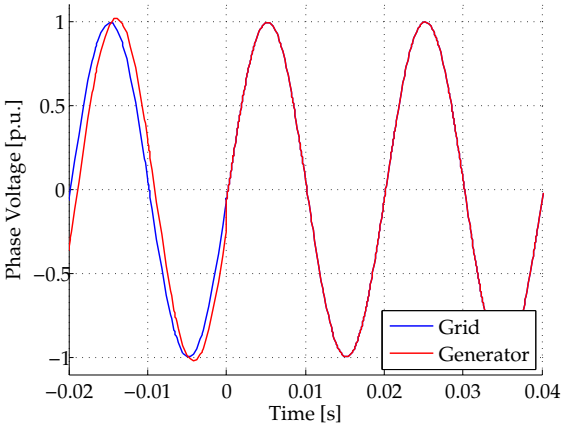

(b) Instantaneous grid and SS-PMG phase voltages during synchronisation with set B threshold values at low wind

Figure 4.5: Traces comparing the simulated voltage waveforms of the grid and SS-PMG during synchronisation with set A and set B threshold values at $u_w = 4\,\text{m/s}$. Synchronisation occurs at $t = 0\,\text{s}$.

than 2 hour intervals, according to [80]. Although both sets will cause larger voltage dips under strong winds, the most frequent re-synchronisation is likely to happen under low winds. Under marginal wind conditions the SS-PMG would need to be disconnected and reconnected more often to capture energy when available without allowing extended periods of motoring operation when the wind falls below 4 m/s. As such, synchronisation at low wind speeds should conform to the 1 % voltage dip restriction and set B provides better performance in this regard.

The traces in Fig. 4.6 show the rotational speed, phase currents, and rotor angle of the SS-PMG during synchronisation at $u_w = 4\,\text{m/s}$. When comparing Fig. 4.6(c) and Fig. 4.6(d), it is evident that the larger phase angle offset in set A leads to a current spike 2,31 times higher than with set B. The initial

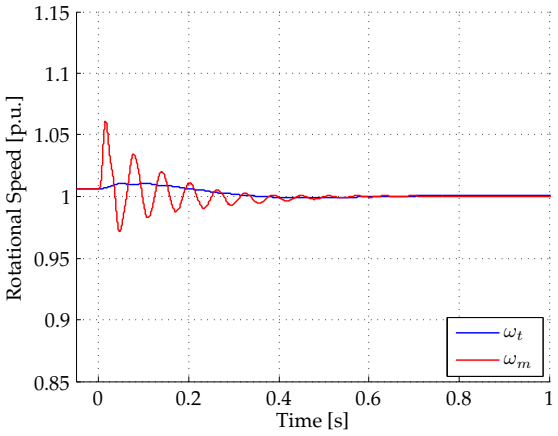

(a) Turbine and PM-rotor speed during synchronisation with required threshold values at low wind

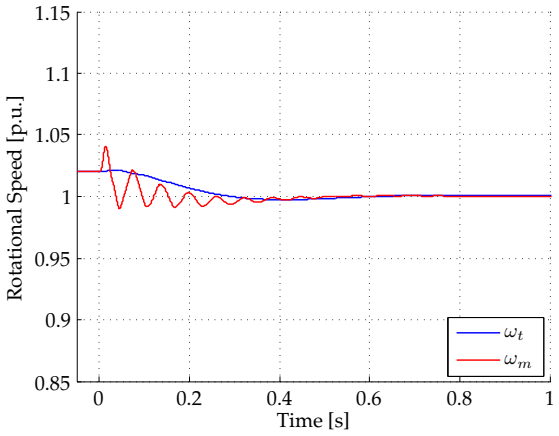

(b) Turbine and PM-rotor speed during synchronisation with alternative threshold values at low wind

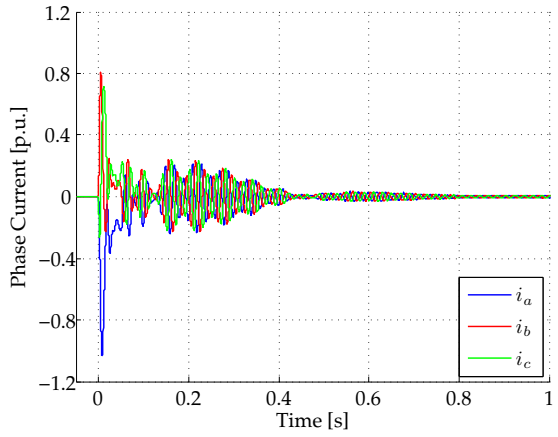

(c) Instantaneous SS-PMG phase currents during synchronisation with required threshold values at low wind

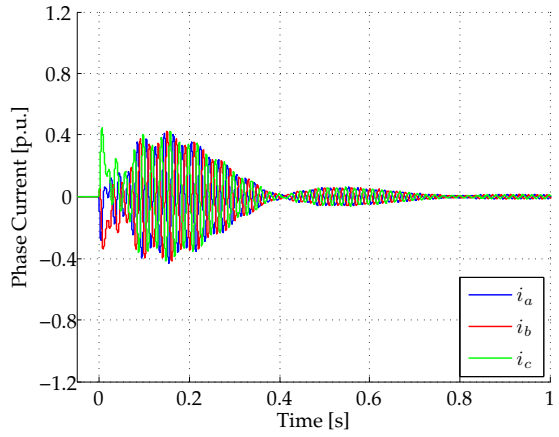

(d) Instantaneous SS-PMG phase currents during synchronisation with alternative threshold values at low wind

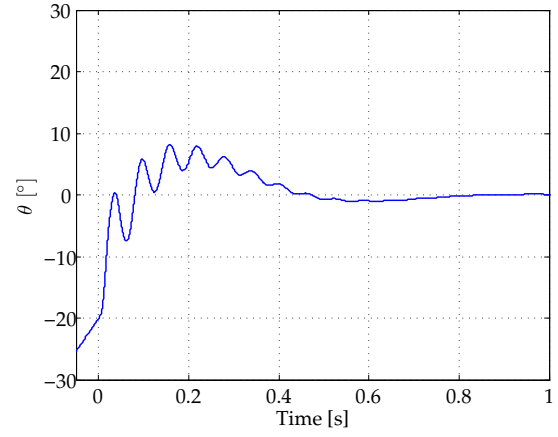

(e) SS-PMG rotor angle during synchronisation with required threshold values at low wind

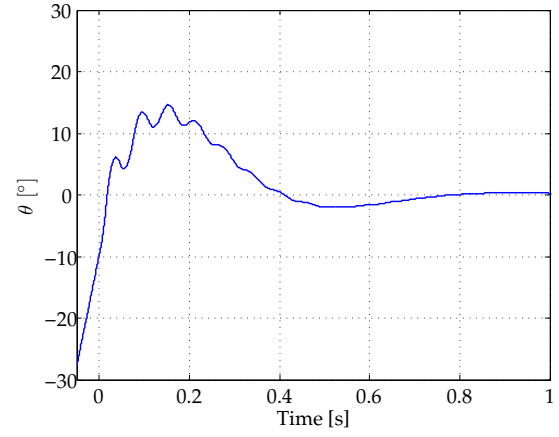

(f) SS-PMG rotor angle during synchronisation with alternative threshold values at low wind

Figure 4.6: Traces of the simulated dynamic response of the SS-PMG during synchronisation at $u_w = 4\,\mathrm{m/s}$. The left column and the right column show results for set A and set B threshold values, respectively. Synchronisation occurs at $t = 0\,\mathrm{s}$.

PM-rotor speed deviation is also larger for set A, as shown by Fig. 4.6(a) and Fig. 4.6(b). This reinforces the impression that set B achieves better results, particularly at low wind speeds.

In contrast to the trends discussed thus far, set A is shown in Fig. 4.4(b) to achieve generally lower rotor angle deviations than set B, which implies greater stability at synchronisation. Because Δf_t is lower for set A than for set B, the energy required to bring the SS-PMG into synchronism is also lower for set A. This is reflected by the rotor angle deviations shown in Fig. 4.6(e) and Fig. 4.6(f), where set A allows for a 44,4 % reduction over set B. Fig. 4.6(c) and Fig. 4.6(d) show that the mean current during the first 0,8 s after synchronisation is lower when the set A limits are employed. Using set B requires a larger energy contribution from the grid.

Despite the different results achieved with set A and set B at lower wind speeds, both sets guarantee stability and current transients below 2 p.u. across the wind speed range. They also deliver almost the same dynamics at rated wind speed. The trade-off between the required and alternative cases could be overcome by combining the two to give $\Delta f_t = 0{,}3$ Hz and $\Delta\phi_t = 10\,°$. However, this would reduce the synchronisation window of opportunity even further and require higher control effort.

Ultimately, the set B limits have been adopted for the rest of the investigation because they reduce the initial current spike, while providing a wider frequency band in which to synchronise. (The Synchronous Frequency Range is thus defined as $f_{grid} \pm 1$ Hz.) This allows the system to meet the 1 % PGC voltage dip limit at low winds, while providing more opportunity to synchronise, which allows the SS-PMG to be connected to the grid more quickly and with less control effort.

4.1.4 Synchronisation Methodology

The synchronisation tolerance limits are $\Delta f_t = 1{,}0$ Hz $= 0{,}02$ p.u., $\Delta V_t = 0{,}1$ p.u., and $\Delta\phi_t = 10\,°$. The flow diagram in Fig. 4.7 illustrates how the synchronisation conditions, based on these limits, are

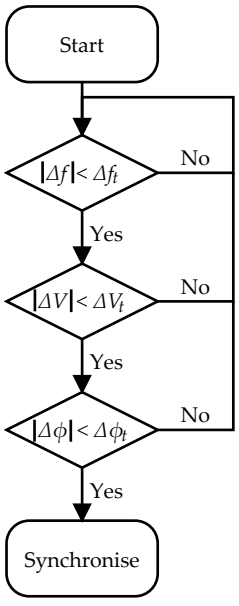

Figure 4.7: Flow diagram of SS-PMG synchronisation subroutine implemented in the GCC.

evaluated. This monitoring process is implemented in both the *Simplorer* simulations and the *TI* MCU, and occurs continuously prior to grid connection of the SS-PMG.

Once all synchronisation conditions are met with the aid of speed control, the SS-PMG is connected to the grid by simultaneously closing switch S3 and switch S4, shown as part of the GCC in Fig. 4.8. As synchronism is achieved, switch S1 and switch S2 are opened. The LVRT mechanism, making use of S3 and S1/S2, can then be activated if a voltage dip occurs.

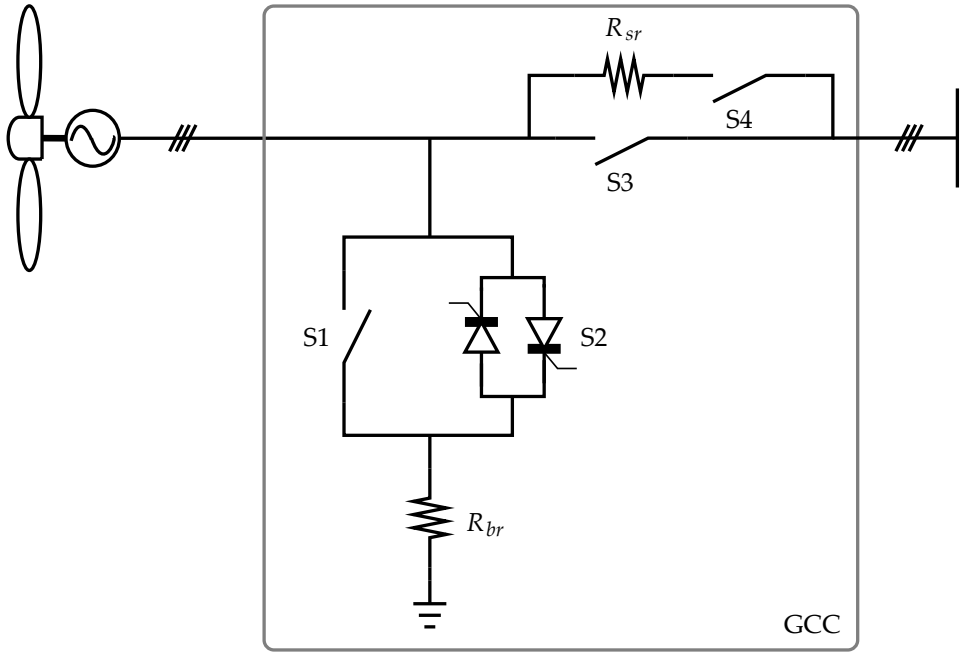

Figure 4.8: Line diagram of the GCC, including speed control, synchronisation, and LVRT actuators.

4.2 Speed Control

Speed control is essential to be able to satisfy the synchronisation conditions and to connect the SS-PMG to the grid consistently under turbulent wind conditions. The objectives of the speed control design are:

1. Bring the SS-PMG to within the synchronous frequency range ($|\Delta f| \leq \Delta f_t$) under all wind conditions where $4\,\mathrm{m/s} \leq u_w \leq 12\,\mathrm{m/s}$.
2. Restrict PM-rotor acceleration $\dot{\omega}_m$ to an acceptable value in the synchronous frequency range. The maximum permissible acceleration in the SFR is determined in Section 4.2.1.1.
3. Prevent excessive speed overshoot to protect the turbine and SS-PMG from excessive forces and over-voltage, respectively. Ideally, overshoot should be less than 10 % but values up to 20 % can be tolerated.

The speed control mechanism introduced in Section 2.2.2 makes use of electromagnetic braking to regulate net torque $T_n = T_t - T_s$, which allows for fast control of speed and acceleration through the relationships established in Section 3.3.1.

This section investigates two speed control strategies, one making use of contactors only and the other employing thyristors. In both cases, the counter-torque developed by the SS-PMG when it is connected to a resistive load is used to regulate the acceleration of the turbine-generator system.

A simplified depiction of the speed controller in the GCC is shown in Fig. 4.8. Switch S1 is a conventional electromechanical contactor, while switch S2 is a back-to-back thyristor pack (triac). Both S1 and S2 engage the braking resistance R_{br}.

4.2.1 Contactor-based Speed Control

Switching in the resistive load R_{br} with a contactor is a simple, robust, and affordable strategy. The drawback of this approach is that the resistive load imposed on the generator is constant, which means T_s becomes a function of ω_m. As such, it is not possible to actively control speed or to respond to changes in wind conditions. The resistive load can be varied in discrete steps by employing multiple contactor and resistance combinations, although this incurs significant cost penalties.

Whether one or multiple stages are used, the contactor braking approach cannot achieve true speed control. Rather, the system serves to limit acceleration $\dot{\omega}_m$ while the SS-PMG passes through the SFR in order to provide more opportunity to synchronise. If synchronisation is not completed during the first pass, then the SS-PMG must be allowed to pass through the SFR again, either by changing the resistive load or by waiting for the wind speed to change sufficiently.

It is desirable to synchronise the SS-PMG on the first pass to maximise system uptime and energy capture. As a result, it is necessary to determine the maximum value of $\dot{\omega}_m$ at which synchronisation is virtually guaranteed, and then to establish how this limit can be maintained across the wind speed range.

4.2.1.1 Synchronisation Opportunity

The PM-rotor acceleration $\dot{\omega}_m$ determines how long the SS-PMG remains in the frequency range in which synchronisation is possible. If $\dot{\omega}_m$ is too high, then it is possible that no opportunity will exist to synchronise during a given pass. To determine the maximum value of $\dot{\omega}_m$ at which a synchronisation opportunity will always exist, the worst case must be examined.

The crucial condition to satisfy once the SS-PMG enters the SFR ($|\Delta f| \leq \Delta f_t$) is that $|\Delta\phi| \leq \Delta\phi_t$. The worst case scenario is for $|\Delta\phi| = \Delta\phi_t$ at the instant before entering the SFR and then for $|\Delta\phi|$ to increase. To re-enter the threshold band, $\Delta\phi$ must then change by $360\,^\circ - 2\Delta\phi_t$. If $\dot{\omega}_m$ is too high, this will not happen before $|\Delta f| > \Delta f_t$ again and another pass will then be necessary to attempt synchronisation.

Fig. 4.9 illustrates a case where $\dot{\omega}_m$ is too high. In Fig. 4.9(a) it can be seen how the SS-PMG moves through the SFR. At the same time, Fig. 4.9(b) shows how there is no instant where phase angle agreement is achieved within the SFR and there is thus no possibility of synchronisation.

The limiting case for synchronisation opportunity is shown in Fig. 4.10(a). It shows that, even in the worst case, $\Delta\phi$ will fall within the phase angle tolerance band for an instant when $\dot{\omega}_m = 0{,}0106$ p.u. If $\dot{\omega}_m$ is lower than this limit then multiple instances will exist where synchronisation can occur, as illustrated in Fig. 4.10(b) where the SS-PMG can be synchronised at any moment in the range $1{,}57\,\text{s} < t < 2{,}36\,\text{s}$.

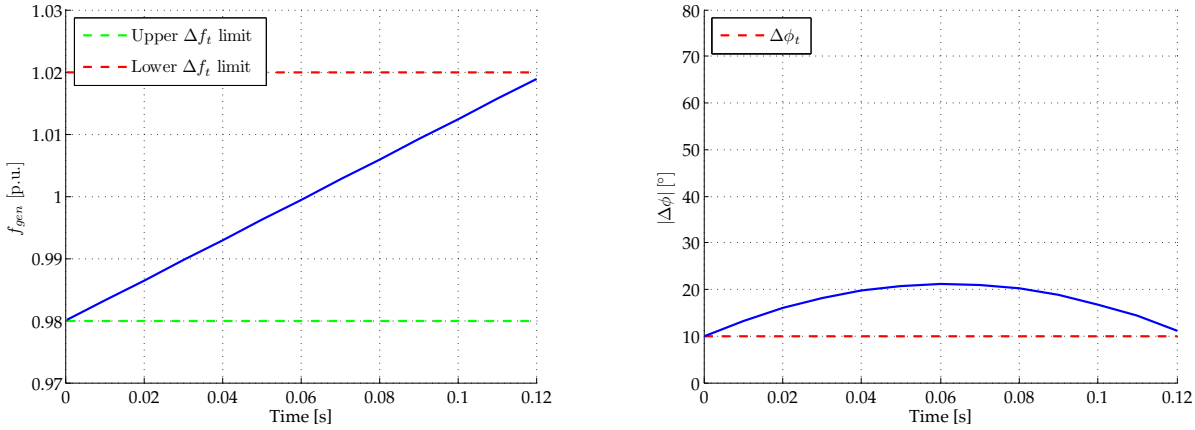

(a) Generator frequency as a function of time

(b) Phase angle difference as a function of time

Figure 4.9: Traces of f_{gen} and $|\Delta\phi|$ passing through the SFR at no-load with $u_w = 12\,\text{m/s}$. Average $\dot{\omega}_m = 0{,}3242\,\text{p.u.}$ No synchronisation opportunity exists.

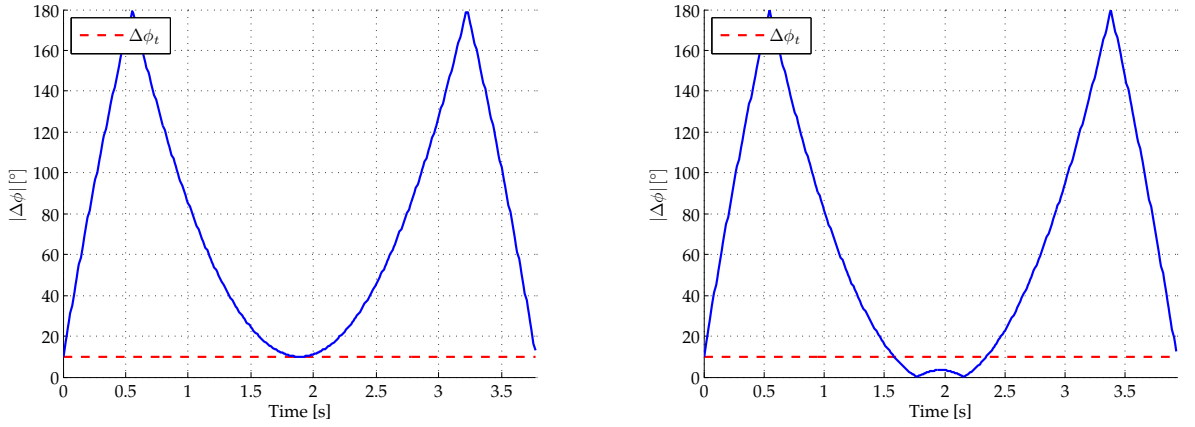

(a) Phase angle difference vs time for $\dot{\omega}_m = 0{,}0106\,\text{p.u.}$

(b) Phase angle difference vs time for $\dot{\omega}_m = 0{,}0102\,\text{p.u.}$

Figure 4.10: Traces of $|\Delta\phi|$ passing through the SFR for two cases where synchronisation opportunities exist.

As long as $\dot{\omega}_m \leq 0{,}0106\,\text{p.u.}$ while $|\Delta f| \leq \Delta f_t$ then an opportunity to synchronise will exist during each pass, even under worst case conditions. On the other hand, a more relaxed limit of $\dot{\omega}_m \leq 0{,}06\,\text{p.u.}$ will suffice under most conditions while placing less stringent demands on the speed control mechanism.

4.2.1.2 Controlling Acceleration

The SS-PMG and turbine torque curves match poorly, as illustrated in Fig. 4.11(a), but it is only essential to achieve good agreement in and around the SFR. Fig. 4.11(b) shows the PM-rotor acceleration at $\Delta f = 0\,\text{p.u.}$ as a function of wind speed. Different curves result from changing the value of R_{br} engaged through switch S1.

By studying Fig. 4.11(b) it is clear that the objective of ensuring $\dot{\omega}_m \leq 0{,}0106\,\text{p.u.}$ is unrealistic for contactor-based electromagnetic braking. The number of switch and resistor combinations required to

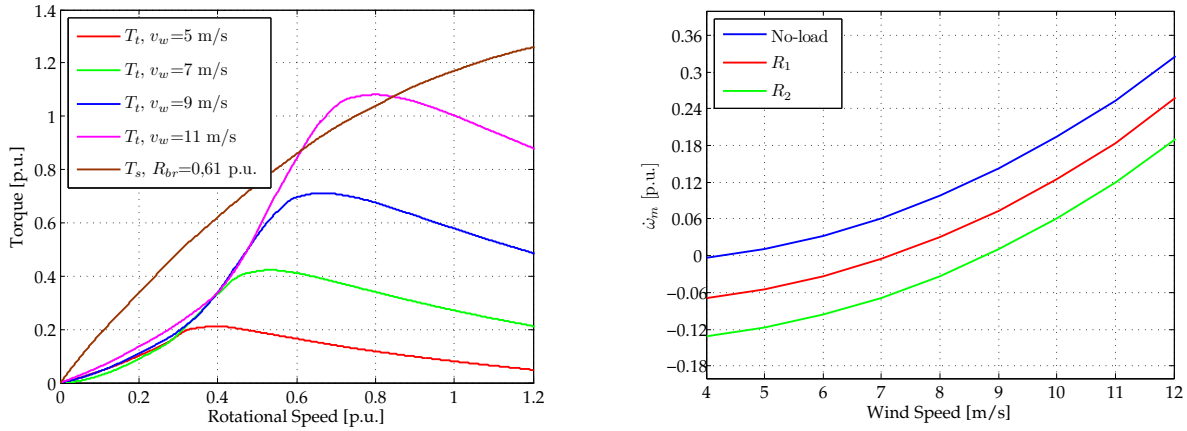

(a) Comparison of turbine and SS-PMG torque-speed curves

(b) SS-PMG acceleration as a function of wind speed with different values of R_{br}: $R_1 = 3{,}98\,\text{p.u.}$ and $R_2 = 1{,}99\,\text{p.u.}$

Figure 4.11: Turbine and SS-PMG torque interactions.

do so across the wind speed range is not feasible. A compromise can be reached, however, by setting a new objective of $\dot{\omega}_m \leq 0{,}06\,\text{p.u.}$, which does not guarantee synchronisation in the worst cases, but will allow one-pass synchronisation in realistic situations. With this relaxed objective, appropriate R_{br} values for the SS-PMG in the SFR can be defined by Eqn (4.7).

$$R_{br} = \begin{cases} \infty & \text{if } u_w \leq 7\,\text{m/s} \\ 3{,}98\,\text{p.u.} & \text{if } u_w \leq 8{,}7\,\text{m/s} \\ 1{,}99\,\text{p.u.} & \text{if } u_w \leq 10\,\text{m/s} \end{cases} \tag{4.7}$$

To synchronise successfully, the wind must be allowed to accelerate the WECS from rest until the SS-PMG exceeds a cut-in rotational speed of $w_m = 0{,}6\,\text{p.u.}$ Then the appropriate resistance can be switched in and the SS-PMG will pass through the SFR with $\dot{\omega}_m \leq 0{,}06\,\text{p.u.}$, at which point synchronisation will usually be able to occur. If no synchronisation opportunity is realised then either the GCC must wait until the SS-PMG re-enters the SFR due to changes in wind speed or a different R_{br} value must be engaged to reduce w_m and repeat the process. The latter approach could lead to oscillatory behaviour if the wind is highly variable.

The proposed control strategy requires two contactor-resistance combinations, and a strategy that can achieve synchronisation up to $u_w = 12\,\text{m/s}$ would require at least four. The cost and complexity of such a system exceeds that of one that employs solid-state switches, without offering the same level of controllability. In addition, synchronisation is not guaranteed on the first pass, due to the relaxed acceleration limit and the finite sampling speed of the GCC. As a result, contactor-based speed control is not deemed appropriate for further investigation.

4.2.2 Thyristor-based Speed Control

By engaging R_{br} with the thyristor switch S2 it is possible to switch more rapidly and to control the effective voltage on the load by varying the thyristor firing delay angle α. As illustrated in Fig. 4.12,

the firing delay angle can be varied in the range $0° \leq \alpha \leq 180°$. In this way, the effective voltage V_R applied to R_{br} can be varied as an inverse function of α. As a result, a single resistance value can be employed: $R_{br} = 0{,}61$ p.u. was chosen because it can extract close to maximum torque from the SS-PMG at rated speed. It also provides a relatively linear increase in torque with rotational speed, which helps to prevent runaway of the turbine under extreme wind conditions.

By varying V_R, one can control the SS-PMG load current and, as a result, the counter-torque produced to regulate speed. Because α can be changed every half-cycle it is possible to vary the SS-PMG counter-torque almost continuously. This allows for the introduction of a closed-loop speed controller, employing a PI regulator. Before a closed loop controller is developed, it is helpful to ensure that the SS-PMG counter-torque can be varied linearly. Once this has been established, control design and testing can be undertaken.

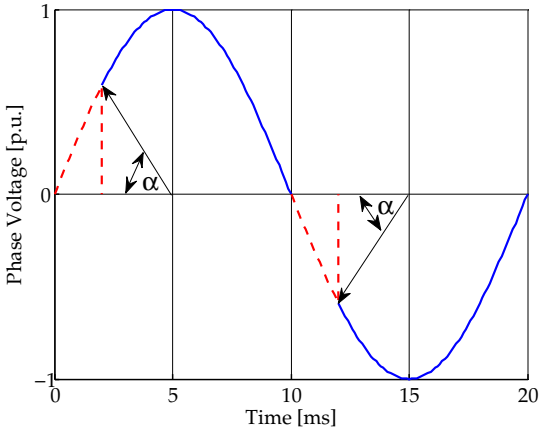

Figure 4.12: The firing delay angle α is applied to both half-cycles of each phase voltage waveform.

4.2.2.1 Thyristor Control Linearisation

For the purposes of speed control, it is desirable to establish a linear relationship between an input reference to the thyristor firing angle controller and the counter-torque that is produced by the SS-PMG. The relationship between α and V_R is not linear. For an ideal source, control of V_R can be linearised by an adaptation of the cosine wave-crossing method described in [84]. However, the non-ideal characteristics of the SS-PMG as a voltage source (particularly its relatively large inductance) render this method ineffective. An empirical approach was thus employed to develop a linear relationship between input reference and output torque.

Firstly, the relationship between α and the direct thyristor load command H_{th} is defined as:

$$\alpha = 180\frac{100 - H_{th}}{100} \tag{4.8}$$

The value of H_{th} is plotted as a function of desired generator load torque T_r at $\omega_m = 1$ p.u. in Fig. 4.13(a). Based on this trend, the relationship between the direct command H_{th} and the linearised

load command H_l is given by:

$$H_{th} = 4{,}195 \times 10^{-5} H_l^3 - 6{,}109 \times 10^{-3} H_l^2 + 0{,}534 H_l + 65{,}562 \tag{4.9}$$

The process by which α is calculated now begins by setting the linear load command: $H_l \rightarrow H_{th} \rightarrow \alpha$. Fig. 4.13(b) illustrates the improvement in linearity obtained by using H_l instead of H_{th} to control T_r at synchronous speed, which is the target speed for the controller. With linearity of control established, it is possible to implement a speed control loop and to tune its design to achieve the stated control objectives.

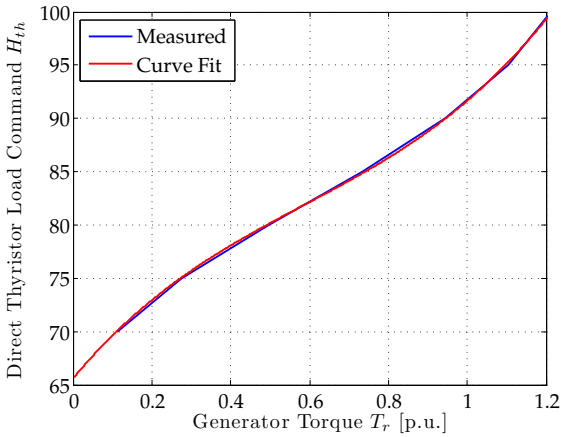

(a) Required direct thyristor load command as a function of SS-PMG counter-torque at synchronous speed

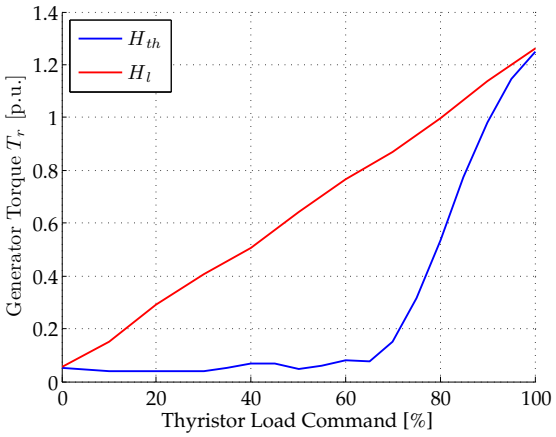

(b) SS-PMG counter-torque as a function of direct and linearised thyristor load commands at synchronous speed

Figure 4.13: SS-PMG torque control linearisation with thyristor-switched $R_{br} = 0{,}61$ p.u.

4.2.2.2 Speed Control Loop

The thyristor-based speed control loop for the SS-PMG is shown in Fig. 4.14. The PI regulator acts upon the frequency error signal $f_{err} = -\left(f_{grid} - f_{gen}\right)$ and its output is limited to ± 50. The negation in the error signal formula causes a positive (increased) loading response when $f_{gen} > f_{grid}$ and vice versa. The PI output is combined with an offset of 50, which determines the default loading level for the SS-PMG.

The combined thyristor input command H_l is converted into a firing delay angle α by the linearisation module described in Section 4.2.2.1. This ensures a linear torque response from the SS-PMG in the SFR particularly. The firing angle signal is applied to the plant—consisting of the turbine, SS-PMG, thyristors, and load—depicted in Fig. 4.15. Changes in wind speed are regarded as disturbances to the control loop.

The instantaneous 3-phase SS-PMG terminal voltage signals are sampled by the controller and transformed into the $\alpha\beta$ reference frame. A second order Butterworth low-pass filter is applied to each of the $\alpha\beta$ signals to filter out the significant harmonic content imposed by the thyristor switching action. Prior to filtering, the THD of the phase voltage signals can exceed 18 %. The filtered signals are used to calculate f_{gen} through the $\alpha\beta$ vector gradient method introduced in Section 2.1.1.2. For the purposes of the speed control loop only, it is assumed that $f_{grid} = f_R$.

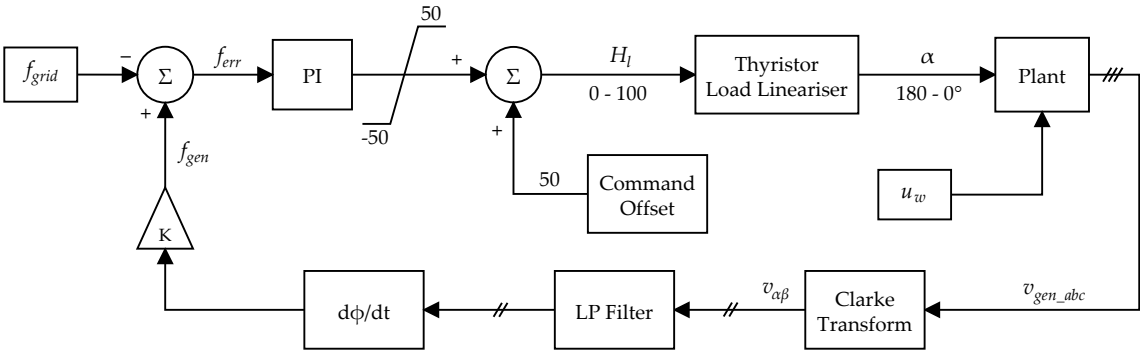

Figure 4.14: Block diagram of the PI speed control loop for the SS-PMG. The PI regulator acts upon the frequency error and generates a command signal H_l that is converted into the thyristor firing angle α. The 3-phase generator voltages are sampled, transformed, and filtered before f_{gen} is calculated. The internal elements of the plant are illustrated in Fig. 4.15.

The internal components of the plant are illustrated in Fig. 4.15. The control input to the plant is α while the disturbance input is u_w. The measured output of the plant is the set of 3-phase SS-PMG terminal voltages v_a, v_b, and v_c. The electrical and mechanical dynamics of the system are governed by the relations discussed in Section 3.3.1.

4.2.2.3 PI Tuning

The PI regulator gains, K_p and K_i, must be tuned to deliver the required performance. With reference to the introduction in Section 4.2, the objectives for the speed controller are, in order of priority:

1. Overshoot: $M_p < 10\,\%$ for $4\,\mathrm{m/s} \leq u_w \leq 12\,\mathrm{m/s}$
2. Tracking: $\Delta f \leq \Delta f_t$ for $4\,\mathrm{m/s} \leq u_w \leq 12\,\mathrm{m/s}$
3. Settling time: $t_s < 5\,\mathrm{s}$, measured from the instant when $f_{gen} \geq 0{,}6\,\mathrm{p.u.}$ for $11\,\mathrm{m/s} \leq u_w \leq 12\,\mathrm{m/s}$

These specifications must be satisfied under both steady and turbulent wind conditions. Settling time and peak time are affected equally by wind speed and PI gains, so specifications have been set for rated wind speed and above. Rise time t_p should also be minimised, but is predominantly a function of

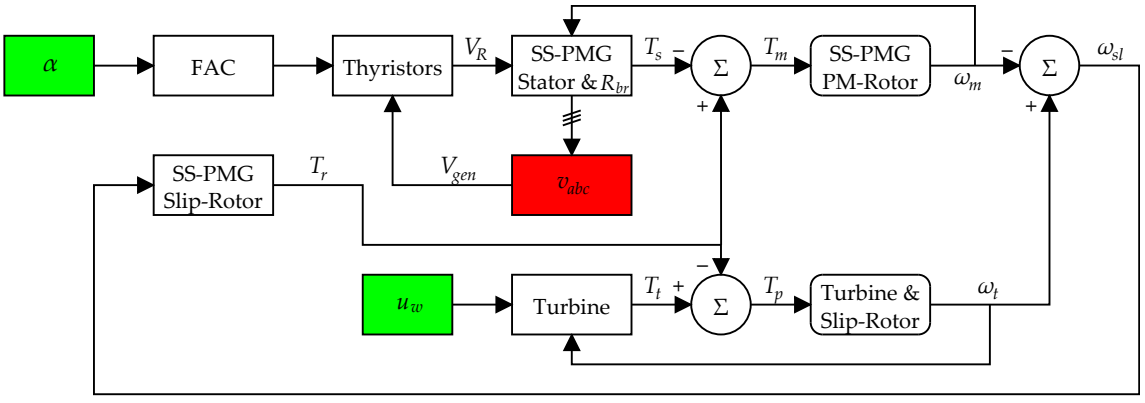

Figure 4.15: Block diagram representing the internal plant from Fig. 4.14. Inputs are shown in green and outputs in red. Rounded rectangles are inertias. Any change to the wind input u_w is regarded as a disturbance.

wind speed, rather than PI gains.

The first case examined in detail is rated power operation: steady wind with $u_w = 11\,\text{m/s}$. Fig. 4.16 shows the relevant time-domain performance results achieved by varying K_p and K_i independently. The first notable trend from Fig. 4.16(a) is that t_r is a very weak function of PI gains and remains effectively constant at 1,62 s for $u_w = 11\,\text{m/s}$. On the other hand, maximum overshoot, depicted in Fig. 4.16(b), is a strong function of gain values: if $K_p > 13$ and/or $K_i > 23$ then $M_p \leq 10\,\%$.

The 2 % settling time is, predictably, a stronger function of K_i than of K_p. This is illustrated in Fig. 4.16(c), where a value of $K_i \geq 10$ is important to achieve $t_s < 5\,\text{s}$. On the other hand, excessively high values of K_p tend to increase t_s. Finally, Fig. 4.16(d) shows that the frequency difference at the end of the 16 s simulation is generally below the 0,02 p.u. limit. However, a combination of $K_p < 20$ and $K_i > 15$ achieves best performance in this regard.

From the results discussed thus far, the following gain values were selected as most appropriate: $K_p = 15$ and $K_i = 20$. Employing these values results in $t_r = 1{,}609\,\text{s}$, $M_p = 6{,}0\,\%$, $t_s = 3{,}391\,\text{s}$, and final $\Delta f = 0{,}5155 \times 10^{-3}\,\text{p.u.}$ This is illustrated by the traces of the transient response in Fig. 4.17 for steady

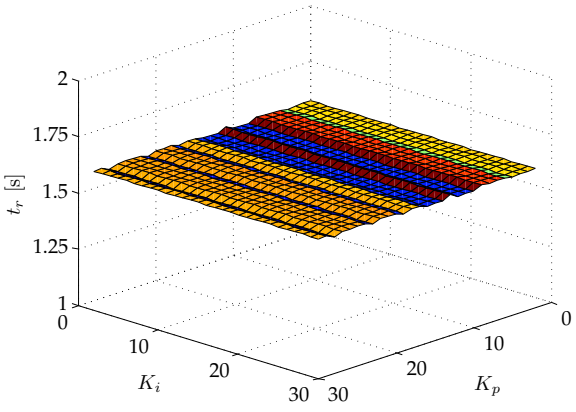

(a) Rise time from $f_0 = 0{,}6\,\text{p.u.}$ as a function of K_p and K_i

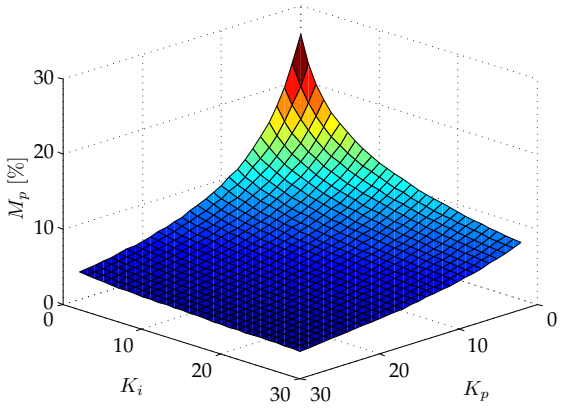

(b) Speed overshoot as a function of K_p and K_i

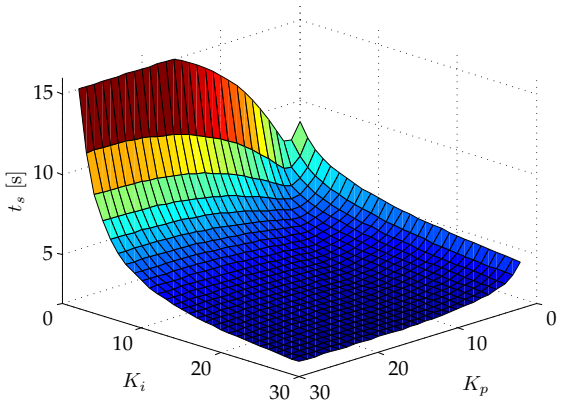

(c) 2 % speed settling time as a function of K_p and K_i

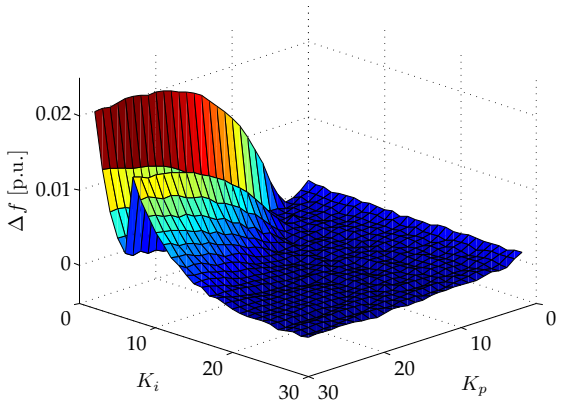

(d) Final Δf as a function of K_p and K_i

Figure 4.16: Time-domain performance results for the thyristor-based PI speed regulator as a function of K_p and K_i at steady $u_w = 11\,\text{m/s}$. Simulation duration was 16 s for each case.

wind conditions with $u_w = 11\,\mathrm{m/s}$.

Fig. 4.17(a) shows that smooth dynamic response is achieved with the thyristor-based speed control. In addition, tracking is consistent with negligible error at steady state. The non-zero torque visible during the first 2 s of the traces in Fig. 4.17(b) results from a combination of rotational losses in the SS-PMG and a 0,05 p.u. torque offset caused by the operation of the *Simplorer* thyristor module.

Fig. 4.18 shows the results achieved when varying K_p and K_i at a steady wind speed of $u_w = 7\,\mathrm{m/s}$. The trends obtained are similar to Fig. 4.16, but the reduction in turbine torque results in longer rise and settling times. Conversely, overshoot and final frequency difference are substantially lower.

The trends at $u_w = 7\,\mathrm{m/s}$ are similar to those observed for $u_w = 11\,\mathrm{m/s}$, suggesting that the same gain values are appropriate. The results obtained when $K_p = 15$ and $K_i = 20$ are: $t_r = 5{,}994\,\mathrm{s}$, $M_p = 1{,}348\,\%$, $t_s = 6{,}791\,\mathrm{s}$, and final $\Delta f = 0{,}1857 \times 10^{-3}$ p.u. These values reflect the inherently slower dynamics at lower wind speeds, but remain favourable in comparison with the results achieved by other gain combinations at $u_w = 7\,\mathrm{m/s}$.

The dynamic performance achieved by the PI regulator as a function of wind speed—with $K_p = 15$ and $K_i = 20$—is summarised in Fig. 4.19. Rise time, shown in Fig. 4.19(a), decreases exponentially with wind speed but the effect is less pronounced for $u_w > 7\,\mathrm{m/s}$. The plot also indicates the usable wind speed range under thyristor control: $5\,\mathrm{m/s} \leq u_w \leq 11{,}6\,\mathrm{m/s}$.

When $u_w < 5\,\mathrm{m/s}$ the turbine torque is less than 0,1 p.u. which results in impractically low acceleration against no-load losses. This is partly due to the 0,05 p.u. base load imposed by the thyristor braking mechanism, indicated in Fig. 4.13. On the other hand, the turbine overcomes the maximum braking capacity of the SS-PMG when $u_w > 11{,}6\,\mathrm{m/s}$ if no yaw offset is imposed to reduce turbine torque. In practice, the mechanical yaw mechanism will reduce turbine torque at high winds, but the operation of this mechanism is not documented well enough to allow incorporation into simulations.

Maximum overshoot increases linearly with wind speed, as indicated in Fig. 4.19(b). For $u_w < 7{,}7\,\mathrm{m/s}$, the overshoot is less than 2 %, the frequency difference limit Δf_t. Up to the limit of control,

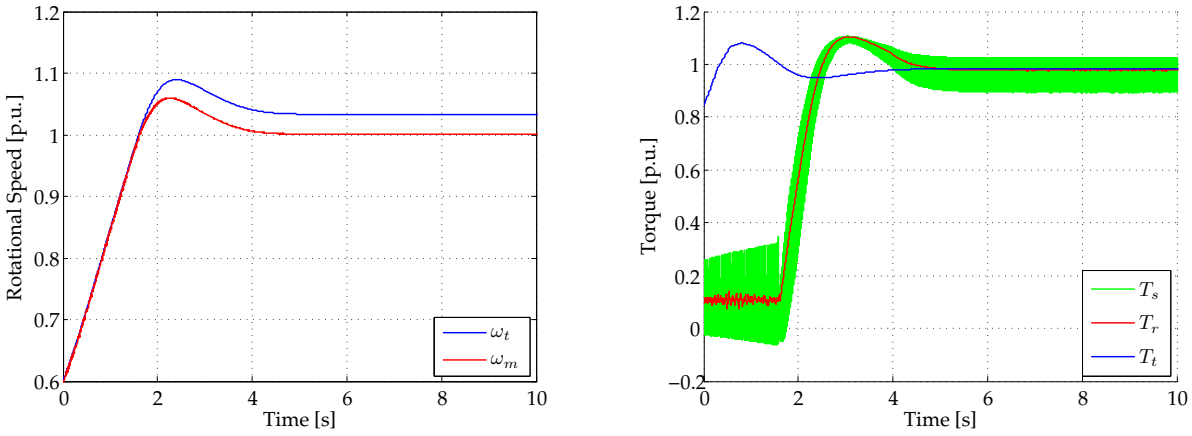

(a) Turbine and PM-rotor speed as a function of time

(b) Stator, slip-rotor, and turbine torque as a function of time

Figure 4.17: Traces of simulation results for thyristor-based PI speed control with $K_p = 15$ and $K_i = 20$ under steady wind conditions with $u_w = 11\,\mathrm{m/s}$.

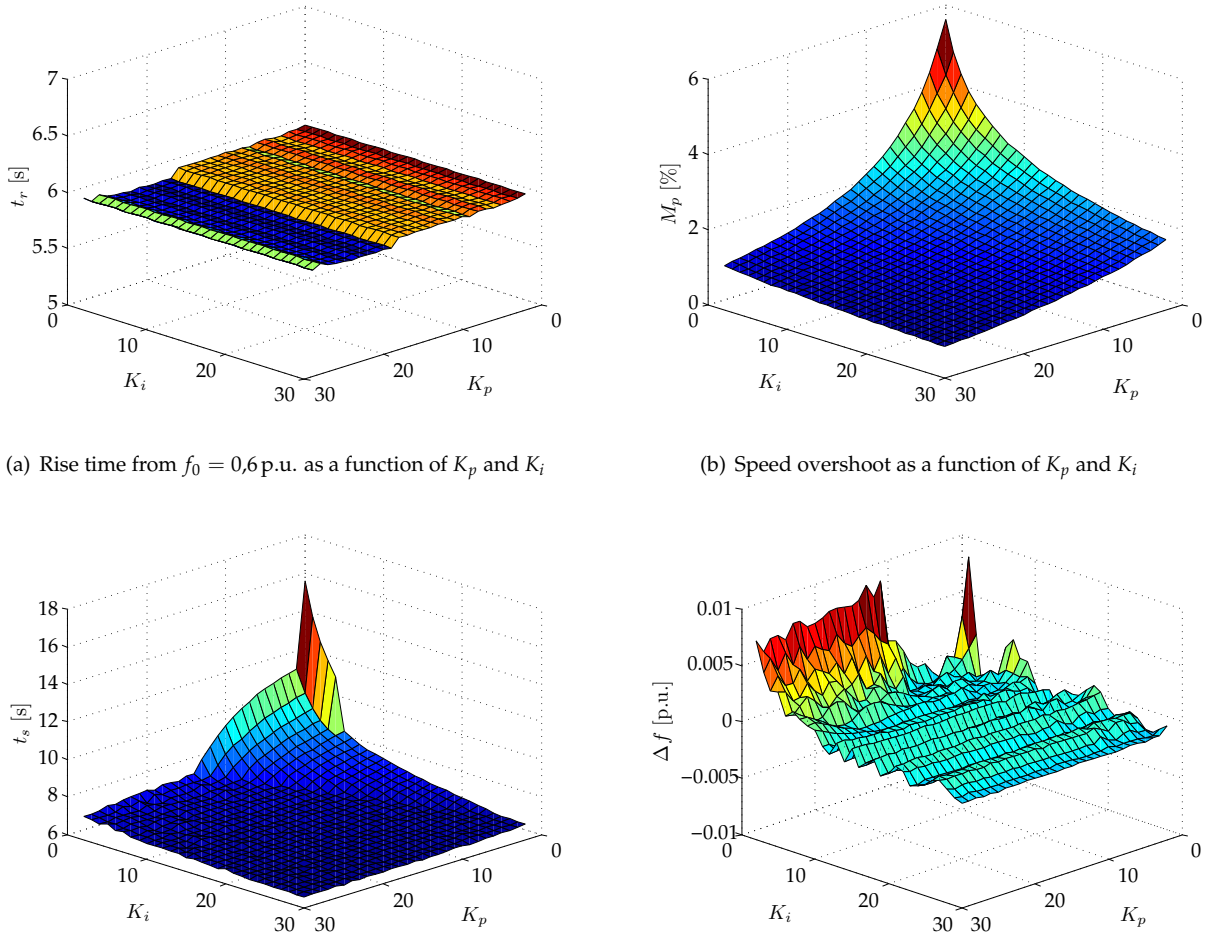

(a) Rise time from $f_0 = 0{,}6$ p.u. as a function of K_p and K_i

(b) Speed overshoot as a function of K_p and K_i

(c) 2 % speed settling time as a function of K_p and K_i

(d) Final Δf as a function of K_p and K_i

Figure 4.18: Time-domain performance results for the thyristor-based PI speed regulator as a function of K_p and K_i at steady $u_w = 7\,\mathrm{m/s}$. Simulation duration was 16 s for each case.

$u_w = 11{,}6\,\mathrm{m/s}$, overshoot never exceeds 7 %, but beyond this the SS-PMG -thyristor combination cannot develop enough torque to control the turbine.

Fig. 4.19(c) shows that settling time is actually lower than rise time for $u_w < 7{,}7\,\mathrm{m/s}$ because overshoot is less than 2 %. In the range $7{,}2\,\mathrm{m/s} \leq u_w \leq 11{,}2\,\mathrm{m/s}$, settling time remains at or below 5 s, but it begins to rise at higher wind speeds as the controller reaches the limit of its actuation capacity.

Synchronous speed tracking consistently achieves the required accuracy, as indicated in Fig. 4.19(d). Performance is independent of wind speed and offset is negligible, except for $u_w > 11\,\mathrm{m/s}$, where the required torque approaches the limit of the SS-PMG. Nonetheless, tracking is still acceptable up to $u_w > 11{,}6\,\mathrm{m/s}$.

Based on the findings from steady wind simulations, the chosen gains of $K_p = 15$ and $K_i = 20$ allow the PI regulator to achieve all three control objectives. As far as possible, overshoot, tracking and settling time conform to the quantitative requirements laid out previously. The main drawback of the thyristor-based strategy is that the operational wind speed range is narrowed to $5\,\mathrm{m/s} \leq u_w \leq 11{,}6\,\mathrm{m/s}$. However, the implementation of turbine torque restriction through a yaw control mechanism will allow

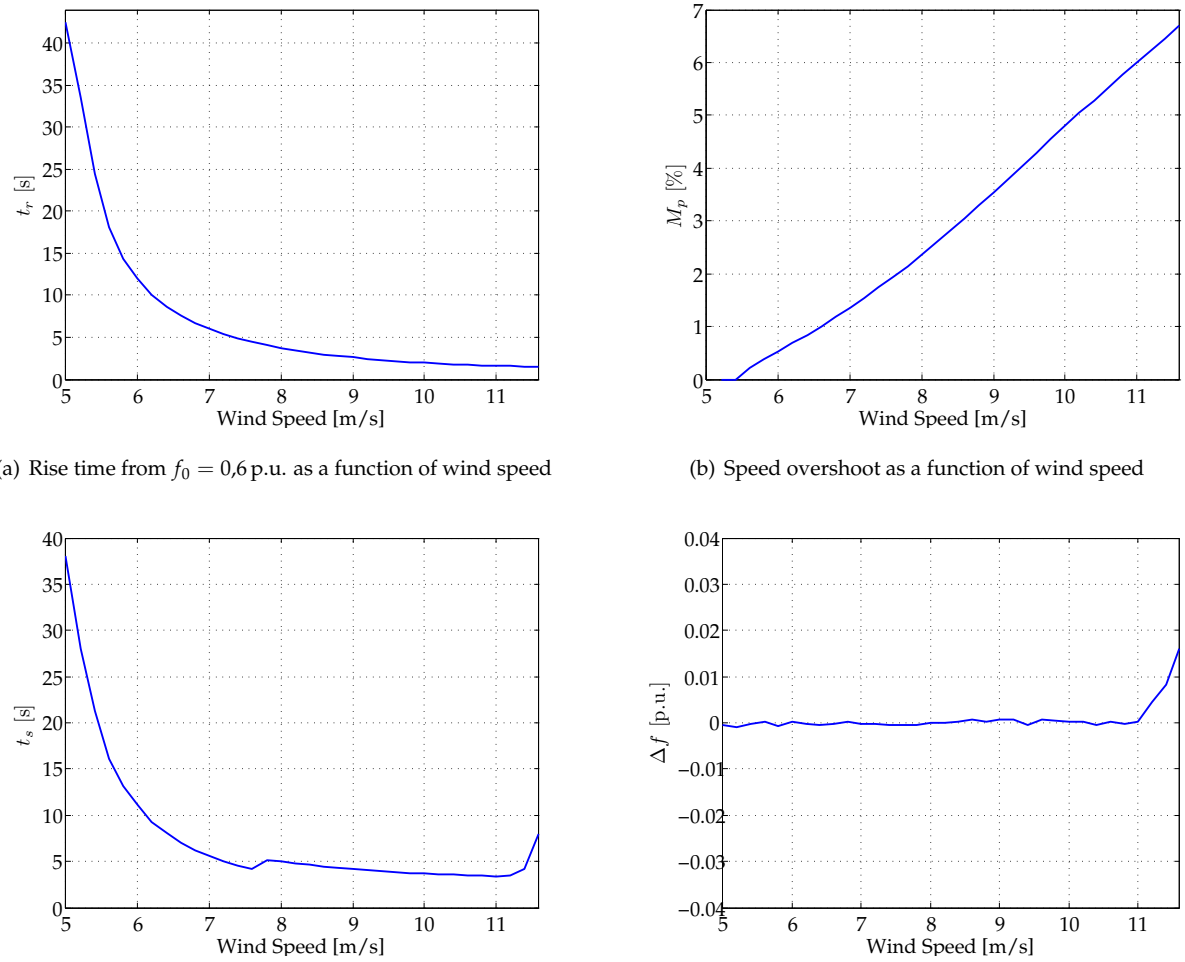

(a) Rise time from $f_0 = 0{,}6$ p.u. as a function of wind speed

(b) Speed overshoot as a function of wind speed

(c) 2 % speed settling time as a function of wind speed

(d) Final Δf as a function of wind speed

Figure 4.19: Time-domain performance results for the thyristor-based PI speed regulator as a function of steady wind speed while $K_p = 15$ and $K_i = 20$.

for operation at higher wind speeds.

4.2.2.4 Speed Control with Turbulent Wind

Despite the positive results from steady wind simulations, it is still necessary to evaluate the performance of the speed controller under realistic conditions. In other words, the PI regulator must be tested with turbulent wind input. Turbulent wind is, by nature, not uniform: different levels of turbulence can be encountered as a result of climatic conditions and local geography. It is thus impractical to simulate every conceivable set of wind conditions that a WECS may encounter. In this case, the turbulent wind model has been tuned to reproduce conditions that will likely be encountered in an on-shore rural wind farm.

In addition to the level of turbulence and the mean wind speed, an important parameter in turbulent wind simulations is the initial behaviour—for example, the wind speed could be ramping up or down as the simulation begins. The following sets of time series show the performance of the thyristor-based speed controller under a variety of wind conditions, with emphasis on more challenging scenarios. The

important requirements of overshoot, tracking, and settling time are examined in each case.

The first case involves a low mean wind speed where u_w first dips then rises in to a number of gusts, as shown in Fig. 4.20(a). Because of the low initial wind speed, rise time is relatively long at $t_r = 9{,}1568\,\text{s}$, but once the SS-PMG has entered the SFR it remains in this band for the remainder of the simulation, as indicated in Fig. 4.20(b). The thyristor speed controller achieves similar performance as to what can be expected under steady wind conditions.

The second example involves a higher base wind speed of $U_w = 8\,\text{m/s}$ with a dip then a strong gust near the end of the time series, illustrated in Fig. 4.21(a). The speed controller achieves an initial settling time of $t_s = 5{,}325\,\text{s}$ with minimal overshoot. The SS-PMG is then held in the SFR until the gust causes a momentary overshoot of 3,12 % but the controller recovers within 2 s.

The next wind time series, presented in Fig. 4.22(a), consists of a sequence of dips and gusts, culminating in a peak of approximately 12 m/s. Fig. 4.22(b) shows that the initial settling time is extended to $t_s = 5{,}662\,\text{s}$ by the wind speed rise that occurs between $t = 4\,\text{s}$ and $t = 5\,\text{s}$. After this, the speed

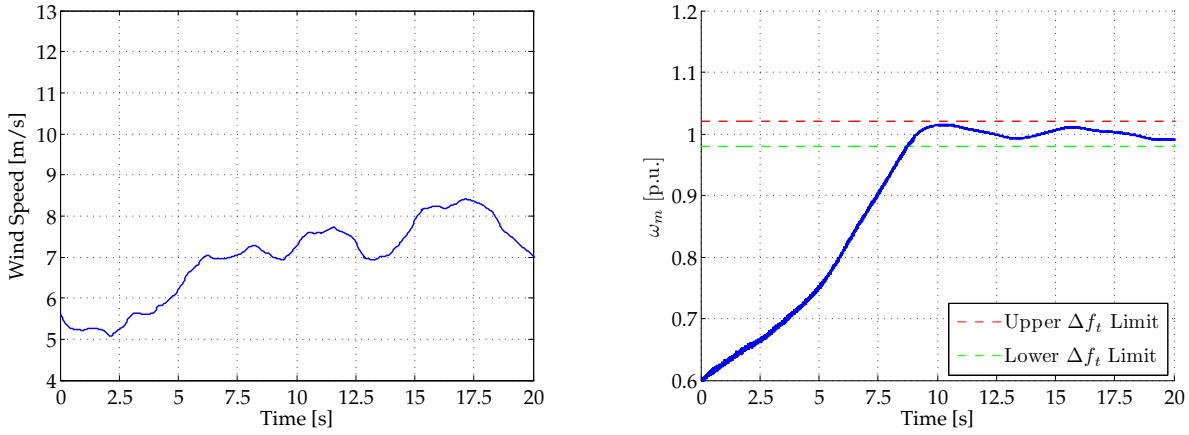

(a) Turbine-sampled wind speed as a function of time

(b) PM-rotor speed as a function of time

Figure 4.20: Traces of simulated turbulent wind speed and SS-PMG speed response with $U_w = 6\,\text{m/s}$.

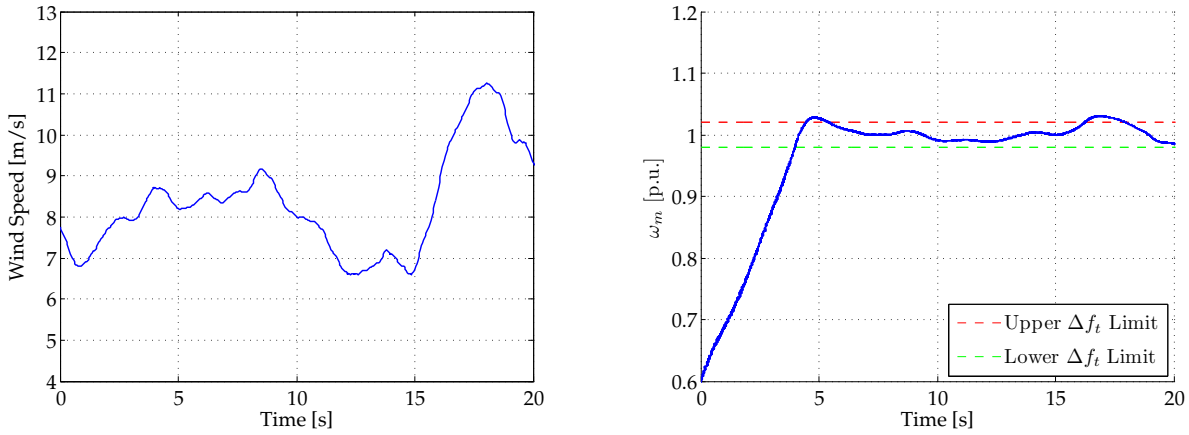

(a) Turbine-sampled wind speed as a function of time

(b) PM-rotor speed as a function of time

Figure 4.21: Traces of simulated turbulent wind speed and SS-PMG speed response with $U_w = 8\,\text{m/s}$.

controller holds the SS-PMG within or near the SFR, with minor excursions taking place as a result of the later dip and gust. The maximum speed deviation of 3,24 % occurs at $t = 18$ s as a result of the final gust.

The final turbulent wind case exposes the SS-PMG to a 13 m/s gust, followed by a sequence of dips and gusts with a low point of 6,5 m/s, as illustrated in Fig. 4.23(a). The initial gust causes a maximum overshoot of $M_p = 13{,}8\,\%$ and the wind speed dip that follows the gust results in a further SS-PMG speed excursion before settling at $t_s = 6{,}58$ s. After the initial disturbances, the speed controller is able to maintain acceptable tracking for the rest of the time series, despite a severe dip at $t = 14$ s.

The turbulent wind cases investigated here show that the PI regulator is able to control overshoot while achieving acceptable settling time and tracking performance. Overshoot is limited to less than 15 %, even at wind speeds beyond the operational limit, and if $u_w \leq 12$ m/s then $M_p < 5\,\%$. Settling time is generally in line with the results obtained under steady wind conditions, although severe gusts and dips can extend the intial settling period. Tracking remains within 0,02 p.u. except during large dips

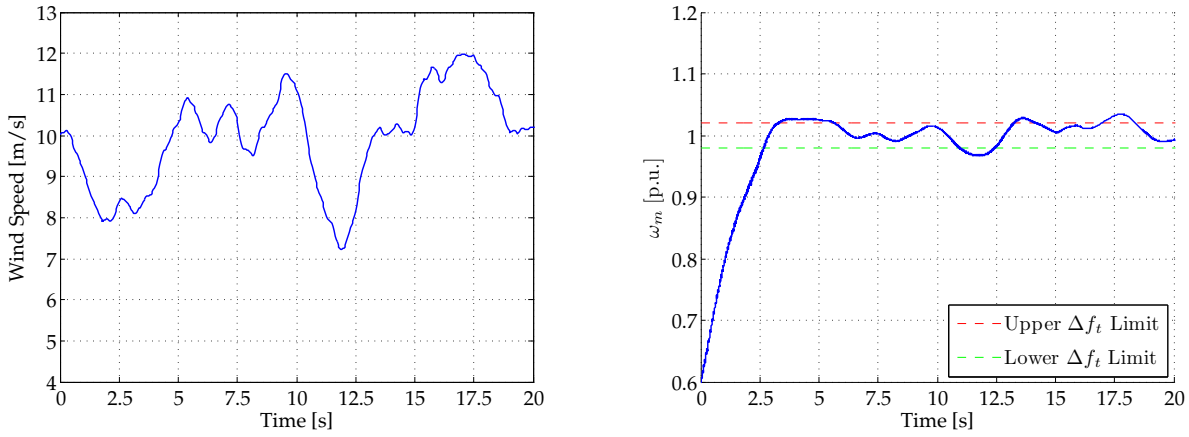

(a) Turbine-sampled wind speed as a function of time

(b) PM-rotor speed as a function of time

Figure 4.22: Traces of simulated turbulent wind speed and SS-PMG speed response with $U_w = 10$ m/s.

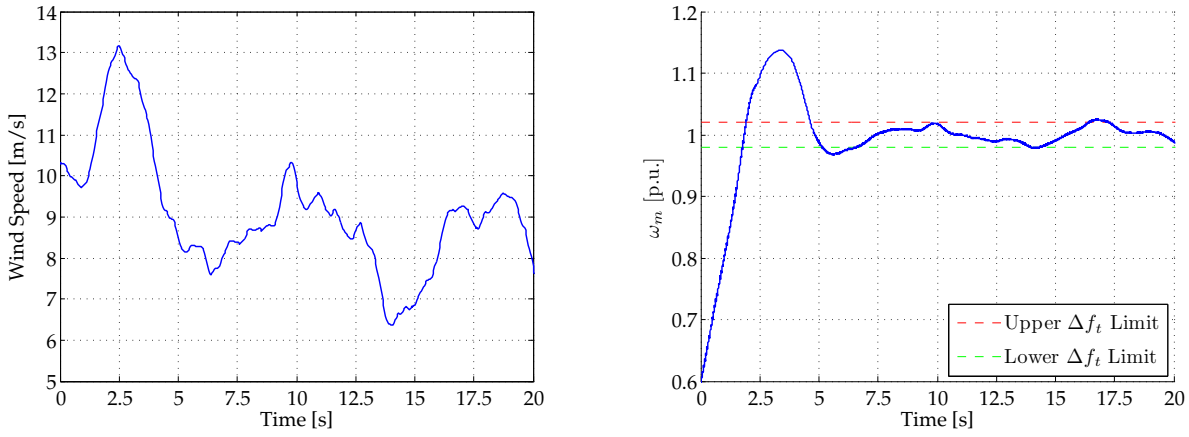

(a) Turbine-sampled wind speed as a function of time

(b) PM-rotor speed as a function of time

Figure 4.23: Traces of simulated turbulent wind speed and SS-PMG speed response with $U_w = 10$ m/s.

or gusts, where short-lived excursions do take place, however, ω_m is typically restored to $1 \pm 0{,}02$ p.u. within 2 s.

As a result of these findings, the thyristor-based speed controller can be deemed appropriate for real-world applications. To be sure, more sophisticated control algorithms could be developed, but the PI regulator achieves the stated objectives and operates successfully under turbulent wind conditions. The control system makes use of robust and widely available components and does not require mechanical modifications to the SS-PMG. What remains is to investigate the combined operation of the speed controller and the synchronisation algorithm.

4.3 Controlled Synchronisation

The final investigation in this chapter combines speed control with synchronisation to test the complete grid connection mechanism for the SS-PMG. If these two functions fulfil their roles simultaneously, then the automatic grid connection of the SS-PMG will be proven to be feasible. To begin with, grid connection under steady wind conditions is tested, after which turbulent wind time series are introduced to evaluate more realistic operation of the system.

The controlled synchronisation procedure involves the parallel operation of speed control and synchronisation functions. The speed controller attempts to bring $\Delta f \approx 0$ p.u. while the synchroniser continuously evaluates the synchronisation conditions. As soon as all conditions are satisfied, the SS-PMG is connected directly to the grid through contactor switch S3 and the thyristors (switch S2) are deactivated—refer again to Fig. 4.8, which illustrates the layout of control components.

4.3.1 Controlled Synchronisation with Steady Wind

The first controlled synchronisation case, shown in Fig. 4.24, is for a steady wind speed of $u_w = 6$ m/s. Fig. 4.24(a) illustrates the speed control dynamics, which match expectations for these conditions: the rise time is relatively long but negligible overshoot occurs. In this case the SS-PMG is synchronised before ever exceeding synchronous speed at $\Delta f = 0{,}0107$ p.u.

The voltage waveforms at synchronisation are shown in Fig. 4.24(b). The measured phase angle difference when when the synchronisation command was generated was $\Delta\phi = 8{,}766\,^\circ$ but at the moment of synchronisation (delayed by the contactor operating lag of 20 ms) $\Delta\phi = 11{,}034\,^\circ$. This exceeds the threshold band but by a small enough margin that current and rotor angle transients are not significantly affected.

According to Fig. 4.24(c), maximum phase current as a result of synchronisation is 0,5235 p.u., which is in good agreement with the predictions made in Fig. 4.4(a). Steady operating conditions are achieved within 1 s of synchronisation, an observation echoed by the rotor angle in Fig. 4.24(d). The maximum rotor angle excursion is significantly lower than what can be expected from Fig. 4.4(b) at this wind speed.

The harmonics caused by thyristor switching are clearly visible on the SS-PMG voltage and current waveforms prior to synchronisation. However, these harmonics do not affect the network because the

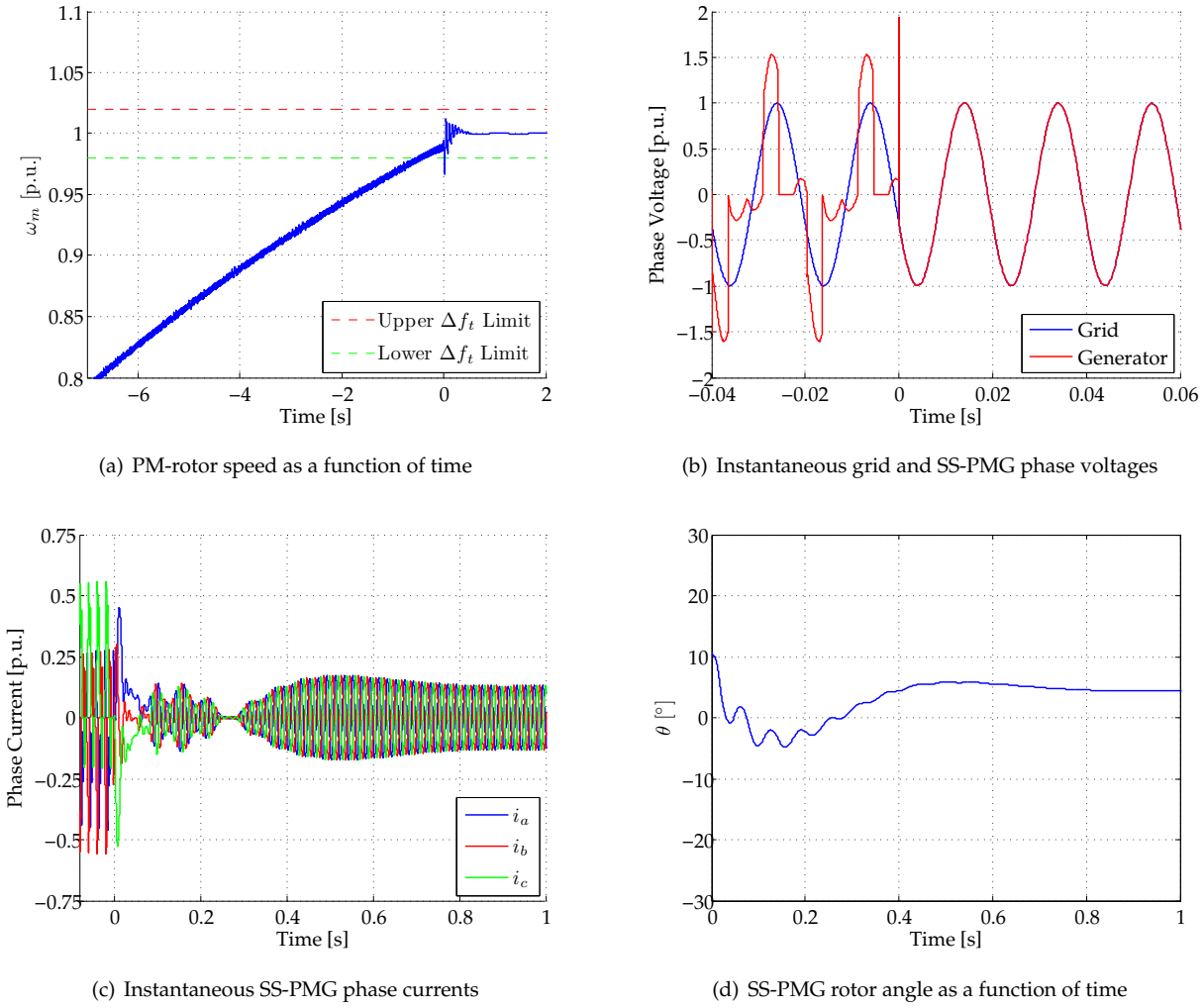

(a) PM-rotor speed as a function of time

(b) Instantaneous grid and SS-PMG phase voltages

(c) Instantaneous SS-PMG phase currents

(d) SS-PMG rotor angle as a function of time

Figure 4.24: Traces showing speed control and synchronisation with $u_w = 6\,\text{m/s}$. Synchronisation takes place at $t = 0\,\text{s}$.

thyristor switching is deactivated as soon as synchronisation occurs. In addition, the RMS grid voltage shows no measurable reduction due to connection of the SS-PMG, which is an important achievement if synchronisation is to occur regularly.

Controlled synchronisation at rated wind speed $u_w = 11\,\text{m/s}$ is illustrated in Fig. 4.25. With rated turbine torque, rise time $t_r = 1{,}716\,\text{s}$, close to the predicted value. Maximum overshoot $M_p = 5{,}96\,\%$ and settling time $t_s = 3{,}498\,\text{s}$ are well within specifications, as shown in Fig. 4.25(a). The synchroniser connects the SS-PMG to the grid shortly after re-entering the SFR at $\Delta f = -0{,}019\,\text{p.u.}$ Once again, the PM-rotor experiences some ocscillation during synchronisation, but this settles within 0,5 s.

Fig. 4.25(b) depicts the grid and generator voltage waveforms, where the switching-induced harmonics are again visible prior to synchronisation. The phase angle difference at the actual moment of closing switch S3 is $\Delta\phi = 9{,}756\,°$, which is again larger than when the synchronisation command was given, 20 m/s earlier.

The maximum phase current at synchronisation, shown in Fig. 4.25(c), is 2,087 p.u. which is higher than anticipated but still tolerable. The same is true for the rotor angle of Fig. 4.25(d) that reaches a

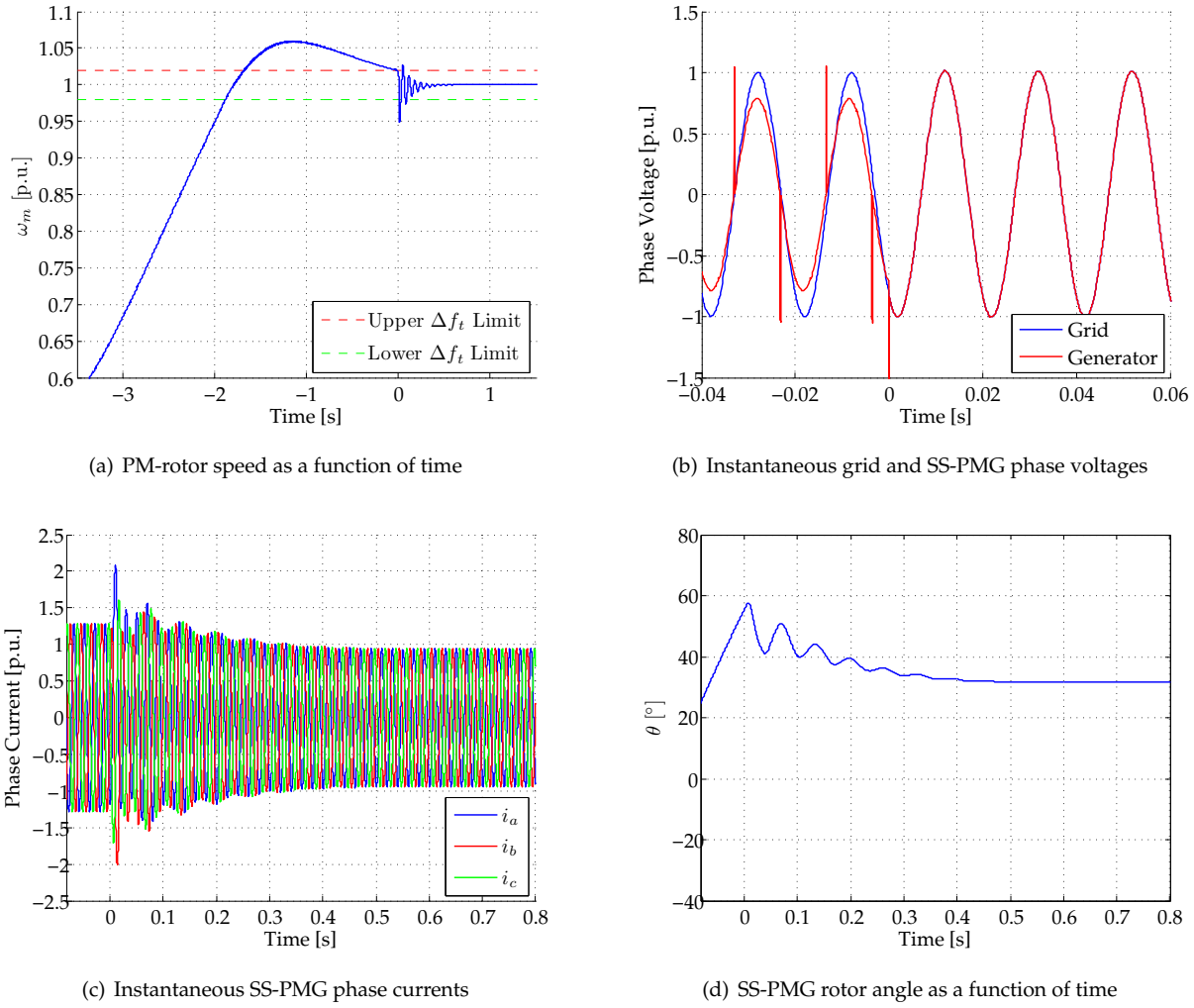

(a) PM-rotor speed as a function of time

(b) Instantaneous grid and SS-PMG phase voltages

(c) Instantaneous SS-PMG phase currents

(d) SS-PMG rotor angle as a function of time

Figure 4.25: Traces showing speed control and synchronisation with $u_w = 11\,\mathrm{m/s}$. Synchronisation takes place at $t = 0\,\mathrm{s}$.

maximum of 57,47 °, instead of the predicted 37 °. This indicates that switching the SS-PMG from full thyristor loading to grid connection introduces larger transients than when connecting the SS-PMG at no-load.

This phenomenon can be explained by referring back to Fig. 4.25(b), which indicates that the terminal voltage of the SS-PMG is 21,51 % lower than that of the grid prior to synchronisation. The SS-PMG is, in other words, under-excited as a result of the large load it is supplying and thus draws reactive power from the grid during the first half-cycle after synchronisation (even though the load is disconnected at synchronisation). This voltage restoration process results in a larger current drain on the grid but is inevitable unless a voltage compensation mechanism is added to the SS-PMG. Such compensation would also be necessary to meet the given synchronisation condition that $\Delta V \leq 10\,\%$, which was overruled to allow synchronisation in this case.

Despite the higher than anticipated transient current and rotor angle deviations, the grid voltage exhibits no measurable reduction and system stability is not under threat. The duration of the current spike is short and the current magnitude then returns to the level predicted earlier. Thus, for the remainder of

this investigation, the ΔV requirement will be relaxed to allow simulation and practical experimentation to continue. Nonetheless, additional compensation will be required to meet the conditions laid out in [80] for operation on the SA grid.

4.3.2 Controlled Synchronisation with Turbulent Wind

In this section synchronisation is undertaken with turbulent wind time series applied to the *Simplorer* model. For comparative purposes, the wind data used is the same as in the speed control examples of Fig. 4.20 and Fig. 4.23. These series are reproduced again in Fig. 4.26 with the time axis centred on the synchronisation instant in each case.

The first case involves turbulent wind with a base speed $U_w = 6\,\text{m/s}$, as indicated in Fig. 4.26(a). The results of the controlled synchronisation process are shown in Fig. 4.27. From Fig. 4.27(a) it can be seen that the turbulent conditions do not significantly affect the speed control dynamics. Acceleration into the SFR is controlled and synchronisation takes place at a similar moment to the steady wind case of Fig. 4.24. In this case $\Delta f = 0{,}0108\,\text{p.u.}$ as the SS-PMG is connected to the grid and the initial PM-rotor oscillations are attenuated within 0,49 s.

The voltage phase angle offset at synchronisation is $\Delta\phi = 11{,}934\,°$, which again exceeds the set threshold due to the combined effects of controller measurement error and contactor delay. The measurement error is primarily due to the harmonic content of the generator voltage waveform, shown in Fig. 4.27(b) which varies as a function of firing angle. Fig. 4.27(c) indicates that the maximum current at synchronisation is nonetheless within the predicted range at 0,4119 p.u. and steady state operation is achieved within 1 s. The rotor angle echoes these findings, with a maximum deviation of 10,64 ° shown in Fig. 4.27(d).

The final scenario studied here employs the highly turbulent wind time series in Fig. 4.26(b), which has a base speed $U_w = 10\,\text{m/s}$. This series actually exceeds the normal operational range of the WECS so represents an extreme case, especially since no form of turbine torque reduction is used in the sim-

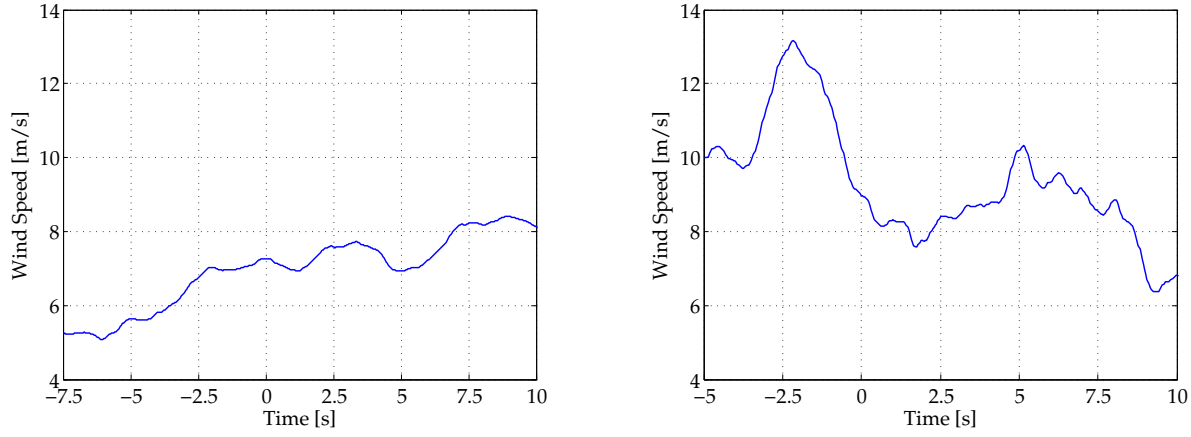

(a) Extract of turbulent wind times series with $U_w = 6\,\text{m/s}$

(b) Extract of turbulent wind times series with $U_w = 10\,\text{m/s}$

Figure 4.26: Turbulent wind data employed for controlled synchronisation examples. Synchronisation takes place at $t = 0\,\text{s}$.

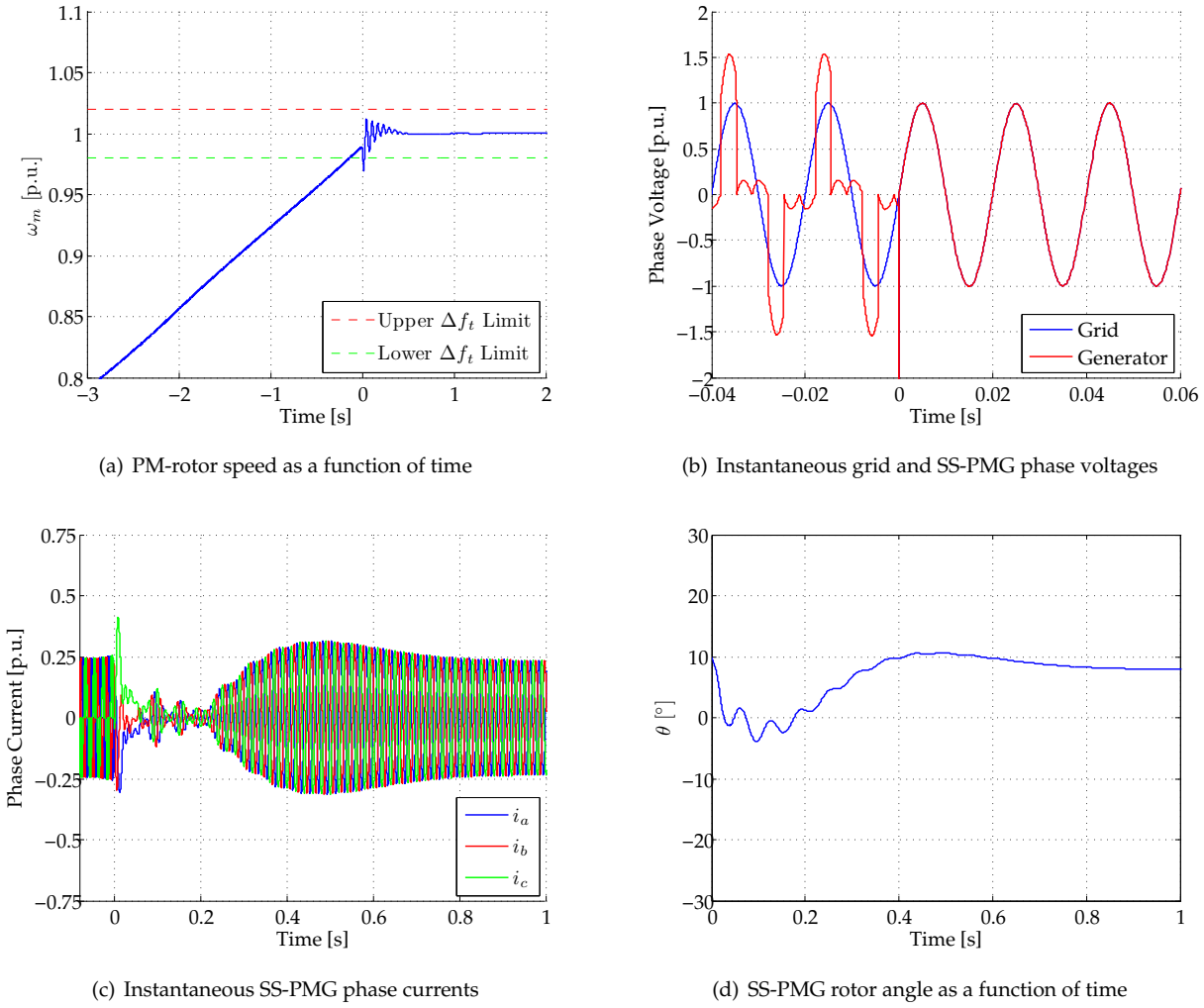

(a) PM-rotor speed as a function of time

(b) Instantaneous grid and SS-PMG phase voltages

(c) Instantaneous SS-PMG phase currents

(d) SS-PMG rotor angle as a function of time

Figure 4.27: Traces showing speed control and synchronisation under the turbulent wind conditions depicted in Fig. 4.26(a). Synchronisation takes place at $t = 0$ s.

ulation. The response of the synchronisation and speed controller to this wind input is depicted in Fig. 4.28.

Unsurprisingly, the PM-rotor speed overshoot, shown in Fig. 4.28(a), exceeds the performance specification at $M_p = 13{,}8\,\%$. This level of overshoot is undesirable but still safe for both turbine and generator, however, it is unlikely to be encountered in practice since turbine torque will be reduced by the mechanical yaw mechanism. The SS-PMG re-enters the SFR 4,98 s after passing the cut-in speed and synchronisation takes place almost immediately with $\Delta f = 1{,}019$ p.u. Steady operation is achieved 0,6 s after synchronisation.

Fig. 4.28(b) indicates that $\Delta\phi = 11{,}196\,^\circ$ as switch S3 is closed, but the difference was only $7{,}02\,^\circ$ when the synchronisation signal was generated 20 ms earlier. Once again, the contactor delay has affected the result, particularly due to the higher rate of acceleration under strong winds. The voltage difference at synchronisation $\Delta V = 20{,}19\,\%$ is also outside of specification, as was discussed in the steady wind case.

Although the voltage and phase angle parameters are out of their respective ranges, the maximum transient current at synchronisation remains within the stated limit at 1,984 p.u., according to Fig. 4.28(c).

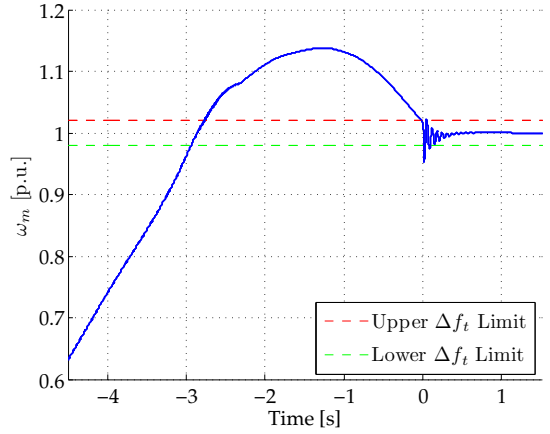

(a) PM-rotor speed as a function of time

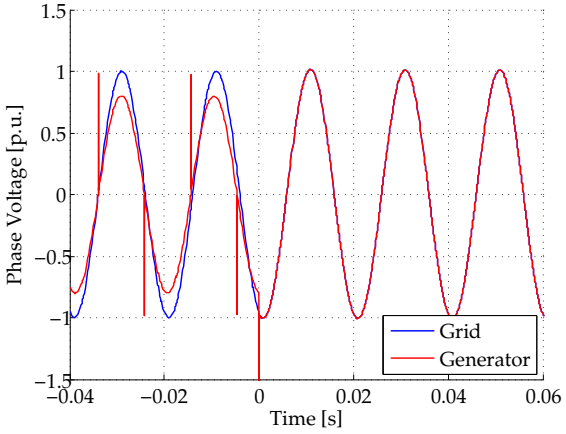

(b) Instantaneous grid and SS-PMG phase voltages

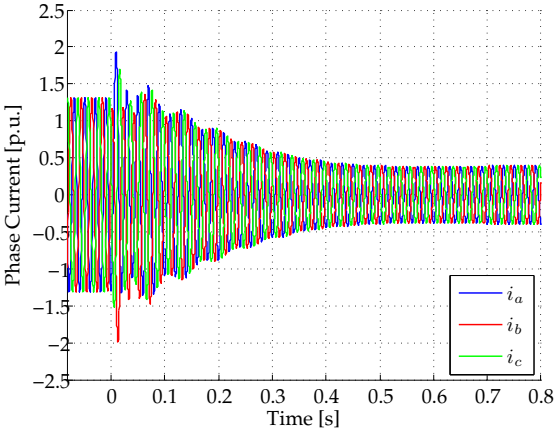

(c) Instantaneous SS-PMG phase currents

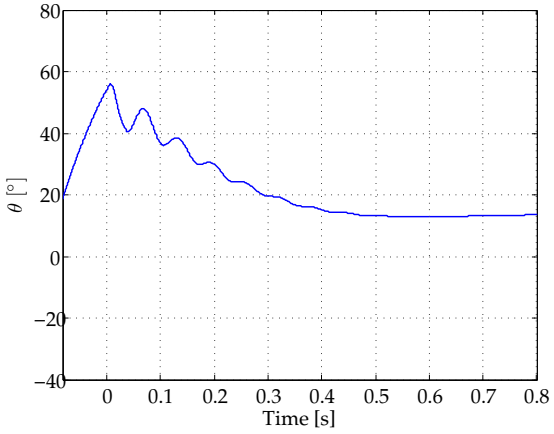

(d) SS-PMG rotor angle as a function of time

Figure 4.28: Traces showing speed control and synchronisation under the turbulent wind conditions depicted in Fig. 4.26(b). Synchronisation takes place at $t = 0$ s.

Additionally, the SS-PMG rotor angle remains stable with a maximum value of 55,97 °. Although both these values are above what was originally predicted, they are still acceptable and allow for successful synchronisation. In any case, wind turbulence does not, in itself, cause the GCC to operate improperly. In fact, all issues mentioned here were already noted and discussed under steady wind conditions.

In conclusion, the GCC has proven to be capable of synchronising the SS-PMG with the electrical network, although two issues remain. Firstly, to meet the phase angle requirement at synchronisation the contactor actuation delay must be accounted for. This can be done by reducing the programmed value of $\Delta\phi_t$ so that the final difference when switch S3 is closed remains below 10 °. Secondly, the SS-PMG terminal voltage drop must be corrected if the ΔV_t limit is to be met. A first approach may be the inclusion of reactive power compensation in the form of shunt capacitors, but the interaction of these with the thyristor circuits must be carefully managed to avoid damage to the hardware. In addition, resonance with the SS-PMG stator inductance must be mitigated.

A further deficiency in the present control design is that $\Delta\phi$ is not explicitly controlled. This implies that $\Delta\phi$ could remain constant if the wind speed were steady and the speed controller tracking were

perfect, in other words if $f_{gen} = f_{grid}$. Under such conditions, there would be no mechanism to cause $|\Delta\phi| < \Delta\phi_t$ and synchronisation could not be completed.

This issue is not significant in practice because speed controller tracking is never perfect: wind turbulence continuously causes small SS-PMG speed deviations which allow $\Delta\phi$ to change until all conditions are met and synchronisation can occur. Thus, although a $\Delta\phi$ control loop could be added, it would constitute an unnecessary computational burden for the DSP and could even result in instability if not designed carefully.

4.4 Summary

This chapter began with an investigation into the applicable synchronisation conditions for the SS-PMG. It was found that applying the limits $\Delta f_t = 0{,}02$ p.u. and $\Delta\phi_t = 10\,^\circ$ achieves the stated stability requirements at synchronisation. After this, a synchronisation methodology was introduced, along with the specific GCC components responsible for implementing it.

With the synchronisation threshold values in place, two speed control techniques, employing electromagnetic braking, were investigated. It was found that braking using contactors does not achieve the necessary level of dynamic control and requires an excessive number of distinct resistor values to operate across the wind speed range.

In contrast, thyristor-switched braking allows for continuous, incremental variations in SS-PMG torque. With this capability, a closed loop speed control system can be developed. A PI regulator was tuned to achieve the stated dynamic performance objectives and the controller was evaluated under turbulent wind conditions, where acceptable results were achieved.

Finally, the synchronisation and speed control functions were combined to investigate automatic grid connection under steady and turbulent wind conditions. Although loading the SS-PMG through thyristors poses certain challenges due to induced harmonics and terminal voltage drop, the controlled synchronisation process was successful. The SS-PMG rotor angle and transient currents were limited to acceptable levels and stable synchronisation was achieved, even under heavily turbulent wind conditions. Performance could, however, be improved by the introduction of reactive power compensation, which would reduce current transients and achieve compliance with the ΔV limit imposed by [80].

In summary, this chapter has documented the initial development and validation of an automatic grid connection controller for the SS-PMG. The next chapter describes further development of the GCC by incorporating low voltage ride-through capabilities.

CHAPTER 5

GRID FAULT COMPENSATION

This chapter focuses on the development of a ride-through strategy for the SS-PMG during grid voltage dips, as specified by network operators. After investigating the dips and ride-through requirements, a compensation strategy is developed by making use of resistive loads, specifically a series resistance and/or a braking resistance. Different approaches are evaluated with the aid of simulations and the chosen strategy is tested under various conditions.

5.1 Grid Code Requirements for Low Voltage Ride-Through

Particular emphasis is currently being placed on the ability of WECS to remain connected to the grid during voltage dips caused by network faults. Other events, such as grid voltage spikes and frequency deviations, must also be managed but the LVRT requirements are generally the most onerous so are covered here in detail. The response of the SS-PMG to wind gusts is also not included in this study, but an introductory investigation can be found in Appendix C.1. These results indicate that the SS-PMG is highly stable under all gust conditions within the operational wind speed range.

Since the SS-PMG is being developed primarily for deployment in South Africa, local LVRT requirements take precedence over other codes. However, at commencement of this investigation comprehensive LVRT requirements for DG in South Africa were not yet published. Consequently, other codes were consulted to determine guidelines for LVRT. A draft of the South African LVRT requirements for DG was, however, released before the completion of this investigation so these requirements are now included for comparative purposes.

Based on comparisons of different grid code requirements for LVRT in [85; 86], it was decided to employ the Irish Distribution Code requirements [87]. The Irish code has relatively strict requirements for grid-connected WECS because the Irish grid is small (total capacity less than 7000 MW) and isolated, which implies that a high penetration of wind power could easily lead to network instability [29]. Continental European grid codes tend to be more lenient towards DG since their national networks are substantially larger and can make use of strong interconnections with neighbouring countries.

5.1.1 Irish LVRT Requirements for DG

The Irish Distribution Code [87] identifies five different categories of wind farms, depending upon the topology of the network connection and the voltage levels involved. For the purposes of this investigation, the layout of the SS-PMG network connection is illustrated by Fig. 5.1(a), with quantitative specifications provided in Appendix A.

The standard PCC voltage dip profile from the Irish Code is presented in Fig. 5.1(b). A less onerous version is applicable to certain wind farm categories, but only the most severe case is investigated here.

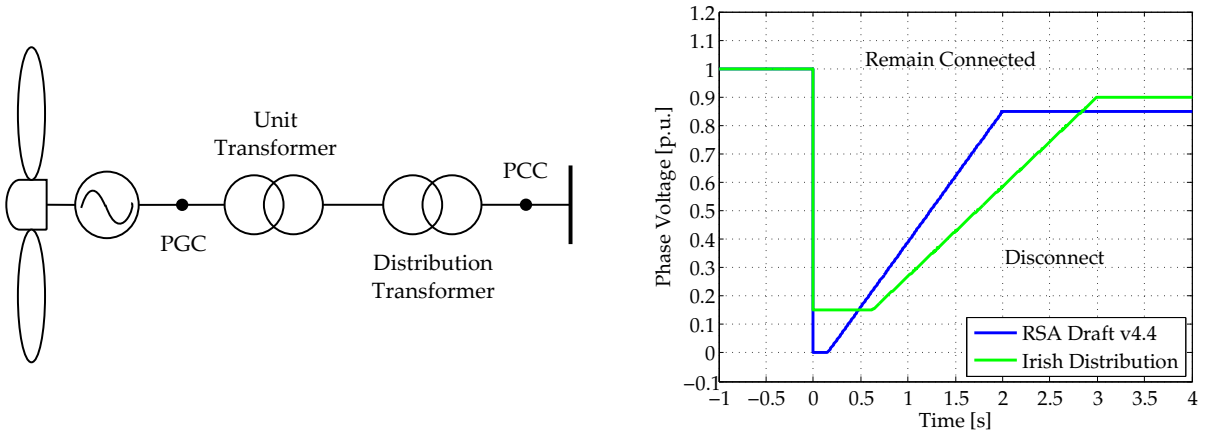

(a) Generic grid connection topology for the SS-PMG

(b) PCC voltage as a function of time during standardised faults, as specified by network regulators

Figure 5.1: SS-PMG grid connection topology and standardised fault profiles for LVRT.

Controllable WECS must remain connected for all 1, 2, or 3 phase voltage dips that fall within the zone above the standard dip profile. As such, if a WECS can remain connected while the standard dip profile is applied at its PCC then it can be expected to withstand all required scenarios.

In addition to achieving ride-through, the following requirements are given for controllable WECS:

- The percentage of rated active power that can be delivered by the WECS must be proportional to $\frac{V_{pcc}}{V_{nominal}}$.
- During a fault, as much reactive power as possible must be delivered by the WECS for at least 0,6 s or until network voltage recovers, whichever comes first.
- The maximum power that can be generated by the WECS, as dictated by wind conditions, must be available for dispatch to the grid no more than 1 s after fault recovery.

The prerequisites described above generally only apply to WECS or wind farms with a rated output of 5 MW or more. Controllability is also a factor: it is recognised that not all WECS are fully controllable so it may not be possible for all designs to meet the complete list of requirements.

Given that the proposed SS-PMG system is not equipped with reactive power control (or turbine torque control), the inherent characteristics of the SS-PMG will determine the active and reactive power support that can be achieved. The primary goal of this investigation is therefore to facilitate ride-through during voltage dips so that the natural grid support behaviour of the SS-PMG can be realised.

5.1.2 South African LVRT Requirements for DG

Grid code requirements for WECS connected to the distribution or transmission network in South Africa have been drafted by Eskom (System Operations and Planning Division) and published by NERSA [88]. This document builds on the requirements of the Grid Code and Distribution Code by providing specific requirements and provisions for WECS, including LVRT. The aspects covered and their applicability to the SS-PMG WECS include:

- Frequency compatibility: there is no particular impediment to the SS-PMG accommodating the required operational frequency range.
- Power-frequency response: if necessary, the required power-frequency response characteristics may be achieved through the appropriate use of the thyristor-controlled dumping load to dissipate excess power.
- Terminal voltage control: the SS-PMG is not currently equipped with a terminal voltage control mechanism.
- Power factor control: the SS-PMG is not currently equipped with a power factor control mechanism.
- Active power restriction: power output restriction is possible through application of the thyristor-controlled dumping load.
- Low voltage ride-through:
  - The WECS must remain connected to the grid through the specified voltage dip profile, shown in Fig. 5.1(b). This profile may occur on one, two or three phases simultaneously and always represents the minimum voltage measured on any phase.
  - Voltage support through controlled reactive power delivery is to be provided according to the stated relations.
  - If disconnection takes place due to the voltage exceeding the dip profile limits, the WECS must reconnect within 1 s after the grid voltage has returned to at least 0,9 p.u.
  - According to [89], the fault ride-through capability of a WECS need only be illustrated by dynamic simulation.

Although these requirements were not obtained early enough to form the basis for the investigation described in this chapter, the gist is broadly the same as for the Irish case. A number of reactive power requirements are presented, which the proposed SS-PMG system is not capable of accommodating but further developments may address these issues. For this investigation, the primary objective is to develop a compensator that will allow the SS-PMG to ride through the specified voltage dip profiles. Further control and compensation is regarded as secondary at this stage.

Comparing the voltage dip profiles in Fig. 5.1(b), the South African version can be seen to include a more severe dip but also a faster rate of recovery than the Irish profile. The restored voltage is 0,05 p.u. lower in the South African case, but returns to a final value of 0,9 p.u. after 120 s. Despite these differences, the two profiles have a similar shape and the ultimate effect on the WECS is likely to be similar. The initial development of the LVRT compensator for the SS-PMG makes use of the Irish voltage dip profile, but final tests are also conducted with the South African profile to determine if performance remains satisfactory.

5.1.3 Types of Grid Voltage Dips

Balanced three-phase faults (to ground) are often employed in both simulations and practical investigations. They are relatively simple to implement and represent the worse case in most systems. However, such faults are rare in practice, where phase-to-phase and single phase-to-ground faults are more pre-

valent [90]. Both Irish and South African LVRT requirements state the the standard voltage dip profile could occur on any combination of phases.

Unbalanced faults also undergo transformations when propagated through Δ-Y transformers, such as those typically used to couple wind farms to the distribution or transmission network. The fault experienced by a generator (and its control circuitry) will thus typically exhibit imbalances and phase angle shifts, which vary depending on the original fault and the interspersed network hardware. These effects are described in detail by [90], which also presents a categorisation system for the original and transformed faults.

In choosing which faults to study, the example of [5] is followed. Firstly, a balanced three-phase fault is used as the base case for developing the LVRT compensator. This type of fault has the most severe effect on electrical machines and is thus appropriate for generic testing purposes. It is also easier to emulate in the laboratory during practical investigations and does not experience any transformation changes, as illustrated in Fig. 5.2(a).

The most commonly occurring fault in practice is a single phase-to-ground fault [90]. As shown by Fig. 5.2(b), this fault experiences magnitude and phase angle changes when passing through a Δ-Y transformer. In order to test the performance of the LVRT compensator under realistic conditions, the transformed version of this fault can be applied at the PGC. As with the balanced fault, the time-dependent RMS values of the phase voltages (on the faulted phases) will follow the specified dip profiles.

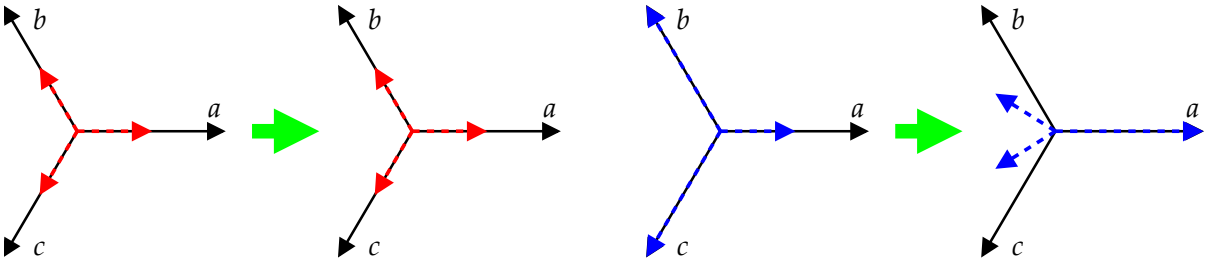

(a) Balanced three-phase fault transformation from source (at left) to generator (at right) shown in red

(b) Single phase-to-ground fault transformation from source (at left) to generator (at right) shown in blue

Figure 5.2: Voltage phasor representation of grid fault transformations through a Δ-Y transformer, from [5].

5.2 Grid Fault Compensator

The basic compensator design to be investigated in this chapter is introduced in Section 2.3.2. The layout of the complete compensation system is repeated in Fig. 5.3 for convenience. This compensator is designed to act on a single SS-PMG and incorporates the speed control mechanisms discussed in Chapter 4. The investigation in this chapter focuses on different switching strategies and the correct choice of resistance values, namely R_{sr} and R_{br}. For thyristor-based braking $R_{br} = 0{,}61\,\text{p.u.}$ but variations in R_{br} are studied for contactor-based switching.

The GCC employs only current and voltage sensors to determine the state of the SS-PMG and the network. The sampled instantaneous values are processed with the aid of the $\alpha\beta$ transform, discussed

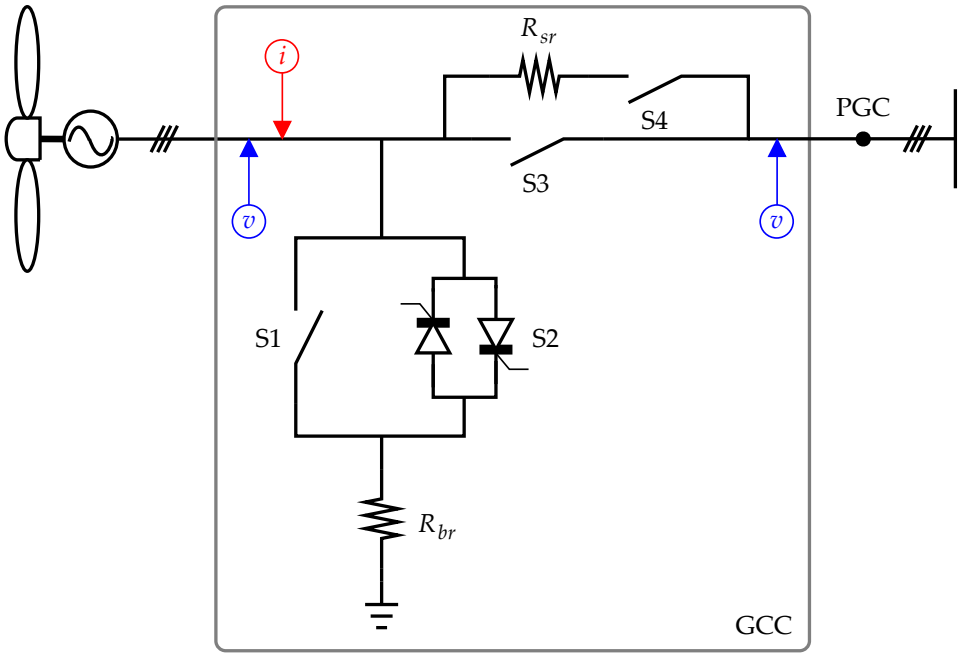

Figure 5.3: Line diagram of the GCC, emphasising LVRT operation. Instantaneous voltage and current samples taken by the GCC are indicated by blue and red arrows, respectively. Compensation is achieved by the actuation of switches S1 or S2, and S3. Switch S4 remains closed as long as the SS-PMG is coupled to the grid.

in Section 2.1.1.2. This approach is known to be effective for balanced systems but may require supplementation to correctly evaluate unbalanced faults.

5.2.1 Objectives of Compensation

The effect of a balanced fault on a synchronous generator is to expose the machine to an extremely low impedance load. Depending upon the sub-transient reactance of the generator, this typically results in large current and torque oscillations. In addition, a power imbalance forms between what the prime mover is delivering and what the load can accept. This can cause the generator rotor angle to increase up to the point where pole-slipping and loss of synchronism occurs. Protection circuitry may prevent this by disconnecting the generator at a predefined instantaneous current level.

In order to achieve fault ride-through it is necessary to limit both instantaneous current transients and rotor angle deviations. This is to prevent damage to the generator, while avoiding loss of synchronism and/or tripping of protection circuitry. The breaker design employed with the SS-PMG has an instantaneous tripping level of 5 p.u. and will undergo a thermal trip if current exceeds 3 p.u. for 3 s or longer. The objectives of the LVRT compensator are thus:

1. Limit the SS-PMG rotor angle θ to no more than 120 °.
2. Restrict current transients to less than 5 p.u.
3. Ensure average fault currents are less than 3 p.u.

These objectives must be achieved while the Irish voltage dip profile of Fig. 5.1(b) is applied to all three phases at the PCC. Compensation must also be effective across the entire operational wind speed range, including turbulent conditions.

5.2.2 Compensation Strategies

The compensation system presented in Fig. 5.3 consists of a series resistance R_{sr} and a shunt resistance R_{br}. Through the use of these resistances, the active power delivery from the SS-PMG can be regulated. The series resistance serves to increase the effective grid impedance, thereby reducing both instantaneous and average current levels. The shunt resistance can absorb whatever active power the grid and series resistance cannot, in order to counteract turbine torque and prevent uncontrolled acceleration.

After the SS-PMG has been synchronised with the grid (switches S3 and S4 closed), the LVRT compensator is activated. The general compensation strategy followed in all cases is described by the flow diagram in Fig. 5.4. Inserting the series compensation involves opening switch S3, while inserting the shunt compensation is achieved by closing switch S1 or S2.

Preliminary investigations, illustrated in Appendix C.2, show that no meaningful advantage is gained by removing compensation early or extending it beyond the duration of the fault. As a result, it was found to be most appropriate to set $V_{res} = V_{min} = 0{,}85$ p.u. when compensating for the Irish dip profile.

The remaining sections in this chapter address the following questions in the context of the objectives laid out in Section 5.2.1:

- To what extent is LVRT compensation required by the SS-PMG ?
- Is it necessary to employ both series and shunt resistance compensation?
- Can contactor switching be employed for both series and shunt resistances?
- What are the most appropriate values for R_{br} and R_{sr}?
- Can a resistor-based compensator meet the performance objectives under all wind conditions?

The first part of this investigation focuses on the response of the SS-PMG to faults without compensation. Following this, the effect of compensating with a single resistance, either shunt or series, is briefly investigated and shown to be insufficient. To achieve better results, the two compensation elements are combined in the configuration shown in Fig. 5.3. A control system is then developed to compensate successfully under all required conditions, including turbulent wind and unbalanced grid faults. This

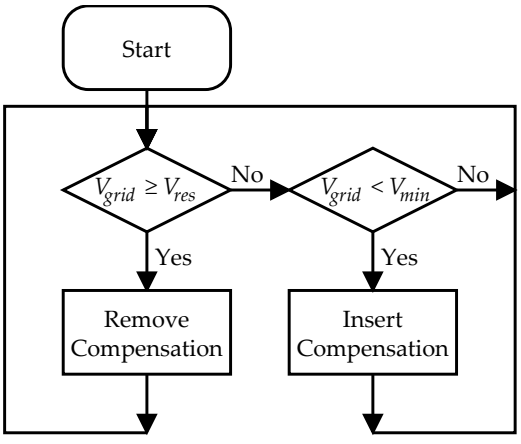

Figure 5.4: Flow diagram of the generic LVRT compensation strategy employed in this study. Compensation can consist of a series resistance R_{sr} and/or a shunt braking resistance R_{br}. The trigging value V_{min} and the restoration value V_{res} can be set independently.

includes an investigation into different switching options for the shunt braking resistance.

5.3 Uncompensated Response

Understanding the natural response of the SS-PMG to network disturbances reveals what type and degree of compensation is necessary. It is desirable, as far as possible, to allow the SS-PMG to exert its inherent voltage support function during grid faults. Additional compensation should only be used to ensure the system remains within the limits established in Section 5.2.1.

Grid fault initiation has been set to coincide with the occurrence of maximum flux linkage in phase A of the SS-PMG. This ensures that phase A exhibits the most severe response to balanced faults beginning at $t = 0$ s, which is confirmed by the simulation results in Appendix C.3. Unless otherwise indicated, all maximum current trends and phase current traces refer to phase A, as it represents the worst case.

Fig. 5.5 shows the transient response of the SS-PMG to the Irish voltage dip profile applied to all phases at the PCC with a steady wind of 6 m/s. The instantaneous PCC phase voltage can be seen in Fig. 5.5(a) to follow the correct profile. The transient current response of the SS-PMG is illustrated in Fig. 5.5(b), where a typical initial current spike with DC offset is evident during the first 0,1 s of the fault. After settling, the current magnitude is proportional to the imposed voltage dip. The initial current peak of 3,178 p.u. is below the required limit of 5 p.u. and the average current during the rest of the fault is also well below 3 p.u.

The PM-rotor experiences minor speed oscillations as the fault begins, while the larger inertia of the turbine means that its speed (along with that of the slip-rotor) is only slightly affected, as shown in Fig. 5.5(c). The rotor angle deviation that occurs in Fig. 5.5(d) is tolerable and short-lived, since the turbine is not imposing a high level of input torque at this wind speed. As such, the stability of the SS-PMG on the grid is never under threat in this case.

With both rotor angle and transient currents remaining below the stated limits, it would appear that no LVRT compensation is necessary for the SS-PMG under the conditions imposed in this example. The results depicted in Fig. 5.6 show this to be the case for a wide wind speed range, even if stator inductance were to vary due to manufacturing deviations or operational conditions.

Fig. 5.6(a) shows that SS-PMG rotor angle stability is maintained under steady wind conditions up to $u_w = 9$ m/s for an unmodified value of L_s. If stator inductance were to increase by 30 %, this threshold would drop to $u_w = 8{,}2$ m/s. On the other hand, the SS-PMG would remain stable in winds up to $u_w = 10{,}4$ m/s without compensation if stator inductance were reduced by 30 %, although stability at low winds would be compromised.

The initial current spike resulting from the fault is a strong inverse function of L_s, increasing by 53,5 % as L_s is reduced from 130 % to 70 % of its measured value. Even in the extreme case, though, maximum current remains below the 5 p.u. limit. In contrast, the initial transient current is a weak function of wind speed, increasing from 3,17 p.u. at $u_w = 4$ m/s to 3,36 p.u. at $u_w = 12$ m/s (with $\Delta L_s = 0$ %).

The turbine speed in Fig. 5.6(c) and the rotor angle in Fig. 5.6(d) at the end of the simulation show that the SS-PMG generally regains stability for $u_w \leq 10$ m/s, even if pole-slipping does occur during

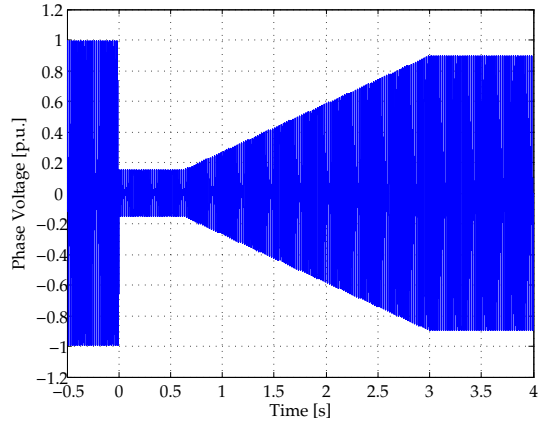

(a) Instantaneous phase voltage at the PCC as a function of time

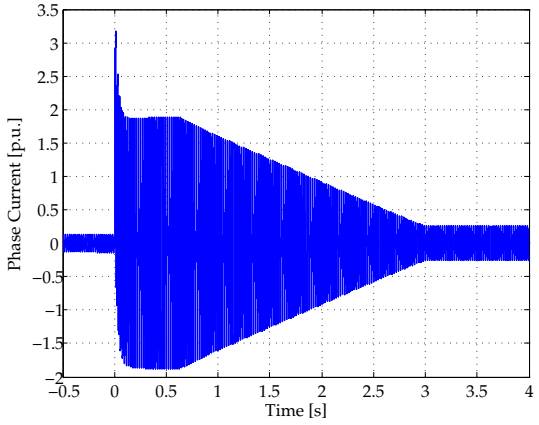

(b) Instantaneous SS-PMG phase current as a function of time

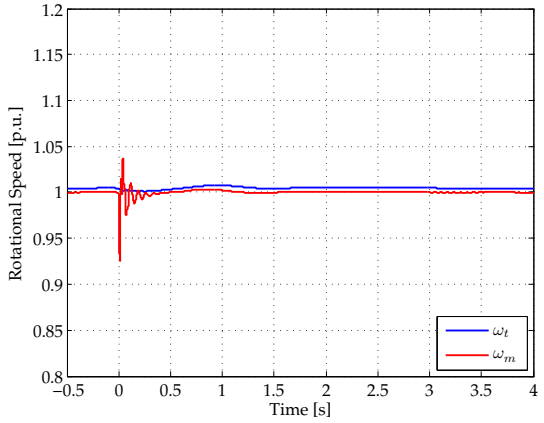

(c) Turbine and PM-rotor speed as a function of time

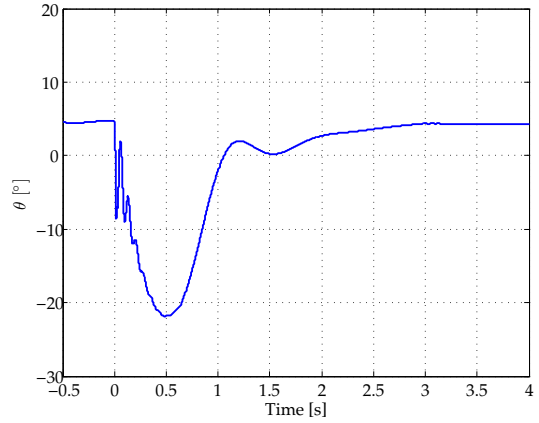

(d) SS-PMG rotor angle as a function of time

Figure 5.5: Transient response of the SS-PMG to a balanced three-phase Irish fault profile at $u_w = 6\,\mathrm{m/s}$ with L_s unmodified.

the fault. In other words, unrecoverable fault conditions typically only manifest near and above rated wind speed, although rotor angle and current limits may still be exceeded in many cases.

The findings from Fig. 5.6 suggest that LVRT compensation is not essential for average wind speeds of less than $9\,\mathrm{m/s}$. Under such conditions, the SS-PMG can tolerate the voltage dip without losing stability or exceeding current limits. In contrast, the SS-PMG becomes unstable during faults at higher wind speeds. Compensation approaches investigated in the remainder of this chapter thus focus on the wind speed range that produces unstable fault responses from the SS-PMG. To leave some margin for error, this wind speed range is taken to be $8\,\mathrm{m/s} \leq u_w \leq 12\,\mathrm{m/s}$.

5.4 Single Resistance Compensation

With the conditions requiring LVRT compensation determined, it is possible to evaluate the efficacy of different compensation approaches for these cases. The most basic compensation approaches employ a singe resistive element, either in series or shunt. The effectiveness of each resistance in isolation is

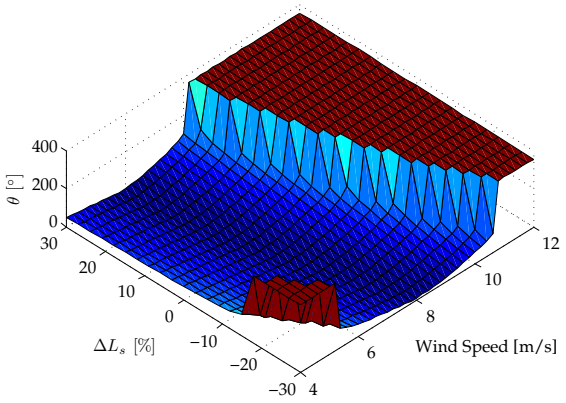

(a) Maximum rotor angle as a function of stator inductance variation and wind speed

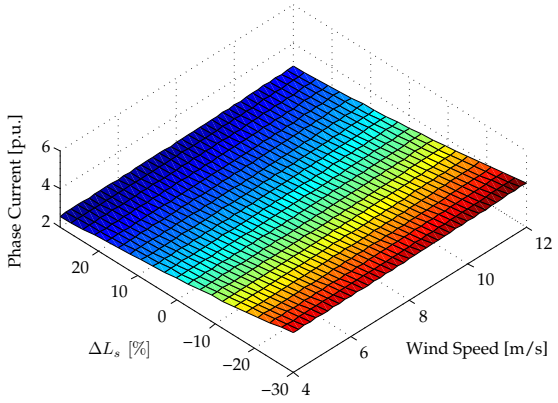

(b) Maximum instantaneous phase current at fault initiation as a function of stator inductance variation and wind speed

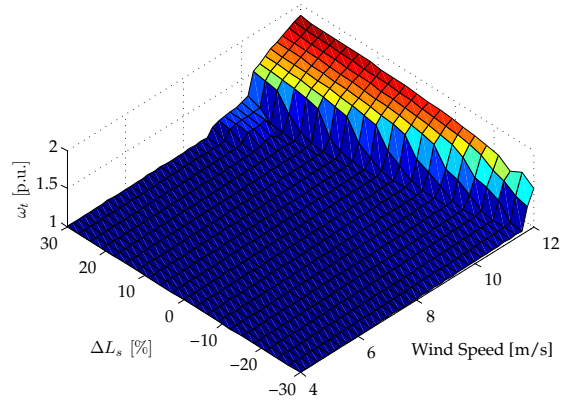

(c) Final turbine speed as a function of stator inductance variation and wind speed

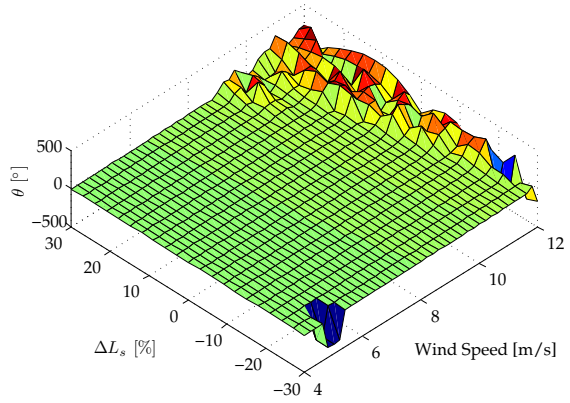

(d) Final rotor angle as a function of stator inductance variation and wind speed

Figure 5.6: The effect of wind speed and stator inductance on rotor angle stability and transient currents for a balanced three-phase fault following the Irish profile.

discussed below.

5.4.1 Series Resistance Compensation

A straight-forward compensation technique is to employ only the series resistance to form a buffer between the SS-PMG and fault by increasing the effective line impedance. Following the switching strategy described in Fig. 5.4, the value of R_{sr} giving the best stability margin was determined at different wind speeds and is shown in Fig. 5.7(a). The wide range of values required for winds between 8 m/s and 12 m/s makes this compensation approach challenging.

The value of R_{sr} required to minimise in-fault currents and compensation removal currents is also shown at each wind speed in Fig. 5.7(a). In-fault current is defined as the current observed after the initial transients caused by fault initiation have settled. Removal current is the transient current that results when the compensation resistance is removed. The best performing R_{sr} values for these two quantities generally follow the same trend as that for rotor angle stability, but diverge sufficiently to

indicate that a trade-off between stability and maximum current will need to be made when selecting R_{sr}.

It is clear that a single value of R_{sr} is not sufficient to compensate for voltage dips across the necessary wind speed range. Employing multiple series resistances is not regarded as feasible, but it may be possible to achieve acceptable results if switch S3 is replaced by back-to-back thyristors (like those employed for switch S2). Varying the firing angle of the thyristors could change the effective resistance experienced by the SS-PMG. The implications of installing in-line thyristors for the SS-PMG are, however, outside the scope of this study so this topic will be deferred to future investigations.

5.4.2 Shunt Braking Resistance Compensation

A shunt-inserted dumping load is a well-known compensation technique for large CSGs in conventional power systems. The function of the load is to absorb excess power from the prime mover, which cannot be transmitted to the grid due to a fault. Since a shunt braking resistance is already incorporated into the GCC for speed control purposes, this compensation option requires no additional hardware to implement. The control strategy follows the familiar pattern of Fig. 5.4: the braking resistance is switched in as soon as a fault is detected, then removed once the SS-PMG restabilises after the grid fault.

The results shown in Fig. 5.7(b) indicate what can be assumed a priori: the braking resistance can only draw more current from the SS-PMG so it does not shield the generator from the effects of the voltage dip. Regardless of the resistance value chosen, the SS-PMG becomes unstable at rated wind speed. The SS-PMG does not benefit from controllable excitation or a regulated prime mover, so a shunt resistance alone cannot compensate for the effects of a grid fault.

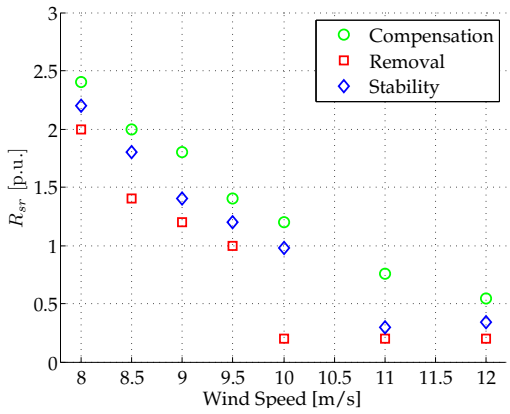

(a) Best value of R_{sr} for minimising compensation current, removal current and rotor angle deviation as a function of wind speed when employing only series resistance LVRT compensation

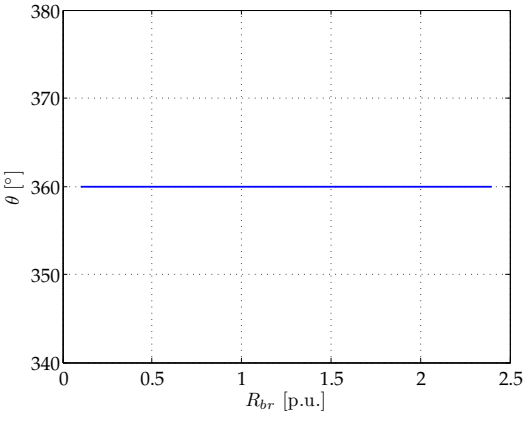

(b) Maximum rotor angle as a function of R_{br} value when employing only shunt resistance LVRT compensation. The SS-PMG is unstable in all cases.

Figure 5.7: Single resistance compensation results when exposed to the standard three-phase Irish fault profile under steady wind conditions.

5.5 Dual Resistance Compensation: Contactor Braking

The previous section indicates that neither series nor shunt resistances alone allow for sufficient flexibility in grid fault compensation. In other words, it is necessary to employ series and shunt resistances simultaneously to accommodate variable wind conditions. The first implementation option is to employ contactor switching for both the series and shunt resistances, that is, to use switches S1 and S3. The proposed compensation strategy again follows the rules laid out in Fig. 5.4. This section begins with selection of R_{sr}, after which R_{br} is determined.

5.5.1 Selection of a Series Resistance Value

When determining R_{sr}, it is preferable to choose the lowest possible value because this allows the SS-PMG to provide more reactive power support to the grid during faults. This aim is however, secondary to rotor angle stability and transient current restriction—the factors which allow ride-through to be achieved. The plots in Fig. 5.8 show the maximum rotor angle resulting from different combinations of R_{sr} and R_{br} at a selection of steady wind speeds. Transient current maxima are shown in Appendix C.4 and follow the same trends.

The stable zone at $u_w = 9\,\mathrm{m/s}$ in Fig. 5.8(a) is a relatively narrow band of high R_{sr} and R_{br} values. This band shifts steadily towards lower resistance values as wind speed rises, evidenced by Fig. 5.8(b) for $u_w = 10\,\mathrm{m/s}$. At rated wind speed and above, shown in Fig. 5.8(c) and Fig. 5.8(d), it is possible to employ almost any value of R_{sr} if the correct value of R_{br} is chosen and vice versa.

The range of R_{sr} values that achieve stable results for all these wind speeds is relatively small, being $2{,}4\,\mathrm{p.u.} \leq R_{sr} \leq 2{,}8\,\mathrm{p.u.}$. In this range, the median value of $R_{sr} = 2{,}6\,\mathrm{p.u.}$ was chosen, as it provides an acceptable tolerance margin.

5.5.2 Selection of a Shunt Braking Resistance Value

Finding a single value of R_{br} to match the chosen R_{sr} is problematic, as already indicated in Fig. 5.8. Below $u_w = 11\,\mathrm{m/s}$ the range of R_{br} values that achieve stability changes dramatically with wind speed, as can be seen in Fig. 5.9(a), which shows the effect that varying R_{br} has on stability at different wind speeds with $R_{sr} = 2{,}6\,\mathrm{p.u.}$

The best performing value of R_{br} in terms of rotor angle stability is plotted as a function of wind speed in Fig. 5.10(a). The trend follows an exponential curve, which means the required value of R_{br} changes rapidly for $8\,\mathrm{m/s} \leq u_w \leq 10\,\mathrm{m/s}$ but stabilises at higher wind speeds. The same trend emerges when comparing the best R_{br} value to SS-PMG output power prior to the fault, in Fig. 5.10(b).

Implementing an effective shunt compensator would thus require multiple braking resistances, each controlled by a separate contactor. This, combined with the need to adjust to dynamically changing wind conditions, already points to the need for thyristor-based switching. Before investigating thyristor control of the shunt resistance, further issues can be brought to light by examining the transient current response of the SS-PMG when employing contactor-only control.

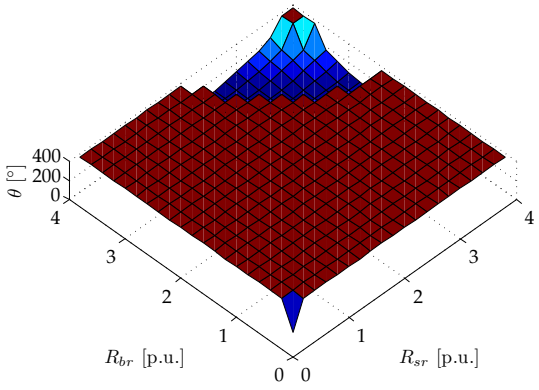

(a) Maximum rotor angle as a function of series resistance and shunt resistance with $u_w = 9\,\mathrm{m/s}$

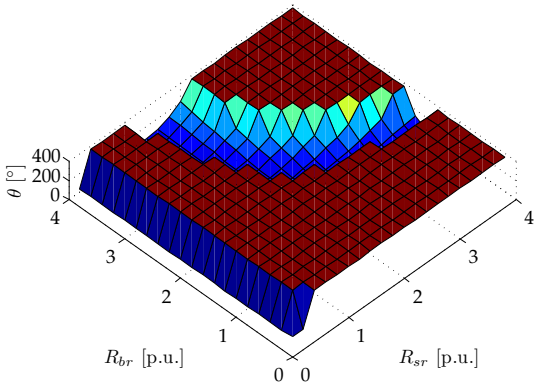

(b) Maximum rotor angle as a function of series resistance and shunt resistance with $u_w = 10\,\mathrm{m/s}$

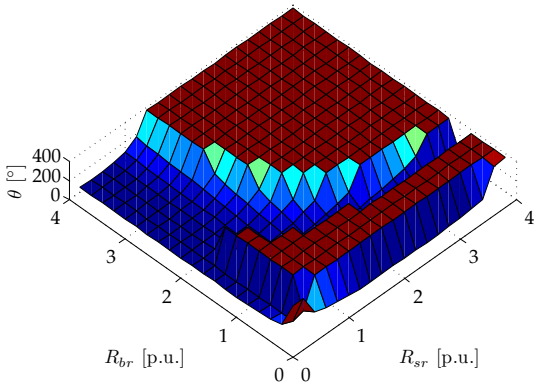

(c) Maximum rotor angle as a function of series resistance and shunt resistance with $u_w = 11\,\mathrm{m/s}$

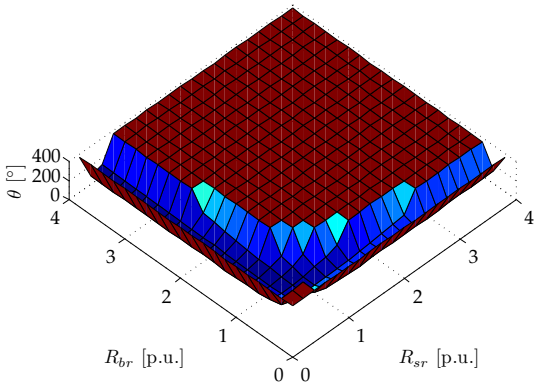

(d) Maximum rotor angle as a function of series resistance and shunt resistance with $u_w = 12\,\mathrm{m/s}$

Figure 5.8: The effect of series resistance value and shunt resistance value on rotor angle stability for the balanced Irish fault profile with steady wind conditions.

Fig. 5.9(b) shows that the current spike at fault initiation is not a function of R_{br} and varies only 9,4 % with wind speed. On the other hand, the in-fault current (after initial settling) follows the same trend as rotor angle stability, as can be seen in Fig. 5.9(c). With the correct choice of R_{br}, this compensation current can remain below 1,2 p.u. up to rated wind speed.

The maximum current transients that result from removing the compensating resistances (opening S2 and closing S3) are shown in Fig. 5.9(d). For the correct R_{br} value, these transients remain below 3 p.u. but there is a small margin of error: if R_{br} deviates 10 % from the ideal value then current transients can exceed 5 p.u. Even in the ideal case, the disturbance created by removing the compensating elements is considerable.

The trends observed in Fig. 5.9 can be explained more clearly by examining the SS-PMG response in a specific case. Fig. 5.11 shows the transient response of the system to the balanced voltage dip profile at a wind speed of $u_w = 10\,\mathrm{m/s}$. In this case, dual resistance compensation is employed with R_{br} set to its best performing value for the wind conditions.

The instantaneous phase current, illustrated in Fig. 5.11(a), exhibits two major disturbances. The

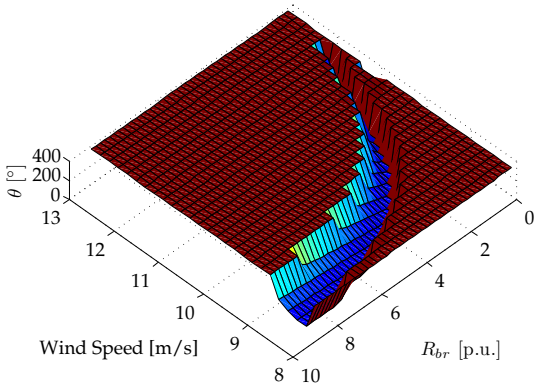

(a) Maximum rotor angle as a function of shunt braking resistance value and steady wind speed

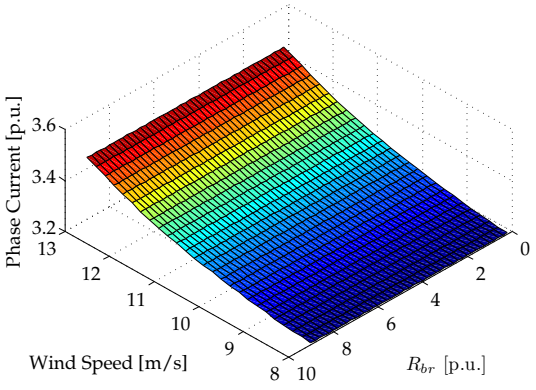

(b) Maximum instantaneous phase current at fault initiation as a function of shunt braking resistance value and steady wind speed

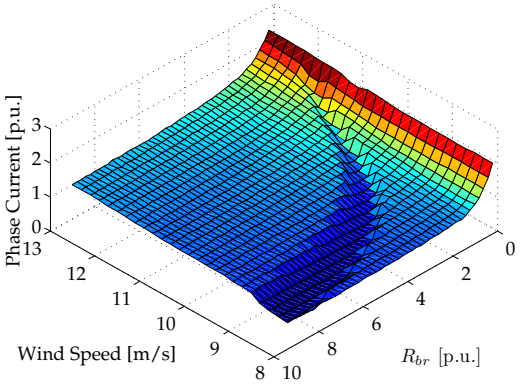

(c) Maximum instantaneous phase current during compensation as a function of shunt braking resistance value and steady wind speed

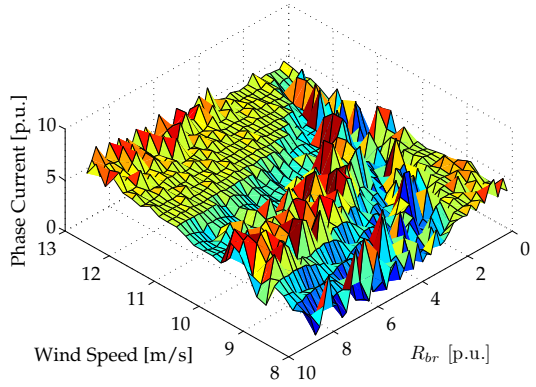

(d) Maximum instantaneous phase current during resistance removal as a function of shunt braking resistance value and steady wind speed

Figure 5.9: The effect of shunt braking resistance value and wind speed on rotor angle stability and current transients for the Irish fault profile.

first is at fault initiation and the second, as the fault clears, is when the compensating resistances are removed from the circuit. Close-up views of these two events are shown in Fig. 5.11(b).

The initial current disturbance is severe but short-lived and does not exceed the 5 p.u. limit. It occurs as a result of the natural SS-PMG response to an on-load short circuit and is not prevented by the LVRT compensator because of the finite response time of the control system. The major component of this response time is the 20 ms actuation delay of the electromechanical contactors, especially S3. As a result, the first cycle after the fault is not compensated.

In the ideal case, the current disturbance at compensation removal does not result in as high a peak as at fault initiation. However, the duration of the disturbance is longer: the SS-PMG requires approximately 0,5 s to settle. This observation is echoed by the PM-rotor speed, shown in Fig. 5.11(c), which experiences a longer, more severe disruption at compensation removal than at fault initiation. Fig. 5.11(d) shows that the rotor angle disturbance when removing the resistances is also relatively large compared

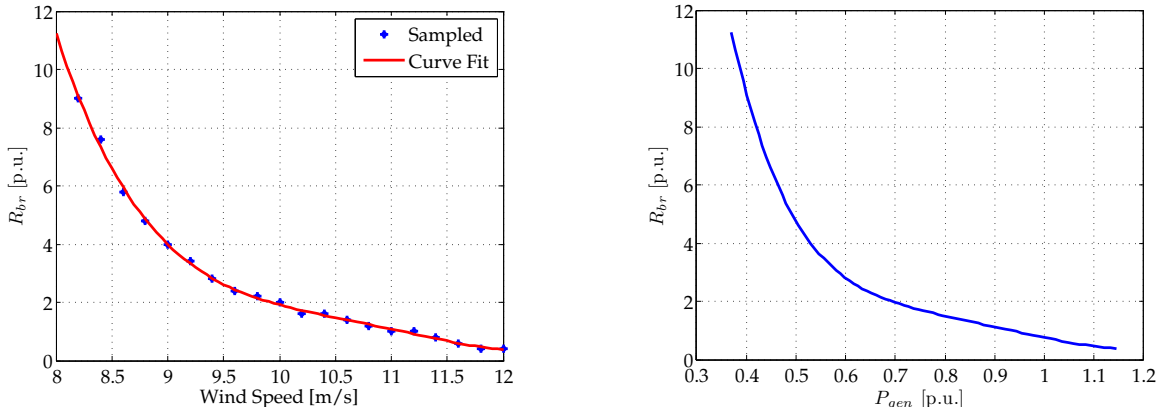

(a) Shunt braking resistance value achieving best response as a function of wind speed

(b) Shunt braking resistance value achieving best response as a function of SS-PMG real output power prior to fault

Figure 5.10: Trends showing the best performing values of contactor-switched R_{br} as part of dual resistance LVRT compensation with $R_{sr} = 2{,}6\,\text{p.u.}$

to that caused by the initial voltage dip.

The severity of the compensation removal transients can be explained by examining the changes in phasor relationships shown in Fig. 5.12. When the series compensation resistance is in place there is significant impedance between the SS-PMG terminals and the PGC. As a result, a phase angle difference $\Delta\phi$ forms between $\mathbf{V_{gen}}$ and $\mathbf{V_{grid}}$, as shown in Fig. 5.12(a). This also increases the rotor angle θ between $\mathbf{E_{gen}}$ and $\mathbf{V_{grid}}$.

When the compensation resistances are removed the GCC effectively becomes a short circuit and the line impedance returns to its original value. $\mathbf{V_{gen}}$ and $\mathbf{V_{grid}}$ are then measured at the same node so $\Delta\phi$ becomes zero and θ must also return to its pre-fault level, as indicated in Fig. 5.12(b). (The θ transition can be seen clearly in Fig. 5.11(d) from $t = 2{,}9\,\text{s}$ onwards.) As the SS-PMG is forced to re-establish equilibrium under these new load conditions, the significant transients observed in Fig. 5.11 are experienced.

In conclusion, the case for contactor-based LVRT compensation is a weak one: if R_{sr} is fixed then multiple values of R_{br} will be required to achieve stable response throughout the steady wind speed range. Furthermore, turbulent conditions could easily lead to instability since this control approach cannot respond incrementally to changing conditions.

Even if rotor angle stability can be regarded as satisfactory, the disturbances caused by the sudden removal of R_{sr} and R_{br} remain problematic. The current transients experienced after removing the resistances are longer lived than those caused by the fault itself, and if the incorrect value of R_{br} is employed these transients can easily exceed the 5 p.u. limit. Overall, then, it would appear that contactor control of both the series and shunt resistances is not flexible enough to achieve satisfactory LVRT compensation.

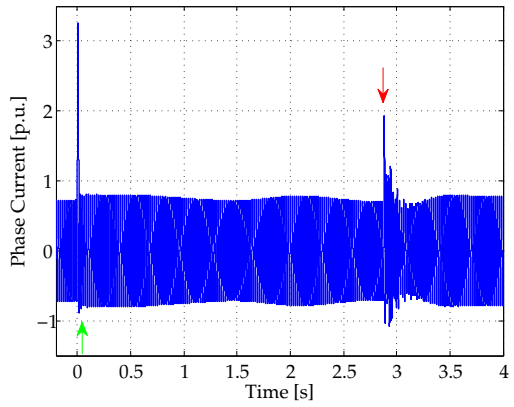

(a) Instantaneous phase current as a function of time

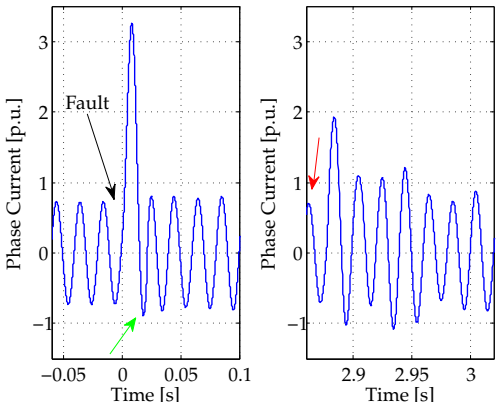

(b) Instantaneous phase current as a function of time—zoomed in on fault initiation and compensation removal

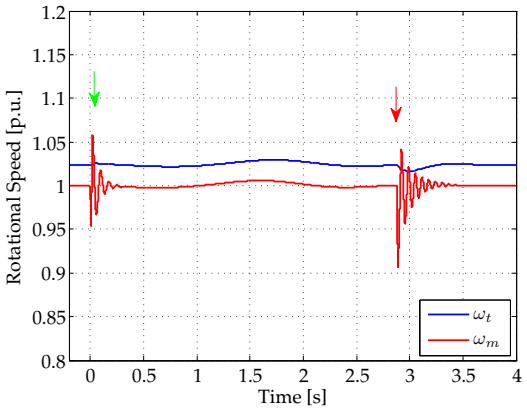

(c) Rotational velocity of turbine and PM-rotor as a function of time

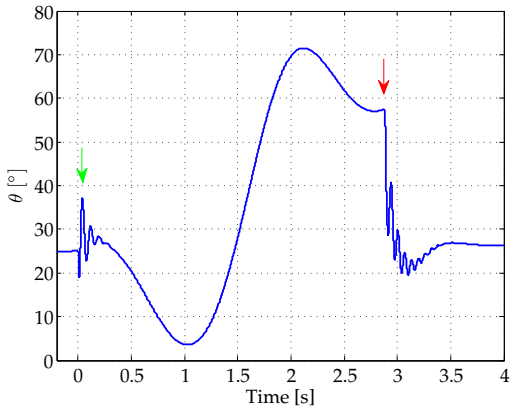

(d) Rotor angle as a function of time

Figure 5.11: Transient response of the SS-PMG to the Irish voltage dip profile with $u_w = 10\,\mathrm{m/s}$ and dual resistance LVRT compensation: $R_{sr} = 2{,}6\,\mathrm{p.u.}$ and contactor-switched $R_{br} = 2{,}0\,\mathrm{p.u.}$ Green arrows indicate compensation insertion and red arrows indicate compensation removal.

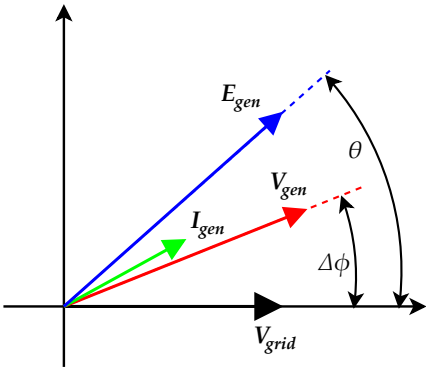

(a) SS-PMG and grid phasor relationships during dual-resistance compensation

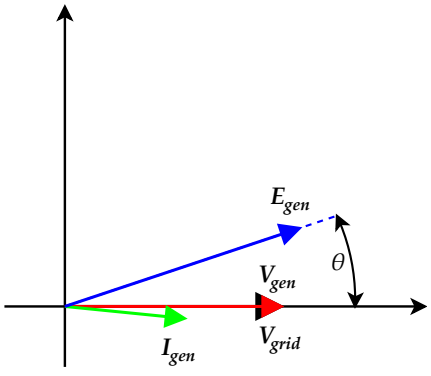

(b) SS-PMG and grid phasor relationships in steady-state after compensation is removed

Figure 5.12: SS-PMG and grid (PGC) phasor relationships during and after dual-resistance compensation.

5.6 Dual Resistance Compensation: Thyristor Braking

The objective in this section is to accommodate variable wind conditions by supplementing the contactor-controlled series resistance with an incrementally variable load. It was shown in the previous section that a single R_{br} value is insufficient to manage the changes in active power across the wind speed range of $8\,\text{m/s} \leq u_w \leq 12\,\text{m/s}$. Instead of installing multiple shunt resistances, however, the effective resistance of one load can be controlled by setting the thyristor firing angle, as previously discussed in Section 4.2.2.

For the purposes of speed control, the braking resistance value is specified as $R_{br} = 0{,}61\,\text{p.u.}$ The results shown in Fig. 5.9(a) and Fig. 5.10 indicate that this value of R_{br} is a suitable minimum for LVRT compensation as well. Manipulation of the thyristor firing angle α can be used to produce higher effective resistance values to allow compensation across the wind speed range. As a result, the thyristor-based braking subsystem can be repurposed for LVRT compensation without any physical changes being required.

5.6.1 Pre-Set Thyristor Firing Angle: Power Mapping

To account for variable wind conditions, the thyristor loading level H_l can be set according the the steady operating conditions immediately prior to a grid voltage dip. The real power P_{gen} delivered by the SS-PMG can be used as a measure of wind conditions and mapped to the correct value of H_l. This allows the shunt braking component of the LVRT compensator to adapt to different base wind speeds automatically, overcoming the inherent limitation contactor-only switching.

5.6.1.1 Power Mapping: Design

A flow diagram indicating the operation of the power mapping LVRT (PM-LVRT) compensation approach is shown in Fig. 5.13(a). The underlying logic follows the principle established in Fig. 5.4 but additional steps are included to adapt to different wind conditions. Fig. 5.13(b) illustrates the computation steps between the pre-fault SS-PMG power output and the firing delay angle that remains set for the duration of the fault. The value of α is determined from H_{l0} according to the relationship developed in Section 4.2.2.1.

If no fault is detected then a moving average of P_{gen} is stored for later use. P_{gen} can be calculated from the $\alpha\beta$ transformed quantities according to Eqn (5.1). If a voltage dip is detected then the previously stored value of P_{gen} is compared to the minimum level at which compensation is employed, P_{min}. For power levels below the limit, no compensation action is undertaken. If P_{gen} exceeds the minimum value then H_{l0} is determined as a function of P_{gen}. With α derived from H_{l0}, switch S2 is activated and switch S3 is opened for the duration of the voltage dip.

$$P_{gen} = \frac{3}{2}\left\|\overline{v}_{gen}\right\|\left\|\overline{i}_{gen}\right\|\cos\left(\angle\overline{v}_{gen} - \angle\overline{i}_{gen}\right) \tag{5.1}$$

In order to define the relationship between H_{l0} and P_{gen}, it is necessary to study the effect of different pre-set thyristor loading levels on SS-PMG response to the standard voltage dip. Fig. 5.14(a) and

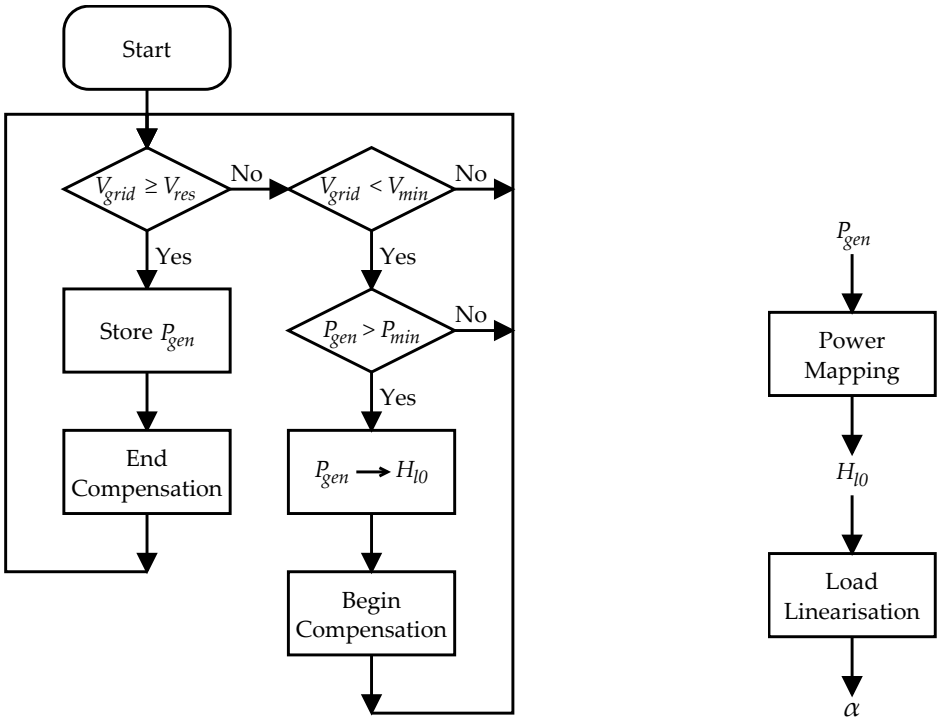

(a) PM-LVRT compensation strategy, employing mapping from SS-PMG output power to thyristor load reference

(b) Detail of the mapping procedure from SS-PMG power to thyristor load reference to firing delay angle

Figure 5.13: Flow diagrams describing the operation of the PM-LVRT strategy.

Fig. 5.14(b) show the effect of loading level on maximum rotor angle and maxium transient current, respectively. In both cases, a narrow band of H_{l0} values achieves acceptable operation at any given wind speed.

Fig. 5.14(c) plots the best performing value of H_{l0} as a function of wind speed. The trend is well described by a second-order polynomial function, as indicated by the closeness of fit achieved for the sampled points. Mapping H_{l0} as a function of power instead of wind speed does away with the need for a wind speed sensor, thus reducing system cost and complexity. To this end, Fig. 5.14(d) displays H_{l0} as a function of P_{gen} prior to the voltage dip. The effective compensation range is $8{,}6\,\text{m/s} \leq u_w \leq 11{,}8\,\text{m/s}$, which translates to $0{,}471\,\text{p.u.} \leq P_{gen} \leq 1{,}087\,\text{p.u.}$.

With this data, H_{l0} is described as a piece-wise defined function of P_{gen} in Eqn (5.2):

$$H_{l0} = \begin{cases} 0 & \text{if } P_{gen} \leq 0{,}471\,\text{p.u.} \\ 42{,}481{P_{gen}}^2 + 93{,}761P_{gen} - 51.970 & \text{if } 0{,}471\,\text{p.u.} < P_{gen} < 1{,}087\,\text{p.u.} \\ 100 & \text{if } P_{gen} \geq 1{,}087\,\text{p.u.} \end{cases} \tag{5.2}$$

5.6.1.2 Power Mapping: Steady Wind Compensation

The results of applying the PM-LVRT compensation strategy across the complete operational wind speed range are shown in Fig. 5.15. Rotor angle stability, illustrated in Fig. 5.15(a), shows two distinct trends. Up to $u_w = 8{,}6\,\text{m/s}$ the response is uncompensated and is only a function of turbine torque,

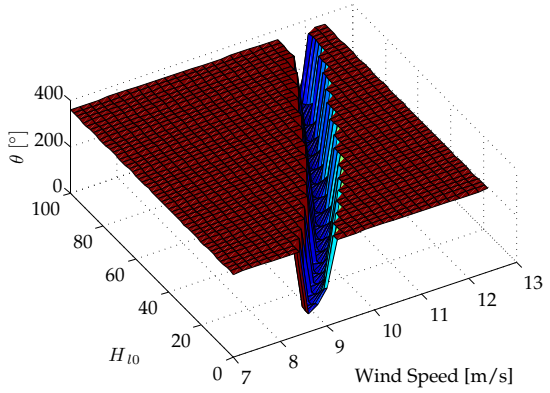

(a) Maximum rotor angle as a function of thyristor loading and steady wind speed

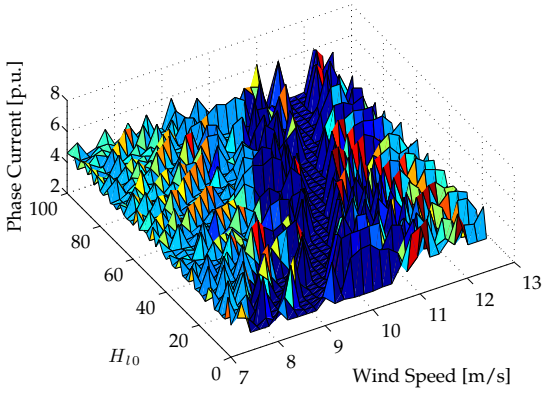

(b) Maximum phase current as a function of thyristor loading and steady wind speed

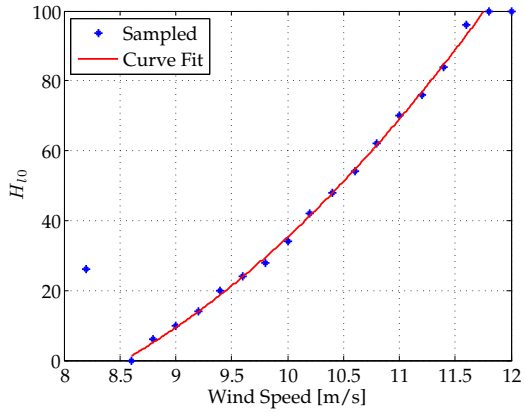

(c) Thyristor loading achieving best rotor stability margin as a function of steady wind speed

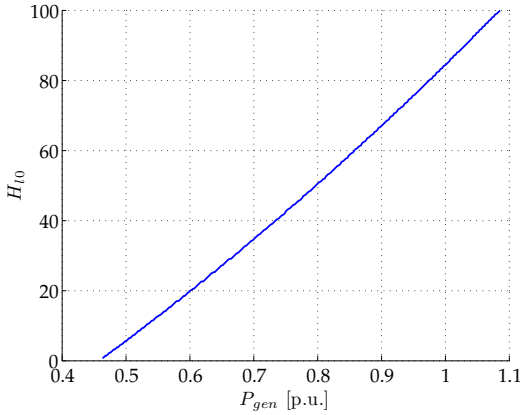

(d) Thyristor loading achieving best rotor stability margin as a function of SS-PMG real power ouput

Figure 5.14: Identification of the best performing thyristor loading level H_l as a function of wind speed and SS-PMG power output for steady wind conditions and the Irish fault profile.

reaching a local maximum of 78,36 °. At higher wind speeds, compensation ensures rotor angle stability is maintained and maximum θ decreases until braking capacity is exceeded above $u_w = 11{,}8\,\mathrm{m/s}$.

Maximum current at fault initiation, shown in Fig. 5.15(b) is once again unaffected by the control strategy because neither contactor nor thyristor switching can respond quickly enough to counteract the first half-cycle transients. The fault-current level is nonetheless well below the tolerable maximum of 5 p.u.

In-fault current is higher in the uncompensated band, as can be seen for $u_w \leq 8{,}6\,\mathrm{m/s}$ in Fig. 5.15(c). In this range, the SS-PMG response is purely a function of the maximum depth of the voltage dip, which remains constant in this case. For $u_w > 8{,}6\,\mathrm{m/s}$, the stability of the SS-PMG must be prioritised over its grid support capabilities and current is limited, becoming a function of wind speed because R_{br} is reduced as u_w increases. The result of this arrangement is that the SS-PMG remains stable in all cases and is able to provide voltage support to the grid when wind conditions allow it.

Despite the relatively low current levels during compensation, PM-LVRT causes substantial disturb-

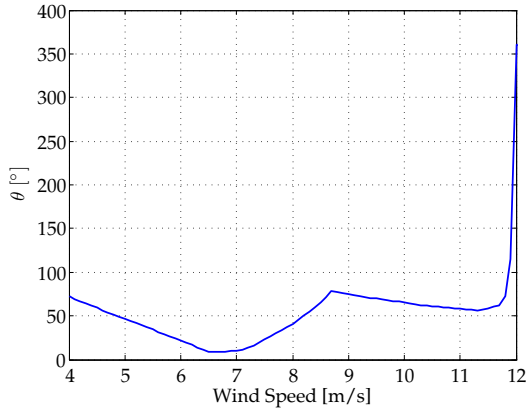

(a) Maximum rotor angle as a function of steady wind speed

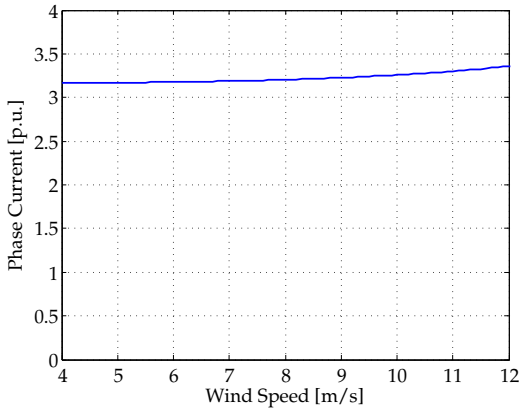

(b) Maximum instantaneous phase current at fault initiation as a function of steady wind speed

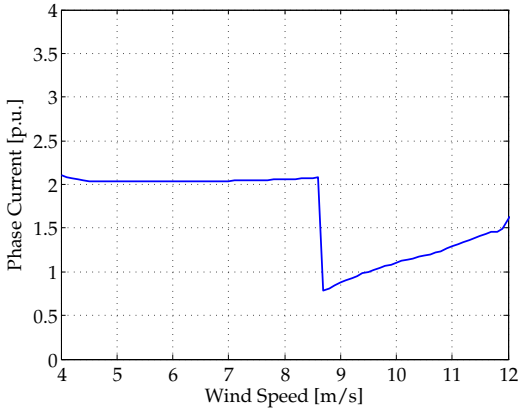

(c) Maximum instantaneous phase current during compensation as a function of steady wind speed

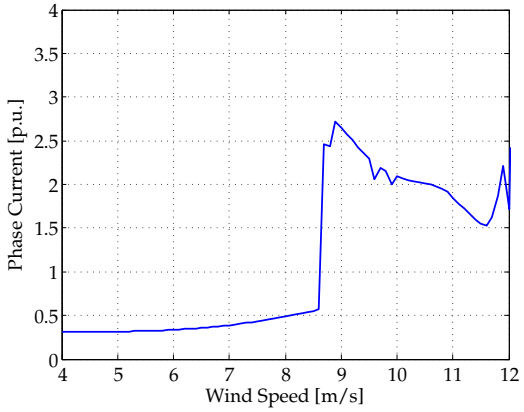

(d) Maximum instantaneous phase current during resistance removal as a function of steady wind speed

Figure 5.15: Performance of the PM-LVRT compensation strategy across the operational wind speed range when exposed to the standard Irish voltage dip profile.

ances when the compensation resistances are disengaged. Fig. 5.15(d) shows that the transient currents at compensation removal approach the level of the initial fault currents for $8{,}6\,\mathrm{m/s} < u_w < 9{,}0\,\mathrm{m/s}$. In this regard, PM-LVRT shows virtually no improvement over contactor-only compensation. This is to be expected, since the same sudden changes in SS-PMG load take place. Although no protection limits are exceeded, it is undesirable to introduce disturbances to the system just as the grid voltage recovers from a fault.

Fig. 5.16 shows the transient response of the SS-PMG with PM-LVRT compensation to the standard voltage dip profile at $u_w = 11\,\mathrm{m/s}$. In Fig. 5.16(b), it can be seen that the average current is well within limits, although two transient periods are still evident—one at fault initiation and one during compensation removal. The current transients at compensation removal are lower than those occurring at the initial fault, however, the duration of the removal transients is longer (mirroring the results from the contactor-only compensation in Fig. 5.11).

The PM-rotor speed oscillation created by removing the resistances is clearly evident in Fig. 5.16(c)

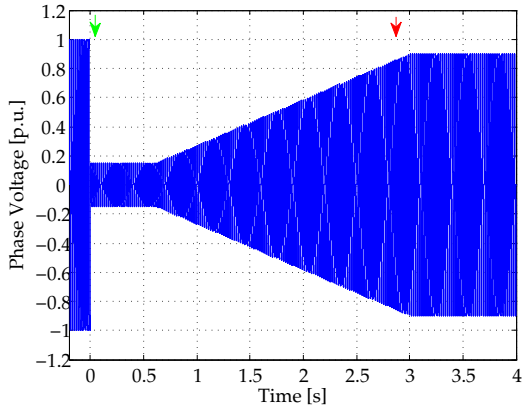

(a) Instantaneous phase voltage at the PCC as a function of time

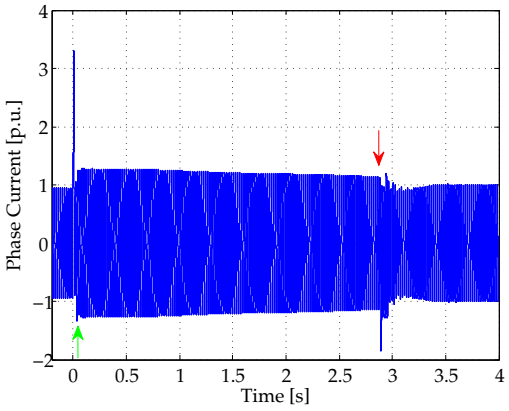

(b) Instantaneous phase current as a function of time

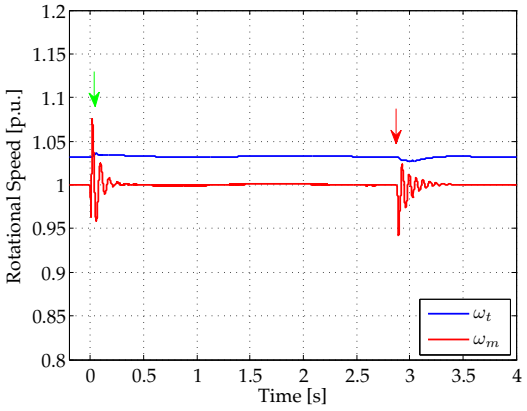

(c) Rotational velocity of turbine and PM-rotor as a function of time

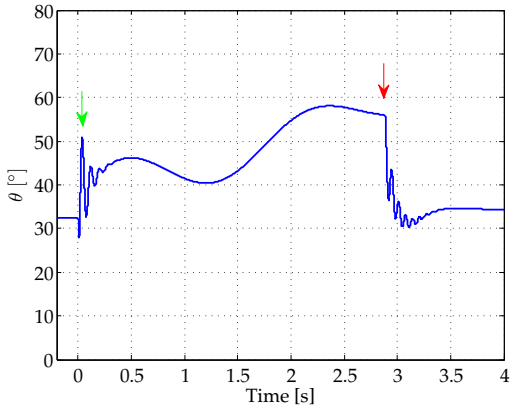

(d) Rotor angle as a function of time

Figure 5.16: Transient response of the SS-PMG with power mapping LVRT compensation to the Irish voltage dip profile at a steady wind speed of $u_w = 11\,\mathrm{m/s}$. Green arrows indicate compensation insertion and red arrows indicate compensation removal.

and is comparable to the initial fault disturbance. The characteristic rotor angle step seen at $t = 2{,}9\,\mathrm{s}$ in Fig. 5.16(d) also results from the sudden resistance removal and can again be explained by referring to Fig. 5.12.

Two conclusions can be drawn from the results discussed above. Firstly, the PM-LVRT approach successfully avoids the need for multiple R_{br} values by varying the firing angle of thyristor switch S2 as a function of P_{gen}. This overcomes the first major deficiency of the contactor-only dual resistance compensator. Secondly, however, PM-LVRT still causes significant disturbances to the SS-PMG and grid when disengaging the resistances. A more gradual or controlled method of ending compensation is needed to avoid severe transients. A further concern with PM-LVRT is its inability to accommodate rapidly changing, turbulent wind since α remains fixed for the duration of the fault.

5.6.2 Variable Thyristor Firing Angle: Phase Angle Control

Continuously variable loading of the SS-PMG can help to achieve smoother, controlled removal of the compensation resistances and to adapt to highly turbulent wind conditions. If the thyristor firing angle is continuously updated during LVRT then the effective load imposed on the SS-PMG can be changed to handle unpredictable wind speeds and restrict removal transients.

Different control strategies can be proposed for α with the ultimate purpose of limiting rotor angle deviations and transient current magnitudes. For example, the speed control loop developed in Section 4.2 can be used to prevent PM-rotor speed excursions during faults. This approach would, however, require impractically high gains to avoid pole-slipping. Instead, a more direct approach can be employed—one that acts upon the rotor angle or phase angle difference directly.

Fig. 5.12(a) indicates that $\Delta\phi$ is chiefly responsible for the steady-state offset in θ during resistance compensation. Minimising $\Delta\phi$ would thus reduce the θ step imposed on the SS-PMG at resistance removal. This, in turn, would minimise both transient current and settling time, while being simpler than controlling θ itself: monitoring θ requires an estimator but $\Delta\phi$ can be determined directly from the $\alpha\beta$ voltage vectors. Dynamically regulating $\Delta\phi$ would also allow the compensator to adjust automatically to changing wind conditions.

5.6.2.1 Phase Angle Control: Design and Gain Selection

Phase angle control LVRT (PAC-LVRT) builds on the PM-LVRT strategy. PAC-LVRT employs the same compensation logic, shown in Fig. 5.13(a), with the major difference being that H_l is no longer fixed. Instead, H_{l0} constitutes a base value for H_l, which can be further modified by the phase angle controller to compensate for dynamic conditions and minimise $\Delta\phi$ at resistance removal. Otherwise, insertion and removal conditions remain the same as for PM-LVRT.

The proposed $\Delta\phi$ control loop is shown in Fig. 5.17. H_l is calculated as the sum of H_{l0} and the output of the PI regulator, which acts upon the phase angle error ϕ_{err}. The reference for $\Delta\phi$ is zero, so the phase angle error is defined as $\phi_{err} = 0\,^\circ - \Delta\phi$.

The control loop acts to minimise $\Delta\phi$, which serves the dual purpose of reducing removal currents and preventing excessive rotor angle deviations. This approach is, however, only stable as long as two conditions are satisfied. Firstly, the frequency difference Δf between PM-rotor and grid must remain zero under steady conditions. If Δf develops a non-zero offset then $\Delta\phi$ will oscillate continuously. Secondly, the SS-PMG must not experience pole-slipping, in order to prevent a step change in $\Delta\phi$. In other words, it is imperative that the rotor angle limit of 120 ° be adhered to in order to provide sufficient stability margin.

The effect of varying the PI gains, $K_{\phi p}$ and $K_{\phi i}$, is demonstrated in Fig. 5.18 for steady wind conditions and the balanced Irish dip profile. Results are shown side-by-side for two representative wind speed cases, namely $u_w = 9\,\mathrm{m/s}$ and $u_w = 11\,\mathrm{m/s}$.

Fig. 5.18(a) indicates that even relatively low gain values of $K_{\phi p} = K_{\phi i} = 5$ result in a maximum θ deviation of only 55,93 ° at $u_w = 9\,\mathrm{m/s}$. This can be reduced by 44,95 % to 30,79 ° by setting $K_{\phi p} = K_{\phi i} = 35$. Increasing gains further shows a diminishing rate of return with maximum θ deviation at

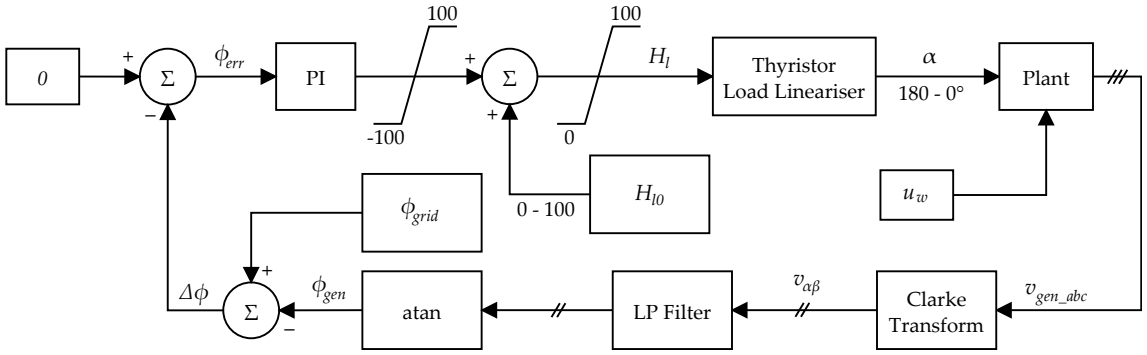

Figure 5.17: Block diagram of the PI phase angle control loop for SS-PMG LVRT. The PI regulator acts upon the phase angle error ϕ_{err} and generates a command signal which is offset by the predetermined value H_{l0} to produce the linear load command H_l. H_l is, in turn, converted into the thyristor firing angle α. The 3-phase generator voltages are sampled, transformed, and filtered before ϕ_{gen} is calculated. The grid phase angle ϕ_{grid} is determined in the same manner and the difference $\Delta\phi$ is returned to the control loop. The internal elements of the plant are illustrated in Fig. 4.15.

$K_{\phi p} = K_{\phi i} = 100$ being 24,80 °. The trend for $u_w = 11\,\mathrm{m/s}$, shown in Fig. 5.18(b), indicates negligible changes in maximum θ from an average of 50,25 °, as long as $K_{\phi p} \geq 10$.

The initial grid fault current is once again not a function of the control strategy, so is not studied further here. The maximum current during compensation also shows little sensitivity to gain values. Fig. 5.18(c) shows that at $u_w = 9\,\mathrm{m/s}$ the maximum in-fault current varies 5,84 % across the studied range of gain combinations. For $u_w = 11\,\mathrm{m/s}$, indicated in Fig. 5.18(d), the in-fault current varies even less—only 3,59 %. For both wind speeds, cases where $K_{\phi p} < 45$ achieve the best results. In all cases, maximum current is well below the 3 p.u. limit.

The crucial performance measure for the PAC-LVRT is the maximum current at resistance removal, which is shown in Fig. 5.18(e) and Fig. 5.18(f) for $u_w = 9\,\mathrm{m/s}$ and $u_w = 11\,\mathrm{m/s}$, respectively. The removal current at $u_w = 9\,\mathrm{m/s}$ follows the same pattern as maximum rotor angle, with gains above 35 providing diminishing returns. At $K_{\phi p} = K_{\phi i} = 35$ maximum current is 1,052 p.u. compared to 2,65 p.u. under PM-LVRT compensation. For $u_w = 11\,\mathrm{m/s}$, all gain combinations in the range $K_{\phi p} > 25$ and $K_{\phi i} > 25$ limit maximum removal current to approximately 1,3 p.u. This again compares well with the PM-LVRT case where maximum current is 1,84 p.u.

The cases studied here indicate that gains of $K_{\phi p} = K_{\phi i} = 35$ allow PAC-LVRT compensation to achieve the desired objectives. Higher gains could be employed but would not deliver significant performance improvement. When compared to PM-LVRT, this approach reduces both rotor angle deviation and resistance removal currents without requiring additional control elements or sensors.

5.6.2.2 Phase Angle Control: Steady Wind Compensation

The performance achieved by PAC-LVRT is compared to that of the PM-LVRT in Fig. 5.19 for steady winds in the range $4\,\mathrm{m/s} \leq u_w \leq 12\,\mathrm{m/s}$. Response below $u_w = 8{,}6\,\mathrm{m/s}$ is the same since compensation is not employed in that range. In the higher wind speed band, marked improvements are, however,

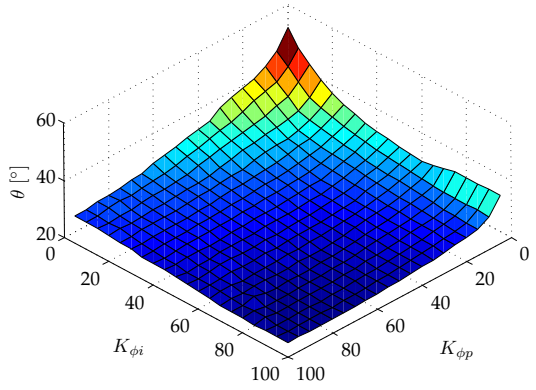

(a) Maximum rotor angle as a function of phase angle controller gains at $u_w = 9\,\mathrm{m/s}$

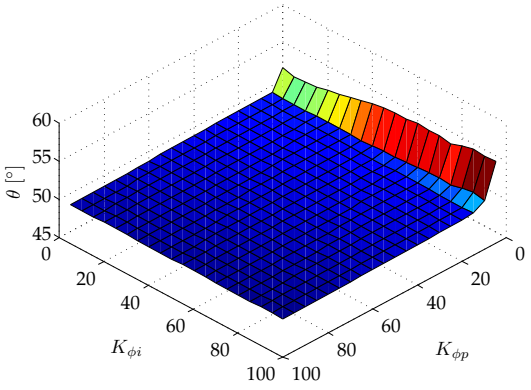

(b) Maximum rotor angle as a function of phase angle controller gains at $u_w = 11\,\mathrm{m/s}$

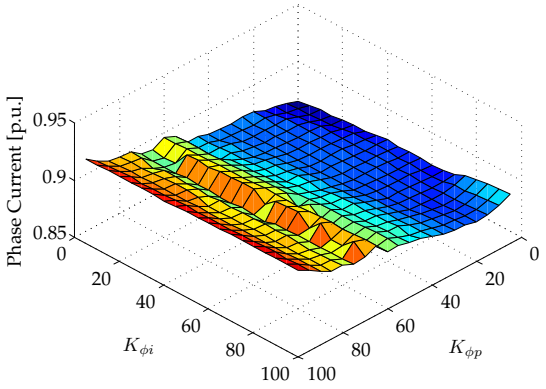

(c) Maximum instantaneous phase current during compensation as a function of phase angle controller gains at $u_w = 9\,\mathrm{m/s}$

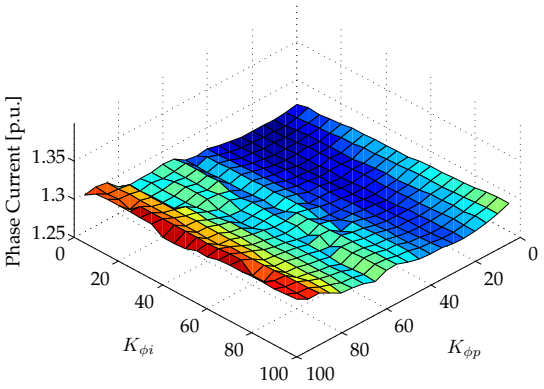

(d) Maximum instantaneous phase current during compensation as a function of phase angle controller gains at $u_w = 11\,\mathrm{m/s}$

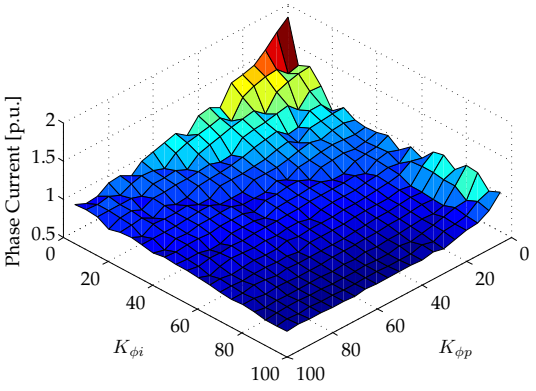

(e) Maximum instantaneous phase current during resistance removal as a function of phase angle controller gains at $u_w = 9\,\mathrm{m/s}$

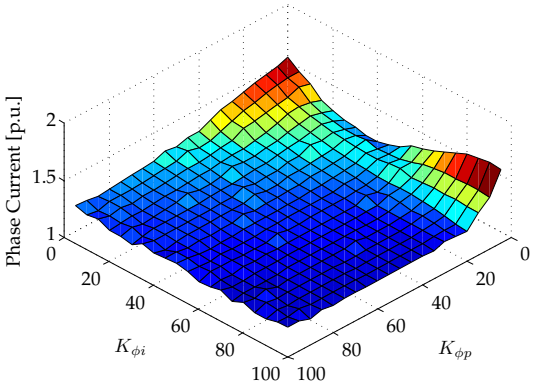

(f) Maximum instantaneous phase current during resistance removal as a function of phase angle controller gains at $u_w = 11\,\mathrm{m/s}$

Figure 5.18: The effect of varying controller gains for PAC LVRT compensation when exposed to the Irish voltage dip profile under steady wind conditions.

visible.

PAC-LVRT reduces maximum rotor angle deviation at most wind speeds, as indicated by Fig. 5.19(a). The greatest improvement is a 63 % reduction compared to the PM-LVRT case at $u_w = 8{,}7\,\mathrm{m/s}$. The level of improvement decreases with wind speed so that performance above $u_w = 11{,}3\,\mathrm{m/s}$ is identical—control effort is constantly at 100 % for higher winds so the two strategies become functionally identical.

As observed previously, the initial fault current is unaffected by the control strategy due to the actuation delay of the switches. Consequently, Fig. 5.19(b) shows that PM-LVRT and PAC-LVRT achieve the same performance in this regard. Since the current level is always below 5 p.u. no further intervention is required, in any case. The in-fault current maxima also remain the same between PM-LVRT and PAC-LVRT (Fig. 5.19(c)). In both cases, the current level is acceptable at all wind speeds.

The most important improvement achieved by PAC-LVRT is in terms of the current maxima experienced during compensation removal. Fig. 5.19(d) illustrates the dramatic reduction in removal current throughout the compensation wind speed range. Significantly, the PAC-LVRT removal currents are not

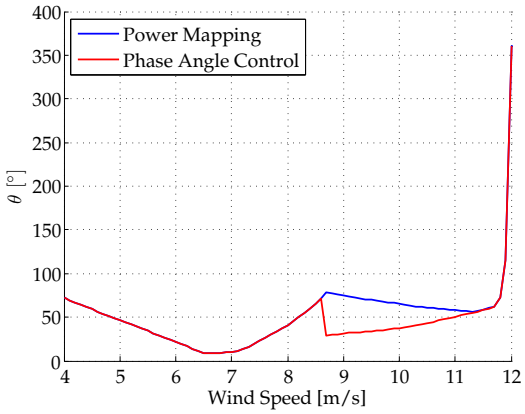

(a) Maximum rotor angle as a function of steady wind speed

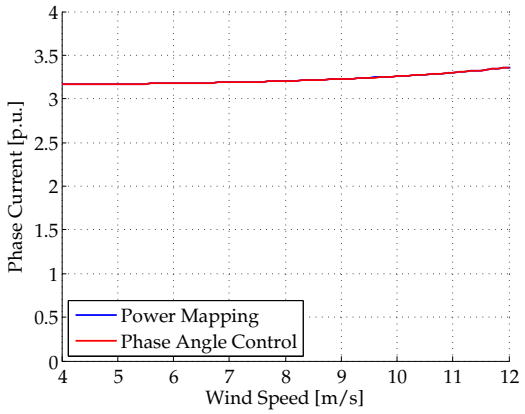

(b) Maximum instantaneous phase current at fault initiation as a function of steady wind speed

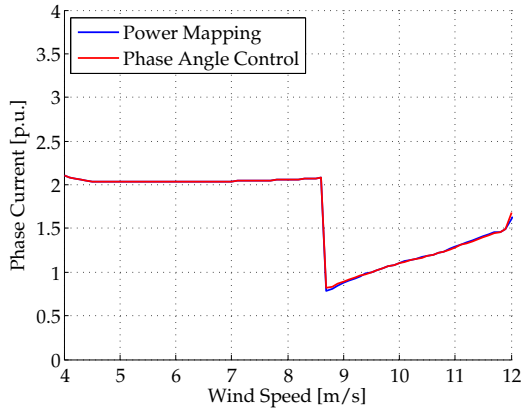

(c) Maximum instantaneous phase current during compensation as a function of steady wind speed

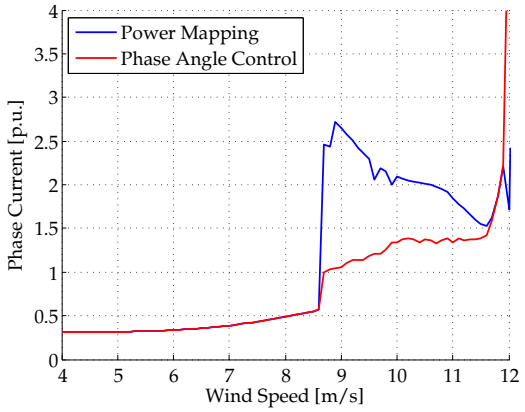

(d) Maximum instantaneous phase current during resistance removal as a function of steady wind speed

Figure 5.19: Performance of PAC LVRT compensation compared to the pre-set power mapping approach across the operational wind speed range when exposed to the standard Irish voltage dip profile.

only lower but also more consistent, remaining below 1,4 p.u. up to $u_w = 11{,}5\,\mathrm{m/s}$.

The transient response of the SS-PMG to the balanced Irish voltage dip with PAC-LVRT compensation at $u_w = 11\,\mathrm{m/s}$ is shown in Fig. 5.20.

Although the instantaneous phase current in Fig. 5.20(b) shows the same initial fault response as in the PM-LVRT case, the compensation removal transients are smaller and of shorter duration. The PM-rotor speed in Fig. 5.20(c) also shows less disruption during compensation removal than is the case with PM-LVRT. The biggest change, though, is in the rotor angle response, shown in Fig. 5.20(d). After the initial transients subside, the rotor angle deviation is, on average, 20 ° less with PAC-LVRT than in the PM-LVRT case. This results in a final step of 6,74 ° instead of 21,66 °.

In comparison with pre-set power mapping, the phase angle control approach delivers significant improvements in rotor angle stability and removal current transients. Performance under balanced Irish fault conditions with steady wind speeds has been shown to be satisfactory, with the exception of winds

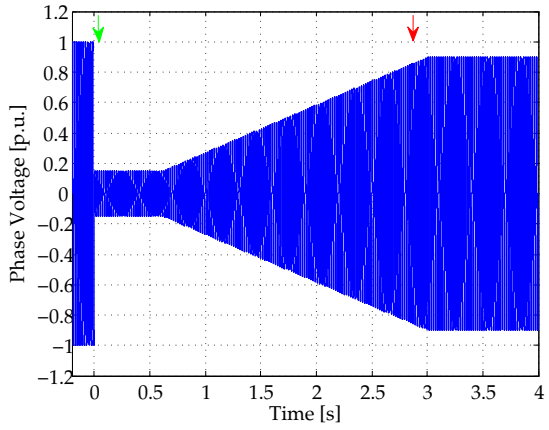

(a) Instantaneous phase voltage at the PCC as a function of time

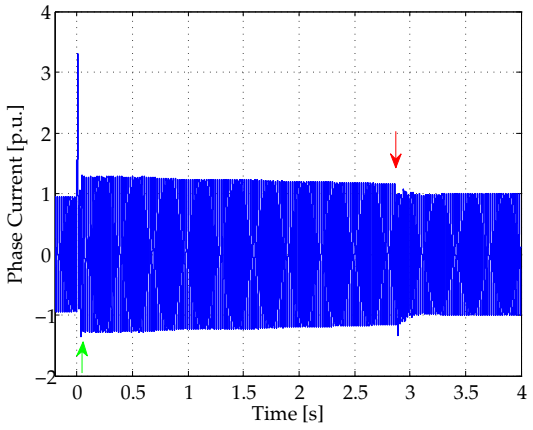

(b) Instantaneous SS-PMG phase current as a function of time

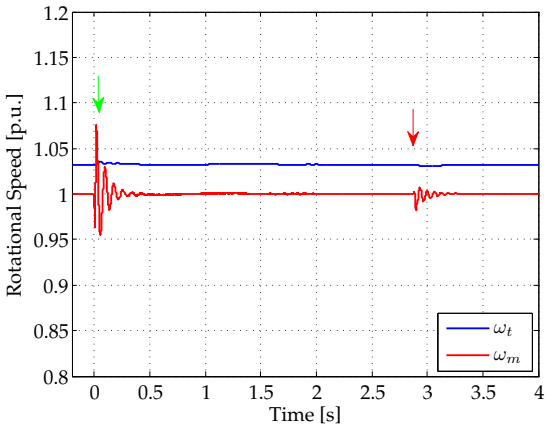

(c) Turbine and PM-rotor speed as a function of time

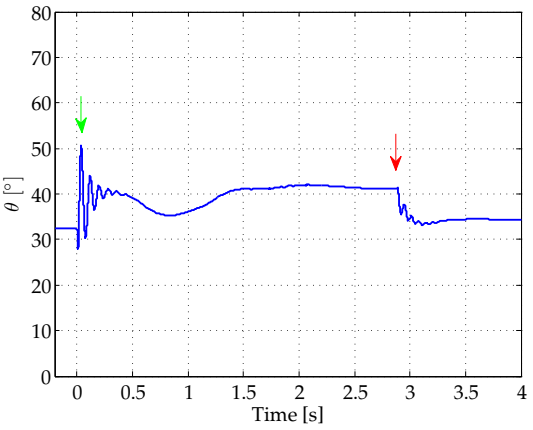

(d) SS-PMG rotor angle as a function of time

Figure 5.20: Transient response of the SS-PMG with PAC LVRT compensation to the balanced Irish voltage dip profile at a steady wind speed of $u_w = 11\,\mathrm{m/s}$. Green arrows indicate compensation insertion and red arrows indicate compensation removal.

above 11,8 m/s. To validate the wider applicability of PAC-LVRT, it is necessary to investigate other faults and wind conditions.

Performance of PAC-LVRT compensation when exposed to the balanced South African voltage dip profile is compared to that achieved under the Irish profile in Fig. 5.21. In the active compensation range of 8,6 m/s $\leq u_w \leq$ 11,8 m/s, the dynamic response to the South African fault is very similar to that for the Irish profile. The uncompensated response at lower wind speeds is not as successful.

The rotor angle plot in Fig. 5.21(a) shows that the uncompensated SS-PMG becomes unstable for $u_w \leq 5$ m/s. This is a result of a significant difference between the South African and Irish fault profiles: even though the South African profile recovers more quickly, it initially drops to 0 p.u., whereas the Irish profile only descends to 0,15 p.u.

The complete short circuit in the South African case also results in consistently higher initial fault currents across the wind speed range, as shown in Fig. 5.21(b). The maximum in-fault current is higher in the uncompensated range as well, but closely matches the Irish case under compensation (Fig. 5.21(c)).

Fig. 5.21(d) shows that, apart from a spike at $u_w = 8{,}6$ m/s, the removal currents with the South African profile closely match those achieved with the Irish profile. Together with the previously discussed observations, this indicates that active PAC-LVRT compensation is nearly as effective for the South African voltage dip as it is for the Irish version. The uncompensated response of the SS-PMG is not satisfactory, though.

By imposing a total short circuit, the South African dip profile temporarily disconnects the SS-PMG from the grid. Without control intervention, the SS-PMG cannot consistently maintain synchronism through such a fault, especially with very low or turbulent wind. A redesign of the compensation approach will thus be necessary to achieve LVRT across the wind speed range for the South African voltage dip profile.

In contrast, Fig. 5.21 indicates that the controlled ride-through achieved at rated wind speed is almost identical between the two dip profiles. Fig. 5.22 shows that the transient response for the South African case under these conditions is very similar to those for Irish case in Fig. 5.20. Discernible differences are limited to higher initial transients due to the deeper dip and marginally higher rotor angle deviation.

The PAC-LVRT strategy meets the compensation objectives for the Irish dip profile under steady wind conditions up to $u_w = 11{,}8$ m/s. At higher wind speeds, turbine torque is too high without any form of aerodynamic torque limitation. The South African voltage dip profile is problematic at low wind speeds, where compensation is not active, but PAC-LVRT can compensate successfully in its operational wind speed range. When compensation is active, the results obtained for the two profiles are very similar.

5.6.2.3 Phase Angle Control: Turbulent Wind Compensation

It has been shown conclusively that PAC-LVRT provides sufficient compensation under steady, predictable wind speeds but realistic wind conditions introduce additional dynamic changes in turbine torque. The control loop is designed to accommodate such variations and the following examples illustrate its effectiveness.

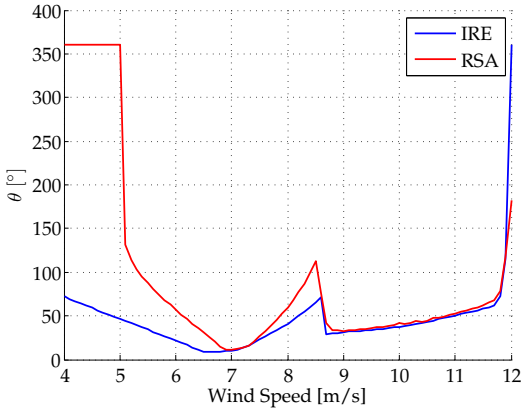

(a) Maximum rotor angle as a function of steady wind speed

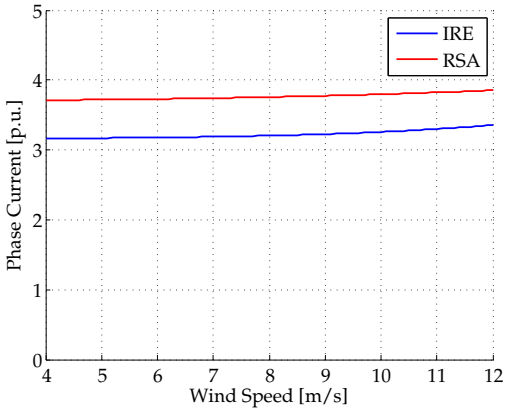

(b) Maximum instantaneous phase current at fault initiation as a function of steady wind speed

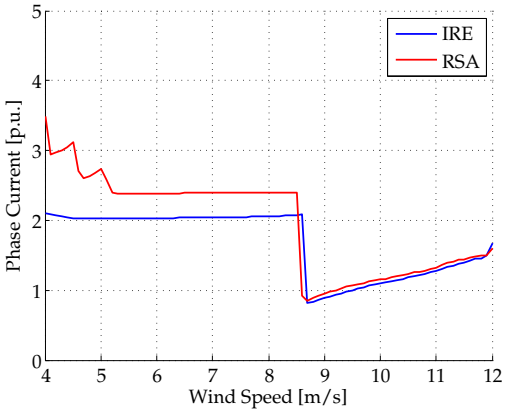

(c) Maximum instantaneous phase current during compensation as a function of steady wind speed

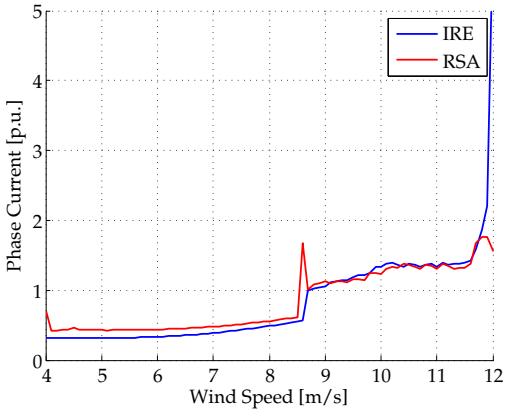

(d) Maximum instantaneous phase current during resistance removal as a function of steady wind speed

Figure 5.21: Comparison of PAC LVRT compensation for Irish and South African balanced voltage dip profiles across the operational wind speed range.

In the first turbulent wind case, shown in Fig. 5.23, the balanced Irish voltage dip is employed. Fig. 5.23(a) indicates that the turbine is exposed to wind gusts that exceed the rated operational range of the WECS. Nonetheless, the PAC-LVRT compensator is able to maintain stability throughout the fault.

Fig. 5.23(d) shows that θ never exceeds 120 °, even though the strong wind does cause it to deviate more than what was recorded in the steady wind scenarios. PM-rotor speed also oscillates more than under steady conditions, as can be seen in Fig. 5.23(c), but remains stable at all times.

After the initial current spike, instantaneous current remains well below 2 p.u. and the resistance removal transients are small and short-lived compared to the longer-term variations caused by the changing wind conditions (Fig. 5.23(b)).

In the second turbulent case, a gradually dropping wind time series, depicted in Fig. 5.24(a), is employed. Fig. 5.24(b) shows that in-fault current is well controlled and removal transients are again short-lived. Deviations in rotational speed are even less substantial (Fig. 5.24(c)) and rotor angle stability is ensured throughout the fault and recovery period, as shown in Fig. 5.24(d). The θ step at compensation

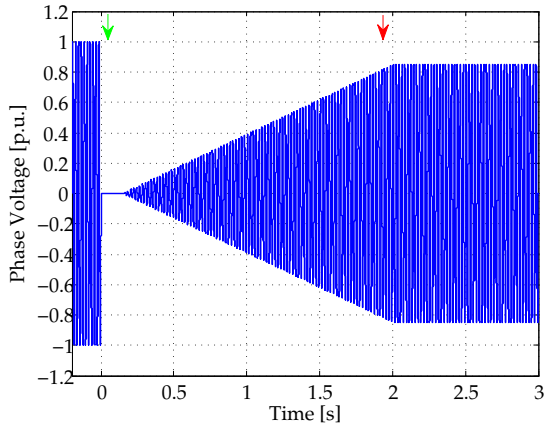

(a) Instantaneous phase voltage at the PCC as a function of time

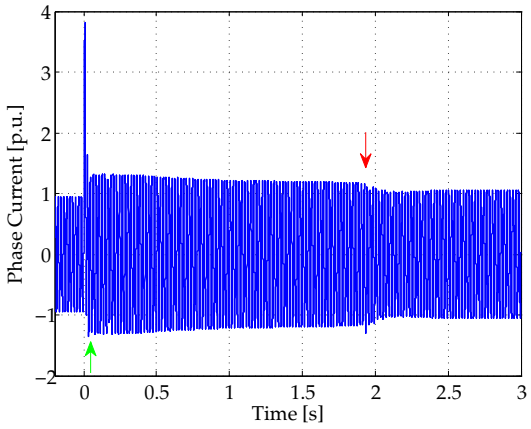

(b) Instantaneous SS-PMG phase current as a function of time

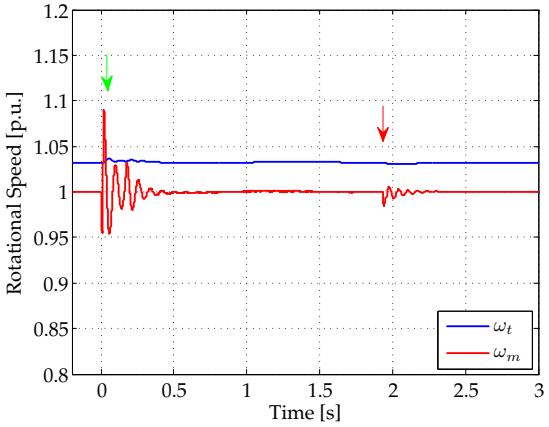

(c) Turbine and PM-rotor speed as a function of time

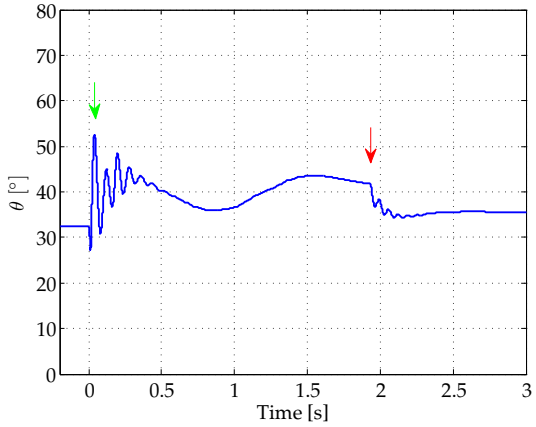

(d) SS-PMG rotor angle as a function of time

Figure 5.22: Transient response of the SS-PMG with PAC LVRT compensation to the balanced South Africa voltage dip profile at a steady wind speed of $u_w = 11\,\mathrm{m/s}$. Green arrows indicate compensation insertion and red arrows indicate compensation removal.

removal is negligible in this case.

The final turbulent wind example involves the balanced South African dip profile applied while wind speed rises towards rated value, as indicated in Fig. 5.25(a). The transient current at fault initiation, shown in Fig. 5.25(b) is higher, as expected, but average current during the rest of the fault and recovery period is well controlled.

Both PM-rotor speed and rotor angle (see Fig. 5.25(c) and Fig. 5.25(d)) show some slow oscillation, resulting from the changing wind speed, but remain within acceptable limits. The resistance removal transients are larger than for steady wind conditions but are comparable to the first two turbulent examples employing the Irish voltage dip.

Although it is not practical to simulate LVRT compensation under every possible set of turbulent wind conditions, the examples shown here do constitute relatively challenging cases. In all three, rotor angle stability and transient current limitation was achieved. Additionally, compensation removal tran-

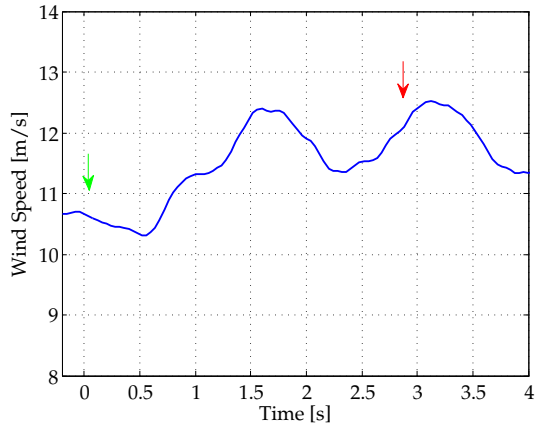

(a) Turbine-sampled wind speed as a function of time

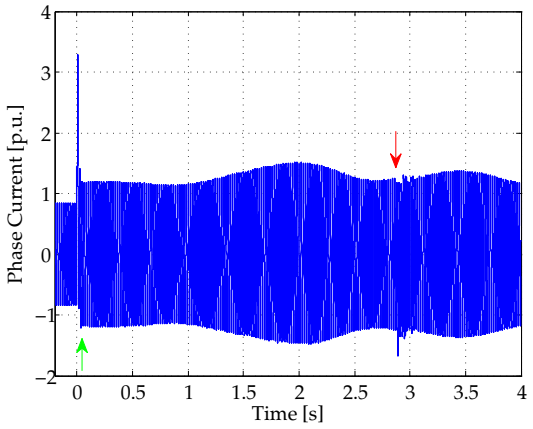

(b) Instantaneous SS-PMG phase current as a function of time

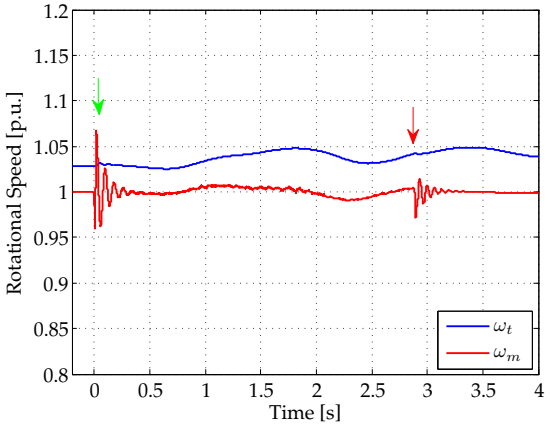

(c) Turbine and PM-rotor speed as a function of time

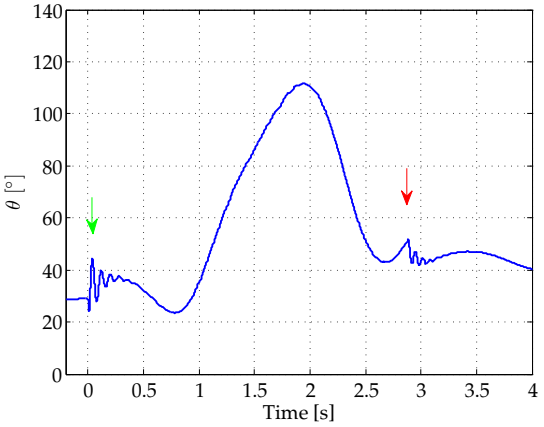

(d) SS-PMG rotor angle as a function of time

Figure 5.23: Transient response of the SS-PMG with PAC LVRT compensation to the balanced Irish voltage dip profile under turbulent wind conditions with $U_w = 11\,\mathrm{m/s}$. Green arrows indicate compensation insertion and red arrows indicate compensation removal.

sients were consistently better than what was observed for pre-set thyristor loading under steady wind conditions. On the whole, PAC-LVRT has proven successful under a wide range of wind conditions for symmetrical voltage dips following both Irish and South African profiles.

5.6.2.4 Phase Angle Control: Compensation of Unbalanced Faults

Unbalanced faults are more common in practice than the balanced voltage dips investigated thus far. They also pose different challenges. To begin with, asymmetrical loading results in uneven current flow between generator phases, which can lead to more severe transients even though total torque is less affected than in balanced faults. The voltage and current imbalances also violate the assumptions made in formulating the $\alpha\beta$ space-vector equations that are instrumental in system condition monitoring. This implies that the compensation algorithms may not function as intended.

The transient response of the SS-PMG to an unbalanced fault with PAC-LVRT is shown in Fig. 5.26.

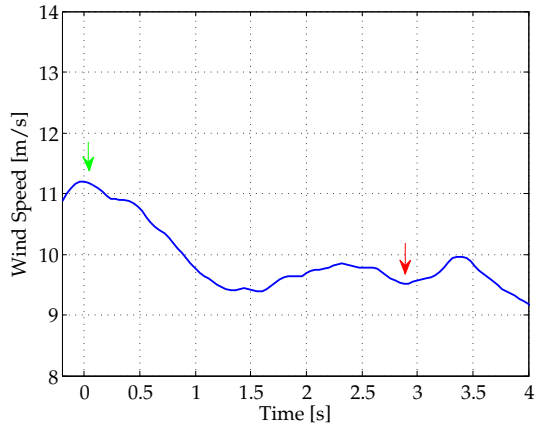

(a) Turbine-sampled wind speed as a function of time

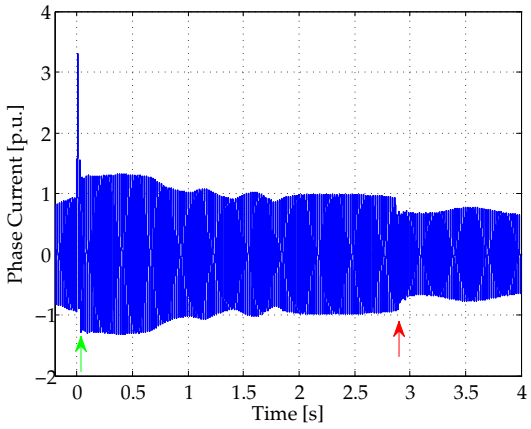

(b) Instantaneous SS-PMG phase current as a function of time

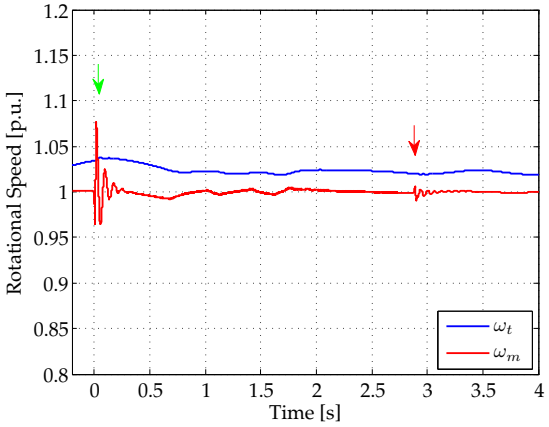

(c) Turbine and PM-rotor speed as a function of time

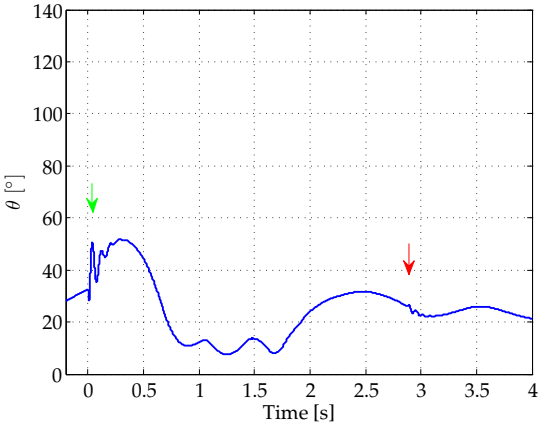

(d) SS-PMG rotor angle as a function of time

Figure 5.24: Transient response of the SS-PMG with PAC LVRT compensation to the balanced Irish voltage dip profile under turbulent wind conditions with $U_w = 10\,\text{m/s}$. Green arrows indicate compensation insertion and red arrows indicate compensation removal.

The voltage dip is the transformed version of a single phase-to-ground fault depicted in Fig. 5.2(b) and the faulted phases follow the South African dip profile. Wind conditions are turbulent, using the same time series as in Fig. 5.25 for comparative purposes.

Fig. 5.26(b) shows that v_a is unaffected by the fault, which implies that higher fault currents will occur on the other phases. The close-in view of voltage waveforms in Fig. 5.26(c) illustrates how v_b and v_c each experience a 30 ° phase angle shift along with magnitude reduction. It is also clear that compensation is disengaged substantially earlier than in the balanced fault case: at $t = 0{,}708\,\text{s}$ instead of at $t = 1{,}928\,\text{s}$. This is a result of the inaccuracy of $\alpha\beta$ voltage magnitude determination under asymmetrical conditions. The $\alpha\beta$ approach lumps the effect of all three phase values into a single magnitude, thus allowing compensation removal even though the RMS values of v_b and v_c are less than 0,25 p.u.

The effect of early compensation removal is depicted in Fig. 5.26(d), which shows a sustained over-current on phase B after $t = 0{,}708\,\text{s}$. The unbalanced over-currents after compensation removal are part

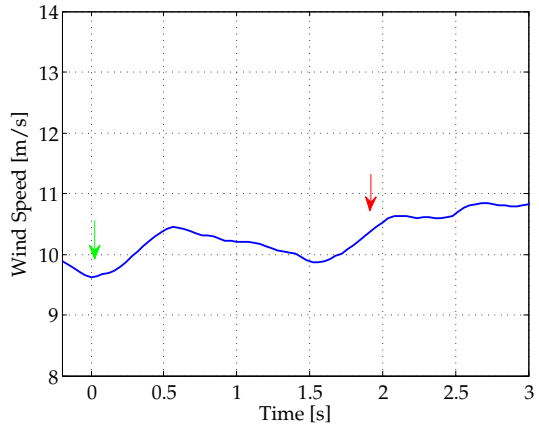

(a) Turbine-sampled wind speed as a function of time

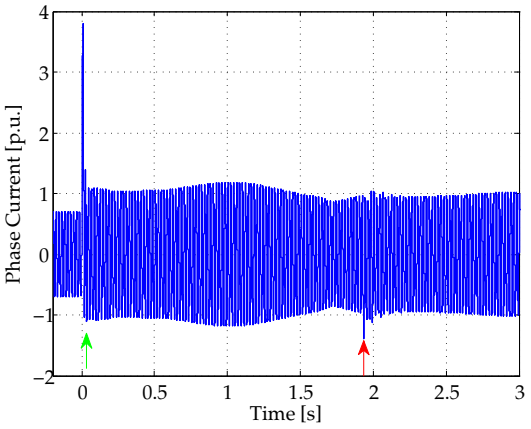

(b) Instantaneous SS-PMG phase current as a function of time

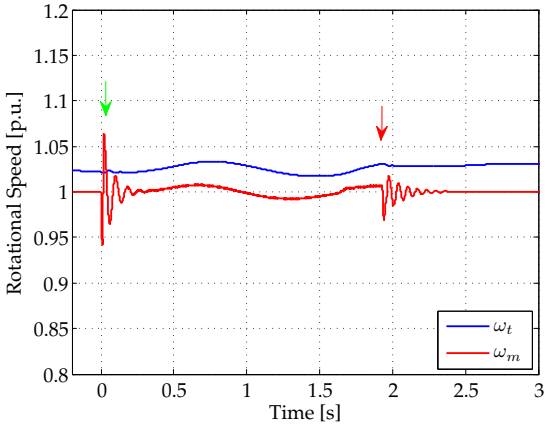

(c) Turbine and PM-rotor speed as a function of time

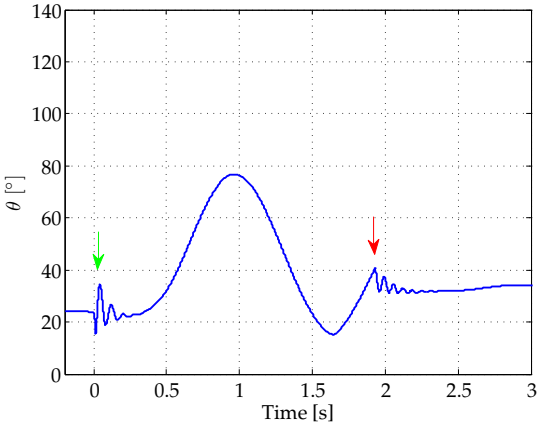

(d) SS-PMG rotor angle as a function of time

Figure 5.25: Transient response of the SS-PMG with PAC LVRT compensation to the balanced South African voltage dip profile under turbulent wind conditions with $U_w = 10\,\text{m/s}$. Green arrows indicate compensation insertion and red arrows indicate compensation removal.

of the natural response of the SS-PMG to an asymmetrical fault. Although the current levels are below the tolerance margin of 3 p.u., sustained operation under these conditions could be damaging to the generator.

The PM-rotor speed shows high-frequency oscillations in Fig. 5.26(e) as a result of direct exposure to the unbalanced fault. The electrical rotor angle does not, however, undergo significant deviations so the fault current levels and oscillations do not lead to a loss of stability (Fig. 5.26(f)).

To delay compensation removal it is necessary to supplement the grid voltage monitoring function with a component that takes the magnitude of each phase voltage into account separately. One option is to employ the per-phase RMS voltage calculation originally discussed in Section 2.1.2. It would then be possible to change the compensation insertion and removal conditions to monitor both combined ($\alpha\beta$) grid voltage and individual (RMS) phase values. Compensation would then be initiated if even one phase experienced a sufficient RMS voltage drop and removal would only take place if the RMS voltage

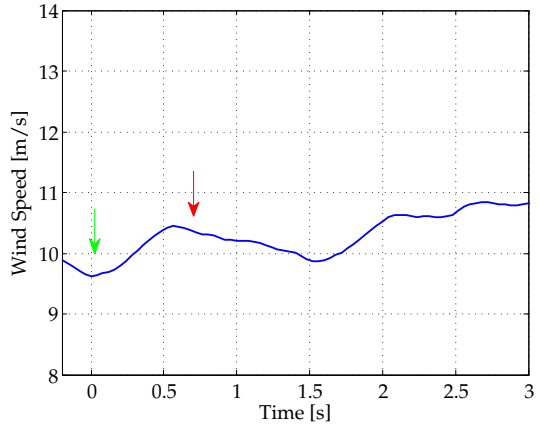

(a) Turbine-sampled wind speed as a function of time

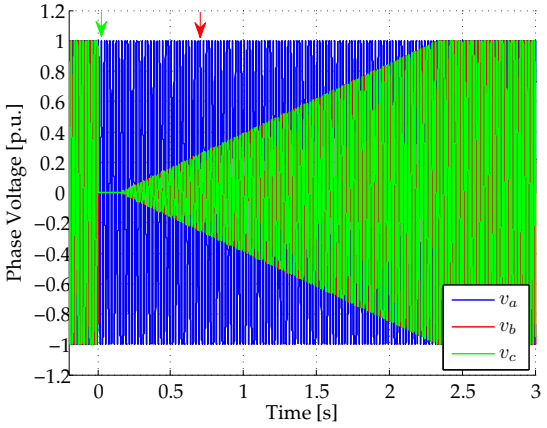

(b) Instantaneous phase voltage at the PCC as a function of time

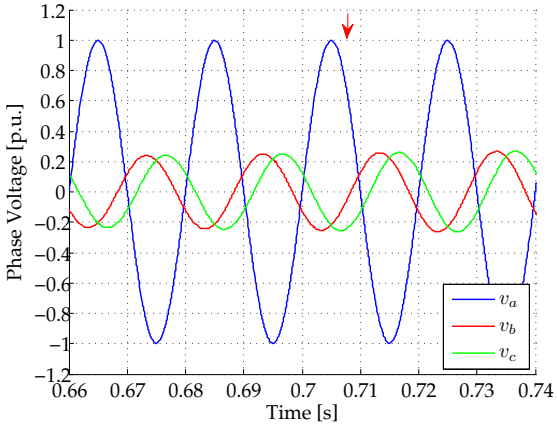

(c) Close-up view of instantaneous phase voltage at the PCC as a function of time

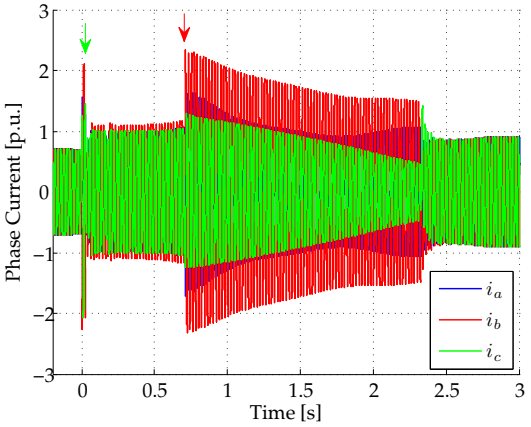

(d) Instantaneous SS-PMG phase current as a function of time

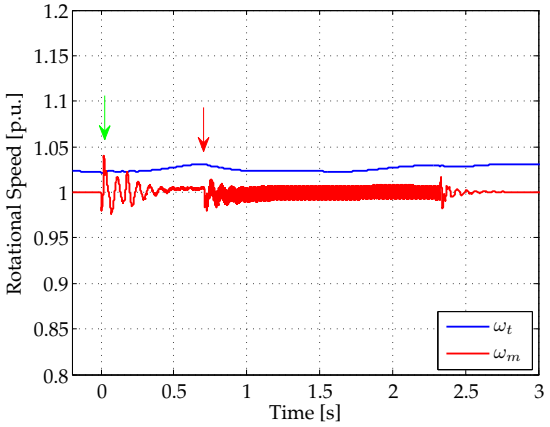

(e) Turbine and PM-rotor speed as a function of time

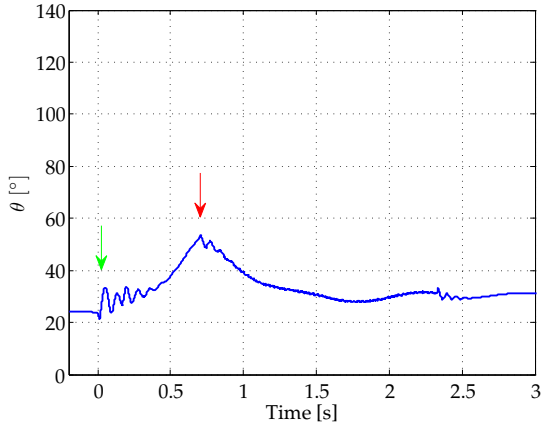

(f) SS-PMG rotor angle as a function of time

Figure 5.26: Transient response of the SS-PMG with PAC-LVRT compensation (no RMS monitoring) to the unbalanced South African voltage dip profile under turbulent wind conditions with $U_w = 10\,\mathrm{m/s}$. Green arrows indicate compensation insertion and red arrows indicate compensation removal.

of each phase exceeded the chosen minimum.

The result such a per-phase monitoring strategy is illustrated in Fig. 5.27. The same grid and wind conditions are employed as in Fig. 5.26 but compensation removal can only take place once all phase voltages have recovered to a minimum level of 0,8 p.u. for South African specifications. Fig. 5.27(b) and Fig. 5.27(c) indicate the removal time has changed to $t = 1{,}955\,\text{s}$, which is in line with the balanced fault scenario.

The phase current response with later removal is less severe and the period of over-current is shorter, as depicted in Fig. 5.27(d). The same change is visible in Fig. 5.27(e) for PM-rotor speed, which undergoes a short period of oscillation before the fault is completely cleared at $t = 2{,}33\,\text{s}$. This ensures better protection for the SS-PMG and less chance of over-heating or demagnetisation.

The performance difference achieved by delaying compensation removal for unbalanced faults is summarised in Fig. 5.28. PAC-LVRT compensation is employed across the steady wind speed range for all four possible cases: with and without RMS monitoring for both the Irish and South African voltage dip profiles.

In terms of rotor angle stability, Fig. 5.28(a) shows that employing RMS monitoring renders up to a $10\,^\circ$ improvement around rated wind speed. The stable operating ranges are, nonetheless, identical in all four cases. Initial fault current, as previously evidenced, is not affected by the chosen control strategy. Wind speed and voltage dip severity do have an effect on fault current, as indicated in Fig. 5.28(b), but the worst recorded value is only half the 5 p.u. limit.

The maximum in-fault current (across all phases) does benefit from PAC-LVRT compensation, as values in the uncompensated wind speed range are significantly higher in Fig. 5.28(c). No measurable improvement is achieved by employing RMS monitoring, though. In contrast, the resistance removal current is consistently lower when RMS monitoring is employed in the active compensation range (Fig. 5.28(d)). The maximum values recorded in the uncompensated wind speed range indicate where removal would have taken place in these cases: RMS monitoring delays removal till later in the fault, when currents are lower.

The advantage achieved by RMS monitoring is that compensation removal is delayed until grid voltage is nearer to complete restoration. This reduces unwanted current transients in the SS-PMG, as can be seen by comparing Fig. 5.26 and Fig. 5.26. Although removal currents and rotor angle deviations are reduced, these improvements do not increase the stable operating range, as shown in Fig. 5.28.

In conclusion, the addition of per-phase RMS monitoring improves the operation of PAC-LVRT compensation during asymmetrical faults, however, this improvement is not essential since protection requirements can be met without it. The choice to implement the additional monitoring then depends on the available processing capabilities in the controller. If the MCU is capable of supporting the extra computational burden then RMS monitoring will improve generator protection but the omission thereof will not compromise the stability of the SS-PMG during faults.

PAC-LVRT compensation has proven capable of supporting the SS-PMG during most fault conditions. It is able to achieve the protection objectives outlined at the beginning of this chapter up to $u_w = 11{,}8\,\text{m/s}$. The natural response of the SS-PMG does, however, become unstable for $u_w \leq 5\,\text{m/s}$

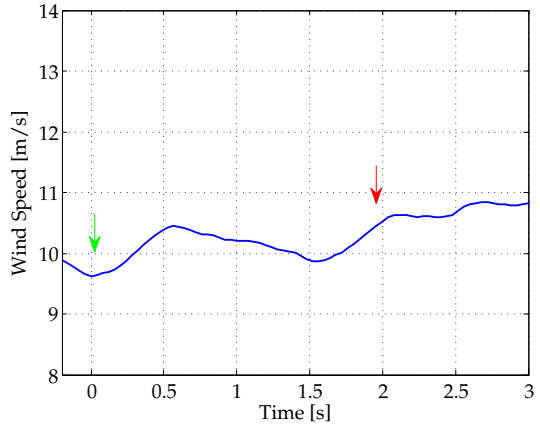

(a) Turbine-sampled wind speed as a function of time

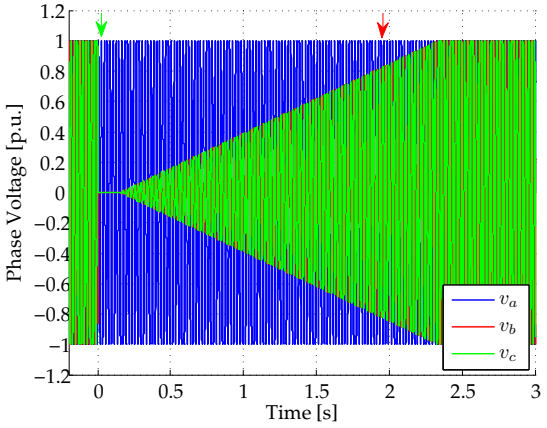

(b) Instantaneous phase voltage at the PCC as a function of time

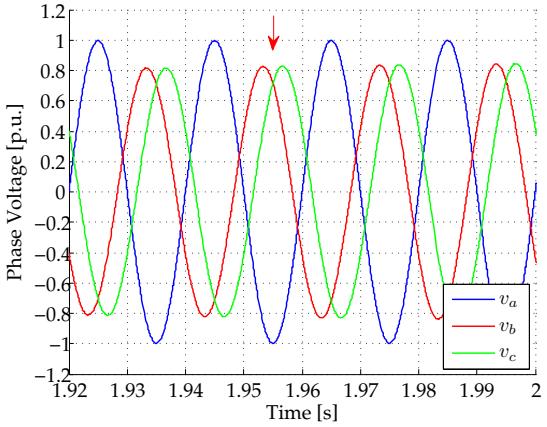

(c) Close-up view of instantaneous phase voltage at the PCC as a function of time

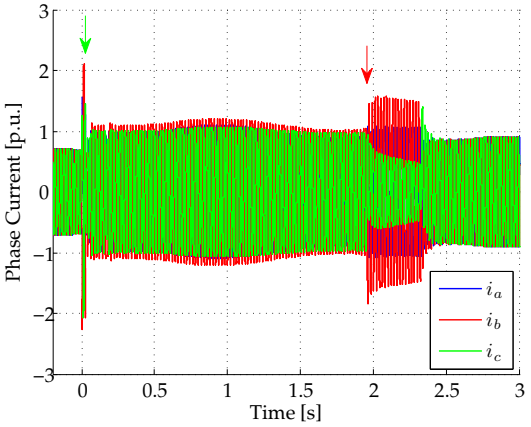

(d) Instantaneous SS-PMG phase current as a function of time

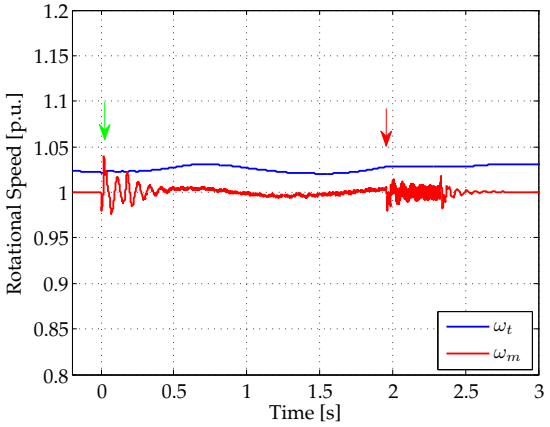

(e) Turbine and PM-rotor speed as a function of time

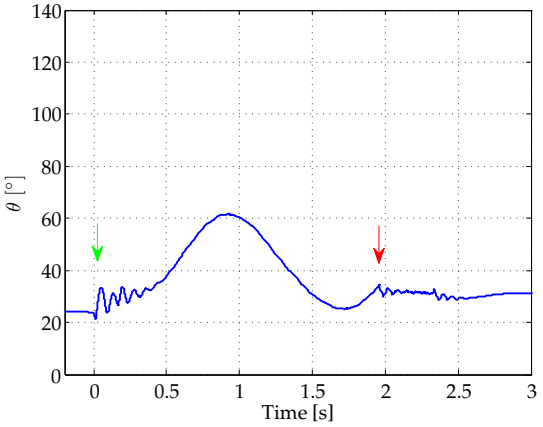

(f) SS-PMG rotor angle as a function of time

Figure 5.27: Transient response of the SS-PMG with PAC-LVRT compensation with RMS monitoring to the unbalanced South African voltage dip profile under turbulent wind conditions with $U_w = 10\,\mathrm{m/s}$. Green arrows indicate compensation insertion and red arrows indicate compensation removal.

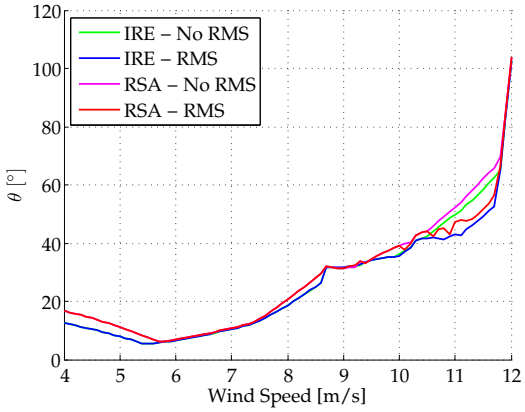

(a) Maximum rotor angle as a function of steady wind speed

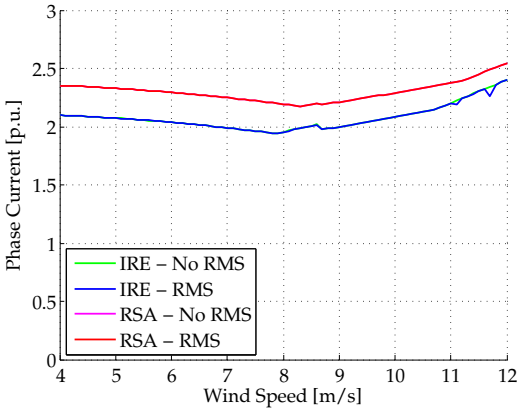

(b) Maximum instantaneous phase current at fault initiation as a function of steady wind speed

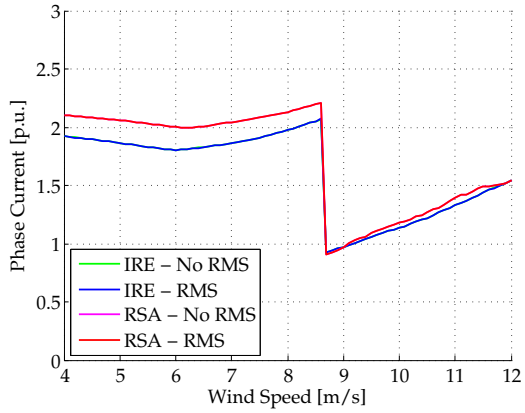

(c) Maximum instantaneous phase current during compensation as a function of steady wind speed

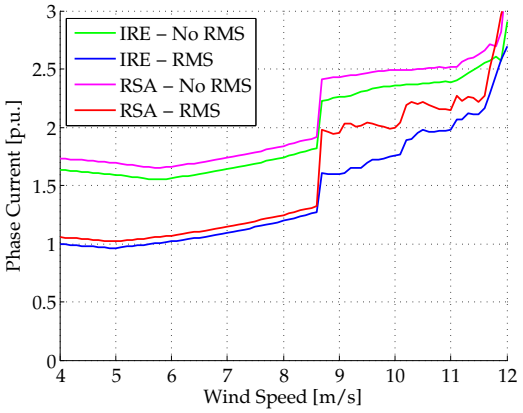

(d) Maximum instantaneous phase current during resistance removal as a function of steady wind speed

Figure 5.28: Comparison of PAC LVRT compensation with RMS monitoring for Irish and South African unbalanced voltage dip profiles across the operational wind speed range. The imposed fault is the transformed version of a single phase-to-ground fault, shown in Fig. 5.2(b). Current values are maxima from across all three phases to account for unbalanced conditions.

when the balanced South African voltage dip profile is employed. This will require a revision of the control strategy since the instability does not manifest under the Irish dip profile, which was the original test case for the compensator design.

Although the PAC-LVRT meets the original control objectives, it cannot provide controlled reactive power compensation to the faulted network, which is a requirement in most grid codes. This capability will require the addition of a controllable reactive power compensation element, which is beyond the scope of this investigation.

5.7 Summary

This chapter presented the development of a low voltage ride-through compensator for the SS-PMG WECS. After the grid code requirements were investigated and defined for this investigation, protection

objectives were established and the basic compensator design was introduced. It was found that the uncompensated SS-PMG remains within the prescribed dynamic limits when exposed to the Irish fault profile at lower wind speeds. As a result, compensation was focused on the wind speed range above $u_w = 8\,\mathrm{m/s}$.

It was shown that compensation using either a series resistance or a shunt braking resistance cannot meet the required objectives under different wind speeds. Combining the series and shunt resistances achieves better results, but the braking resistance needs to be varied (by using switching in different resistances) to operate successfully across the whole wind speed range.

To overcome the need for multiple braking resistance values, the thyristor switching mechanism first employed in speed control has been re-introduced. By setting the firing delay angle of the thyristors, it is possible to compensate for grid faults across the steady wind speed range. However, disturbances caused when removing the resistances remain a problem and turbulent wind conditions can still result in instability.

By regulating the phase angle difference between the SS-PMG terminal voltage and the PGC voltage during faults, it is possible to reduce the transients experienced at compensation removal. In addition, the closed-loop control can compensate for changes in turbine torque resulting from turbulent wind conditions. Although it was not part of the original design specifications, the South African voltage dip profile can also be accommodated by the PAC-LVRT.

Unbalanced faults were also investigated and were found to reduce the accuracy of the original grid voltage monitoring function. The addition of per-phase RMS voltage monitoring raises reliability to the same level achieved during balanced faults. Employing this enhancement reduces unbalanced current transients and is recommended for implementation in the LVRT component of the GCC.

The proposed LVRT compensation approach is capable of meeting the original protection objectives under a variety of wind and grid fault conditions. Further improvement of the compensator could come in the form of reactive power control, both to meet grid code requirements and to allow the SS-PMG to produce more torque so that higher wind speed conditions can be accommodated. The compensation approach under low wind speeds should also be re-evaluated to handle the South African dip profile more effectively.

CHAPTER 6

GCC IMPLEMENTATION

Following the theoretical outcomes of Chapter 4 and Chapter 5, this chapter describes the realisation of the GCC for the purposes of laboratory and field testing. The implementation process involves both hardware and software development. The description begins with the major hardware components, after which the programming of the controller MCU is detailed. Finally, specific challenges experienced during the implementation and testing process are discussed.

6.1 Hardware

The line diagram of the GCC is reproduced in Fig. 6.1. One change over previous representations is that a second contactor, switching in a capacitor bank, has been added under the label S1. This is to improve the emergency braking capabilities of the SS-PMG without interfering with the normal operation of the thyristor braking circuit. The capacitor bank increases available SS-PMG torque by providing reactive power compensation to counteract the effect of the relatively high stator inductance.

Another change is that the two switches constituting S1 are normally closed. This is a fail-safe measure to protect the turbine and generator during controller power failure. In such a case, the SS-PMG will be automatically disconnected from the grid and switched on to the braking load to prevent runaway of the turbine.

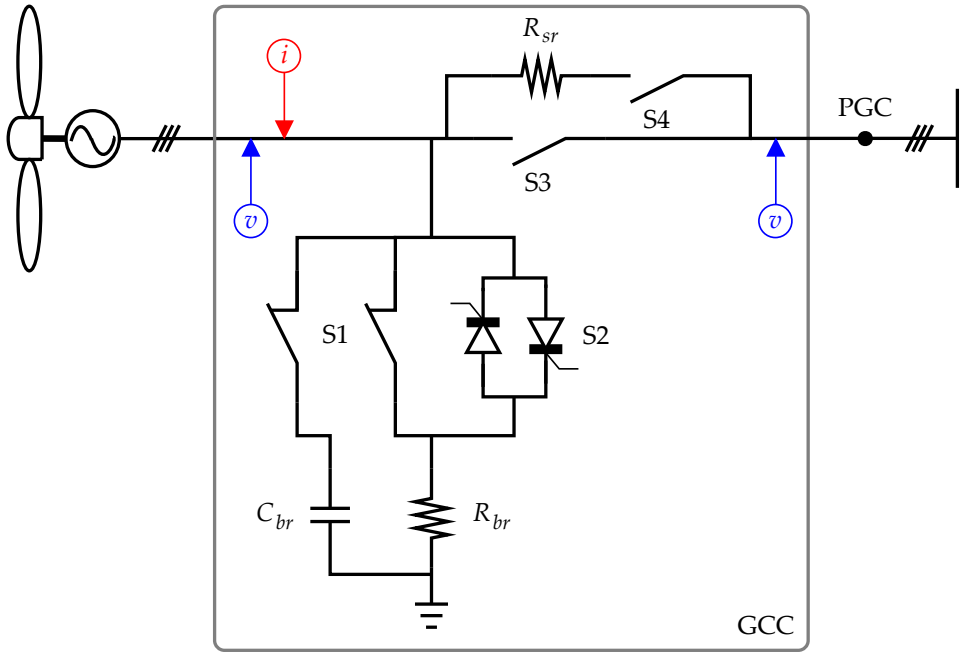

Figure 6.1: Single line diagram of the GCC. Instantaneous voltage and current samples taken by the GCC are indicated by blue and red arrows, respectively.

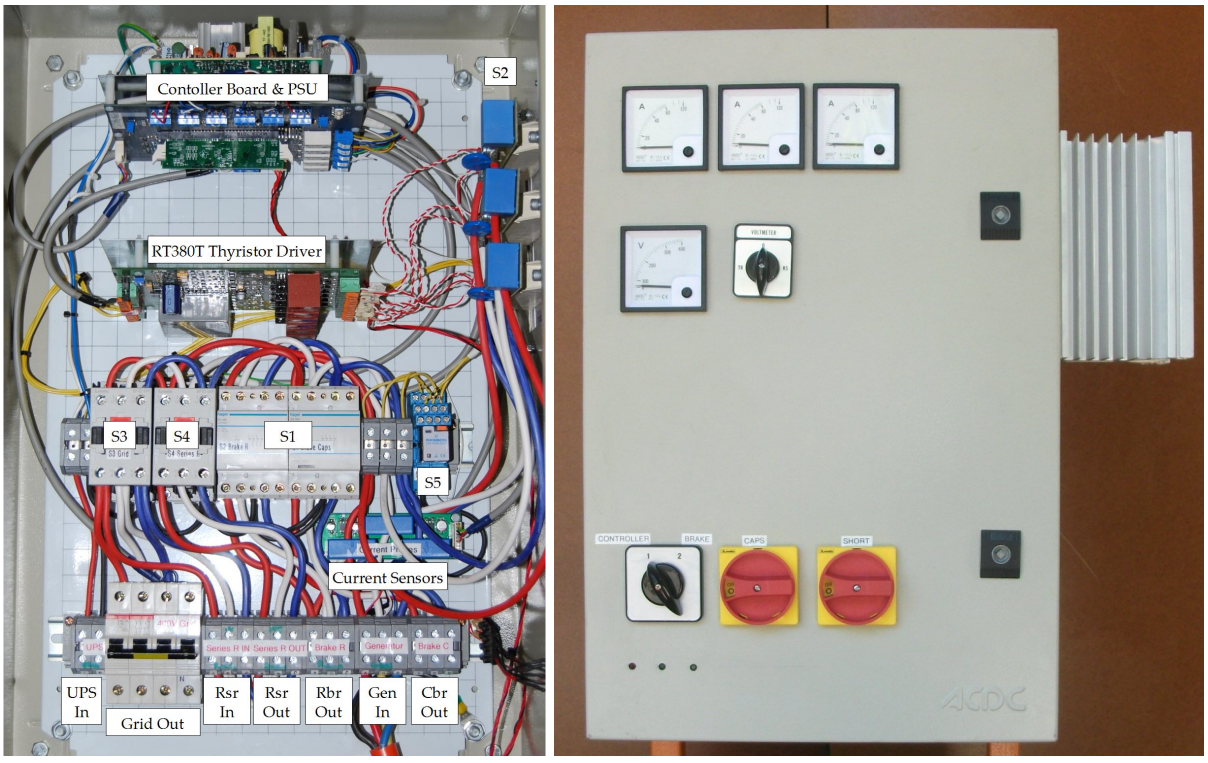

(a) GCC interior

(b) GCC exterior with monitoring dials and cut-out switches

Figure 6.2: Interior and exterior views of the GCC cabinet, including the thyristors, heatsink and driver.

The GCC cabinet, ready for field deployment, is shown in Fig. 6.2. The components installed inside the cabinet, illustrated in Fig. 6.2(a), include current sensors; electro-mechanical contactors; an AC-to-AC three-phase thyristor pack; a thyristor driver (firing angle controller); an MCU controller board (including voltage sensors); and an AC-DC power supply. The exterior of the latest generation GCC cabinet includes monitoring gauges and manual over-ride switches, shown inFig. 6.2(b). The heatsink for the thyristor pack is also visible on the right hand-side of the cabinet's exterior. The shunt braking resistor, AC capacitors, and series compensation resistor are housed separately, as discussed in Section 6.1.3.

In line with the aims of the project, off-the-shelf components are employed wherever possible. The only custom-made components in Fig. 6.2 are the controller board and the current sensor block. The most significant controller components mentioned here are discussed in further detail in the remainder of this section.

6.1.1 Controller Board

The controller board, shown in Fig. 6.3(a), is the most important purpose-built component in the GCC. It was developed for the author by downscaling the controller board used in the full-scale converter for a PMSG WECS. Because this board is a prototype design for testing purposes it makes use of a removable micro-controller. The Texas Instruments F28027 MCU is integrated into a controlCARD module that can easily be inserted and removed—see Fig. 6.3(b). This cuts development time by pre-packaging supporting circuitry and allows re-use of the MCU in revised versions of the controller board, or in

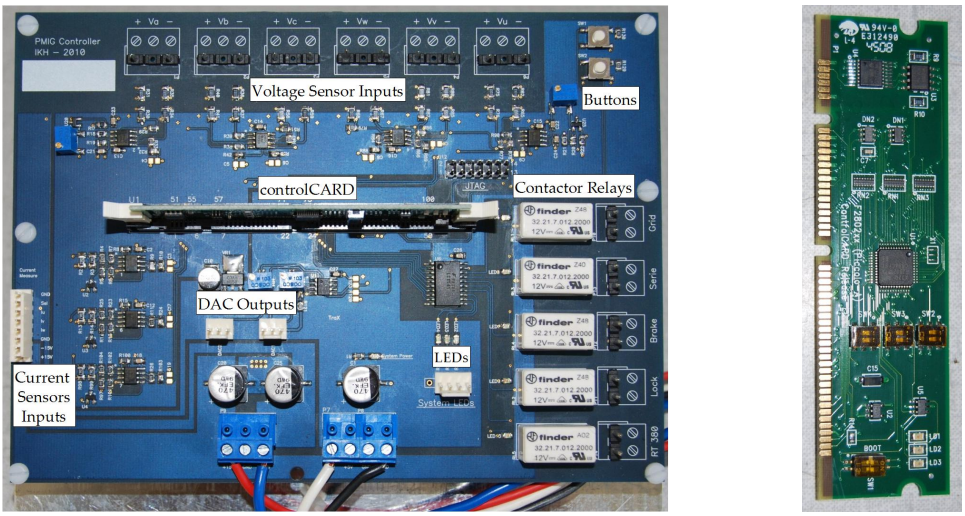

(a) GCC controller board on mounting plate with power cabling (b) ControlCARD

Figure 6.3: GCC controller board and plug-in Texas Instruments F28027 ControlCARD.

different projects altogether.

The TMS320F28027 *Piccolo* MCU is an entry-level 32-bit micro-controller that operates at 60 MHz. It features thirteen 12-bit ADC channels, eight PWM outputs, as well as configurable digital input-output pins. The pin layout can be customised, depending upon the functions required for a particular application. This reduces pin-count and cost but implies that not all features can be used simultaneously. To ensure that the MCU is not over-burdened, the ADC-sampling rate is set at 1 kHz.

As shown in Fig. 6.3(a), the controller board connects the MCU controlCARD to six phase voltage sensors; three phase current sensors; a two-channel DAC via SPI; and relays to control the electromechanical contactors. For user interface purposes, the board also hosts two push-buttons and three LEDs. Externally mounted LEDs can also be connected for easier status monitoring.

The controller board receives 5 V and ±15 V DC supplies from a Meanwell PT-65C PSU. The PSU is fed from an uninterruptible power supply mounted outside the GCC cabinet. It is estimated that the GCC can operate without a functional grid for an hour before shutting down into the fail-safe state described previously.

6.1.2 Thyristor Package

The three-phase back-to-back (W3C) thyristor stack employed in the GCC is sourced from Semikron. Based on three SKKT 27/16 *Semistack* modules, the W3C package has an RMS phase current rating of 35 A at a line voltage of 400 V. As illustrated in Fig. 6.4(a), the stack is pre-mounted on a passively cooled heat sink, which is installed outside the GCC cabinet for better air flow.

An RT380T thyristor trigger module, also from Semikron, produces the firing pulses to drive the thyristor stack. The RT380T, shown in Fig. 6.4(b) is a three-phase analogue thyristor driver which accepts a 0 V – 5 V input command to set the firing delay angle. When the command input is set to 0 V the delay angle is 180 ° and the thyristors do not fire. With an input of 5 V the delay angle is set to 0 ° and maximum

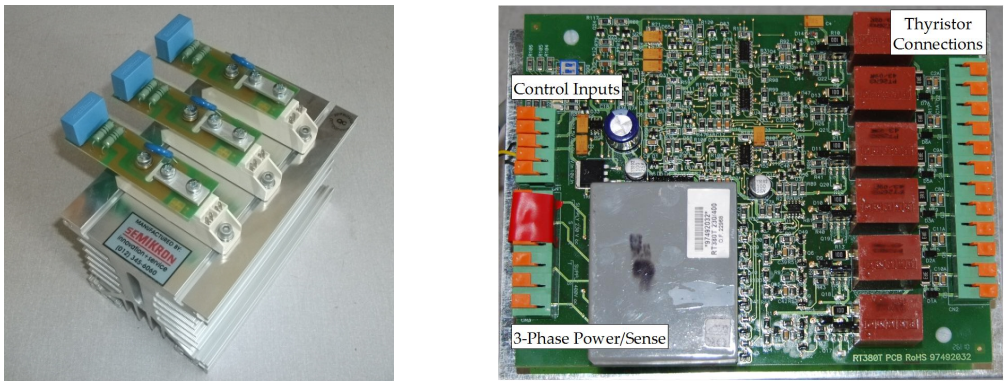

(a) Semikron W3C thyristor stack with heatsink

(b) Semikron RT380T thyristor driver

Figure 6.4: Semikron thyristor stack and driver.

current is transmitted. The command signal for the RT380T is generated by one of the DAC channels available on the controller board.

The RT380T is rated to operate at 340 V – 440 V line voltage with a supply frequency of 45 Hz – 65 Hz. Practical investigations revealed that it can operate successfully from 30 Hz ($f_{gen} = 0{,}6$ p.u.), which is thus the pre-set cut-in frequency for speed control operation. The RT380T samples the line voltages through its own three-phase power supply. To protect it from out-of-range voltages and frequencies, a relay, labelled S5 in Fig. 6.2(a), is used to engage the RT380T when the SS-PMG frequency is in the correct range.

6.1.3 Resistor Cage

The shunt braking resistance and series compensation resistance are both packaged in a self-standing resistor cage, shown in Fig. 6.5. Industrial heating elements, similar to those used in conventional ovens and hot water cylinders, are connected in parallel to form the loads. Multiple elements are used to give a margin of safety and allow passive cooling during the developmental stage. Later realisations may make use of smaller elements that are rated for a lower duty cycle

In addition to the resistors, AC capacitors, constituting C_{br}, are mounted in an add-on enclosure to the cage. The function of these capacitors is to boost SS-PMG counter-torque during emergency electromagnetic braking, as illustrated in Fig. 6.6. This is a safety provision to ensure the SS-PMG can brake the turbine at higher wind speeds. The capacitors are only engaged during emergency and maintenance conditions through switch S1. Separate contactors must be used for R_{br} and for C_{br} to isolate the capacitors from the thyristor circuit.

6.1.4 Costing

A preliminary cost comparison between a converter-fed PMSG WECS and the SS-PMG WECS is made in Table 6.1. A cost of 1 is assigned to the standard multi-pole PMSG used with a full-scale converter. This generator is effectively identical to the sync-side of the SS-PMG —see Fig. 3.6(a). All other component

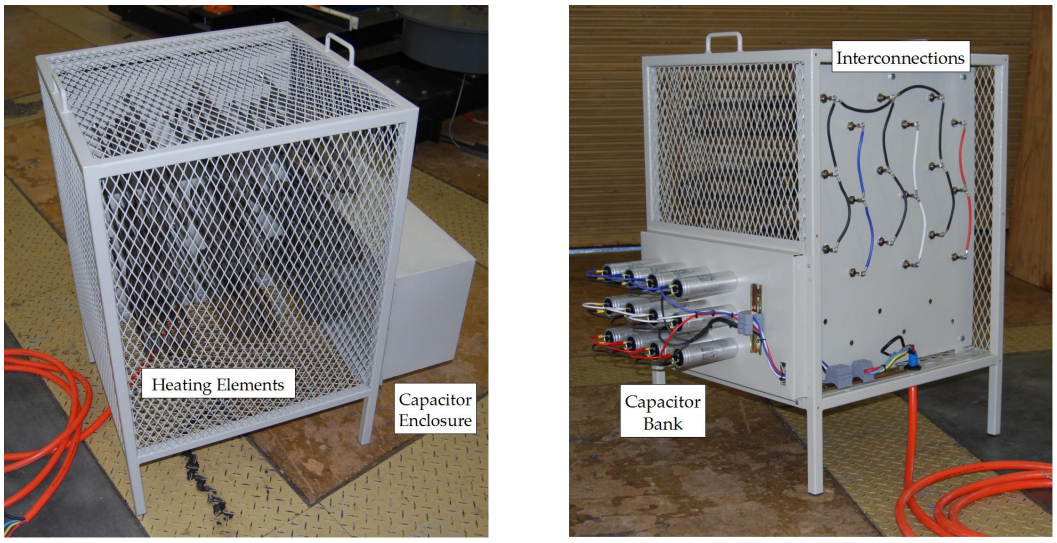

(a) Resistor cage - front view

(b) Resistor cage - open rear view

Figure 6.5: Views of the resistor cage, housing industrial heating elements and an AC capacitor bank. Provision is made for series compensation resistors in the bottom row of the cage, but these are not yet installed.

costs are scaled in comparison with this.

In both cases, the relatively high cost of the turbine and tower is evident but crucial differences emerge in two areas: the generator and the electronics. The GCC is substantially cheaper than a full-scale converter, reducing system cost by 0,89 p.u., despite a slightly higher cost for the dumping load.

On the other hand, the SS-PMG is more expensive to construct than a conventional PMSG. Since design optimisation is still under way, the final comparative cost for the SS-PMG is not yet known—a rough figure of 1,5 p.u. is listed, but with a significant margin of uncertainty.

The economic advantage of the SS-PMG WECS is not limited to investment cost, though. It also offers significant potential savings in O&M requirements. For example, the power electronics used with the SS-PMG are simpler, more robust, and less frequently used than those in a full-scale converter. As a

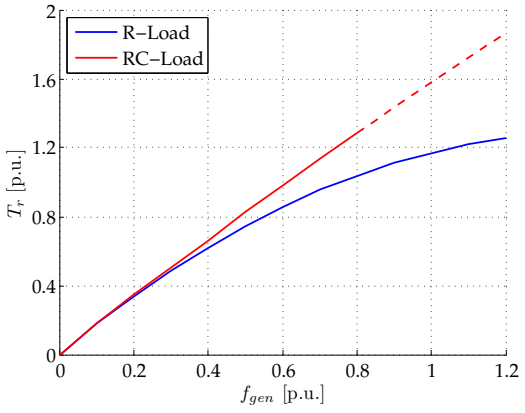

Figure 6.6: Emergency braking torque capacity of the SS-PMG with $R_{br} = 0{,}61$ p.u. and $C_{br} = 0{,}63$ p.u. The RC-load torque values for $f_{gen} > 0{,}8$ p.u. are extrapolated because they exceed the breakdown torque of the slip-rotor available at the time of testing.

Table 6.1: Comparative hardware costs for a converter-fed PMSG WECS and the SS-PMG WECS with GCC.

Subsystem	**Cost for PMSG WECS [p.u.]**	**Cost for SS-PMG WECS [p.u.]**
Turbine	0,94	0,94
Nacelle	0,25	0,25
Lattice Tower	1,09	1,09
Generator	1,00	$1{,}5 \pm 0{,}3$
Cabling	0,15	0,15
Control & Electronics	1,16	0,27
Dumping Load	0,12	0,13
Total	4,72	$4{,}34 \pm 0{,}3$

result, these components are less likely to require repair or replacement during the life of the WECS.

During faults it is the SS-PMG, rather than a frequency converter, that is first exposed to overloading. The SS-PMG can endure operation under fault conditions for longer than power electronics can, which implies a lower risk of hardware damage during faults. Should failures occur in the GCC, replacement of components will be easier than for a frequency converter due to simpler design and the use of commonly available, off-the-shelf components.

Despite these promising indications, considerable uncertainty remains in the costing and economics of the SS-PMG. The final word on the feasibility of an SS-PMG WECS will only be available after design optimisation of the generator is completed and extensive real-world testing has been conducted alongside a full-scale converter-fed WECS. Facilitating this comparison is a major goal of this work.

6.2 Programming

The MCU is programmed to interface with the I/O hardware and to execute monitoring, speed control, synchronisation, and protection functions. Programming of the TI F28027 MCU is conducted in C using the *Code Composer Studio* IDE. In this section, the most pertinent procedures and functions are described to provide an overview of the operation of the GCC.

6.2.1 Management Functions

At the highest level of the MCU program hierarchy are the functions that initialise the software environment and sequence all other functions, depending upon system conditions.

6.2.1.1 Initialisation and Sequencing

As illustrated by Fig. 6.7(a), the main function—listed in Appendix D.1.1—begins MCU operation from cold start by calling a number of support functions to set up the environment and initialise components such as the ADC, SPI, timers, and interrupts. Once main has called all the necessary initial functions, further operation of the MCU is interrupt-driven.

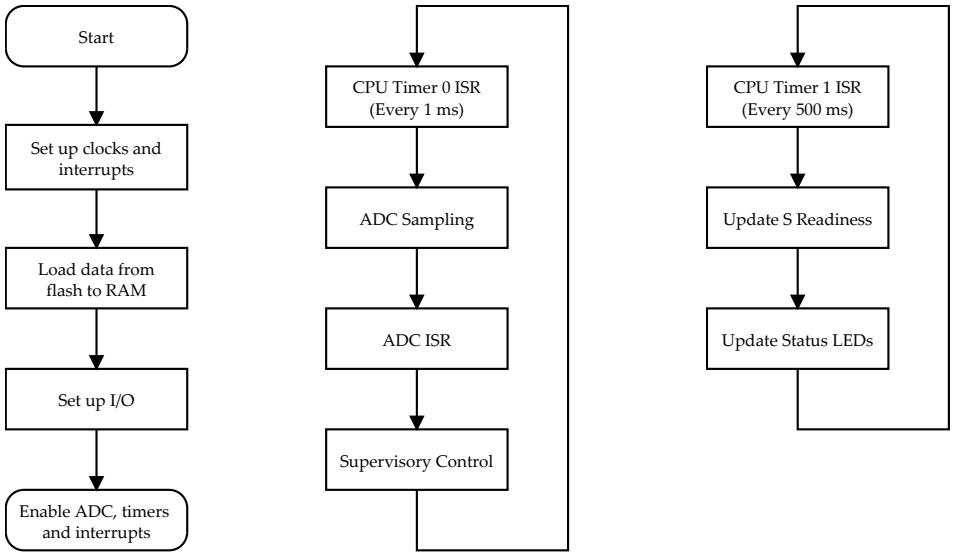

(a) main (b) CPU Timer 0 (c) CPU Timer 1

Figure 6.7: Flow diagrams for initialisation and program scheduling functions.

Two CPU timers are employed to regularly trigger the most important interrupts. The ADC sampling function is triggered by CPU Timer 0. Once sampling is completed, the ADC ISR is triggered. This, in turn, calls the supervisory control function, which is responsible for orchestrating all further monitoring and control actions. The process is repeated at 1 ms intervals, as indicated in Fig. 6.7(b).

In parallel with the primary interrupt loop, CPU Timer 1 triggers its own ISR every 0,5 s (Fig. 6.7(c)). This interrupt activates periodic updates of the status LEDs (allowing them to blink at 1 Hz when necessary) as well as an update of the contactor readiness counters. These timing counters are used to ensure that the electromechanical contactors are not switched at an excessive rate. The delay between actuations can be set individually for each contactor.

The ISRs discussed above are listed in Appendix D.1.2, along with two external interrupts for the user input push-buttons on the controller board. The functionality of these buttons can differ depending on the present application (for example: debugging, experimentation, in-field operation).

6.2.1.2 Supervisory Control

The supervisory control function (listed in Appendix D.1.3) is called once per interrupt cycle, after ADC sampling and conversion has occurred. It is responsible for facilitating comprehensive processing of the sampled voltage and current signals; determining the appropriate control mode; and calling the necessary control functions to facilitate either synchronisation or on-grid protection of the SS-PMG.

The supervisory function makes use of system state information stored in a C structure, which is updated each sampling period by different analysis functions. In this way, a central up-to-date information repository is available to all querying functions in the environment. This includes a selection of status flags and a six-bit error code, which can be used to inform the operator of recent system errors through the external LEDs. The C definition for the system status structure is shown below:

```
// System status structure:
struct stateStruct {
  Uint16 syncd      : 1;    // Is the SS-PMG synchronised?
  Uint16 VgridNom   : 1;    // Is grid voltage within nominal limits?
  Uint16 VgridErr   : 1;    // Is there a grid voltage fault?
  Uint16 FgridErr   : 1;    // Is there grid frequency fault?
  Uint16 gridOK     : 1;    // Are all grid conditions nominal?
  Uint16 goSync     : 1;    // 1 = enable sync / 0 = disable sync
  Uint16 goSpCn     : 1;    // 1 = enable speed control / 0 = disable speed control
  Uint16 goOnln     : 1;    // 1 = allow normal GCC operation / 0 = enforce shut down
  Uint16 gridOff    : 1;    // Has grid fault been present for > anti-islanding limit?
  Uint16 ovSpd      : 1;    // Has an over-speed event just occurred?
  Uint16 errCode    : 6;    // Error code
  };
```

A simplified flow diagram of the operation of the supervisory control function is displayed in Fig. 6.8. After determining the SS-PMG and grid conditions from analyses performed on the sampled signals, the supervisory control function checks whether the SS-PMG is synchronised, in which case on-grid protection functions are called. If the SS-PMG is not yet synchronised, then appropriate action is taken, based on f_{gen}. Below cut-in frequency, the turbine and SS-PMG are allowed to rotate freely. In the speed control band (0,6 p.u. $\leq f_{gen} \leq$ 1,3 p.u.) thyristor operation is engaged. If over-speed is detected then emergency braking is employed. These operational zones are depicted graphically in Fig. 6.11(a).

6.2.2 Analysis Functions

The analysis functions process data into forms that can be used by the control and protection routines.

6.2.2.1 Space Vector Analysis

The space vector analysis function, listed in Appendix D.2.1, calls other functions to calculate the $\alpha\beta$ components of $\overline{v}_{grid}$, $\overline{v}_{gen}$, and $\overline{i}_{gen}$ and then to determine vector magnitudes and angles. To counteract the effect of harmonics and measurement noise, the $\alpha\beta$ components are filtered using digital LP-filter functions obtained from *Winfilter* by Adrian Kundert.

Furthermore, the vector magnitudes are averaged and scaled to effective phase (RMS) values for easier application in synchronisation conditions. Finally, the current balance is checked and the real power flow is determined using Eqn (5.1).

6.2.2.2 Clarke Transformation

Functions to perform the $\alpha\beta$ Clarke transform and to determine the magnitude and angle of the resulting space vector are listed in Appendix D.2.2. These functions make use of the Texas Instruments *C28x IQmath Library*, which allows virtual floating-point calculations to be performed efficiently on the fixed-point F28027 MCU.

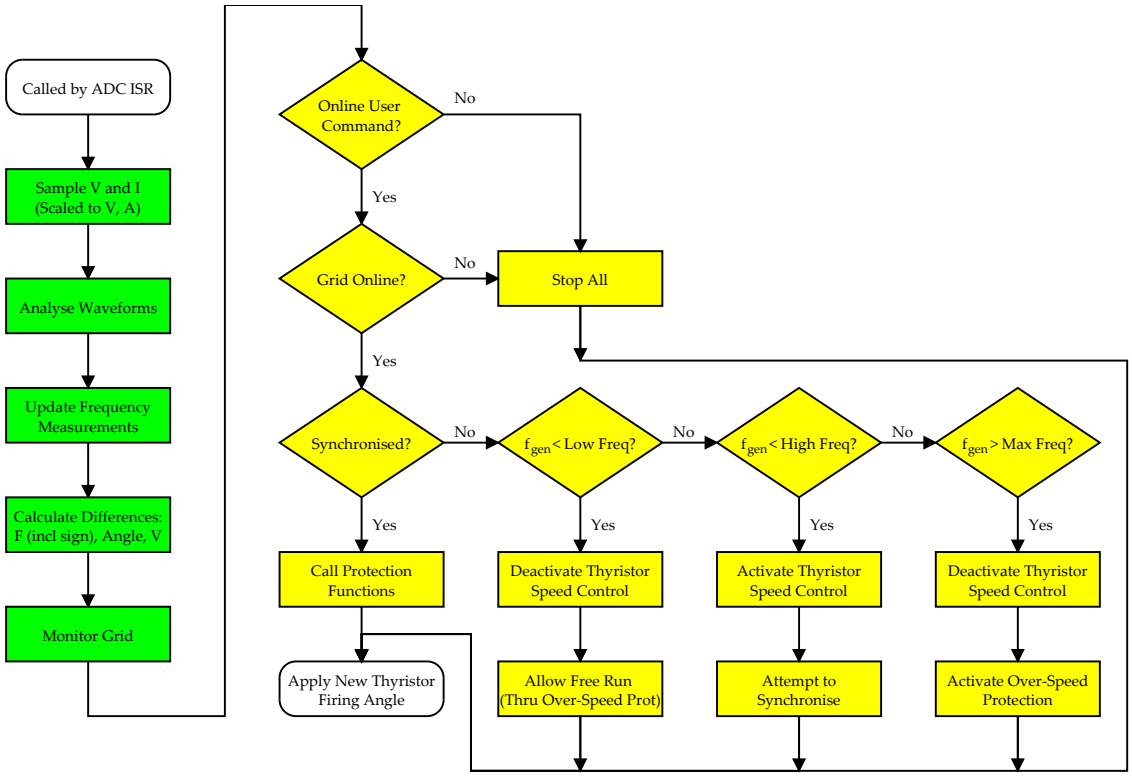

Figure 6.8: Flow diagram of the supervisory control function. Monitoring actions are shown in green while control actions are shown in yellow.

6.2.2.3 Frequency Measurement

An example of the frequency measurement function applied separately to $\overline{v}_{grid}$ and $\overline{v}_{gen}$ is listed in Appendix D.2.3. The function measures the change in space vector gradient between consecutive voltage samples to determine the rotational velocity of the vector and, as a result, the grid or SS-PMG frequency. The flow diagram for this function is illustrated in Fig. 6.9(a).

The vector velocity is averaged across half-cycles (a new value is determined each time the vector gradient passes through zero or makes a $\pm 180\,^{\circ}$ transition). Further averaging, as well as a digital LP-filter, is then applied to obtain a stable value. This is once again necessary due to the high harmonic content of the SS-PMG voltages under thyristor switching.

An advantage of the vector gradient approach is that rotational direction can also be inferred by the sign of gradient change. This allows the GCC to prevent synchronisation if there is a phase-order mismatch between the SS-PMG and the grid.

The performance of the SS-PMG frequency measurement method is illustrated in Fig. 6.10, which indicates that the measurement error remains below 0,02 p.u. throughout the active speed control range for a variety of thyristor loading levels.

6.2.2.4 Grid Condition Monitoring

The grid status monitoring function, listed in Appendix D.2.4, is responsible for setting all the grid-related status flags in the system status structure described in Section 6.2.1.2. The function evaluates

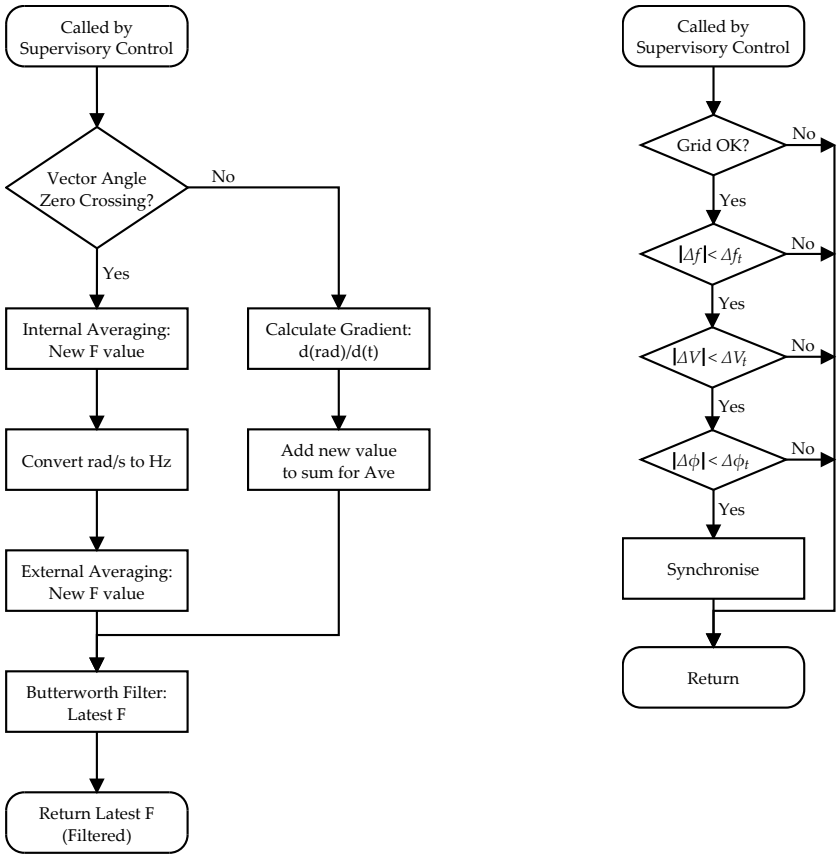

(a) Frequency Determination (b) Synchronisation

Figure 6.9: Flow diagrams for frequency calculation from vector velocity and for synchronisation.

the grid voltage and categorises it as either nominal, tolerable, or faulted. The SS-PMG is less sensitive to small frequency variations so grid frequency is classified more simply as either nominal or faulted. The voltage and frequency bands are illustrated in Fig. 6.11(b) and Fig. 6.11(c), respectively. Upper and lower margins are equal and are set with reference to [91], but each margin can be adjusted individually, if required.

In the event of a long term grid outage (due to maintenance or a fault), this function also times the

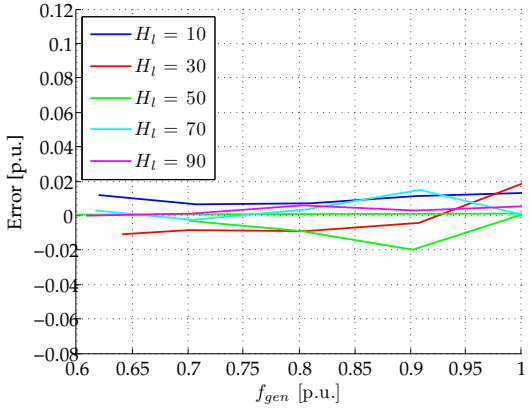

Figure 6.10: GCC frequency measurement error as a function of f_{gen} for different thyristor loading levels.

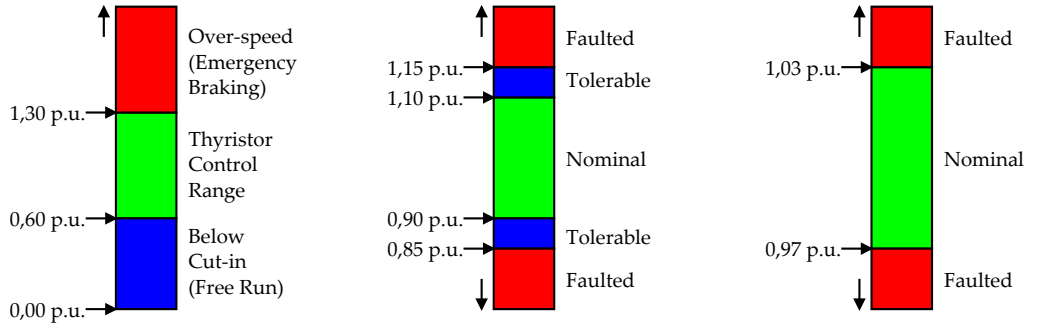

(a) Rotational speed bands (b) Grid voltage bands (c) Grid frequency bands

Figure 6.11: Classification bands for SS-PMG speed control, grid voltage magnitude, and grid frequency.

off-line period to detect if the SS-PMG should be shunt down to prevent islanding. Once the grid has been off-line for longer than the allowable limit, the gridOff status bit is set to indicate to the relevant protection function that the SS-PMG should be disconnected and shut down.

6.2.3 Control Functions

The functions discussed here facilitate the controlled synchronisation of the SS-PMG, according to the procedure determined in Chapter 4.

6.2.3.1 Synchronisation

The synchronisation function follows the same logic developed in Section 4.1.4 with the inclusion of an extra condition to check that the grid conditions are nominal, as indicated in Fig. 6.9(b). Both grid frequency and voltage must be within their respective nominal bands (refer to Fig. 6.11) before synchronisation can occur. The synchronisation process involves simultaneously closing switches S3 and S4, after which the syncd status flag is set. The code for the synchronisation function is listed in Appendix D.3.1.

6.2.3.2 Speed Control

The digital PI speed control function is listed in Appendix D.3.2 and implements the control loop originally illustrated in Fig. 4.14. It applies internal limits to both the integral component and the final command signal, H_l. This function is called during all non-synchronised modes so that H_l is continuously updated, which ensures smoother transitions when thyristor speed control is activated.

H_l serves as input to the thyristor load linearisation function, listed in Appendix D.3.3. This function sets the DAC output to the RT380T thyristor driver in a manner that achieves linear change in SS-PMG torque with H_l. The establishment of the linear relationship is discussed further in Section 6.3.2.

6.2.4 Protection Functions

To allow for safe laboratory and field testing of the SS-PMG, it is necessary to implement various protection functions. Apart from ensuring a basic level of safety, these functions also attempt to comply

with the protection requirements in the relevant South African grid codes. The protection functions are called by the supervisory control function.

It is also necessary to inform the operator about the present status of the WECS. Although only equipped with three LEDs, the GCC is capable of displaying status information about the grid and the SS-PMG. This includes a basic error log (using the errCode field in the system status structure). A detailed description of the LED status indications is given in Appendix E.

6.2.4.1 Grid Code Protection Requirements

Grid code requirements relating specifically to LVRT are discussed in Section 5.1. Further South African protection requirements from [80] for EGs connected to the distribution grid include the following:

- If the grid circuit breaker opens, the EG is to cease energising the local network within 2 s.
- Typically, a 10 s to 30 s limit should be applied before tripping on reverse power (generator motoring). The negative power detection level should be 10 % to 20 %.
- The EG must protect itself against negative phase sequence over-currents (unbalanced faults).

The protection functions discussed here cater for these requirements, amongst others.

6.2.4.2 Grid Fault Protection

The on-grid fault protection function, listed in Appendix D.4.1 becomes operational once the SS-PMG is synchronised. It activates LVRT compensation if a grid voltage fault is detected and clears compensation once the grid voltage has recovered. Immediate disconnection occurs in the case of a frequency fault. A delay is included to prevent actions during synchronisation since weaker grids may experience transients that register as a fault when the SS-PMG is connected under strong wind conditions.

6.2.4.3 Anti-Islanding

Because the SS-PMG relies on the grid to impose a fixed frequency when on-line, the simplest indication of grid failure (or an open breaker) is a sustained grid frequency error. The frequency being measured after an upstream breaker has opened is actually the uncontrolled SS-PMG frequency, which will begin to vary immediately due to turbulent wind and active power imbalance. Fast protection in the case of such a failure is provided by the on-grid fault protection function, which disconnects the SS-PMG as soon as a frequency fault is detected.

Long-term anti-islanding protection is provided by a combination of the grid condition monitoring function and the supervisory control function. The condition monitoring function sets the gridOff status bit if any grid fault has persisted for longer than the allowable period. The supervisory control function responds to the gridOff bit being set by shutting down the GCC, as illustrated in Fig. 6.8. Normal operation resumes once the grid conditions recover to within nominal limits.

6.2.4.4 Over-Current Protection

If any sample of ${i_a}^2$, ${i_b}^2$, or ${i_c}^2$ exceeds a pre-set limit of 4 p.u.^{2} then the SS-PMG is automatically disconnected from the grid by the over-current protection function, listed in Appendix D.4.2.

6.2.4.5 Reverse Power Protection

The reverse power protection function measures how long the SS-PMG is motoring during a window period and disconnects if excessive motoring is detected (see Appendix D.4.3). The function counts the number of sample periods where reverse power (motoring) occurs during a pre-set period. If the occurrences of reverse power exceed a chosen limit value, then the SS-PMG is deemed to be motoring and is disconnected.

It is important to set the limit value correctly to prevent both nuisance tripping and unnecessary motoring. Since the SS-PMG is a direct-connected synchronous generator, it can easily motor in low, variable winds so a low limit will cause frequent disconnection at many sites. Building in too much tolerance for motoring, on the other hand, can allow the SS-PMG to become a net consumer of energy under certain conditions. Tuning of the limit value based on practical experience is thus necessary to obtain the best results for a given wind site.

6.2.4.6 Phase Imbalance Protection

In practice, the need to ride through (unbalanced) grid faults must be measured against the need to monitor for possible short-circuit faults in the SS-PMG itself. The phase imbalance protection function, listed in Appendix D.4.5, counts the sample periods where severely unbalanced phase currents are recorded. If the number of samples exceeds a threshold then the WECS is permanently shut down and can only be restarted by manually resetting the GCC. This is to alert the operator that the SS-PMG should be checked for any possible internal short-circuits. Once again, the threshold must be set to avoid nuisance tripping while still ensuring sufficient protection.

6.2.4.7 Over-Speed Protection

During speed control it is possible that wind speeds may exceed 12 m/s occasionally, producing more turbine torque than the SS-PMG can counteract with thyristor braking. Under such conditions, the turbine and SS-PMG may repeatedly exceed the maximum speed limit of 1,3 p.u. Each time the WECS over-speeds, emergency braking is used to bring the system back to below cut-in speed (the SS-PMG is switched on to the braking load with capacitor compensation by switch S1).

To prevent repetitive and potentially damaging behaviour, the over-speed protection function counts the number of unique over-speed events that occur in a window period. If the count exceeds a set limit then the WECS is shut down completely for a cool-down period to allow the average wind speed to drop sufficiently. The full over-speed protection function is listed in Appendix D.4.4.

6.3 Implementation Issues

In this section, the significant challenges encountered during the practical implementation of the GCC are discussed. Solutions, where available, are also presented.

6.3.1 Voltage Neutral Point

The GCC measures phase voltages on both the grid and SS-PMG terminals. The original arrangement was to measure voltages between phase and neutral, with both SS-PMG and grid neutrals being available. When preparing the GCC for field testing it became apparent that the SS-PMG neutral is not accessible when the WECS is installed on a tower, making phase-to-neutral measurements impossible.

Various solutions were considered, including the creation of a virtual neutral point with a set of star-connected capacitors. Ultimately, it was elected to use the grid neutral as the base measurement point for both SS-PMG and grid voltage measurements. This has proven effective in both laboratory and field tests, without any noticeable changes in control performance.

6.3.2 Thyristor Loading Linearity

The non-linear change in SS-PMG counter-torque with thyristor firing angle α is already a well-known phenomenon from simulation studies, as discussed Section 4.2.2.1. It has also already been noted that the SS-PMG is not an ideal voltage source as it possesses a relatively high stator impedance. The upshot of this characteristic is that conventional current linearisation techniques, such as the cosine wave-crossing method, prove ineffective.

As with the simulation case, it was elected to map SS-PMG counter-torque to α through measured results, then to use a polynomial function to produce linear torque response to a change in the input command H_l. Although this can only be done accurately for a single speed, achieving linearity at and around synchronous speed was deemed sufficient.

A further problem emerged when attempting to implement the empirical mapping strategy. The system exhibits a zone of unstable thyristor operation, where torque development collapses. It was thought this may be remedied by connecting the star points of the SS-PMG and resistive load, but this configuration failed to achieve marked improvement.

The RMS load current as a function of H_l, when mapped directly to α, is shown in Fig. 6.12(a) for three source cases: the grid, the SS-PMG, and the SS-PMG with neutral point connected. In this case, $H_l = 0$ gives $\alpha = 180\,^\circ$ and $H_l = 100$ gives $\alpha = 0\,^\circ$.

It is clear from this example that the origin of the problem is not in the fundamental operation of the thyristors, thyristor driver, or the signal from the controller board to the driver. For the grid-source case, the trend of current against H_l is precisely as expected—the response can also be linearised successfully with conventional mapping methods. In contrast, when the SS-PMG acts as source for the thyristors the trend collapses for $H_l > 65$, with the addition of the neutral connection having limited remedial value.

Changing the load resistance value is shown to produce insufficient improvement in Fig. 6.12(b), especially considering the loss in torque that accompanies an increase in R_{br}. It was concluded that the poor performance of the thyristors stemmed from the high harmonic content of the terminal voltage waveform during thyristor switching.

The SS-PMG current and voltage waveforms under thyristor action are shown in Fig. 6.12(c) and the harmonic content for the signals is listed in Table 6.2. The presence of these harmonics degrades the performance of the thyristor driver itself by making zero-crossings more difficult to detect. In addition,

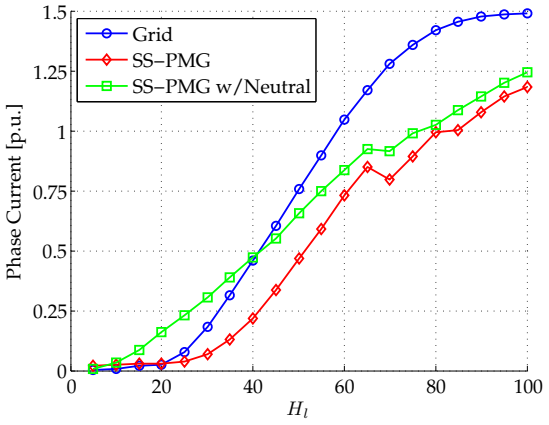

(a) RMS phase current as a function of H_l directly mapped to α at $f_{gen} = 1$ p.u.

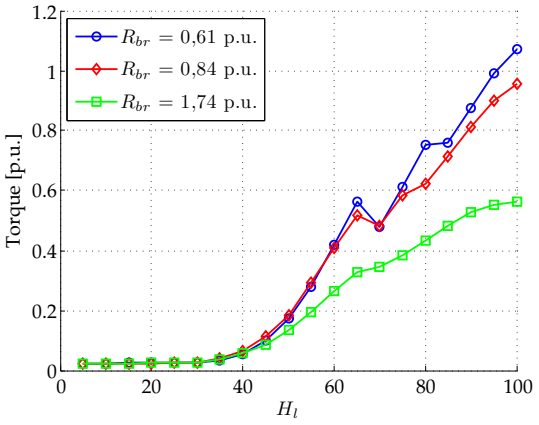

(b) SS-PMG counter-torque T_r as a function of H_l directly mapped to α at $f_{gen} = 1$ p.u. with different values of R_{br}

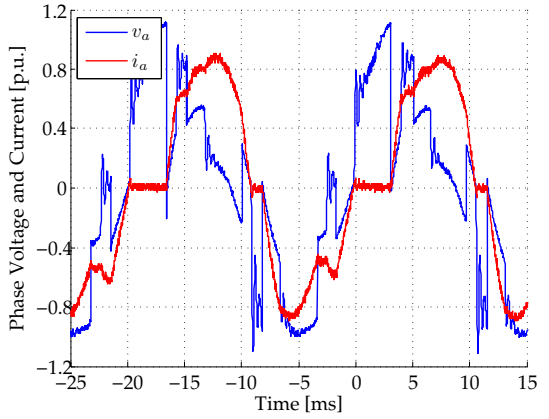

(c) SS-PMG phase voltage and phase current waveforms under thyristor action with direct $H_l = 60$ and $R_{br} = 0{,}61$ p.u. at $f_{gen} = 1$ p.u.

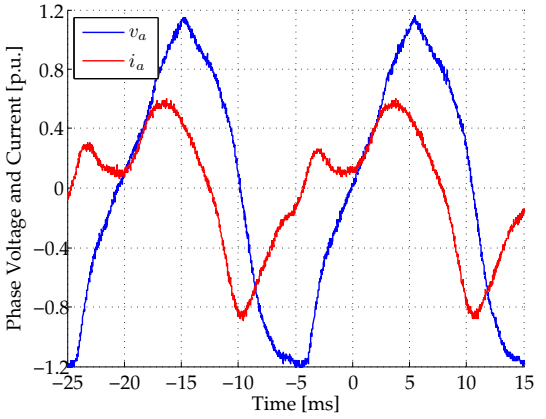

(d) SS-PMG phase voltage and phase current waveforms under thyristor action with direct $H_l = 35$, $R_{br} = 1{,}18$ p.u., and $C_{cs} = 0{,}631$ p.u. at $f_{gen} = 1$ p.u.

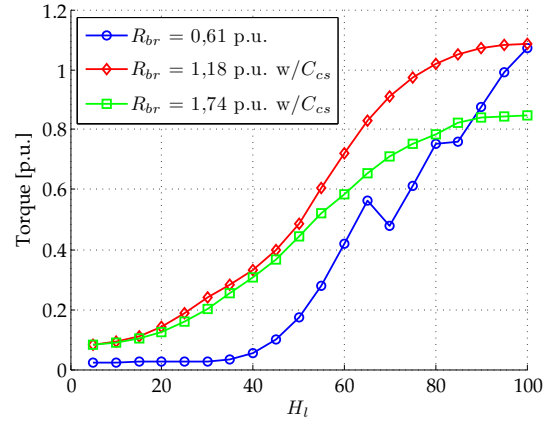

(e) SS-PMG counter-torque T_r as a function of H_l directly mapped to α at $f_{gen} = 1$ p.u. with different values of R_{br} and $C_{cs} = 0{,}631$ p.u.

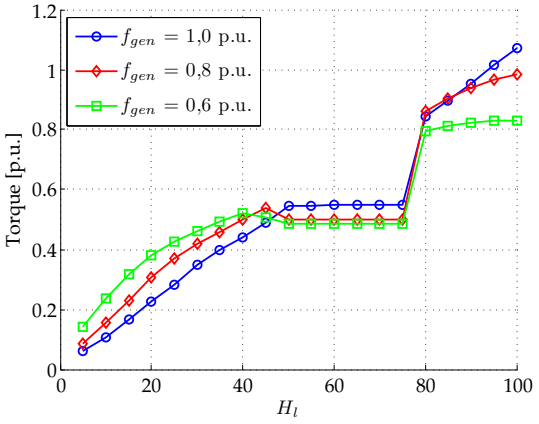

(f) SS-PMG counter-torque T_r as a function of H_l empirically mapped to α (with skip-band) for $R_{br} = 0{,}61$ p.u.

Figure 6.12: Thyristor loading linearity practical investigations.

Table 6.2: Thyristor voltage and current harmonics with direct $H_l = 60$, $R_{br} = 0{,}61$ p.u., and $f_{gen} = 1$ p.u.

Harmonic Order	Voltage Magnitude [p.u.]	Current Magnitude [p.u.]
1	0,759	0,778
2	0,180	0,225
4	0,118	0,068
5	0,171	0,099
8	0,152	0,051
10	0,110	0,030
11	0,085	0,021
THD	21,3 %	11,6 %

the operation of each thyristor is affected by the switching transients of those operating on the other phases.

To determine if a more sophisticated thyristor driver could overcome the problem, the analogue RT380T was replaced by the microprocessor-based MP410T, also from Semikron. However, no performance improvement was achieved with this approach. It was then decided to reduce the harmonic content of the voltage waveforms by adding permanent shunt capacitance to the circuit, as shown in Fig. 6.13. This approach had a dramatic effect on voltage and current waveforms, which are shown in Fig. 6.12(d) at synchronous speed.

The directly-mapped torque curves that can be achieved with higher values of R_{br} in combination with $C_{cs} = 0{,}631$ p.u. are shown in Fig. 6.12(e). The capacitor-compensated curves approach the ideal (grid-source) case, with the torque collapse at $H_l > 65$ being virtually non-existent.

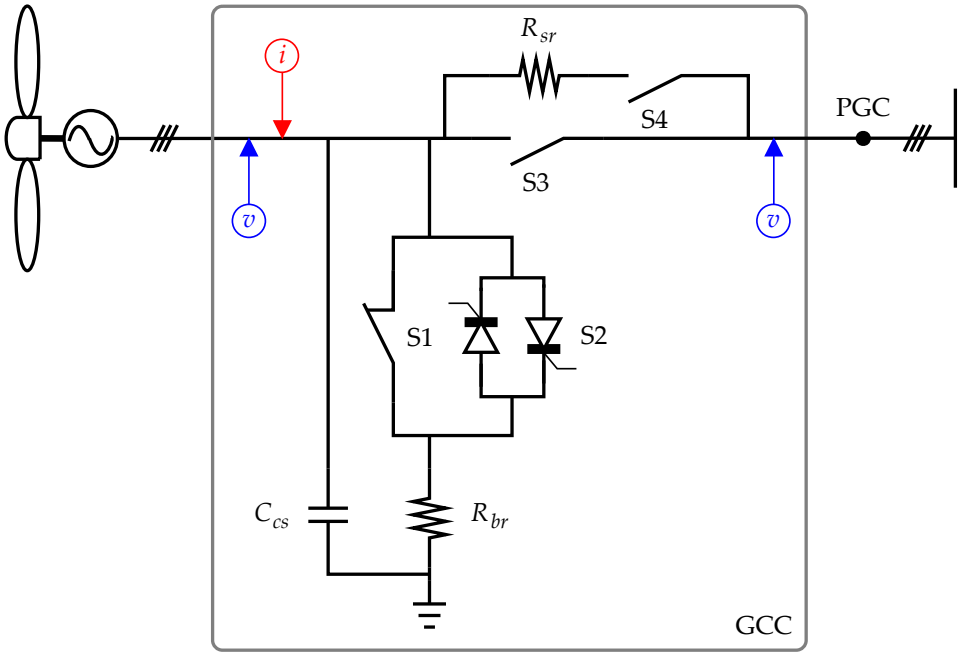

Figure 6.13: Single line diagram of the GCC including a permanently active compensation capacitor bank C_{cs}.

Employing capacitors in this way does, however, introduce certain complications. Resonance between the stator inductance and the capacitances is a real possibility and manifests itself around $f_{gen} = 1$ p.u. with $R_{br} = 1{,}18$ p.u. and $C_{cs} = 0{,}631$ p.u. Changing the resistance value to $R_{br} = 1{,}74$ p.u. helps to reduce the resonance, but also reduces maximum torque to an insufficient level. Other issues, such as the change in SS-PMG terminal voltage at $f_{gen} = 1$ p.u., also need to be addressed.

Although use of capacitor compensation is promising, proper implementation of this strategy is beyond the scope of this work and may yet have unforeseen consequences. It may even be necessary to re-design the SS-PMG stator with such compensation in mind to achieve best results.

As such, a more straight-forward solution was needed to complete this initial investigation into SS-PMG speed control and synchronisation. The chosen approach was to avoid the use of firing angles in the unstable band of $50 \leq H_l \leq 70$ and to create separate mapping curves for the stable zones above and below this band.

During thyristor-based speed control, unstable operation is avoided as follows: when H_l (generated by the PI speed control function) enters the unstable band, the thyristor control function holds its output signal to the RT380T at the last stable value until H_l re-enters one of the stable zones. This results in a torque plateau when traversing H_l, but still allows for stable control.

The SS-PMG torque curves obtained while varying H_l at three different frequencies are shown in Fig. 6.12(f). Since the mapping was targeted at $f_{gen} = 1$ p.u. the curve at this speed is close to linear, except for the plateau through the skip-band. The curves at lower frequencies are less linear but response is stable. It was found that speed control investigations could continue with this arrangement, although a more satisfactory solution will be required in the long term.

6.4 Summary

In this chapter, the hardware and software implementation of the GCC has been discussed in detail. The major hardware components have been listed and the physical construction of the GCC has been presented, including the resistive load cage. The components used are widely available off-the-shelf, with the exception of the controller board and the current sensor module.

From a costing perspective, a SS-PMG-based WECS is expected to require a lower initial investment than a converter-fed WECS using the same type of PMSG. The economic advantage of the SS-PMG is not based on installation cost alone, though. The greater simplicity of the electronics employed (and their lower utilisation) is expected to give the SS-PMG WECS a lower maintenance bill, along with higher availability. A major goal of this work is to facilitate the in-field testing of comparable SS-PMG WECS and converter-fed WECS to allow more concrete answers to the question of economic feasibility.

From a software perspective, a number of important functions have been developed to achieve the operational objectives of the GCC. These include supervisory, control, and protection functions. The latter group plays an important part in both safety and grid code compliance.

The final section of this chapter addresses some significant implementation hurdles that had to be overcome before useful experimentation could take place. The most challenging issue was that of the stability and linearity of thyristor loading. After evaluating a number of potential solutions, it was

elected not to alter the original hardware configuration of the GCC but rather to work around the zone of instability. More comprehensive solutions to this problem have, however, been proposed for future investigations.

CHAPTER 7

LABORATORY AND FIELD TESTS

While Chapter 6 describes the implementation of the GCC, this chapter presents the results obtained from practical investigations in the laboratory and in the field. These investigations focus on the speed control and synchronisation functions of the GCC. A suitable LVRT test methodology has not yet been implemented so validation of the PAC-LVRT compensator is deferred to future work.

7.1 Laboratory Tests

This section describes the investigations conducted under controlled conditions in the laboratory. Firstly, the test equipment is detailed, after which the results of synchronisation and speed control experiments are presented.

7.1.1 Laboratory Test Setup

The test setup in the laboratory consists of a mechanical test bench and a grid connection point for the SS-PMG, along with instruments to measure and log system dynamics.

7.1.1.1 Mechanical Test Bench

The mechanical test bench replaces the wind turbine as a torque source during laboratory investigations. As such, it should replicate the torque-speed characteristics of the wind turbine. It should also be capable of varying its output as a function of time to mimic turbulent wind conditions.

In this case, the test bench consists of a 4-pole 45 kW geared induction motor, driven by a 37 kW *Powerflex* VSD from Allen-Bradley. The VSD can be set to regulate either speed or torque of the IM. A Lorenz *DR-2212* in-line torque sensor provides real-time torque data through a USB-logging interface. The complete mechanical test bench with the 15,9 kW SS-PMG is shown in Fig. 7.1(a).

The VSD-IM combination exhibits torque-speed behaviour that is markedly different to the torque curves of the wind turbine, shown in Fig. 3.1(a). The torque output of the turbine is highly dependent on rotational speed, whereas the VSD allows the IM to produce rated torque from near standstill to rated speed. As a consequence, the VSD-driven IM can produce faster rates of acceleration than what would be observed in the field. By controlling the ramp rate and maximum torque output of the VSD it is possible to achieve similar acceleration times to those predicted by simulations. The acceleration is, however, more linear than that caused by the turbine.

Operating the VSD in speed regulation mode is convenient for many steady-state tests and calibration. To test the speed control capabilities of the GCC it is, however, necessary to employ the torque regulation mode of the VSD. In this mode the drive, in theory, acts a torque source in a similar manner

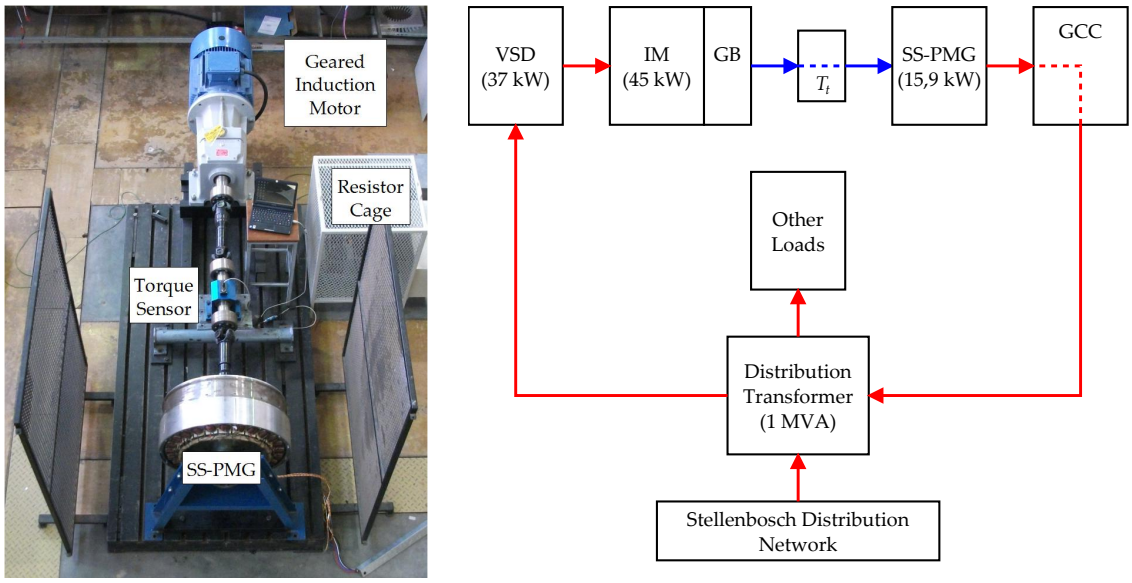

(a) Mechanical test bench components

(b) Power flow in laboratory experiments. Red arrows indicate electrical power transfer. Blue arrows indicate mechanical power transfer

Figure 7.1: Laboratory test arrangement.

to the wind turbine itself. Although the performance of the VSD-IM is not wholly satisfactory in this regard (as illustrated later in this chapter), it is sufficient to verify the operation of the GCC.

Attempts to emulate turbulent wind conditions by providing the VSD with a torque reference that varies with both time and rotational speed proved unsuccessful. As a compromise, the torque reference to the VSD can be varied manually to test the tracking capabilities of the GCC speed control.

7.1.1.2 Electrical Network

Two distribution transformers are used to supply electrical power to the engineering faculty at Stellenbosch University. One feeds general loads while a second is used primarily to supply large loads, such as VSDs and large motors. To prevent interaction between the SS-PMG and the VSD, the SS-PMG was originally connected to the transformer feeding general loads. This compromised the performance and stability of the SS-PMG due to the high harmonic content of the grid voltage waveform. As a result, the GCC was set to connect the SS-PMG to the same distribution transformer that supplies the VSD because the harmonic contamination of this connection is lower.

The flow of energy while running the SS-PMG in generator mode on the test bench is illustrated in Fig. 7.1(b). Because a feedback loop does exist between the SS-PMG output and the VSD supply, the potential for undesired interactions does exist. However, the local network is sufficiently stiff that neither the SS-PMG nor the VSD have a significant effect on grid conditions.

7.1.1.3 Measuring Instruments

A Tektronix digital phosphor oscilloscope, equipped with differential voltage probes and a clamp-on current transducer, allows comparison and recording of SS-PMG and grid voltage waveforms, as well

as phase current. A LEM *Norma* power analyser provides additional measurements of 3-phase power and torque. To record mechanical speed, a resolver is connected to the PM-rotor shaft and its output is logged to a PC via a converter.

7.1.2 Synchronisation Tolerance Limits

In Section 4.1 the synchronisation condition limits for the SS-PMG are determined by examining the simulated transient response to changes in Δf and $\Delta\phi$ at synchronisation. It is found that $\Delta f_t = 0{,}02$ p.u. and $\Delta\phi_t = 10\,^\circ$ ensure successful synchronisation across the wind speed range.

The following procedure can be used to verify the sensitivity of the SS-PMG to $\Delta\phi$:

1. Set VSD to speed regulation mode with reference $f = 1$ p.u.
2. Set GCC to synchronise with an increment of $\Delta\phi_t$.
3. Allow VSD-IM to bring SS-PMG up to speed under no-load.
4. Allow GCC to synchronised SS-PMG automatically.

An example of the oscilloscope measurements taken during a synchronisation run is shown in Fig. 7.2. In this case, the contactor closing delay is 13,8 ms, suggesting that the 20 ms delay chosen for simulations is conservative. In other cases, longer closing delays were observed, so a safety margin is appropriate to account for stochastic variations in contactor performance.

Once the actual moment of contactor closing is identified $\Delta\phi$ at synchronisation can be determined by comparing the voltage waveforms. For the case in Fig. 7.2, a phase angle difference of 9,9 ° results in a transient current maximum of 0,584 p.u., which is 16,8 % above the predicted value.

The results of a number of experimental runs are plotted in Fig. 7.3, which shows that the general trend is, in fact, lower than predicted by simulation. The significant spread in measured results is attributed to differences in the SS-PMG rotor position at the moment of synchronisation. As noted for the dynamic simulation results, the contactor closing delay can result in changes in $\Delta\phi$ before synchron-

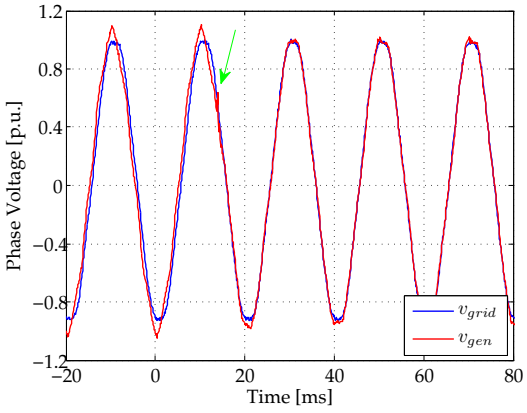

(a) SS-PMG and grid instantaneous phase voltage as a function of time

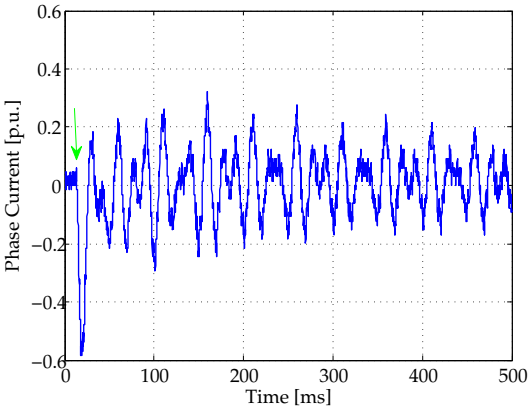

(b) Instantaneous phase current as a function of time

Figure 7.2: Transient voltage and current captures during no-load synchronisation. Synchronisation signal is generated at $t = 0$ ms and contactors close at $t = 13{,}8$ ms, as indicated by the green arrows. At synchronisation $\Delta\phi = 9{,}9\,^\circ$ and $\Delta f \approx 0$ p.u.

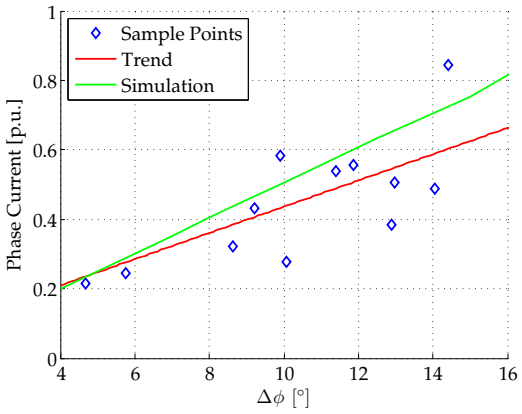

Figure 7.3: Maximum phase current during synchronisation as a function of $\Delta\phi$ with $\Delta f \approx 0$ p.u. and shaft torque equivalent to $u_w = 4\,\mathrm{m/s}$.

isation, which may further increase current transients. For these reasons, the GCC has been set with $\Delta\phi_t = 5\,^\circ$ to ensure that $\Delta\phi$ at synchronisation is well within the original limit and transients remain acceptable.

A similar investigation for Δf was not performed because to do so requires setting the VSD speed reference to a value other than 1 p.u. At synchronisation, the VSD speed regulator counteracts the necessary transition to $f = 1$ p.u. This results in an unnaturally severe response, which skews results. To account for f_{gen} measurement error and the possibility of higher than expected transients due to Δf, the GCC is set with $\Delta f_t = 0{,}01$ p.u.

Another synchronisation example, this time with rated torque supplied by the VSD-IM, is shown in Fig. 7.4. In this case, the VSD is operating in torque control mode and thyristor output is near 100 %. With the new threshold values, $\Delta\phi = 4{,}91\,^\circ$, $\Delta f = 0{,}0083$ p.u., and $\Delta V = 0{,}1668$ p.u. at the moment S3 closes. The 1,414 p.u. current spike that results from synchronisation compares well with simulated on-load synchronisation cases but exceeds the no-load prediction by 0,26 p.u. Additionally, maximum grid voltage drop is higher than specification at 1,83 %. These discrepencies are also observed in simulation and are a result of the high value for ΔV, which is caused by SS-PMG terminal voltage drop under load. Nonetheless, the current transients are short-lived and within tolerance margins, indicating stable synchronisation.

Despite the success of synchronisation, a long-term oscillation in current magnitude is evident in Fig. 7.4(b). This phenomenon is also visible, to a certain extent, in the first synchronisation example at low torque in Fig. 7.2(b). For the present case, the slip-rotor torque (Fig. 7.4(c)) and the PM-rotor speed (Fig. 7.4(d)) show sustained oscillations after synchronisation as well. The frequency of these oscillations is the same as that of the long-term current oscillations: 0,25 p.u., indicating that the two effects are linked.

These sustained current, torque and rotor speed oscillations are present at different input torque levels and remain evident under steady conditions. Since they are not a product of the process of synchronisation, they point to either an oscillation in the test bench or to an inherent instability in the PM-rotor of the SS-PMG when connected to the grid. Evidence in Section 7.2.3 supports the first possib-

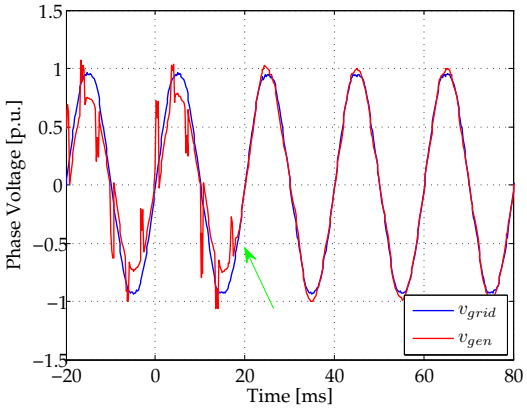

(a) SS-PMG and grid instantaneous phase voltage as a function of time

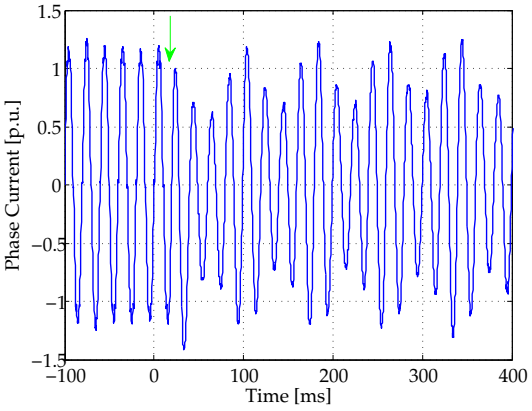

(b) Instantaneous phase current as a function of time

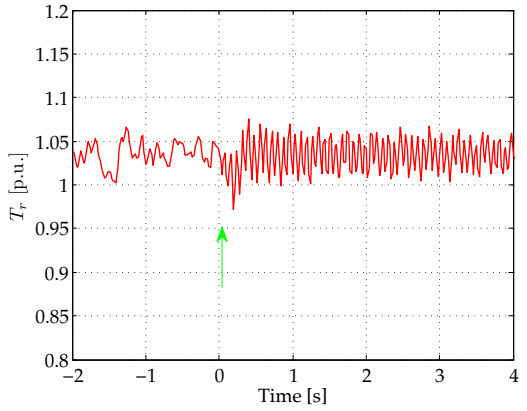

(c) Slip-Rotor torque as a function of time

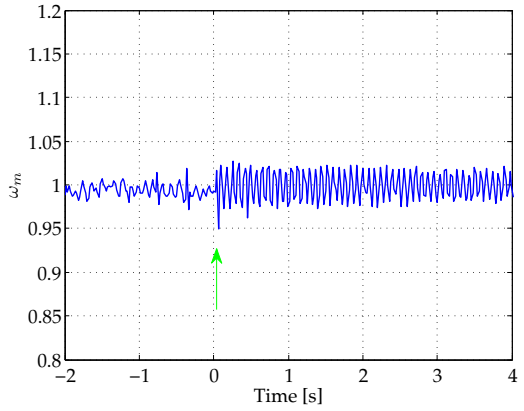

(d) PM-rotor speed as a function of time

Figure 7.4: Transient signal captures during synchronisation with thyristors on 97 % load. Synchronisation signal is generated at $t = 0$ ms and contactors close at $t = 18{,}6$ ms, as indicated by the green arrows. At synchronisation $\Delta\phi = 4{,}91\,^{\circ}$, $\Delta f = 0{,}0083$ p.u., and $\Delta V = 0{,}1668$ p.u.

ility: the test bench experiences these oscillations due to unstable interactions between the VSD control loops and the grid as both influence the PM-rotor speed after synchronisation.

In conclusion then, practical investigations have shown the theoretically determined synchronisation conditions to be valid. These limits lead to successful synchronisation with generally acceptable transients. To counteract the effects of thyristor operation and variations in rotor angle position, Δf_t and $\Delta\phi_t$ have nonetheless been halved in the GCC implementation. Although this ensures lower transients during synchronisation, sustained oscillations remain evident in the grid-connected SS-PMG. These oscillations appear to be related to the test bench setup and the operation of the VSD.

7.1.3 Thyristor-Based Speed Control

After the synchronisation conditions are derived in Chapter 4, a speed controller based on electromagnetic braking is developed to meet those requirements. Verifying the speed control design involves a study of the effect of PI gains, as well as investigations into the dynamics achieved during steady and

time-varied input torque.

7.1.3.1 PI Gain Tuning with Steady Input Torque

A simulation sweep shows that $K_p = 15$ and $K_i = 20$ are appropriate PI gains for the thyristor-based speed control loop of Fig. 4.14. When employing these gains in the laboratory setup, the PM-rotor tends to exhibit unstable oscillatory behaviour. This phenomenon is more pronounced at low input torque levels.

High controller gains result in substantial changes in stator torque T_s as the measured speed varies. This causes continuous changes in PM-rotor acceleration that can, in turn, lead to larger measured speed variations, ultimately reaching instability.

With the high-inertia wind turbine driving the slip-rotor at a relatively stable speed, these oscillations should be naturally damped by the interaction between PM-rotor and slip-rotor. In the case of the test rig, it appears that the VSD detects changes in slip-rotor speed or counter-torque, and that it attempts to respond to these variations by changing its own output. This double control intervention from the GCC and the VSD may explain why gains that are safely employed in simulation cause instability in the test setup.

To avoid instability, the speed controller can be set with lower gain values, but dynamic performance must not be unduly compromised. The effectiveness of speed control with reduced PI gains can be evaluated for the test setup using the following steps:

1. Set VSD to torque regulation mode.
2. Pre-set VSD torque reference and ramp rate to emulate the behaviour of the wind turbine at rated wind speed.
3. Set GCC controller gains.
4. Start VSD.
5. Capture SS-PMG frequency dynamics until a stable operating point is reached.

Key results from the PI gain investigation are shown in Table 7.1. Peak overshoot exceeds the recommended maximum of 0,1 p.u. in all cases and approaches the safety limit of 0,2 p.u. with the lowest gains tested. On the other hand, settling time can be held within the required limit of 5 s for most gain combinations and tracking is uniformly good, remaining within the margin of 0,02 p.u.

From these results, the revised gains for the GCC are set as $K_p = 5$ and $K_i = 6$. These values allow the GCC to achieve the dynamic control requirements while minimising PM-rotor oscillation. The major disadvantage is that overshoot exceeds the ideal limit of 0,1 p.u. in high winds, but safe operation is still achieved.

The speed control dynamics observed during a 0,95 p.u. step in input torque are shown in Fig. 7.5. The PM-rotor speed is shown from 0,6 p.u. (Fig. 7.5(a)), which is the cut-in speed for thyristor operation. The commencement of active speed control can be seen by the torque disturbance at $t = 1{,}4$ s in Fig. 7.5(b) as the thyristors begin switching on to the resistive load.

Fig. 7.5(a) indicates that $M_p = 16\,\%$, $t_s = 5{,}4$ s, and tracking remains within 0,02 p.u. until the end of the recorded period. Settling time is longer than expected, but the critical parameters, overshoot

Table 7.1: Measured time-domain performance of thyristor-based speed control as a function of PI gain values. All cases are for steady rated input torque.

K_p	K_i	Overshoot M_p [p.u.]	Settling Time t_s [s]	Tracking Accuracy Δf [p.u.]
3	3	0,19	6,0	0,013
5	6	0,15	4,8	0,015
7	9	0,13	4,0	0,015
10	12	0,11	3,5	0,015

and tracking, are both acceptable. The positive outcome of the lower gains is that PM-rotor speed oscillations are reduced from ±0,03 p.u. to ±0,01 p.u., improving both tracking and stability under low input torque conditions. So, although performance cannot match what was predicted with higher gains in simulation, the thyristor-based speed controller functions correctly and meets all requirements to allow for safe synchronisation.

7.1.3.2 Performance with Time-Varied Input Torque

With the PI speed regulator tuned successfully for steady input conditions, it is necessary to test performance under variable input conditions. In simulation, turbulent wind conditions do not have a detrimental effect on control dynamics, but the lower gain values employed in practice may change this picture. In Fig. 7.6 the measured speed controller response to time-varied torque input is shown.

The major degradation in performance, compared to the steady input case, is in terms of tracking. Control during the first 6,5 s follows the same pattern as for steady input. As input torque drops ever more dramatically during the remainder of the interval, the controller struggles to hold f_{gen} in the required range.

This response is to be expected when prime mover input drops substantially. The thyristor-based speed controller is a braking mechanism so it can merely cease intervention when input torque collapses.

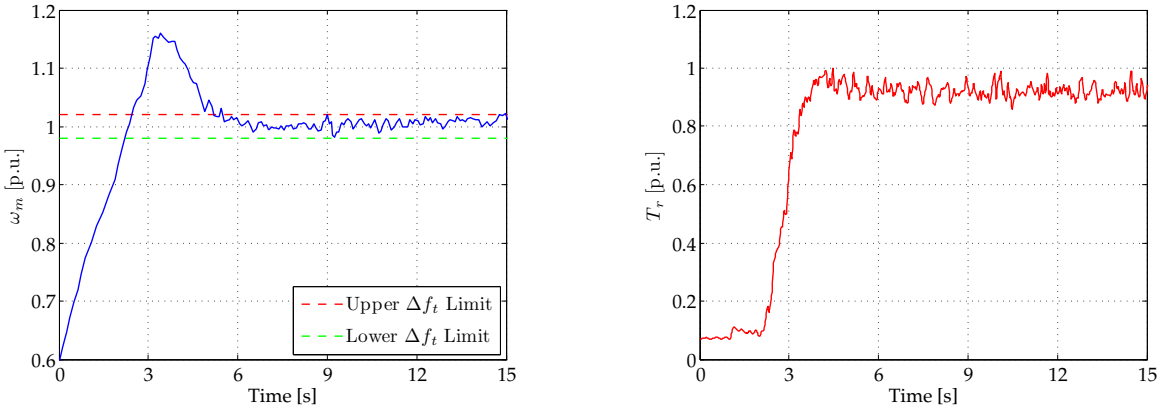

(a) PM-rotor speed as a function of time

(b) Slip-rotor torque as a function of time

Figure 7.5: Measured dynamic response of the thyristor-based speed controller to a 0,95 p.u. torque step from $\omega_m = 0{,}6$ p.u. PI gains are $K_p = 5$ and $K_i = 6$.

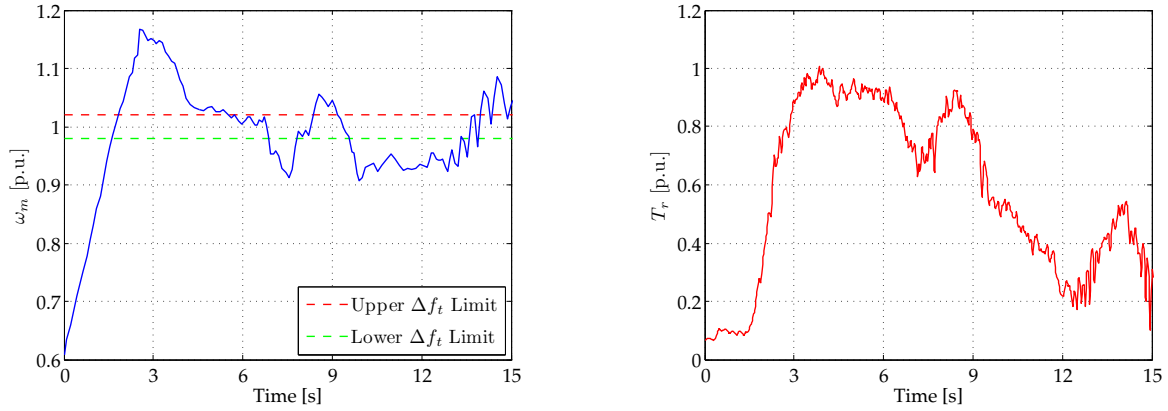

(a) PM-rotor speed as a function of time

(b) Slip-rotor torque as a function of time

Figure 7.6: Measured dynamic response of the thyristor-based speed controller to a time-varied torque reference from $\omega_m = 0{,}6$ p.u. PI gains are $K_p = 5$ and $K_i = 6$. The turbine input is similar to that simulated in Fig. 4.23.

The lower PI gains slow the process of counter-torque reduction so f_{gen} is allowed to drop below the minimum tracking threshold for significant periods (although never below 0,9 p.u.). The simulated response of the speed controller to a similar input profile in Fig. 4.23 is more effective because the higher gains allow faster reaction to falling input torque.

Although this behaviour may delay synchronisation it does not imply a total failure of the system. Despite the under-speed events, significant synchronisation opportunities still exist and tracking remains within 0,1 p.u. It is also possible that controller gains could be increased with the actual wind turbine as prime mover, which would improve tracking under such conditions.

More effective control is achieved for rising input torque, as indicated in Fig. 7.7. In this case, tracking remains predominantly within 0,02 p.u. and would, in fact, be even better were it not for increased PM-rotor oscillations that occur as input torque rises. A similar increase in oscillations is evident in Fig. 7.6 for $t > 13$ s as torque rises from 0,2 p.u. These effects are, to some extent, associated with the VSD-IM as prime mover.

Speed control performance with time-varied torque input is less effective than simulation predictions due to lower controller gains and oscillatory tendencies within the drive train. Nonetheless, overshoot and tracking are controlled well enough to ensure safety and sufficient synchronisation opportunity, respectively. There is also the potential to increase gains and restore performance when the wind turbine is used as prime mover.

7.1.4 Synchronisation with Thyristor Speed Control

Combining the speed control and synchronisation functions allows the GCC to achieve its first major objective: automatic synchronisation of the SS-PMG. Simulated examples of controlled synchronisation are shown in Section 4.3.2. Measured synchronisation transients are discussed here to verify the simulation results.

The first case of controlled synchronisation is illustrated in Fig. 7.8 and takes place under the influ-

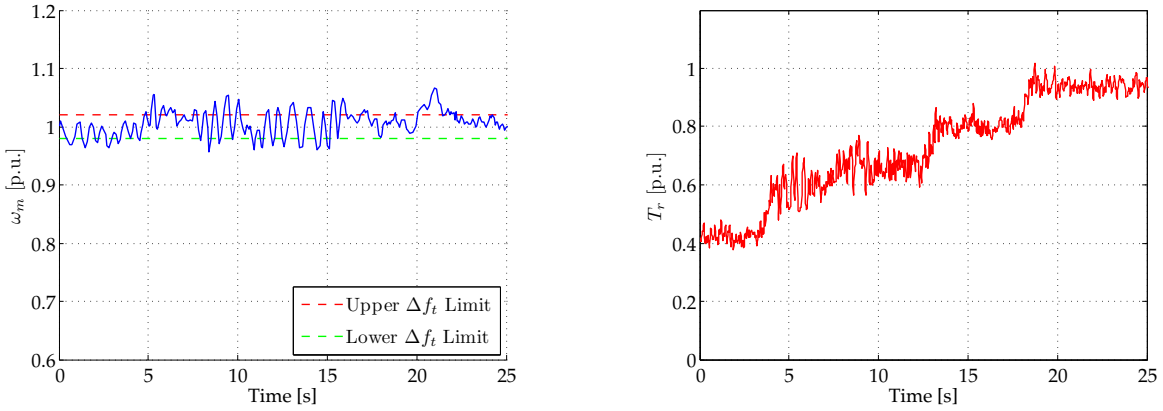

(a) PM-rotor speed as a function of time

(b) Slip-rotor torque as a function of time

Figure 7.7: Measured dynamic response of the thyristor-based speed controller to a time-varied torque reference from $\omega_m = 1{,}0$ p.u. PI gains are $K_p = 5$ and $K_i = 6$.

ence of a 0,3 p.u. torque step. In this case, the resolver could not be used to measure PM-rotor speed, so this was sampled using the *Norma* power analyser. As a result, no further changes in rotor speed are registered once the SS-PMG is synchronised—this obscures the on-grid oscillations shown in previous rotor speed measurements. The presence of these oscillations can still be inferred by the persistent torque and phase current ripples after synchronisation, shown in Fig. 7.8(b) and Fig. 7.8(d), respectively.

Fig. 7.8(a) shows that overshoot is minimal at this low torque level and synchronisation occurs within 1,2 s after the SS-PMG first enters the frequency tolerance band with $\Delta f = 0{,}006$ p.u. Despite the harmonic content of v_{gen} in Fig. 7.8(c), the phase angle agreement at synchronisation is good: $\Delta\phi = 3{,}46\,^\circ$. The voltage difference is lower than in the rated torque case, at $\Delta V = 0{,}14$ p.u. As a result, synchronisation transients are relatively low with a maximum transient current of 0,8 p.u.

After successful synchronisation under low input torque, two further cases, in Fig. 7.9, illustrate the PM-rotor dynamics for synchronisation with torque steps of 0,5 p.u. and 0,75 p.u., respectively. The PM-rotor speed for case 2, shown in Fig. 7.9(a), experiences overshoot of 7,5 %. Synchronisation takes place within 1,1 s after the SS-PMG first enters the correct frequency range. On-grid torque in Fig. 7.9(b) shows significant ripple.

For case 3, maximum overshoot is measured at 13 % in Fig. 7.9(c). Here, synchronisation occurs within 2 s of first entering the frequency tolerance band. Slip-rotor torque, shown in Fig. 7.9(d), exhibits less on-grid ripple than in case 2. Prior to synchronisation, however, a period of significant oscillation occurs in the range $-1\,\text{s} < t < 0s$. This occurs because the thyristor firing angle controller is being forced to skip the unstable band discussed in Section 6.3.2. As a result, the SS-PMG is exposed to step changes in thyristor loading while input torque remains within the $0{,}5\,\text{p.u.} < T_t < 0{,}7\,\text{p.u.}$ range.

The measured results shown here lead to three observations. Firstly, synchronisation typically occurs within 2 s of entering the frequency tolerance band. This means that long-term tracking during unsteady input conditions is not especially important. Secondly, interactions between the VSD control loops and the electrical network result in PM-rotor speed, current and torque ripple after synchronisation. This effect is more pronounced at lower torque levels but it remains to be seen what ripple will

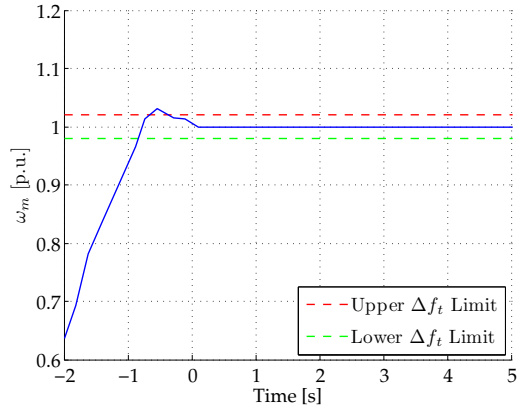

(a) PM-rotor speed as a function of time

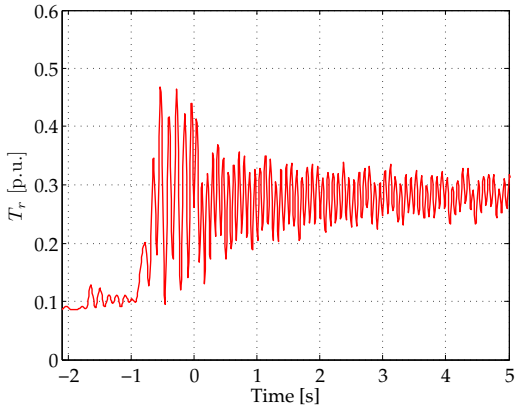

(b) Slip-rotor torque as a function of time

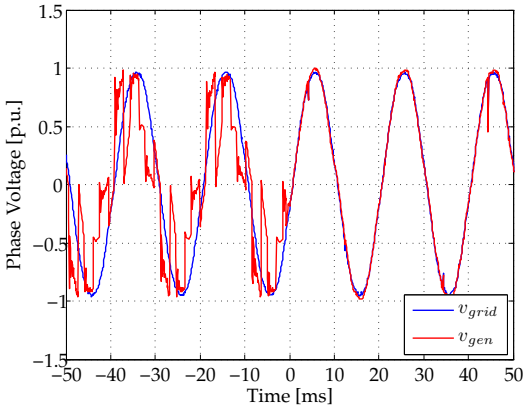

(c) SS-PMG and grid instantaneous phase voltage as a function of time

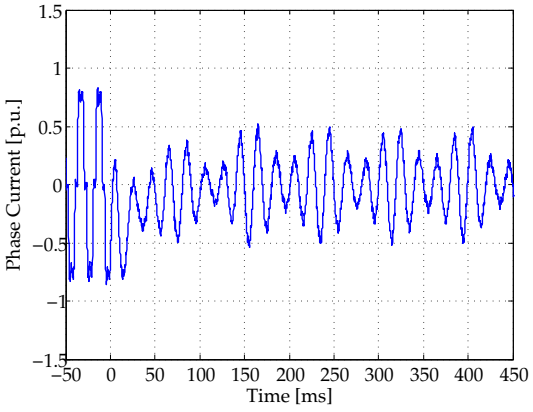

(d) Instantaneous phase current as a function of time

Figure 7.8: Dynamic response during SS-PMG synchronisation with thyristor speed control active. Synchronisation occurs at $t = 0$ s.

be present during in-field testing. Finally, the implementation challenges with thyristor control that were discussed in the previous chapter do not prevent the successful operation of the GCC. However, smoother performance could be achieved if these issues were resolved completely.

7.2 Field Tests

Laboratory test results show that the simulation design process rendered valid results and that the GCC is capable of automatically synchronising the SS-PMG with the grid under a variety of steady conditions. Certain questions do remain about the influence of the VSD-IM-GB on the stability and dynamics of the system, though. To resolve these issues and to verify operation under fully realistic wind conditions, the SS-PMG and GCC are now tested as part of a functioning wind turbine system. After the field test setup is described, the effectiveness of speed control and synchronisation are investigated.

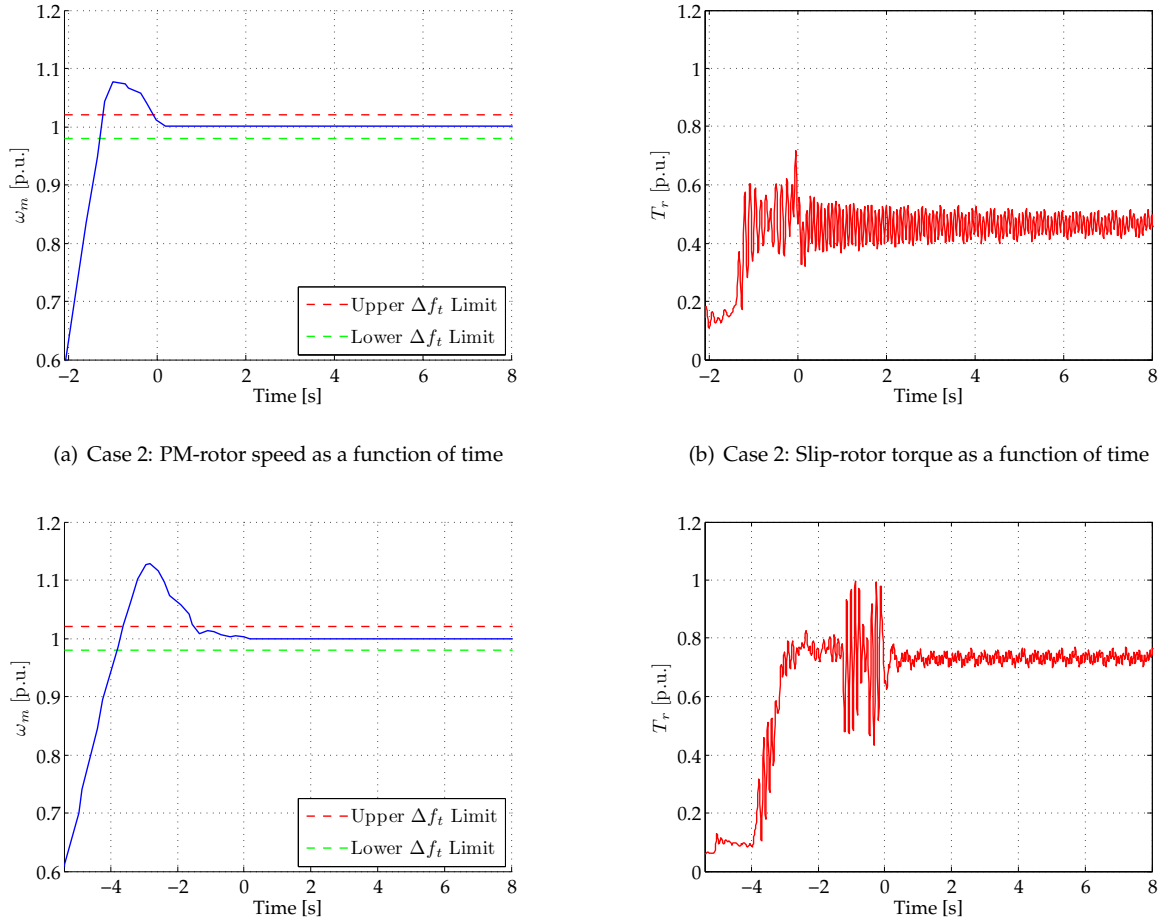

(a) Case 2: PM-rotor speed as a function of time

(b) Case 2: Slip-rotor torque as a function of time

(c) Case 3: PM-rotor speed as a function of time

(d) Case 3: Slip-rotor torque as a function of time

Figure 7.9: Further examples of dynamic response during SS-PMG synchronisation with thyristor speed control active. Synchronisation occurs at $t = 0$ s.

7.2.1 Field Test Setup

7.2.1.1 Siting and Wind Characteristics

A wind turbine test site has been established directly behind the engineering faculty at Stellenbosch University. The wind conditions in this area are, however, far from ideal. In addition to normal seasonal and diurnal variations, the wind is turbulent and unpredictable due to the proximity of numerous buildings and tall trees. Although strong gusts and high wind speeds do occur during certain seasons, the average wind speed at the site is less than 4 m/s. Time constraints did not allow testing during ideal conditions so the results presented here were generally recorded for wind speeds below 8 m/s.

7.2.1.2 Installation of the Turbine, SS-PMG, and GCC

The 7,2 m wind turbine and 15,9 kW SS-PMG were installed atop a tubular tower with an added extension, giving a hub height of approximately 18 m. The extension was added in an attempt to reach wind zones with less turbulence and higher average speed.

The tower is attached to a hinged base, which allows it to be laid horizontally on the ground. Mount-

ing the WECS on the tower begins with connecting the SS-PMG and nacelle to the top flange of the tower while at ground level. The spring-tensioned tail vane is then connected to the nacelle (for a description of the yaw control mechanism, see Section 3.1.2).

Finally, the three turbine rotor blades are mounted directly to the front plate of the SS-PMG slip-rotor. The tower must be lifted slightly to allow the final blade to be installed, after which the nose cone can be screwed in place. Once all components are secure, the tower can be lifted into its vertical position by a crane, as shown in Fig. 7.10(a). Bolts secure the tower to the base-plate, which is itself secured to a foundation block.

The fully installed WECS is shown in Fig. 7.10(c), where the nose-cone, blades, SS-PMG, nacelle, and tail vane are all visible. Close inspection will reveal that the tensioning spring for the tail vane has been replaced by steel cable, effectively holding the tail vane perpendicular to the rotor plane. This was after the spring became damaged in the lifting process. The upshot of this arrangement is that no rotor torque reduction can occur under high winds, but none were encountered during the test period so the effect of this change was minimal.

Underground armoured cabling connects the SS-PMG to the GCC, which is installed in a nearby distribution room, shown in Fig. 7.10(b). The GCC employed for the field tests was not equipped with monitoring dials or manual override switches so an external monitoring console that provides these features is also visible. The GCC, in turn, connects directly to the low-voltage electrical distribution board shown in the figure. The resistor cage was carried outside to improve cooling during prolonged testing but could be left in the distribution room during normal operation.

7.2.1.3 Measuring Instruments

In the absence of a shaft-speed resolver, the *Norma* power analyser was again called upon to measure and log f_{gen}. A Tektronix oscilloscope with differential voltage probes and a clamp-on current probe was used to measure line voltages and phase current. Phase voltages could no longer be measured because the neutral point of the SS-PMG was not available through the slip-ring coupling in the nacelle—this coupling is necessary because it allows the nacelle to rotate freely without risking cable twist.

An anemometer providing real-time wind speed data was not available during the field tests. As such, it is only possible to attach an average wind speed value to the measurements presented in the sections that follow.

7.2.2 Speed Control

Laboratory investigations indicate that the reduced-gain PI speed controller is functional but does not deliver ideal results under turbulent conditions. To verify these observations, the performance of the thyristor-based speed controller was tested with a real turbine as prime mover under turbulent wind conditions.

Controller gains were set according to the values chosen in Section 7.1.3.1 and, for comparative purposes, synchronisation was not enabled. Under this arrangement the turbine and SS-PMG are allowed

(a) Raising the 15 kW SS-PMG WECS and tubular tower on a pivoting base. The extension segment allows for a hub height of 18 m

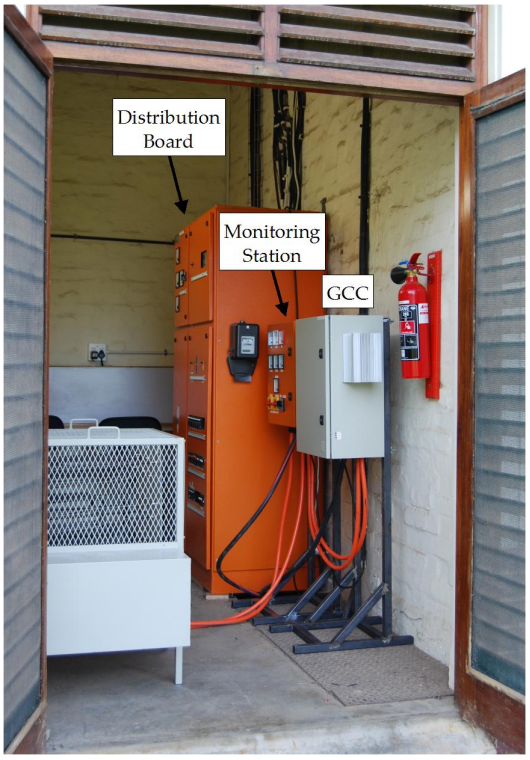

(b) Indoor location of the GCC, where it connects the WECS to the local grid through a distribution board. The monitoring station and resistor cage are also visible.

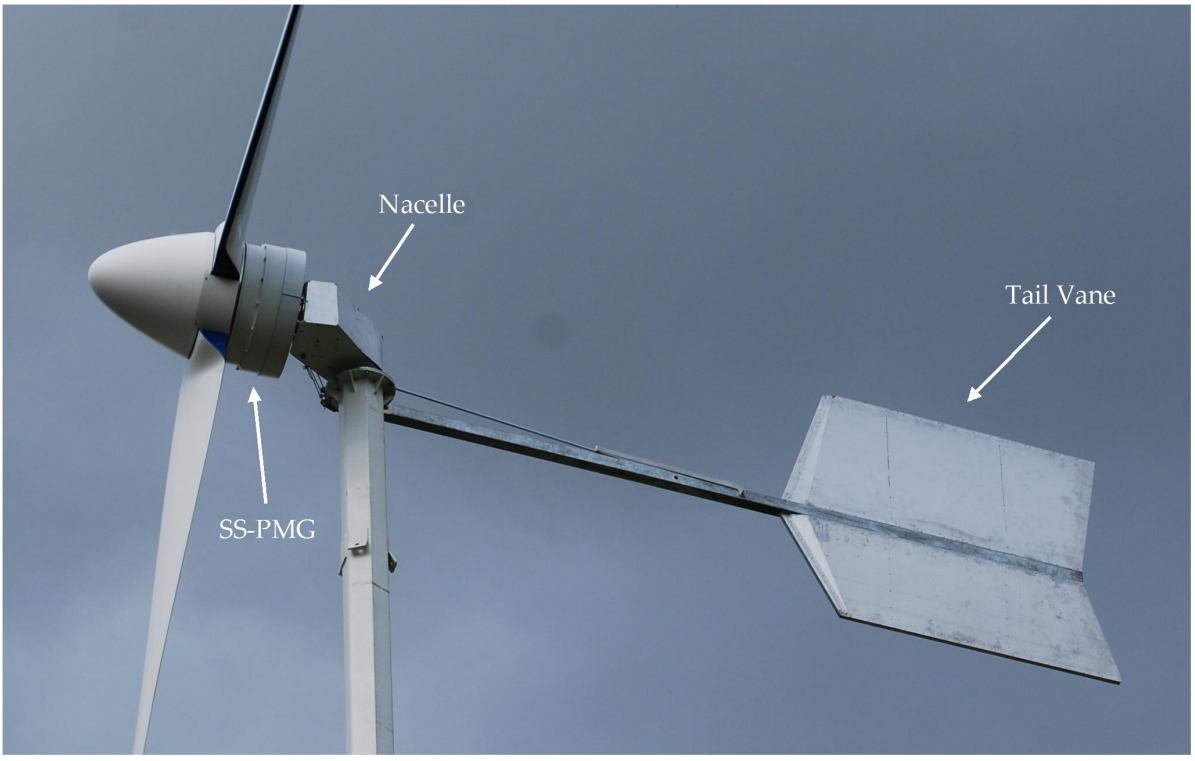

(c) Close-up view of the tower-top components of the WECS, including the SS-PMG, nacelle and yaw-controlling tail vane

Figure 7.10: In-field test setup.

to run freely until the cut-in rotational speed ($f_{gen} = 0{,}6$ p.u.) is reached, at which point the speed controller attempts to maintain f_{gen} at 1 p.u. indefinitely.

The PM-rotor speed traces in Fig. 7.11 are for low to moderate wind speeds with significant turbulence present. In Fig. 7.11(a) and Fig. 7.11(b) the effectiveness of speed control over relatively long periods is illustrated. Tracking is well centred on $f_{gen} = 1$ p.u. and $\Delta f_t < 0{,}02$ p.u. for the majority of both traces. The significant deviations that occur involve f_{gen} falling below the target frequency band, reflecting the same limitation that is discussed in Section 7.1.3.2: the speed control mechanism can only reduce net torque, not increase it. If wind speed falls below 4 m/s then a reduction in f_{gen} is inevitable.

On the other hand, wind speeds too low to hold the turbine at synchronous speed will not allow the SS-PMG to act as a net exporter of energy. When connected to the grid under such wind conditions, the SS-PMG will ultimately switch over to motoring mode to hold the WECS at speed, which is an undesirable situation. The GCC detects reverse power and disconnects the SS-PMG after a set period, but it may be preferable to avoid synchronisation altogether during marginal wind conditions.

The remainder of the PM-rotor speed plots show tracking over shorter periods. In Fig. 7.11(d), turbulent conditions cause rotor speed oscillations between $t = 20$ s and $t = 40$ s but control is recovered for the remainder of the recorded period. Fig. 7.11(c), Fig. 7.11(e), and Fig. 7.11(f) exhibit consistent tracking as long as the wind speed remains high enough to support it. Overshoot never exceeds 8 %.

These in-field measurements show that the thyristor-based speed controller is successful at achieving its design objectives under low to moderate wind conditions. It can be expected that f_{gen} deviations will increase at higher average wind speeds with stronger gusts, but a significant margin of safety exists—overshoot can double compared to the values recorded in Fig. 7.11 without posing a danger to the turbine or SS-PMG.

There is also no sign of the rotor oscillations that occurred during speed control with the VSD-IM as prime mover. As predicted, the wind turbine imparts a more damped response. This leaves room for the speed controller gains to be increased, if necessary, to cope with sites that have higher average wind speeds.

7.2.3 Synchronisation

Experimental results from the laboratory show that the GCC is capable of synchronising the SS-PMG successfully under a variety of steady input torque levels. With speed control shown to be effective, it is now possible to evaluate automated synchronisation under truly turbulent conditions.

In Fig. 7.12 an example of synchronisation at an average wind speed of approximately 4 m/s is shown. Despite the low rate of acceleration evidenced in Fig. 7.12(a), synchronisation occurs within 2,2 s of entering the correct frequency band. $\Delta f = 0{,}0062$ p.u. at the moment of connection, while from Fig. 7.12(b) it can be determined that $\Delta\phi = 5{,}32\,^\circ$ and $\Delta V = 0{,}0212$ p.u.

With all synchronisation conditions met, the maximum current transient after connection reaches 0,199 p.u. and the maximum grid voltage drop is 0,92 %. All dynamic conditions for successful synchronisation are thus satisfied. It is also interesting to note that the steady-state phase current in Fig. 7.12(c) is relatively stable, despite continuous changes in wind speed.

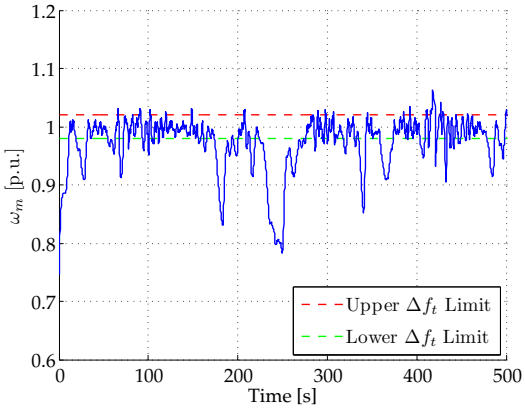

(a) PM-rotor speed as a function of time: case 1

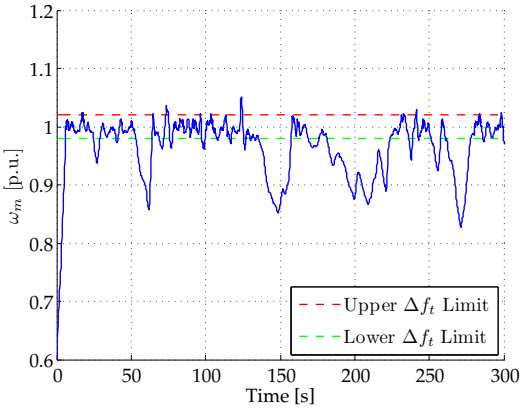

(b) PM-rotor speed as a function of time: case 2

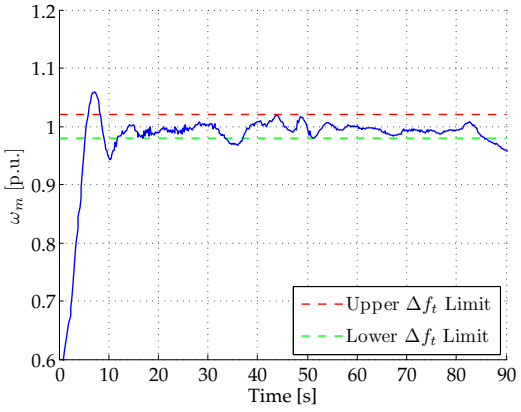

(c) PM-rotor speed as a function of time: case 3

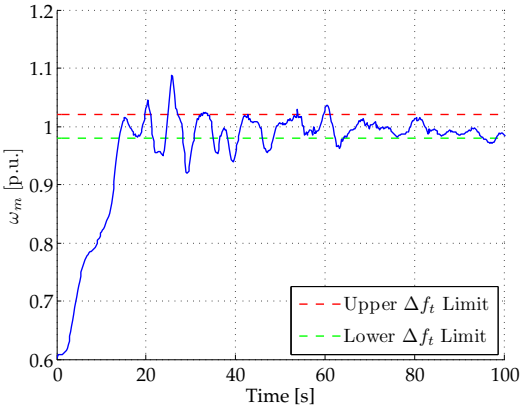

(d) PM-rotor speed as a function of time: case 4

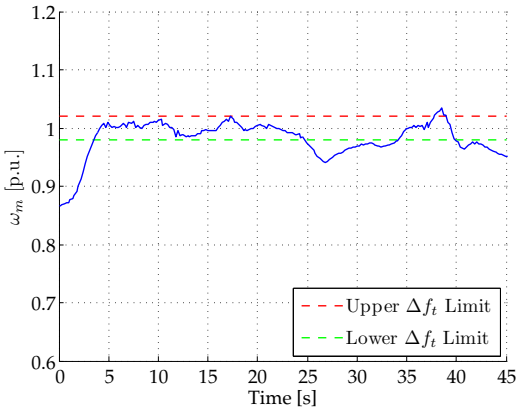

(e) PM-rotor speed as a function of time: case 5

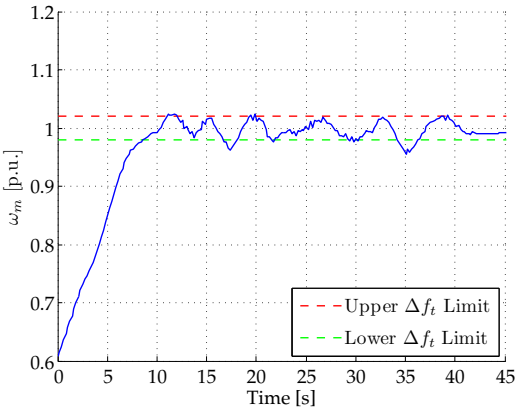

(f) PM-rotor speed as a function of time: case 6

Figure 7.11: Speed control performance of the GCC during field tests. Wind conditions were highly variable, with frequent gusts and directional changes. Wind speed at hub height was in the range $2\,\mathrm{m/s} < u_w < 8\,\mathrm{m/s}$ during these cases.

A second example of synchronisation—this time at an average wind speed of approximately 5 m/s—is illustrated in Fig. 7.13. With higher acceleration, synchronisation occurs within 1,4 s of the f_{gen} first entering the frequency tolerance band, as indicated in Fig. 7.13(a). At the time of connection, $\Delta f =$

0,0081 p.u., $\Delta\phi = 1{,}80\,°$, and $\Delta V = 0{,}0255$ p.u.

Fig. 7.13(c) shows that the maximum current transient during synchronisation is 1,33 p.u., which is an extreme case: other similar synchronisation runs generated current maxima of no more than 0,75 p.u. The grid voltage drop during the first post-connection cycles reaches 2,6 %, thus exceeding the regular re-connection limit of 1 %. In other respects, the synchronisation is successful and stable—transients attenuate within 400 ms and steady-state phase current is remarkably free of ripple.

These examples illustrate that the GCC is able to meet Δf and $\Delta\phi$ requirements, ensuring stable synchronisation, even though ΔV cannot be controlled in the same manner. It is also evident that the speed controller typically only needs to provide a window of 2 s to 3 s where $\Delta f \leq \Delta f_t$ to facilitate grid connection.

As seen in the simulations and laboratory experiments, ΔV inevitably increases with load. The grid voltage drop after synchronisation also tends to increase with wind speed. The GCC cannot, however, influence these trends without some form of reactive power compensation.

To return to the matter of on-grid stability, a comparison between the current ripple measured in the

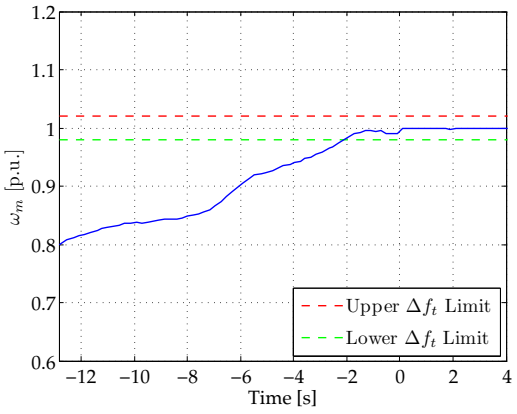

(a) PM-rotor speed as a function of time

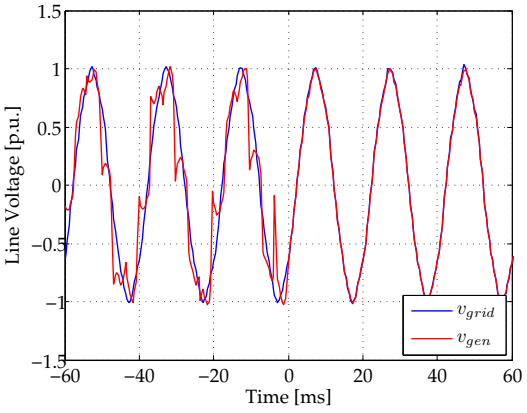

(b) SS-PMG and grid instantaneous line voltage as a function of time

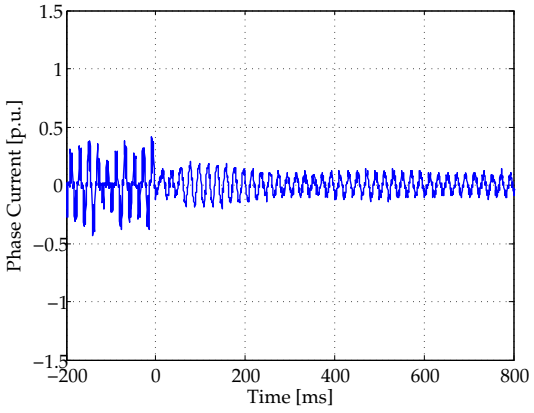

(c) Phase current as a function of time

Figure 7.12: Synchronising the SS-PMG WECS to the grid with the aid of thyristor-based speed control under low wind conditions. Synchronisation occurs at $t = 0$ s.

laboratory and in the field is presented in Fig. 7.14. The comparison is made for RMS phase current below 0,3 p.u., which is typically where the test bench shows worst performance but is also coincidentally the most common level encountered during field testing.

The difference between the two cases is significant: worse case ripple in the field example is 35,73 %, compared to 483,3 % between minimum and maximum in the laboratory. Considering that the torque input from the VSD-IM is nominally constant, whereas wind conditions vary continuously, this difference is even more surprising.

Clearly, the laboratory test bench introduces unstable interactions into the system, which are not inherent to the SS-PMG. This implies that the test bench results can serve as a worst case scenario in terms of ripple and stability. When the SS-PMG is driven by the wind turbine its on-grid dynamics are more stable and prove a closer match to the predictions made using simulations. This, in turn, further validates the theoretical design.

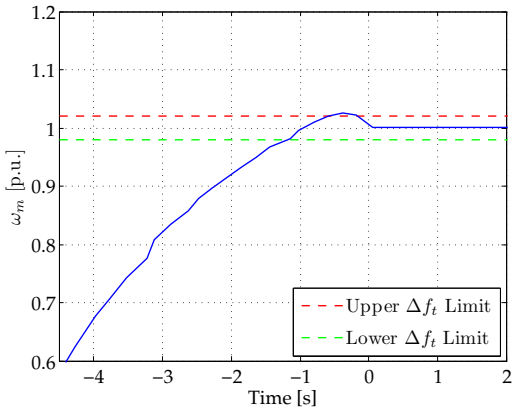

(a) PM-rotor speed as a function of time

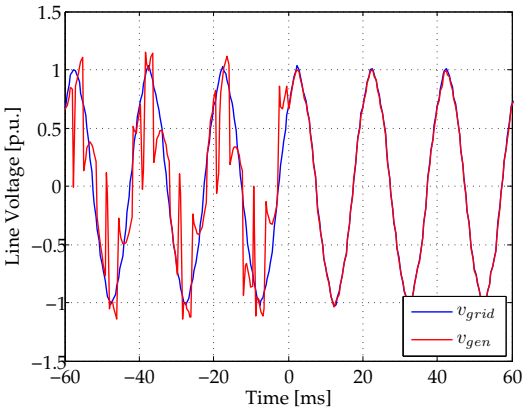

(b) SS-PMG and grid instantaneous line voltage as a function of time

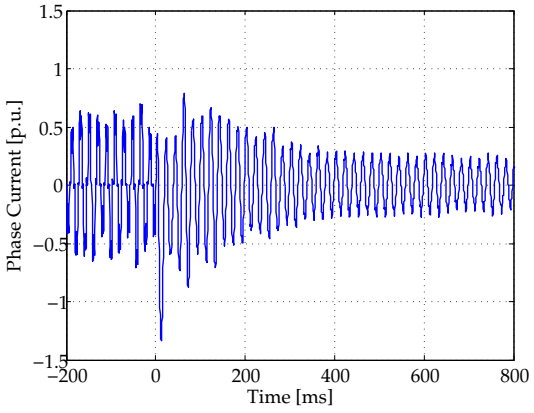

(c) Phase current as a function of time

Figure 7.13: Synchronising the SS-PMG WECS to the grid with the aid of thyristor-based speed control under moderate wind conditions. Synchronisation occurs at $t = 0$ s.

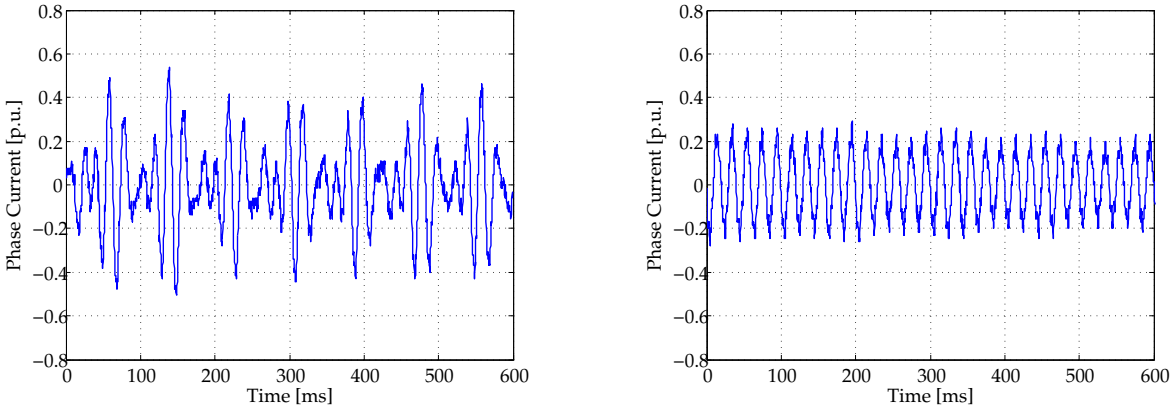

(a) Instantaneous phase current as a function of time during on-grid operation in the laboratory with $I_{rms} = 0{,}27$ p.u.

(b) Instantaneous phase current as a function of time during on-grid operation in the field with $I_{rms} = 0{,}20$ p.u.

Figure 7.14: Current ripple in the laboratory and in the field after synchronisation at low input torque.

7.3 Summary

In this chapter, practical investigations were used to validate the design and performance of the GCC. The aspects covered included speed control and synchronisation, in both the laboratory and as part of an operational WECS. LVRT measurements have been deferred to later studies because an appropriate test setup is still under development.

Laboratory measurements indicate that the theoretically-derived synchronisation conditions achieve acceptable results, although the tolerance bands programmed into the MCU have been narrowed to account for uncertainties in the system. Significant oscillations were encountered during grid connection and more so during thyristor-based speed control. As a result, the GCC speed controller gains have been reduced to ensure stable operation. Lower gains affect the dynamics of the controller but still facilitate acceptable tracking and overshoot under a variety of torque steps.

Due to the reduced controller gains, tracking during time-varied input is not on par with simulated predictions. However, controlled synchronisation experiments indicate that long-term tracking is unnecessary since the SS-PMG is typically connected to the grid within 3 s of first entering the frequency tolerance band. The transients at synchronisation are also acceptable, with the exception of grid voltage drop that exceeds the 1 % limit for $T_t > 0{,}2$ p.u.

Field test results show improved speed control dynamics compared to the laboratory case. Overshoot (under low to moderate wind conditions) is below 10 % and most speed excursions are due to falling wind speed.

Automatic synchronisation is also undertaken successfully and the GCC holds all controllable parameters to within their defined limits. Maximum transient current varies but never exceeds the nominal 2 p.u. limit. To the author's knowledge, this is the first recorded case where an operational SS-PMG WECS has been synchronised with the national grid.

Field tests also indicate that the on-grid current ripple experienced in the laboratory is a product of interactions between the VSD-IM-GB and the grid. In contrast, the on-grid characteristics of the SS-PMG

in the field approach those predicted by simulations. This suggests that the GCC speed controller gains can be raised, if necessary, without experiencing the negative affects noted during laboratory tests.

In conclusion, practical investigations have shown the GCC concept to be valid and feasible. It meets all basic operational requirements and is capable of automatically synchronising the SS-PMG with the national grid during turbulent wind conditions. This opens the door to longer term tests of the SS-PMG WECS at more appropriate wind sites.

CHAPTER 8

CONCLUSIONS AND RECOMMENDATIONS

8.1 Conclusions

The aim of the work documented in this report is to develop a grid connection controller for a small-scale SS-PMG in a wind turbine application. The GCC is to facilitate automated synchronisation with the grid, low voltage ride-through, and necessary protection against other adverse conditions. Referring to the objectives stated in Section 1.4.3, the following conclusions can be drawn:

8.1.1 Synchronisation Conditions

The conditions for successful synchronisation relate to frequency difference, voltage difference, and phase angle difference between the SS-PMG and the grid. Additionally, input torque should be minimised, along with rotor acceleration. (It is not possible to control turbine torque for the small-scale WECS under investigation but acceleration can be minimised through speed control.)

Appropriate tolerance margins for frequency and phase angle difference are $\Delta f_t = 0{,}02\,\text{p.u.}$ and $\Delta\phi_t = 10\,^\circ$. The recommended margin for voltage is $\Delta V_t = 0{,}1\,\text{p.u.}$ but SS-PMG terminal voltage is a function of both rotational speed and loading. As a result, ΔV is dependent upon Δf and SS-PMG load current.

Simulations show that ΔV must be controlled to meet grid code requirements and minimise post-synchronisation current spikes. If, however, the current maxima and the grid voltage reduction can be tolerated then controlling ΔV is not otherwise necessary for successful synchronisation. Satisfying Δf and $\Delta\phi$ is sufficient to ensure stable grid connection of the SS-PMG.

8.1.2 Synchronisation Controller

Based on examples from literature, the synchronisation mechanism of the GCC consists of an electromagnetic braking circuit for speed control and an electromechanical contactor to connect the SS-PMG directly to the grid. Frequency, phase angle, and voltage magnitude of both SS-PMG and grid are calculated from filtered $\alpha\beta$ quantities. This allows for a sensorless design that reduces costs and improves reliability: only instantaneous SS-PMG and grid voltages, as well as SS-PMG currents, are sampled directly.

In terms of speed control, switching in resistances with contactors is shown to be infeasible—too many separate resistance values would be required to limit acceleration across the whole wind speed range. Switching with back-to-back thyristors (triacs) allows the effective load to be controlled through the firing delay angle. The ability to vary the SS-PMG load incrementally (and the speed at which load changes can be made) allows for a closed-loop speed controller to be employed.

Simulations show that the GCC speed controller, with a PI regulator, is able to prevent excessive overshoot and ensure $|\Delta f| < \Delta f_t$ under both steady and turbulent wind conditions. This enables fast and reliable synchronisation, although the contactor actuation delay can result in $\Delta\phi$ exceeding $\Delta\phi_t$ at the moment of connection. There is also a possibility that $\Delta\phi$ may become fixed outside the tolerance range—thus preventing synchronisation—if perfect frequency tracking is achieved.

8.1.3 Low Voltage Ride-Through

For the purposes of this study, LVRT compensation implies maintaining SS-PMG rotor angle stability and limiting fault currents during grid voltage dips. Literature suggests that both series and shunt resistances may be employed to assist in this compensation process.

Simulation studies indicate that the SS-PMG can ride-through the balanced Irish fault profile for $u_w < 9\,\mathrm{m/s}$. Compensation is required for wind speeds in the range $9\,\mathrm{m/s} \leq u_w \leq 12\,\mathrm{m/s}$ but neither series nor shunt resistance compensation alone is capable of ensuring stability across this range. A combination of contactor-switched series and shunt compensators is also not flexible enough to accommodate changes in input power.

The LVRT compensator can be made more adaptable by employing the same thyristor-switched braking topology used for speed control. Setting the thyristor load command according to the pre-fault power level ensures that a wide range of wind speeds can be accommodated, however, compensation removal transients and turbulent wind conditions are still problematic.

To further improve compensation it is possible to introduce a control loop that dynamically changes thyristor loading to minimise $\Delta\phi$ during the fault. In this way, it is possible to respond to changing wind conditions while reducing compensation removal transients to an acceptable level.

This PAC-LVRT compensator ensures stability during both the Irish and South African voltage dip profiles, even under turbulent wind conditions. It also functions acceptably during unbalanced faults, but performance can be improved by the addition of per-phase RMS voltage monitoring to prevent premature compensation removal.

The implementation of PAC-LVRT and development of an appropriate test setup is still ongoing so practical investigation results are not yet available.

8.1.4 Implementation

The GCC can be realised with mainly off-the-shelf components—the most important exception is a custom-designed controller board to interface the MCU with sensors and actuators. It is substantially cheaper to build than a full-scale frequency converter, but the feasibility of the SS-PMG WECS also depends on other factors, such as: the comparative cost of the generator; O&M requirements; and energy yield.

The MCU is responsible for implementing the various control and protection functions. Its program sequence is interrupt-driven and is managed by a supervisory control function, which activates different functions depending on the state of the SS-PMG. Protection functions are necessary for over-speed, over-current, phase imbalance, reverse power, and islanding.

As a result of the high reactance of the SS-PMG, thyristor operation is compromised in a certain band of firing delay angles. The thyristor driver ceases to operate correctly in this range due to harmonic distortion of the terminal voltage waveforms. Adding capacitors in shunt between the SS-PMG terminals and the neutral point of the load can remedy this behaviour but introduces new issues, including resonance and changes to the RMS value of the terminal voltage.

8.1.5 Practical Testing

In laboratory tests, the effect of $\Delta\phi$ at synchronisation follows a similar trend to what was theoretically determined, but with a high degree of scatter. To account for this uncertainty and to counteract the contactor closing delay, $\Delta\phi_t$ and Δf_t are set to half their original values in the MCU programming.

The PI gains for the speed controller have also been reduced from $K_p = 15$ and $K_i = 20$ to $K_p = 5$ and $K_i = 6$ in order to prevent unstable behaviour in the PM-rotor during laboratory testing. The speed controller still achieves good tracking under steady input conditions and overshoot does not exceed the safety limit of 20 % but tracking under time-varied input is less effective than with the higher gains. Nonetheless, controlled synchonisation is achieved reliably under various conditions.

The GCC and SS-PMG operate successfully as part of an operational WECS. Speed control is satisfactory, both in terms of tracking and limiting overshoot, although strong wind conditions were not encountered. The GCC synchronises the SS-PMG with the grid according to the set limits and the resulting transients are also within tolerance margins.

The on-grid stability of the SS-PMG WECS is substantially improved over the laboratory case, indicating that a geared induction motor driven by a VSD is not an ideal substitute for a wind turbine. This also suggests that the GCC speed controller gains can be increased, if necessary, under stronger wind conditions. In conclusion, a functional GCC is now available to allow long-term field testing of the SS-PMG WECS.

8.2 Recommendations

Following on from the conclusions reached above, a number of recommendations can be made for future investigations:

- Thyristor-based speed control could be refined by employing more sophisticated control techniques and testing the response with a better wind turbine simulator in the laboratory. A PM-rotor with a higher inertia could also serve to improve stability.
- The present speed controller makes use of a 3-phase dumping load, switched (AC-to-AC) by 3 pairs of back-to-back thyristors. This arrangement could be replaced by a DC dumping load with chopper circuit, connected to the SS-PMG through an uncontrolled 3-phase diode rectifier. Effective load resistance could then be controlled by the chopper, thereby allowing the SS-PMG load current to be varied incrementally. This approach, proposed for IG WECS in [52], would overcome the thyristor implementation issues, while reducing cost and complexity. A related possib-

ility would be to change the thyristor pack configuration from AC-AC to AC-DC, which would reduce the number of cables and resistors required.

- Whichever type of braking load is employed, the SS-PMG will still exhibit a terminal voltage drop under load. This results in the ΔV_t condition being violated under stronger wind conditions, contributing to voltage flicker in surrounding parts of the network. Installing shunt capacitors, as illustrated in Fig. 6.13, can counteract this problem and improve thyristor performance. Issues such as resonance between the capacitors and stator inductance, increased current harmonics, and excessive changes to the terminal voltage must be resolved for this approach to succeed.
- The propensity of the SS-PMG to motor under marginal wind conditions should be pre-empted by ceasing all operation during wind speeds in the range of $0\,\mathrm{m/s} \leq U_w < 4\,\mathrm{m/s}$. A timed shut-down could be employed to allow wind conditions to improve before attempting to synchronise again.
- The PAC-LVRT was initially designed to compensate for the Irish voltage dip profile, where compensation is not necessary during low winds. It should now be optimised for the South African dip profile, which includes a period of 0 p.u. voltage at the PCC. This zero voltage period effectively disconnects the SS-PMG from the grid, meaning control intervention is required under all wind conditions to ensure that the SS-PMG remains in synchronism.
- In the case of a wind farm based on the SS-PMG, a thyristor-based tap-changing transformer may be employed between the farm and the national grid. A series compensation resistance could then be installed in parallel with the transformer thyristors. The current flow through this resistor would be controlled by the firing delay angle of the thyristors, which could be varied as a function of the PCC voltage error during grid faults. In this way, the operation of the series compensation resistance at each WECS could be replaced by a single function at the transformer, reducing the cost and complexity of the system. The ability to remove the series resistance incrementally would also serve to smooth the LVRT response.
- A tap-changing transformer, coupled with selectable shunt capacitors, could be used to control the collective terminal voltage and power factor of all SS-PMG WECS in a wind farm. This form of compensation would supplement the present GCC functionality to achieve better grid code compliance.

Appendices

APPENDIX A

SYSTEM PARAMETERS

Table A.1: System Parameters

Parameter	Symbol	Value
Turbine Parameters		
Air density	ρ	1,225 kg·m^{-3}
Operational wind speed range		4 – 12 m/s
Survival wind speed range		0 – 25 m/s
Nominal hub height	h_t	10 m
Terrain roughness constant	k_σ	0,189
Blades		3
Rotor diameter	D_t	7,2 m
Mass moment of inertia	J_t	226,99 kg·m^2
SS-PMG Mechanical Parameters		
Rotational speed range		0 – 200 rpm
Rated rotational speed	ω_R	150 rpm
Rated input torque	T_R	1000 Nm
Slip-rotor mass moment of inertia	J_r	5,497 kg·m^2
Slip-rotor static friction constant	B_{r0}	3,779 Nm
Slip-rotor viscous friction coefficient	B_r	0,119 98 Nm/rad·s^{-1}
PM-rotor mass moment of inertia	J_m	8,515 kg·m^2
PM-rotor static friction constant	B_{m0}	11,338 Nm
PM-rotor viscous friction coefficient	B_m	0,3599 Nm/rad·s^{-1}
SS-PMG Electrical Parameters		
Phases		3
Poles (slip-rotor and PM-rotor)	N_p	40
Rated line voltage	V_R	400 V
Rated phase current	I_R	23 A
Rated power	S_R	15,93 kVA
Rated frequency	f_R	50 Hz
Stator phase resistance	R_s	0,4 Ω
Stator d-axis inductance	L_{ds}	11,25 mH
Stator q-axis inductance	L_{qs}	15,0 mH
Stator PM-flux linkage	λ_{ms}	1,0396 Wb·t

Parameter	**Symbol**	**Value**
Slip-rotor phase resistance	R_r	3,84 µΩ
Slip-rotor d-axis inductance	L_{dr}	0,125 µH
Slip-rotor q-axis inductance	L_{qr}	0,15 µH
Slip-rotor PM-flux linkage	λ_{mr}	3,693 mWb·t
Electrical Network Parameters		
LV line voltage		400 V
MV line voltage		10 kV
HV line voltage		110 kV
Network source phase voltage	E_{grid}	230 V
Network phase resistance	R_{grid}	0,15 Ω
Network phase reactance	X_{grid}	0,15 Ω
Transformer phase resistance	R_x	0,129 Ω
Transformer phase reactance	X_x	0,26 Ω
Controller Parameters		
Contactor actuation delay	t_c	20 ms
Thyristor forward voltage	V_F	1,45 V
Thyristor bulk resistance	R_B	8,5 mΩ
Thyristor reverse resistance	R_R	100 kΩ
ADC sampling frequency	f_s	1 kHz

APPENDIX B

TURBULENT WIND MODEL

The turbulent wind signal generator for simulations is represented in Fig. 3.4, which is repeated here:

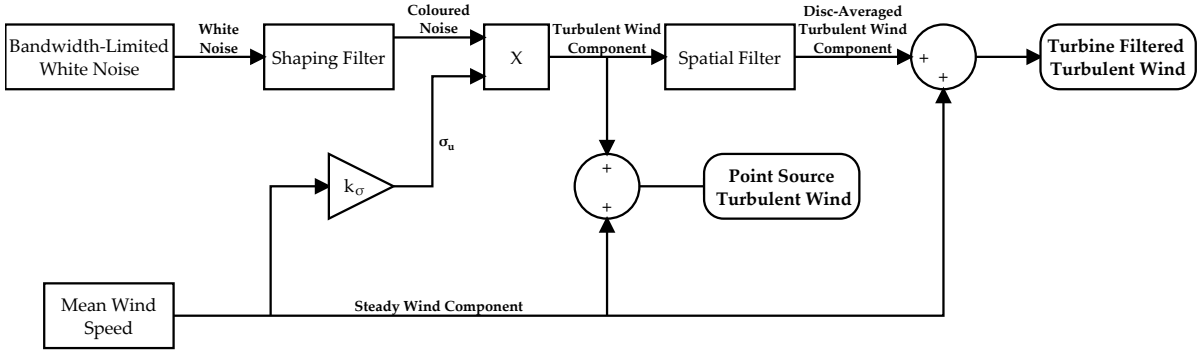

Figure B.1: Block diagram of the turbulent wind signal generator. In addition to the point-source turbulent speed signal, a turbine disc-averaged signal is also output.

The signal generator is based on the implementation of the Von Karman model in [6], which is explained here. The first step is to generate white noise with a standard deviation $\sigma = 1$. This signal must be modified by a shaping filter in order to impart the correct power spectrum frequency distribution. The continuous time transfer function required to impart a Von Karman power spectrum is given by Eqn (B.1), where K_F is the filter gain and t_F is the filter time constant.

$$W_{VK}(s) = \frac{K_F}{(1 + st_F)^{5/6}} \tag{B.1}$$

Implementing the filter of Eqn (B.1) in numerical simulation software is problematic due to its non-rational denominator. An approximation in the form of Eqn (B.2) can be used instead. In this case, $m_1 = 0{,}4$ and $m_2 = 0{,}25$, while the time constant t_F is a function of the turbulence length scale L and mean wind speed U_w, as shown by Eqn (B.3). The turbulence length is dependant on terrain conditions but can be approximated as linearly proportional to turbine hub height, as given by Eqn (B.4).

$$W_{Ni}(s) = K_F \frac{m_1 t_F s + 1}{(t_F s + 1)(m_2 t_F s + 1)} \tag{B.2}$$

$$t_F = \frac{L}{U_w} \tag{B.3}$$

$$L = 6{,}5\, h_t \tag{B.4}$$

In order to ensure that the standard deviation of the shaped white noise (coloured noise) is still 1, the filter gain constant K_F is determined by Eqn (B.5). The beta function $B(x, y)$ is given by Eqn (B.6) and is found to have a value of 11,1 for the chosen sampling time $t_S = 0{,}04\,\text{s}$.

$$K_F \approx \sqrt{\frac{2\pi}{B(x,y)} \cdot \frac{t_F}{t_S}} \tag{B.5}$$

$$B(x,y) = \int_0^1 t^{x-1}(1-t)^{y-1}\mathrm{d}t \tag{B.6}$$

The coloured noise must then be scaled by the turbulent intensity σ_u, which is given by Eqn (B.7). This imparts the correct standard deviation to the signal.

$$\sigma_u = k_\sigma U_w \tag{B.7}$$

The proportionality constant k_σ is dependant upon terrain conditions (Table B.1) and was chosen to be 0,189 in this case.

Table B.1: k_σ values for different terrain types at $h_t = 10\,\mathrm{m}$ [6].

Terrain type	k_σ
Sea	0,123
Lakes	0,145
Open areas	0,123
Built-up areas	0,285
City centre	0,434

The scale coloured noise constitutes the turbulent wind component, which can be added to the steady wind component to generate the point-source turbulent wind speed, as shown in Fig. B.1. To produce the effective wind speed experienced by the wind turbine as a whole, an additional spatial filter must be applied to account for the disc averaging effect. The transfer function for this filter is shown in Eqn (B.8) with μ determined by Eqn (B.9). The decay factor γ_s is taken to be 1,3 .

$$W_{AV}(s) = \frac{\sqrt{2} + \mu s}{(\sqrt{2} + \sqrt{0{,}55}\,\mu s)(1 + \mu s\sqrt{0{,}55})} \tag{B.8}$$

$$\mu = \frac{\gamma_s D_t}{2U_w} \tag{B.9}$$

The disc-averaged turbulent component can be summed with the steady wind component to generate the wind speed that is effectively experienced by the turbine as a whole. This value can be applied, along with rotational speed, to the turbine-torque lookup table of Section 3.1.3.

APPENDIX C

ADDITIONAL SIMULATION RESULTS

C.1 Wind Gust Response

Wind disturbances not actually under investigation here, but for illustrative purposes the stability of the SS-PMG under different wind steps is shown in Fig. C.1. Any wind speed dip can be accommodated and wind speed gusts up to a final speed of $u_w = 12\,\mathrm{m/s}$ can also always be tolerated. Even at $u_w = 12\,\mathrm{m/s}$, a further 30 % step increase in wind speed is accepable. In all these cases, maximum transient current remains well below 3 p.u. and SS-PMG rotor angle does not exceed 120 °, as illustrated by Fig. C.1(a) and Fig. C.1(b), respectively.

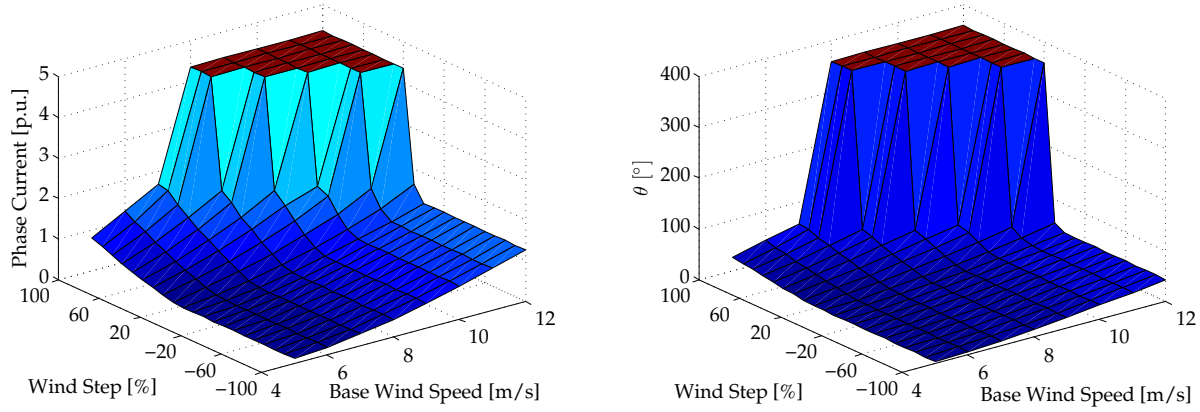

(a) Maximum instantaneous phase current as a function of wind speed and wind step proportion

(b) Maximum rotor angle as a function of wind speed and wind step proportion

Figure C.1: The effect of applying a step in wind speed to the SS-PMG WECS at different base wind speeds. The size of the wind step is given as a proportion of the base wind speed in each case.

C.2 Compensation Removal Conditions

The effect of varying the restoration voltage level V_{res} is shown in Fig. C.2. No particular change in performance is achieved by reducing V_{res} to less than V_{min}.

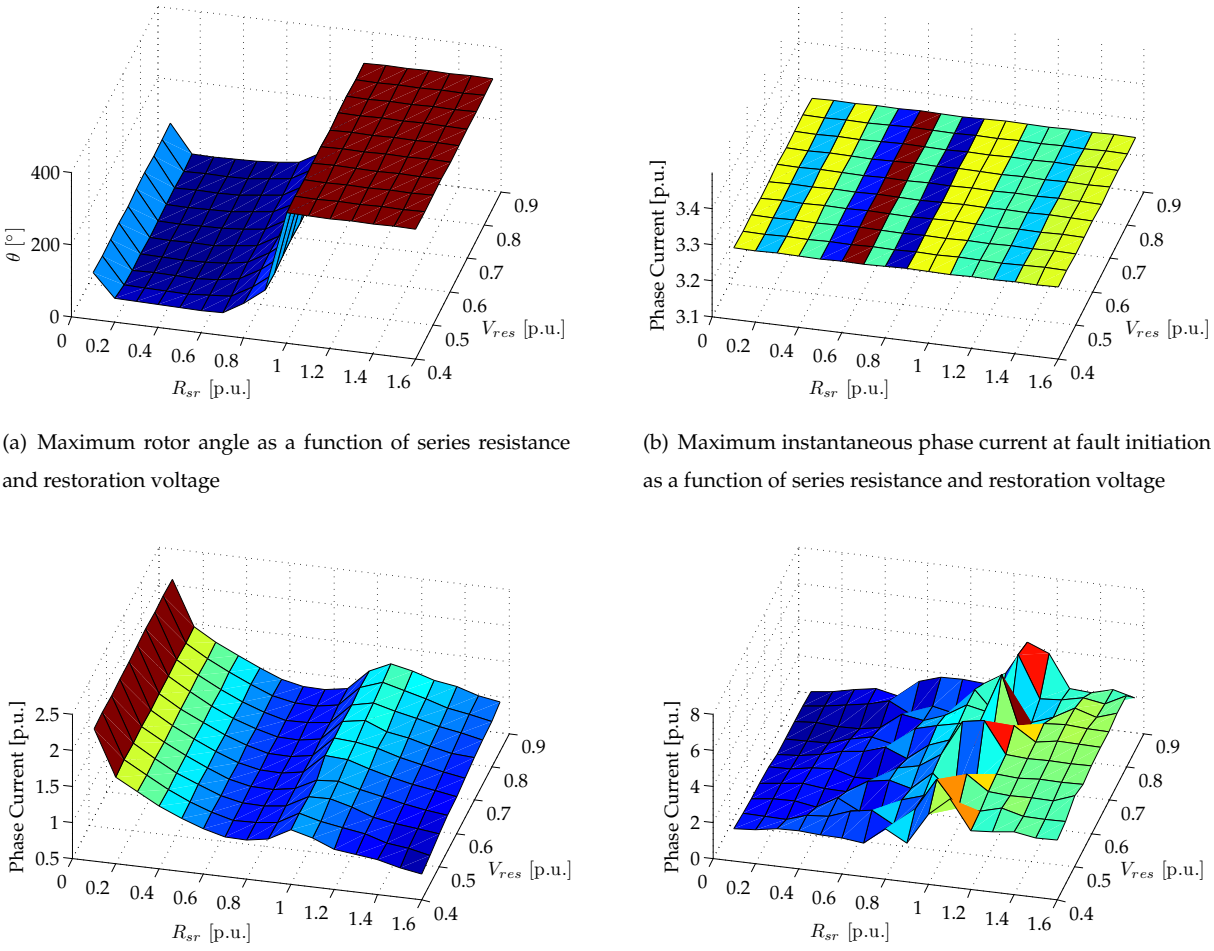

(a) Maximum rotor angle as a function of series resistance and restoration voltage

(b) Maximum instantaneous phase current at fault initiation as a function of series resistance and restoration voltage

(c) Maximum instantaneous phase current during compensation as a function of series resistance and restoration voltage

(d) Maximum instantaneous phase current during resistance removal as a function of series resistance and restoration voltage

Figure C.2: The effect of series resistance value and restoration voltage level on transients and stability for the Irish fault profile with $u_w = 11\,\mathrm{m/s}$.

The effect of delaying compensation removal time is illustrated in Fig. C.3. Once again, no real advantage is gained over removing compensation according to $V_{res} = V_{min}$.

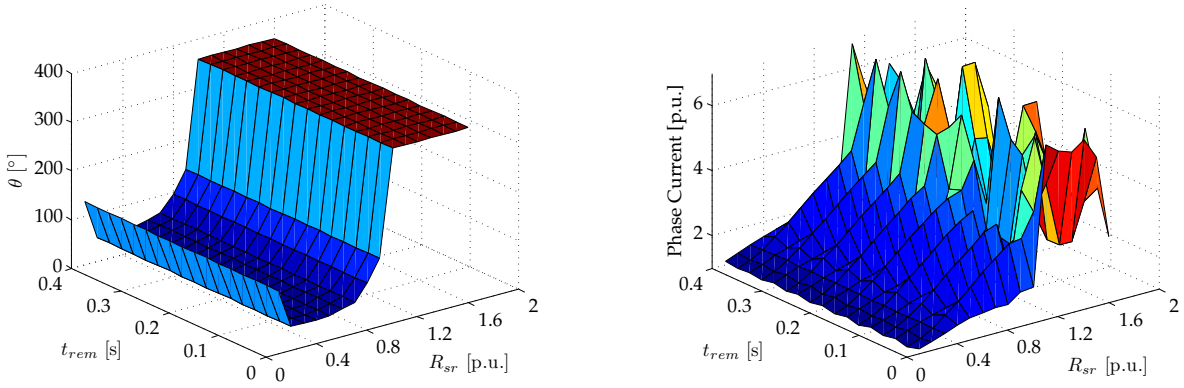

(a) Maximum rotor angle as a function of series resistance and restoration voltage

(b) Maximum instantaneous phase current during resistance removal as a function of series resistance and restoration voltage

Figure C.3: The effect of series resistance value and removal delay time on rotor angle stability and current transients for the Irish fault profile with $u_w = 11\,\mathrm{m/s}$.

C.3 SS-PMG Sensitivity to Fault Conditions

C.3.1 Sensitivity to Rotor Position at Fault Initiation

It is necessary to initiate the grid fault at a certain instant (SS-PMG rotor position) to ensure the worst case conditions are captured. The current maxima shown in Fig. C.4(a) indicate that the worst case response is achieved on phase A when faults are initiated at the set time $t = 0\,\mathrm{s}$. As a result, all further simulations employ faults initiated at this time. Rotor angle stability, shown in Fig. C.4(b), is not, however, a function of fault initiation instant, so does not warrant specific timing.

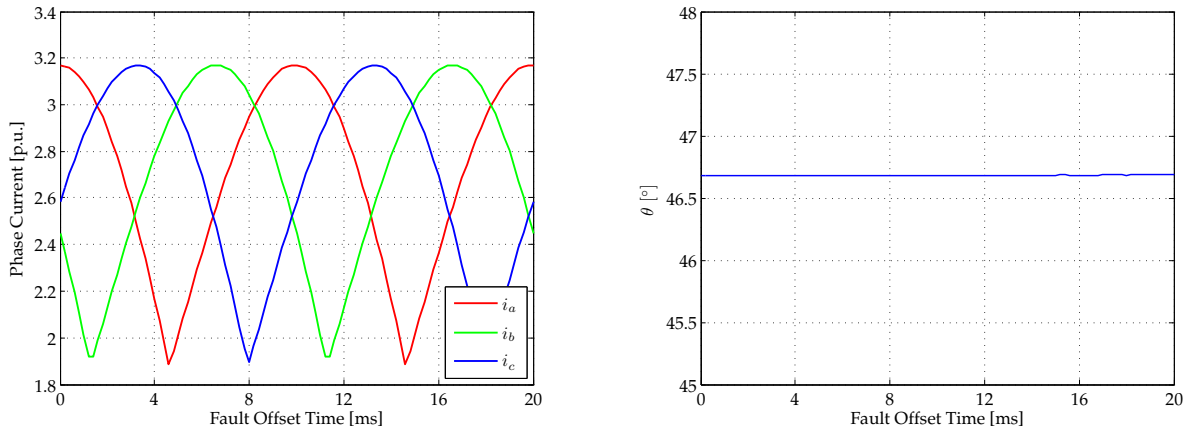

(a) Maximum instantaneous phase current at fault initiation as a function of fault initiation offset time

(b) Maximum rotor angle as a function of fault initiation offset time

Figure C.4: The effect of fault initiation time on initial transients and stability at $u_w = 5\,\mathrm{m/s}$.

C.3.2 Sensitivity to Voltage Step Magnitude and Changes in Stator Inductance

The results shown in Fig. C.5 indicate the SS-PMG response to normal voltage steps, both above and below rated voltage. Depending upon the stator inductance L_s the SS-PMG remains stable for lower or higher voltage dips. The trade-off is that lower stator inductances lead to higher fault currents, which will trip protection circuitry even if the SS-PMG may be able to remain stable under the imposed fault.

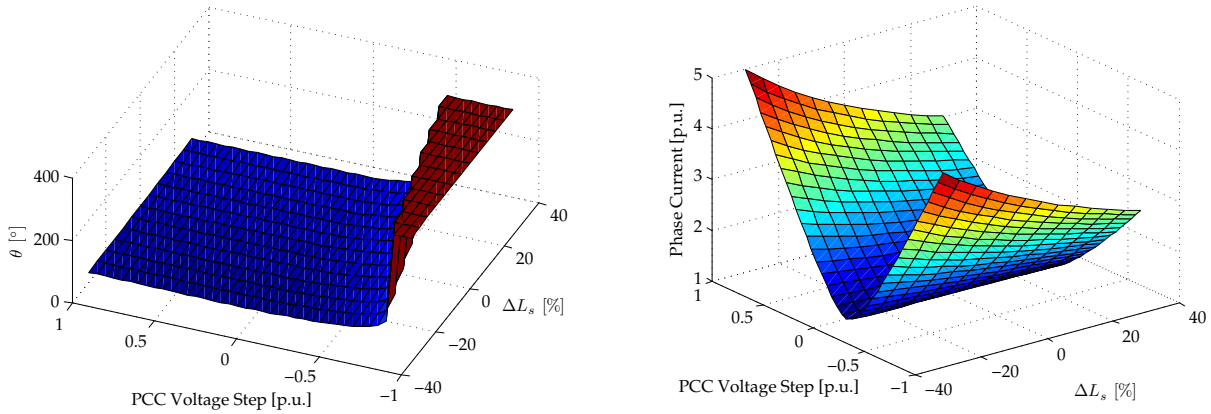

(a) Maximum rotor angle as a function of PCC voltage step and stator inductance variation

(b) Maximum instantaneous phase current at fault initiation as a function of PCC voltage step and stator inductance variation

Figure C.5: The effect of different levels of voltage step and stator inductance on rotor angle stability and current transients at $u_w = 11\,\mathrm{m/s}$.

C.4 Varying Resistance Values under Dual Resistance LVRT

These are additional results to those presented in Section 5.5.1.

C.4.1 Initial Current Spike

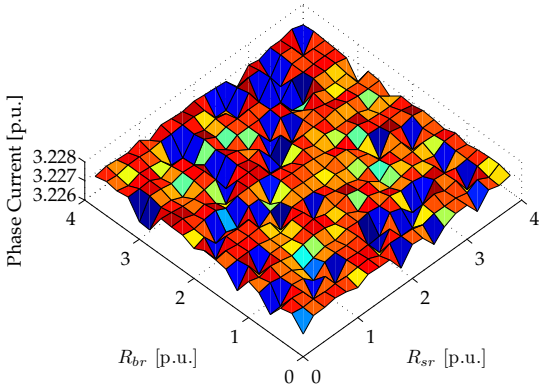

(a) Maximum instantaneous phase current at fault initiation as a function of series resistance and shunt resistance with $u_w = 9\,\mathrm{m/s}$

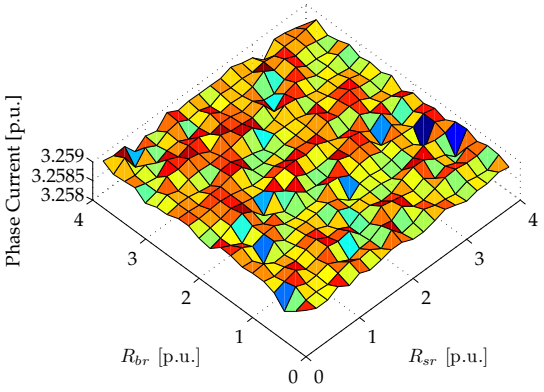

(b) Maximum instantaneous phase current at fault initiation as a function of series resistance and shunt resistance with $u_w = 10\,\mathrm{m/s}$

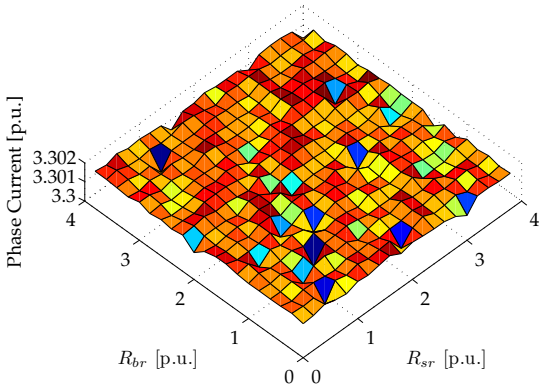

(c) Maximum instantaneous phase current at fault initiation as a function of series resistance and shunt resistance with $u_w = 11\,\mathrm{m/s}$

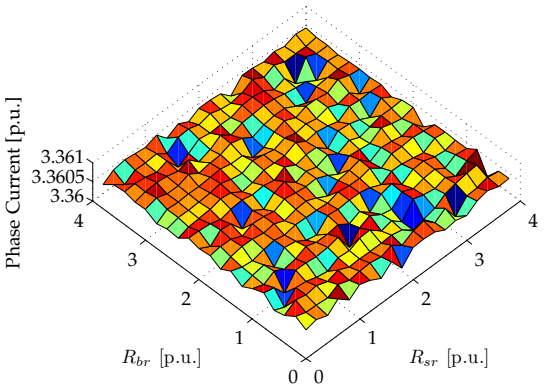

(d) Maximum instantaneous phase current at fault initiation as a function of series resistance and shunt resistance with $u_w = 12\,\mathrm{m/s}$

Figure C.6: The effect of series resistance value and shunt resistance value on initial transient current for the Irish fault profile with steady wind conditions.

C.4.2 Compensation Current

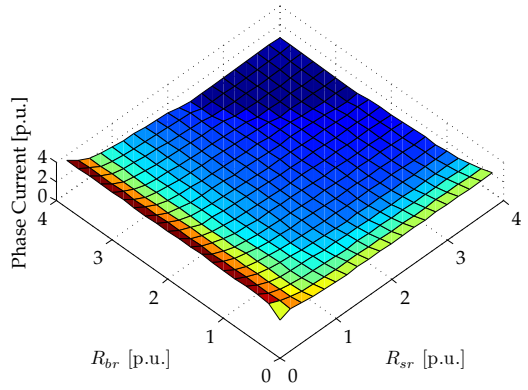

(a) Maximum instantaneous phase current during compensation as a function of series resistance and shunt resistance with $u_w = 9\,\mathrm{m/s}$

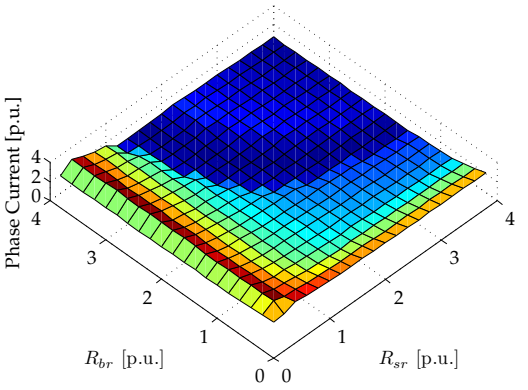

(b) Maximum instantaneous phase current during compensation as a function of series resistance and shunt resistance with $u_w = 10\,\mathrm{m/s}$

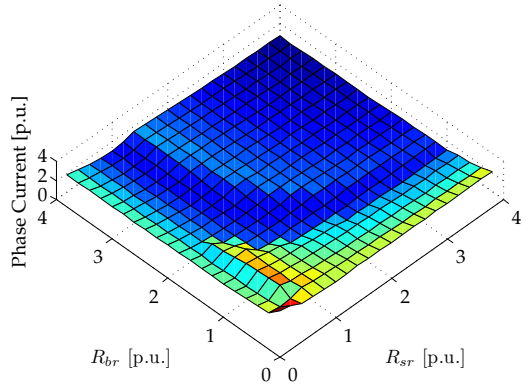

(c) Maximum instantaneous phase current during compensation as a function of series resistance and shunt resistance with $u_w = 11\,\mathrm{m/s}$

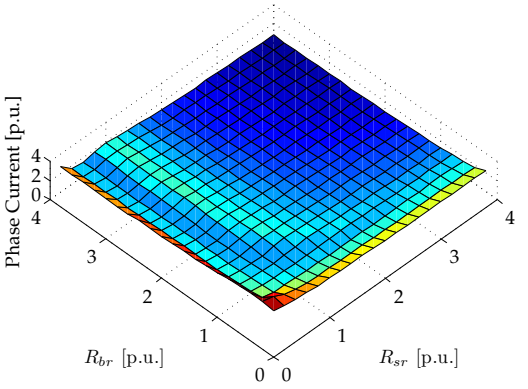

(d) Maximum instantaneous phase current during compensation as a function of series resistance and shunt resistance with $u_w = 12\,\mathrm{m/s}$

Figure C.7: The effect of series resistance value and shunt resistance value on compensation current for the Irish fault profile with steady wind conditions.

C.4.3 Resistance Removal Current

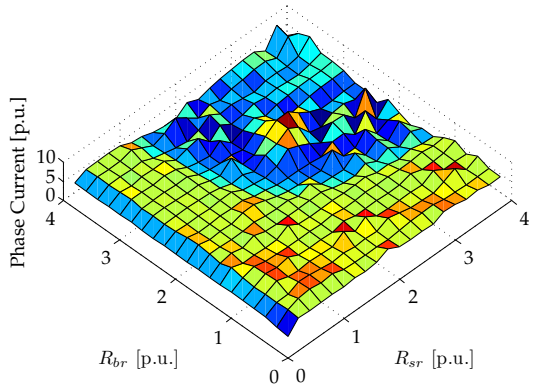

(a) Maximum instantaneous phase current during resistance removal as a function of series resistance and shunt resistance with $u_w = 9\,\mathrm{m/s}$

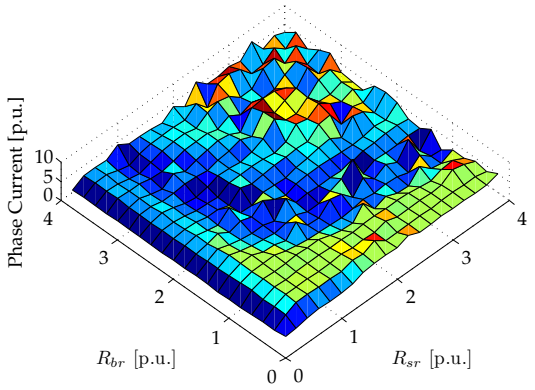

(b) Maximum instantaneous phase current during resistance removal as a function of series resistance and shunt resistance with $u_w = 10\,\mathrm{m/s}$

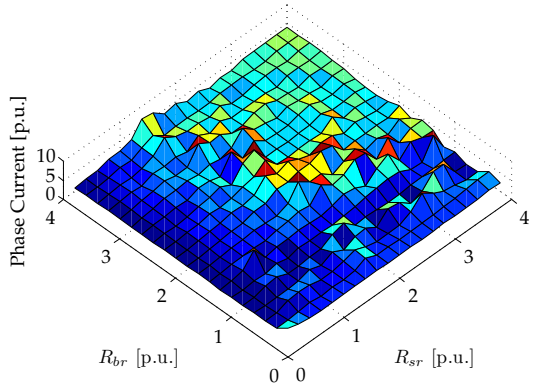

(c) Maximum instantaneous phase current during resistance removal as a function of series resistance and shunt resistance with $u_w = 11\,\mathrm{m/s}$

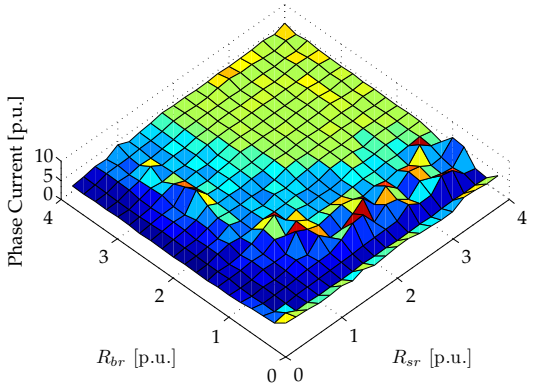

(d) Maximum instantaneous phase current during resistance removal as a function of series resistance and shunt resistance with $u_w = 12\,\mathrm{m/s}$

Figure C.8: The effect of series resistance value and shunt resistance value on removal current for the Irish fault profile with steady wind conditions.

APPENDIX D

C SOURCE CODE

This appendix contains the C code listings for significant functions from the MCU source code produced by the author.

D.1 Program Management Functions

D.1.1 main

```
1  /* Main program function */
2  void main(void)
3  {
4  // 0. Unlock CSM (for the moment dummy PW's 0xFFFF used)
5    CsmUnlock();
6
7  // 1. Initialize System Control:
8    // PLL, WatchDog, enable Peripheral Clocks
9    InitSysCtrl();                  //DSP2802x_SysCtrl.c
10
11 // 2. Clear all interrupts and initialize PIE vector table:
12   setupINTs();                  //ISRFuncs.c
13
14 // 3.1. Load time-critical (and other special) funcs into RAM:
15   MemCopy(&RamfuncsLoadStart, &RamfuncsLoadEnd, &RamfuncsRunStart);
16
17 // 3.2. Load frequently accessed const's into RAM
18   MemCopy(&RamConstsLoadStart, &RamConstsLoadEnd, &RamConstsRunStart);
19
20 // 3.3. Call Flash Initialization to setup flash waitstates
21     InitFlash();
22
23 // 4. Initialise CPU timers:
24   setupTimers();
25
26 // 5. Initialise output functions (LEDs, relays and SPI to DAC):
27   setupGPIOs();                 //OutputFuncs.c
28
29 // 6. Initialise and configure the ADC:
30   InitAdc();                    //InputFuncs.c
31   setupADC();
32
33 // 7. Enable/Disable Functions (initially):
34   sysStatus.goSync = 0;
35   sysStatus.goSpCn = 1;
```

```
36    sysStatus.goOnln = 0;
37
38  // 8. Enable ADC, Timers and Interrupts:
39    enableADC();
40    startTimers();
41    enableINTs();                 //ISRFuncs.c
42    setupSPI();                   //OutputFuncs.c
43
44  // 9. IDLE loop:
45     for(;;);
46  }
```

D.1.2 Interrupts

```
1   /** CUSTOM ISR FUNCTIONS**/
2   /* ISR for CPU Timer 0 (TINT0) - ADC Triggering */
3   interrupt void cpu_timer0_isr(void)
4   {
5     CpuTimer0.InterruptCount++;
6
7       // Acknowledge this interrupt to receive more interrupts from group 1:
8       PieCtrlRegs.PIEACK.all = PIEACK_GROUP1;
9   }
10
11  /* ISR for CPU Timer 1 (TINT1) - Status Updates*/
12  interrupt void cpu_timer1_isr(void)
13  {
14    CpuTimer1.InterruptCount++;
15
16    // Update readiness status of contactors:
17    updateSReady();
18
19    // Update status indicators:
20    updateStatusLEDs();
21
22    // Increment over-speed protection timer:
23    ovSpdProt(0);
24  }
25
26
27  /* ISR for ADC Conversion Complete (Batch SOC1 - 9) */
28  interrupt void ADC_isr(void)
29  {
30    // High level control for pre- and post-sync situations:
31    superviseControl();
32
33    // Clear ADCINT1 flag to allow next interrupt:
34    AdcRegs.ADCINTFLGCLR.bit.ADCINT1 = 1;
35
```

```
36    // Acknowledge interrupt to PIE:
37    PieCtrlRegs.PIEACK.all = PIEACK_GROUP1;
38  }
39
40  /* ISR for button 1 (XINT1)*/
41  interrupt void button_1_isr(void)
42  {
43    // Toggle between normal operation and all-stop mode:
44    sysStatus.goOnln = 1 - sysStatus.goOnln;
45
46    // Acknowledge this interrupt to receive more interrupts from group 1
47      PieCtrlRegs.PIEACK.all = PIEACK_GROUP1;
48  }
49
50  /* ISR for button 2 (XINT2)*/
51  interrupt void button_2_isr(void)
52  {
53    // Toggle sync permission:
54    sysStatus.goSync = 1 - sysStatus.goSync;
55
56    // Acknowledge this interrupt to receive more interrupts from group 1
57      PieCtrlRegs.PIEACK.all = PIEACK_GROUP1;
58  }
59  /** END - CUSTOM ISR FUNCTIONS**/
```

D.1.3 Supervisory Control Function

```
1   /* Manage high-level control functions */
2   void superviseControl (void)
3   {
4     /** SAMPLE AND PROCESS SIGNALS **/
5
6     /* Sampling and processing functions: */
7     // Process A/D samples:
8     sampleVnI();
9
10    // Set output to DAC-B
11    outVar(p_gen,0.1);
12
13    // Convert values to alpha-beta vector mag+ang, calc diff's:
14    analyseWFs();
15
16    // Update GENERATOR and GRID frequency measurements:
17    f_gen      = getGenFreq(1);
18    f_grid     = getGridFreq(1);
19
20    // Determine freq (orig. NOT abs val), magnitude and angle differences:
21    diff_f     = f_grid - f_gen;            // [Hz]
22    diff_m     = Vgrid_mag - Vgen_mag;          // [V]
```

```
23    diff_a     = (Vgrid_ang - Vgen_ang) * radDegScale; // [Deg]
24
25    // Check for direction mismatch:
26    if (f_grid * f_gen < 0.0)
27    {
28      sysStatus.errCode = 8;
29    }
30
31    // Get absolute value for further evaluation
32    if (f_gen < 0.0)
33    {
34      f_gen    = f_gen * (-1.0);
35    }
36
37    if (f_grid < 0.0)
38    {
39      f_grid   = f_grid * (-1.0);
40    }
41
42    // Monitor condition of the grid before allowing sync etc:
43    monGrid();
44
45    /** CONTROL SPEED AND GRID CONNECTION **/
46    // Undertake normal speed control, synchronisation and on-grid compensation:
47    if(sysStatus.goOnln && !sysStatus.gridOff)
48    {
49      if(sysStatus.syncd)
50      {
51        // Increment on-grid timer:
52        if (onGridTmr < onGridThres)
53        {
54          onGridTmr++;
55        }
56
57        // Monitor gen-grid status and take action if necessary:
58        monSync();
59
60        // Implement over-current protection:
61        currProt();
62
63        // Protect against motoring under low wind:
64        revPowProt();
65      }
66      else
67      {
68        // Reset on-grid timer:
69        onGridTmr = 0;
70
71        // Determine action depending on generator frequency range:
```

```
72        if (f_gen < f_ll)
73        {
74          /*  Allow turbine to run freely until wind is strong enough
75            to cause it to accelerate into the operational speed range */
76
77          // De-activate thyristors (under-voltage/freq):
78          turnOffSwitch(5);
79
80          // Clear overspeed protection and allow free acc. IF timer has elapsed:
81          ovSpdProt(2);
82        }
83        else if (f_gen > f_l && f_gen < f_u && !sysStatus.ovSpd)
84        {
85          // Activate thyristor control:
86          turnOffSwitch(1);
87          switchReady.S5 = 1;      //Bypass switching delay
88          turnOnSwitch(5);
89
90          // Attempt to synchronise to grid:
91          trySync();
92        }
93        else if (f_gen > f_uu && Vgen_mag > V_ll)
94        {
95          // Prevent dangerous over-speed:
96          ovSpdProt(1);
97        }
98
99        // Update PI speed control signal:
100       thyCn = PIDFreq(f_gen);
101     }
102
103     // Protect against imbalance (phase failure):
104     balProt();
105   }
106   // Perform forced shut down due to emergency condition or maintenance:
107   else
108   {
109     stopAll();
110   }
111
112   // Set thyristor firing level (0 - 100) (DAC-A):
113
114   if (sysStatus.goSpCn)
115   {
116     setThy(thyCn);
117   }
118   else
119   {
120     setThy(thyUnCn);
```

```
121   }
122 }
```

D.2 Analysis Functions

D.2.1 Space Vector Analysis

```
1  void analyseWFs (void)
2  {
3    // 1. Variable Instantiation:
4    // New Alpha-Beta Components:
5    float nVgen_alp, nVgen_bet;
6    float nVgrid_alp, nVgrid_bet;
7    float ni_alp, ni_bet;
8
9    // Internal variables for averaging:
10   static int aveCnt = 0;
11   static float Vgen_tmp, Vgrid_tmp, i_tmp = 0;
12
13   // 2. Alpha-Beta Operations:
14   // 2.1. Convert to alpha-beta domain:
15   clarke(Vgen_u, Vgen_v, Vgen_w, &nVgen_alp, &nVgen_bet);
16   clarke(Vgrid_a, Vgrid_b, Vgrid_c, &nVgrid_alp, &nVgrid_bet);
17   clarke(i_u, i_v, i_w, &ni_alp, &ni_bet);
18
19   // 2.2. Filter alpha-beta values:
20   filtVgen(nVgen_alp, nVgen_bet);
21   filtVgrid(nVgrid_alp, nVgrid_bet);
22   filtIgen(ni_alp, ni_bet);
23
24   // 2.3. Determine vector magnitudes and angles:
25   Vgen_tmp  += mag(Vgen_alp, Vgen_bet);
26   Vgen_ang  = ang(Vgen_alp, Vgen_bet);
27
28   Vgrid_tmp   += mag(Vgrid_alp, Vgrid_bet);
29   Vgrid_ang   = ang(Vgrid_alp, Vgrid_bet);
30
31   i_tmp   += mag(i_alp, i_bet);
32   i_ang   = ang(i_alp, i_bet);
33
34   // 2.4. Average vector magnitudes:
35   if (aveCnt < magAveCnts)
36   {
37     aveCnt++;
38   }
39   else
40   {
41     Vgen_mag  = (Vgen_tmp / aveCnt) * PkToRMS;
```

```
42      Vgrid_mag    = (Vgrid_tmp / aveCnt) * PkToRMS;
43      i_mag    = (i_tmp / aveCnt) * PkToRMS;
44      aveCnt     = 0;
45      Vgen_tmp   = 0;
46      Vgrid_tmp    = 0;
47      i_tmp      = 0;
48    }
49
50    // 2.5. Current summation for balance checking:
51    i_sum = i_u + i_v + i_w;
52
53    // 2.6. Real electrical power calc in kW (0.003*0.85):
54    p_gen = 0.00255 * Vgen_mag * i_mag * (_IQtoF(_IQcos(_IQ(Vgen_ang - i_ang))));
55  }
```

D.2.2 Clarke Calculations

```
1  /** ALPHA-BETA FUNCTIONS **/
2  /* Convert input ABC signals into alpha-beta equivalents */
3  void clarke(float x_a, float x_b, float x_c, float *Ptr_alpha, float *Ptr_beta)
4  {
5    *Ptr_alpha       = 0.666667 * (x_a - 0.5 * (x_b + x_c));
6    *Ptr_beta        = ovRt3 * (x_b - x_c);
7  }
8
9  /* Calculate the magnitude of the space vector for the given
10    alpha-beta components */
11 float mag(float x_alp, float x_bet)
12 {
13   return (_IQtoF(_IQmag(_IQ(x_bet), _IQ(x_alp))));
14 }
15
16 /*  Calculate the angle of the space vector for the given
17   alpha-beta components (-Pi to Pi RAD)*/
18 float ang(float x_alp, float x_bet)
19 {
20   return (_IQtoF(_IQatan2(_IQ(x_bet), _IQ(x_alp))));
21 }
22 /** END - ALPHA-BETA FUNCTIONS **/
```

D.2.3 Frequency Measurement

```
1  float getGenFreq (char instr)
2  {
3    static float genFreq  = 0;  // Averaged, unfiltered generator frequency
4    static float Vgen_ang_p = 0;  // Previous generator angle
5    static float accum    = 0;  // Accumulated grad vals to ave
6    static int cntr     = 0;  // Count number of samples between ZCs
```

```
7   float genFreqF      = 0;  // Filtered generator frequency
8
9   if (instr == 1)
10  {
11    int ang_p = (int)Vgen_ang_p;  // Integer value of previous angle
12    int ang_n = (int)Vgen_ang;    // Integer value of latest angle
13
14    // XOR of sign bits to determine zero crossing:
15    if ((ang_p >> 15) ^ (ang_n >> 15))
16    {
17      // Don't try to calc grad with this pair!
18
19      // Calculate average:
20      if (cntr != 0)
21      {
22        genFreq = (accum / cntr) / dPi;
23
24        // Reset for next segment:
25        accum = 0;
26        cntr = 0;
27
28        // Apply external averaging:
29        genFreq = aveFgen (genFreq);
30      }
31    }
32    else
33    {
34      accum += (Vgen_ang - Vgen_ang_p) / Timer0Int_s;
35      cntr++;
36    }
37
38    // Store latest angle value to be prev value next time:
39    Vgen_ang_p = Vgen_ang;
40
41    //Filter freq signal:
42    genFreqF = filtFgen(genFreq);
43  }
44
45  // Only return non-zero freq. is voltage is above basic limit:
46  if (Vgen_mag > V_fl)
47  {
48    return genFreqF;
49  }
50  else
51  {
52    return 0.0;
53  }
54 }
```

D.2.4 Grid Status Monitoring

```
/* Provide grid status indicators for other functions */
void monGrid (void)
{
  // Grid down-time timer to allow islanding prevention
  // and to disconnect according to code req:
  static unsigned int gridOffTime = 0;

  // Monitor grid voltage level:
  // Nominal:
  if (Vgrid_mag > Vgrid_nomMin && Vgrid_mag < Vgrid_nomMax)
  {
    sysStatus.VgridErr  = 0;
    sysStatus.VgridNom  = 1;
  }
  // Tolerable:
  else if (Vgrid_mag > Vgrid_absMin && Vgrid_mag < Vgrid_absMax)
  {
    sysStatus.VgridErr  = 0;
    sysStatus.VgridNom  = 0;
  }
  // Faulted:
  else
  {
    sysStatus.VgridErr  = 1;
    sysStatus.VgridNom  = 0;
  }

  // Monitor grid frequency:
  // Nominal:
  if (f_grid > Fgrid_nomMin && f_grid < Fgrid_nomMax)
  {
    sysStatus.FgridErr  = 0;
  }
  // Faulted:
  else
  {
    sysStatus.FgridErr  = 1;
  }


  // Determine if grid is nominal:
  if (sysStatus.VgridNom && !sysStatus.FgridErr)
  {
    sysStatus.gridOK  = 1;
  }
  else
  {
    sysStatus.gridOK  = 0;
```

```
49    }
50
51    // Monitor grid fault duration:
52    // If no fault is present:
53    if (!sysStatus.VgridErr && !sysStatus.FgridErr)
54    {
55      // Reset grid 'off-time' timer:
56      gridOffTime      = 0;
57    }
58    // If fault is present and grid is NOT yet marked as 'offline':
59    else if (!sysStatus.gridOff)
60    {
61      // Increment off-timer once per ms cycle.
62      gridOffTime++;
63    }
64    // Determine if grid has been faulted ('offline') for too long:
65    if (gridOffTime < maxGridOff)
66    {
67      sysStatus.gridOff    = 0;
68    }
69    else
70    {
71      sysStatus.gridOff    = 1;
72      sysStatus.errCode = 2;
73    }
74  }
```

D.3 Control Functions

D.3.1 Synchronisation

```
1  /* Synchronise if system is within pre-determined margins */
2  void trySync (void)
3  {
4    // Test sync conditions:
5    // Grid voltage and frequency must be nominal:
6    if(sysStatus.gridOK)
7    {
8      // Frequency (speed) and direction condition:
9      if (diff_f < pMarg_f && diff_f > nMarg_f)
10     {
11       // Voltage (RMS) amplitude condition:
12       if (diff_m < pMarg_m && diff_m > nMarg_m)
13       {
14         // Voltage waveform phase angle condition:
15         if (diff_a < pMarg_a && diff_a > nMarg_a)
16         {
17           // Synchronise:
```

```
18            if (sysStatus.goSync)
19            {
20              // Switch in both direct and series R grid connections:
21              turnOnSwitch(3);
22              turnOnSwitch(4);
23            }
24
25            if (checkSwitch(3))
26            {
27              sysStatus.syncd = 1;
28
29              // !!! Delay removal of Dumping Load:
30              switchReady.S5 = sDelay;
31              //(Standard delay used, but may be changed...)
32            }
33          }
34        }
35      }
36    }
37  }
```

D.3.2 PI Speed Control

```
1  /* Apply closed-loop PI control to f_gen thru thyrsitors */
2  float PIDFreq (float f_gen)
3  {
4    static float s_i = 0;
5    float f_err = 0;
6    float s_p = 0;
7    float sig = 0;
8
9    // Determine error signal (reversed to give least FA and biggest error):
10   f_err = f_gen - f_ref;
11
12   // PI:
13   s_p = Kp * f_err;            // Proportional component
14   s_i = s_i + Ki * f_err * Timer0Int_s; // Forward Euler intergral component
15
16   /* Note: we neglect dividing delta_f by the time step because this is
17         a constant term that needlessly adds to computational burden
18         so the effect is incorporated into the Kd value pre-runtime. */
19
20   // Limit integral value:
21   if (s_i < s_iMin)
22   {
23     s_i = s_iMin;
24   }
25   else if (s_i > s_iMax)
26   {
```

```
27      s_i = s_iMax;
28    }
29
30    sig = s_p + s_i + s_offset;
31
32    // Limit overall value:
33    if (sig < 0)
34    {
35      sig = 0;
36    }
37    else if (sig > 100)
38    {
39      sig = 100;
40    }
41
42    return sig;
43  }
```

D.3.3 Thyristor Control

```
1  /*  Determine DAC output reference from percentage load signal (empirically derived).
2    The output signal is determined from a polynomial equation, which varies
3    depending on the magnitude of the command signal 'H_l' = u */
4  void setThy(float u)
5  {
6    static float sig = 0;
7    float uSq, uCu;
8
9    if(u < 0)
10   {
11     u = 0;
12   }
13   else if(u > 100)
14   {
15     u = 100;
16   }
17
18   uSq = u * u;
19   uCu = uSq * u;
20
21   if(u < sect1)
22   {
23     sig = s1a * uCu + s1b * uSq + s1c * u + s1d;
24   }
25   else if(u > sect2)
26   {
27     sig = s2a * uCu + s2b * uSq + s2c * u + s2d;
28   }
29
```

```
30   setDACA(sig);
31 }
```

D.4 Protection Functions

D.4.1 On-Grid Fault Protection

```
1  /* Monitor gen-grid interaction AFTER sync */
2  void monSync (void)
3  {
4    // OnGridTmr delays action at sync to allow any grid disturbance
5    // caused by sync to settle.
6    if (onGridTmr >= onGridThres)
7    {
8      // Disconnect immediately on grid freq fault:
9      if (sysStatus.FgridErr)
10     {
11       // Remove gen from grid:
12       emergDisconn();
13
14       sysStatus.errCode = 3;
15     }
16     // Apply LVRT compensation for grid voltage fault:
17     else if (sysStatus.VgridErr)
18     {
19       // Open S3:
20       if (checkSwitch(3))
21       {
22         // Force S3 to be ready
23         switchReady.S3 = 1;
24
25         turnOffSwitch(3);
26       }
27
28       // Activate PAC-LVRT:
29       //...
30
31       // Signal LVRT was activated:
32       sysStatus.errCode = 7;
33     }
34     // If no faults are present:
35     else
36     {
37       // Disconnect caps, dumping load and thyristors if still in use:
38       if (checkSwitch(1))
39       {
40         turnOffSwitch(1);
41       }
```

```
42        if (checkSwitch(5))
43        {
44          turnOffSwitch(5);
45        }
46
47        // Remove any series compensation:
48        if (!checkSwitch(3))
49        {
50          turnOnSwitch(3);
51        }
52
53      }
54    }
55  }
```

D.4.2 Over-Current Protection

```
1  /* Monitor RMS current and protect against over current */
2  void currProt (void)
3  {
4    if ((i_u * i_u > i_sq_lim) || (i_v * i_v > i_sq_lim) || (i_w * i_w > i_sq_lim))
5    {
6      emergDisconn();
7
8      sysStatus.errCode = 4;
9    }
10 }
```

D.4.3 Reverse Power Protection

```
1  /*  Monitor real direction to disconnect during low wind conditions. */
2  void revPowProt (void)
3  {
4    static unsigned int pCnt  = 0;     // Sample counter
5
6    // Increment sample counter:
7    pCnt++;
8
9    /* Increment reverse power instance counter if current and voltage
10     are out of phase. Voltage and current references are
11     opposite, i.e. voltage on gen ref, current on grid ref. Hence
12     the product of the phase angles must be greater than zero, not
13     less than zero for revPow condition. The revPowLim threshold is
14     important to set correctly to both prevent nuisance tripping
15     (if too low) and non-detection (if too high). Basically, the
16     protection works by counting the indcidents of revPow in a
17     certain time and trips if the incidents exceed revPowLim. */
18   if (Vgen_ang * i_ang > 0)
```

```
19    {
20      revPow++;
21    }
22
23    if (pCnt > pCntLim)
24    {
25      pCnt = 0;
26
27      if (revPow > revPowLim)
28      {
29        emergDisconn();
30
31        // Force S3,4 off for longer delay:
32        switchReady.S3    = 15;
33        switchReady.S4    = 15;
34
35        sysStatus.errCode   = 5;
36      }
37
38      revPow = 0;
39    }
40  }
```

D.4.4 Over-Speed Protection

```
1   /* Protect against and manage multiple occurences of over-speed events */
2   void ovSpdProt (char instr)
3   {
4     // Local static variables:
5     static unsigned int ovSpdCnt  = 0;        // Incident counter
6     static unsigned int ovSpdTmr  = ovSpdPer;     // Timer
7     static unsigned int incident  = 0;        // Capture single overspeed incident
8
9     // Decrement timer:
10    if (instr == 0)
11    {
12      ovSpdTmr--;
13
14      if (ovSpdTmr == 0)
15      {
16        ovSpdCnt = 0;
17        ovSpdTmr = ovSpdPer;
18      }
19    }
20    // Act on detected overspeed:
21    else if (instr == 1)
22    {
23      stopAll();
24
```

```
25      // Increment count of over-speed events in sampling period
26      if (!incident)
27      {
28        // Indicate overspeed incident has taken place:
29        incident = 1;
30
31        // Increment incident counter:
32        ovSpdCnt++;
33      }
34
35      // Indicate over-speed occurence and prevent normal operation
36      // until low speed is achieved and cooldown (if needed) is over:
37      sysStatus.errCode   = 1;
38      sysStatus.ovSpd    = 1;
39
40      // Activate cooldown if excessive over-speeds have occured in this period:
41      if (ovSpdCnt > ovSpdLim)
42      {
43        ovSpdTmr = ovSpdCooldwn;
44      }
45    }
46    // Clear overspeed detection if timer is elapsed:
47    else if (ovSpdCnt <= ovSpdLim)
48    {
49      // Allow free acceleration:
50      turnOffSwitch(1);
51
52      // Clear overspeed status:
53      sysStatus.ovSpd = 0;
54
55      // Indicate overspeed incident is over:
56      incident = 0;
57    }
58  }
```

D.4.5 Phase Imbalance Protection

```
1  /* Monitor RMS current balance and disconnect if phase failure occurs
2    Note: the timer DOES NOT automatically reset after an imbalance -
3    the MCU must be hard-reset to allow continued operation      */
4  void balProt (void)
5  {
6    static unsigned int unbalTime = 0;
7
8    if (i_sum > unbalLim)
9    {
10     unbalTime++;
11   }
12
```

```
13    if (unbalTime > unbalTLim)
14    {
15      sysStatus.goOnln = 0;
16
17      sysStatus.errCode = 6;
18    }
19  }
```

APPENDIX E

LED STATUS INDICATIONS

The three externally mounted status LEDs convey WECS status information to the operator. The first two indicate the present status of the grid and SS-PMG/GCC, while the third records the latest error logged by the GCC.

E.1 Grid Status LED

Table E.1: Grid status LED interpretation.

LED State	Message
On	All grid conditions are nominal
Off	Grid voltage or frequency fault
Blinking	Tolerable grid voltage deviation

E.2 Mode LED

Table E.2: Mode LED interpretation.

LED State	Message
On	SS-PMG is connected to the grid (S3 and S4 closed)
Off	GCC is in 'Stop All' mode - all functions deactivated
Blinking	GCC is attempting to synchronise the SS-PMG with the grid

E.3 Error LED

Error LED messages begin with a long blink then consecutive short blinks that add up to represent the error number. The number of blinks stated below refers to the short blinks after the long blink. The pattern of long then short blinks is repeated indefinitely until a new error is recorded. The error LED therefore indicates the most recent error condition to have occurred.

Table E.3: Error LED interpretation.

Short Blinks	**Message**
0	No errors recorded since GCC was initialised
1	Temporary 'Stop All': generator over-speed
2	Temporary shut down: grid off-line timer (anti-islanding)
3	Temporary disconnect: grid frequency fault
4	Temporary disconnect: over-current
5	Temporary disconnect: reverse power (low wind)
6	Permanent disconnect: phase imbalance detected
7	LVRT triggered: grid voltage fault
8	Synchronisation blocked: rotational direction mismatch between SS-PMG and grid

BIBLIOGRAPHY

[1] REN21: Renewables 2011 Global Status Report. Tech. Rep., REN21 Secretariat, Paris, 2011.

[2] Hansen, A. and Hansen, L.: Wind turbine concepts market penetration over ten years (1995 to 2004). *Wind Energy*, vol. 10, no. 1, pp. 81 – 97, 2007.

[3] Westlake, A., Bumby, J. and Spooner, E.: Damping the power-angle oscillations of a permanent-magnet synchronous generator with particular reference to wind turbine applications. *IEE Proceedings on Electric Power Application*, vol. 143, no. 3, pp. 269 – 280, 1996.

[4] Hansen, M.O.: *Aerodynamics of Wind Turbines*. James and James, London, UK, 2000.

[5] Timbus, A., Teodorescu, R., Blaabjerg, F. and Liserre, M.: Synchronization methods for three phase distributed power generation systems. an overview and evaluation. In: *Power Electronics Specialists Conference, 2005. PESC '05. IEEE 36th*, pp. 2474 –2481. Recife, Brazil, June 2005.

[6] Stannard, N. and Bumby, J.: Performance aspects of mains connected small scale wind turbines. *IET Generation, Transmission & Distribution*, vol. 1, no. 2, pp. 348 – 356, 2007.

[7] Ipinnimo, O., Chowdhury, S. and Chowdhury, S.: Effects of distributed generation (DG) on voltage dips in electricity networks. In: *20th Southern African Universities Power Engineering Conference*. Cape Town, 2011.

[8] Eskom: More rolling blackouts [Online] (2007). Available at: http://bit.ly/qBcY9J, [2011, Aug. 10].

[9] Guezuraga, B., Zauner, R. and Poelz, W.: Life cycle assessment of two different 2 mw class wind turbines. *Renewable Energy*, vol. 37, pp. 37 – 44, 2012.

[10] Department of Energy: Integrated Resource Plan for Electricity 2010 – 2030 [Online] (2011). Available at: http://bit.ly/rlJu1P, [2011, Sep 30].

[11] Renewables bidders conference reflects high levels of interest in SA roll-out [Online] (2011). Available at: http://bit.ly/nkEzeg, [2011, Sep. 14], .

[12] Manufacturing jobs vulnerable to yet more power price increases [Online] (2011). Available at: http://bit.ly/oVtADq, [2011 Oct 8], .

[13] Painuly, J.P.: Barriers to renewable energy penetration; a framework for analysis. *Renewable Energy*, vol. 24, no. 1, pp. 73 – 89, 2001. ISSN 0960-1481.

[14] Turkay, B. and Telli, A.: Economic analysis of standalone and grid connected hybrid energy systems. *Renewable Energy*, vol. 36, no. 1, pp. 1931 – 1943, 2011.

[15] Reddy, S. and Painuly, J.P.: Diffusion of renewable energy technologies – barriers and stakeholders' perspectives. *Renewable Energy*, vol. 29, no. 9, pp. 1431 – 1447, 2004. ISSN 0960-1481.

[16] Simplified tender being prepared for small renewables projects [Online] (2011). Available at: http://bit.ly/r67cS2, [2011, Sep. 30], .

[17] Kestrel Small Wind Turbines for Renewable Energy [Online] (2010). Available at: http://bit.ly/obDShn, [2010, Nov. 15].

[18] African Wind Power [Online] (2010). Available at: http://bit.ly/qnQgSI, [2010, Nov. 15].

[19] Isivunguvungu Wind Energy Converter [Online]. Available at: http://bit.ly/p8g7EJ, [2011, Oct 6].

[20] Thiringer, T.: Grid-friendly connecting of constant-speed wind turbines using external resistors. *IEEE Transactions on Energy Conversion*, vol. 17, no. 4, pp. 537 – 542, December 2002. ISSN 0885-8969.

[21] Gomez, S. and Amenedo, J.: Grid synchronisation of doubly fed induction generators using direct torque control. In: *IEEE Industrial Electronics Conference (IECON)*, pp. 3338 – 3343. Sevilla, Spain, 5 - 8 Nov 2002.

[22] Hansen, L.H., Helle, L., Blaabjerg, F., Ritchie, E., Munk-Nielsen, S., Bindner, H., Sorensen, P. and Bak-Jensen., B.: Conceptual survey of generators and power electronics for wind turbines. Tech. Rep., Riso National Laboratory, Roskilde, Denmark, December 2001.

[23] Hosaka, N. and Kumano, T.: Evaluation of voltage fluctuation in electric power system with wind power generators. In: *Power and Energy Society General Meeting - Conversion and Delivery of Electrical Energy in the 21st Century, 2008 IEEE*, pp. 1 –6. jul 2008. ISSN 1932-5517.

[24] Resende, F. and Lopes, J.: Evaluating the performance of external fault ride-through solutions used in wind farms with fixed speed induction generators when facing unbalanced faults. In: *PowerTech, 2009 IEEE Bucharest*, pp. 1 –6. Bucharest, jul 2009.

[25] de Mello, F., Feltes, J., Hannett, L. and White, J.: Application of induction generators in power systems. *IEEE Transactions on Power Apparatus and Systems*, vol. PAS-101, no. 9, pp. 3385 –3393, September 1982. ISSN 0018-9510.

[26] Brenna, M., Foiadelli, F. and Zaninelli, D.: The impact of the wind generation connected to weak grids. In: *International Symposium on Power Electronics, Electrical Drives, Automation and Motion (SPEEDAM)*, pp. 1481 –1485. June 2008.

[27] Polinder, H., van der Pijl, F.F.A., de Vilder, G.-J. and Tavner, P.J.: Comparison of direct-drive and geared generator concepts for wind turbines. *IEEE Transactions on Energy Conversion*, vol. 21, no. 3, pp. 725 – 733, Sep 2006.

[28] Morel, L., Godfroid, H., Mirzaian, A. and Kauffmann, J.: Double-fed induction machine: converter optimisation and field oriented control without position sensor. *IEE Proceedings on Electric Power Applications*, vol. 145, no. 4, pp. 360 –368, jul 1998. ISSN 1350-2352.

[29] Lalor, G., Mullane, A. and O'Malley, M.: Frequency control and wind turbine technologies. *IEEE Transactions on Power Systems*, vol. 20, no. 4, pp. 1905 – 1913, November 2005. ISSN 0885-8950.

[30] Akhmatov, V.: Modelling and ride-through capability of variable speed wind turbines with permanent magnet generators. *Wind Energy*, vol. 9, no. 4, pp. 313–326, 2006. ISSN 1099-1824.

[31] Eltamaly, A.M.: Modeling of wind turbine driving permanent magnet generator with maximum power point tracking system. *Engineering Science*, vol. 19, no. 2, pp. 223 – 237, 2007.

[32] Jiang, H., Dorsey, J., Habetler, T. and Eckroth, K.V.: A cost effective generator brake for improved generator transient response. *IEEE Transactions on Power Systems*, vol. 9, no. 4, pp. 1840 – 1846, 1994.

[33] Yingcheng, X. and Nengling, T.: Review of contribution to frequency control through variable speed wind turbine. *Renewable Energy*, vol. 36, no. 6, pp. 1671 – 1677, 2011. ISSN 0960-1481.

[34] Baroudi, J.A., Dinavahi, V. and Knight, A.M.: A review of power converter topologies for wind generators. *Renewable Energy*, vol. 32, no. 14, pp. 2369 – 2385, 2007. ISSN 0960-1481.

[35] Potgieter, J. and Kamper, M.: Design of new concept permanent magnet induction wind generator. In: *IEEE Energy Conversion Congress and Exposition (ECCE)*, pp. 2403 –2408. Atlanta, Georgia, USA, Sep 2010.

[36] Potgieter, J.: *Design and Analysis of Gearless Direct-Grid Permanent Magnet Induction Wind Generator*. Master's thesis, Electrical and Electronic Engineering, University of Stellenbosch, Stellenbosch, South Africa, March 2011.

[37] Hansen, A. and Michalke, G.: Multi-pole permanent magnet synchronous generator wind turbines' grid support capability in uninterrupted operation during grid faults. *Renewable Power Generation, IET*, vol. 3, no. 3, pp. 333 –348, September 2009. ISSN 1752-1416.

[38] Svensson, J.: Synchronisation methods for grid-connected voltage source converters. *IEE Proceedings on Generation, Transmission and Distribution*, vol. 148, no. 3, pp. 229 –235, May 2001. ISSN 1350-2360.

[39] Mueller, H., Poeller, M., Basteck, A., Tilscher, M. and Pfister, J.: Grid compatibility of variable speed wind turbines with directly coupled synchronous generator and hydro-dynamically controlled gearbox. In: *Sixth Int. Workshop on Large-Scale Integration of Wind Power and Transmission Networks for Offshore Wind Farms*, pp. 307 – 315. Delft, Netherlands, Oct 2006.

[40] Grabic, S., Celanovic, N. and Katic, V.: Permanent magnet synchronous generator cascade for wind turbine application. *IEEE Transactions on Power Electronics*, vol. 23, no. 3, pp. 1136 –1142, May 2008. ISSN 0885-8993.

[41] Bouwer, P., Potgieter, J. and Kamper, M.: Modelling and dynamic performance of a direct-drive direct-grid slip permanent magnet wind generator. In: *IEEE International Electrical Machines and Drives Conference (IEMDC)*, pp. 137 – 142. Niagara Falls, Canada, 15 - 18 May 2011.

[42] Troester, E.: *Hochpolige Asynchronmaschine mit Permanentmagnetzwischenlaufer als windkraftgenerator*. Ph.D. thesis, Technischen Universitaet Darmstadt, 2009.

[43] Herbert, G.J., Iniyan, S., Sreevalsan, E. and Rajapandian, S.: A review of wind energy technologies. *Renewable and Sustainable Energy Reviews*, vol. 11, no. 6, pp. 1117 – 1145, 2007. ISSN 1364-0321.

[44] Tavner, P., Bussel, G.V. and Spinato, F.: Machine and converter reliabilities in wind turbines. In: *3rd IET Conference on Power Electronics, Machines and Drives*, pp. 127 – 130. Dublin, Ireland, Mar 2006.

[45] Walford, C.: Wind turbine reliability: Understanding and minimizing wind turbine operation and maintenance costs. Tech. Rep. SAND2006-1100, Sandia National Laboratories, mar 2006.

[46] Blaabjerg, F., Teodorescu, R., Liserre, M. and Timbus, A.: Overview of control and grid synchronization for distributed power generation systems. *IEEE Transactions on Industrial Electronics*, vol. 53, no. 5, pp. 1398 –1409, October 2006. ISSN 0278-0046.

[47] Liu, Y., Zhu, Z.Q. and Howe, D.: Instantaneous torque estimation in sensorless direct-torque-controlled brushless dc motors. *IEEE Transactions on Industry Applications*, vol. 42, no. 5, pp. 1275 –1283, September 2006. ISSN 0093-9994.

[48] Gonzalez, L., Figueres, E., Garcera, G., Carranza, O. and Gonzalez-Espin, F.: Synchronization techniques comparison for sensorless control applied to wind energy conversion systems (WECS). In: *13th European Conference on Power Electronics and Applications (EPE '09)*, pp. 1 –9. September 2009.

[49] Nagliero, A., Mastromauro, R., Liserre, M. and Dell'Aquila, A.: Synchronization techniques for grid connected wind turbines. In: *35th Annual Conference of IEEE Industrial Electronics (IECON '09)*, pp. 4606 –4613. Porto, Portugal, Nov 2009. ISSN 1553-572X.

[50] Gonzalez, M., Cardenas, V. and Alvarez, R.: A fast detection algorithm for sags, swells, and interruptions based on digital rms calculation and kalman filtering. In: *International Power Electronics Congress, 10th IEEE*, pp. 1 –6. Puebla, Mexico, oct 2006.

[51] Muljadi, E., Pierce, K. and Migliore, P.: Control strategy for variable-speed, stall-regulated wind turbines. In: *The American Control Conference*, vol. 3, pp. 1710 –1714 vol.3. June 1998.

[52] Rajambal, K., Umamaheswari, B. and Chellamuthu, C.: Electrical braking of large wind turbines. *Renewable Energy*, vol. 30, no. 15, pp. 2235 – 2245, 2005. ISSN 0960-1481.

[53] Spooner, E. and Williamson, A.: Direct coupled, permanent magnet generators for wind turbine applications. *IEE Proceedings on Electric Power Applications*, vol. 143, no. 1, pp. 1 –8, jan 1996. ISSN 1350-2352.

[54] Chen, Z. and Spooner, E.: Power conversion system for a modular, direct-drive, permanent-magnet wind turbine generator. In: *IEE Colloquium: Power Electronics for Renewable Energy*. june 1997.

[55] Conroy, J. and Watson, R.: Low-voltage ride-through of a full converter wind turbine with permanent magnet generator. *Renewable Power Generation, IET*, vol. 1, no. 3, pp. 182 –189, september 2007. ISSN 1752-1416.

[56] Tamura, J., Yamazaki, T., Ueno, M., Matsumura, Y. and Kimoto, S.: Transient stability simulation of power system including wind generator by pscad/emtdc. In: *Power Tech Proceedings, 2001 IEEE Porto*, vol. 4, p. 5 pp. vol.4. Porto, Portugal, sep 2001.

[57] Ali, M. and Wu, B.: Comparison among stabilization methods of fixed-speed wind generator system. In: *IEEE Energy Conversion Congress and Exposition (ECCE)*, pp. 2667 – 2674. San Jose, California, 2009.

[58] Causebrook, A., Atkinson, D. and Jack, A.: Fault ride-through of large wind farms using series dynamic braking resistors (march 2007). *IEEE Transactions on Power Systems*, vol. 22, no. 3, pp. 966 –975, August 2007. ISSN 0885-8950.

[59] Zhang, J., Yin, Z., Xiao, X. and Di, Y.: Enhancement voltage stability of wind farm access to power grid by novel svc. In: *Industrial Electronics and Applications, 2009. ICIEA 2009. 4th IEEE Conference on*, pp. 2262 – 2266. may 2009.

[60] Narimani, M. and Varma, R.: Application of static var compensator (svc) with fuzzy controller for grid integration of wind farm. In: *Electrical and Computer Engineering (CCECE), 2010 23rd Canadian Conference on*, pp. 1 – 6. may 2010. ISSN 0840-7789.

[61] Molinas, M., Suul, J.A. and Undeland, T.: Low voltage ride through of wind farms with cage generators: Statcom versus svc. *IEEE Transactions on Power Electronics*, vol. 23, no. 3, pp. 1104 –1117, may 2008. ISSN 0885-8993.

[62] Aouzellag-Lahacani, N., Aouzellag, D. and Mendil, B.: Static compensator for maintaining voltage stability of wind farm integration to a distribution network. *Renewable Energy*, vol. 35, pp. 2476 – 2482, 2010.

[63] Hossain, M., Pota, H. and Ramos, R.: Robust statcom control for the stabilisation of fixed-speed wind turbines during low voltages. *Renewable Energy*, vol. 36, pp. 2897 – 2905, 2011.

[64] Yukita, K., Goto, Y., Ichiyanagi, K. and Hirose, K.: A study of electric power quality using storage system in distributed generation. In: *9th International Conference on Electrical Power Quality and Utilisation*. Barcelona, Spain, 9 - 11 Oct 2007.

[65] Ali, M., Murata, T. and Tamura, J.: Transient stability augmentation by fuzzy logic controlled braking resistor in multi-machine power system. In: *Transmission and Distribution Conference and Exhibition 2002: Asia Pacific. IEEE/PES*, vol. 2, pp. 1332 – 1337 vol.2. oct 2002.

[66] Ali, M., Murata, T. and Tamura, J.: Effect of coordination of optimal reclosing and fuzzy controlled braking resistor on transient stability during unsuccessful reclosing. *IEEE Transactions on Power Systems*, vol. 21, no. 3, pp. 1321 –1330, August 2006. ISSN 0885-8950.

[67] Freitas, W., Morelato, A. and Xu, W.: Improvement of induction generator stability using braking resistors. *IEEE Transactions on Power Systems*, vol. 19, no. 2, pp. 1247 – 1249, May 2004. ISSN 0885-8950.

[68] Ghazi, R. and Aliabadi, H.: Stability improvement of wind farms with fixed speed turbine generators using breaking resistors. In: *Electricity Distribution - Part 1, 2009. CIRED 2009. 20th International Conference and Exhibition on*, pp. 1 –4. Prague, Czech Republic, jun 2009. ISSN 0537-9989.

[69] Hansen, M., Sorensen, J., Voutsinas, S., Sorensen, N. and Madsen, H.: State of the art in wind turbine aerodynamics and aeroelasticity. *Progress in Aerospace Sciences*, vol. 42, no. 4, pp. 285 – 330, 2006. ISSN 0376-0421.

[70] Slootweg, J., de Haan, S., Polinder, H. and Kling, W.: General model for representing variable speed wind turbines in power system dynamics simulations. *IEEE Transactions on Power Systems*, vol. 18, no. 1, pp. 144 – 151, February 2003. ISSN 0885-8950.

[71] Yin, M., Li, G., Zhou, M. and Zhao, C.: Modeling of the wind turbine with a permanent magnet synchronous generator for integration. In: *Power Engineering Society General Meeting, 2007. IEEE*, pp. 1 –6. June 2007. ISSN 1932-5517.

[72] Li, S., Haskew, T. and Xu, L.: Conventional and novel control designs for direct driven pmsg wind turbines. *Elsevier Electric Power Systems Research*, vol. 80, no. 1, pp. 328 – 338, 2010.

[73] Nichita, C., Luca, D., Dakyo, B. and Ceanga, E.: Large band simulation of the wind speed for real time wind turbine simulators. *IEEE Transactions on Energy Conversion*, vol. 17, no. 4, pp. 523 – 529, 2002.

[74] Dolan, D. and Lehn, P.: Real-time wind turbine emulator suitable for power quality and dynamic control studies. In: *Internationa Conference on Power Systems Transients*. Montreal, Canada, 2005.

[75] Li, H., Zhao, B., Yang, C., Chen, H. and Chen, Z.: Analysis and estimation of transient stability for a grid-connected wind turbine with induction generator. *Renewable Energy*, vol. 36, no. 5, pp. 1469 – 1476, 2011. ISSN 0960-1481.

[76] Krause, P., Wasynczuk, O. and Sudhoff, S. (eds.): *Analysis of Electric Machinery and Drive Systems, 2nd Ed.* IEEE Press/Wiley-Interscience, 2002.

[77] International Electrotechnical Commission: *Tech. Report 60725: Consideration of reference impedances and public supply network impedances for use in determining disturbance characteristics of electrical equipment having a rated current less than or equal to 75 A per phase*. IEC, Geneva, Switzerland, 2005.

[78] Davies, T., Jefferson, C. and Mayer, R.: Automated synchronisation. In: *IEE Colloquim on Microcomputer Instrumentation and Control Systems in Power Electronics*. London, 1988.

[79] Hinrichsen, E. and Nolan, P.: Dynamics and stability of wind turbine generators. *IEEE Transactions on Power Apparatus and Systems*, vol. 101, no. 8, pp. 2640 – 2648, August 1982.

[80] van Zyl, S.: Dst 34-1765: Distribution standard for the interconnection of embedded generation. Available at: http://bit.ly/mTXdnk, [2011, June 3], March 2011.

[81] IEEE Standards Coordinating Committee 21: IEEE Standard for Interconnecting Distributed Resources with Electric Power Systems. Sep 2008.

[82] Olulope, P., Folly, K., Chowdhury, S. and Chowdhury, S.: Transient stability prediction of power system with distributed generation using recurrent neural network. In: *20th Southern African Universities Power Engineering Conference*. 2011.

[83] Mo, N., Zou, Z., Chan, K. and Pong, T.: Transient stability constrained optimal power flow using particle swarm optimisation. *Generation, Transmission Distribution, IET*, vol. 1, no. 3, pp. 476 –483, may 2007. ISSN 1751-8687.

[84] Bose, B.K.: *Modern Power Electronics and AC Drives*. Prentice Hall PTR, Upper Saddle River, NJ, 2002.

[85] Kanabar, M. and Khaparde, S.: Evaluation of rotor speed stability margin of a constant speed wind turbine generator. In: *Joint International Conference on Power System Technology and IEEE Power India Conference (POWERCON)*, pp. 1 –6. New Delhi, October 2008.

[86] Kyaw, M.M. and Ramachandaramurthy, V.: Fault ride through and voltage regulation for grid connected wind turbine. *Renewable Energy*, vol. 36, no. 1, pp. 206 – 215, 2011. ISSN 0960-1481.

[87] ESB-Networks: Irish Distribution Code. Ireland, Oct 2007.
Available at: http://bit.ly/sZjhyg

[88] The RSA Grid Code Secretariat: Grid code requirements for wind turbines connected to transmission or distribution systems in South Africa. Available at: http://bit.ly/smTwhB, [2011, Sep. 05], .

[89] The RSA Grid Code Secretariat: Grid code compliance test for wind energy facility connected to transmission or distribution grids in South Africa rev. 4.4. Available at: http://bit.ly/v9lQ6L, [2011, Sep. 05], .

[90] Ignatova, V., Granjon, P. and Bacha, S.: Space vector method for voltage dips and swells analysis. *IEEE Transactions on Power Delivery*, vol. 24, no. 4, pp. 2054 –2061, oct 2009. ISSN 0885-8977.

[91] South African Bureau of Standards: Nrs048-2: Electricity supply - quality of supply, part 2: Voltage characteristics, compatibility levels, limits and assessment methods. 2007.